

ABSTRACT

JOHNSON, CHARLES MILLER. Fabrication and Behavior of 3-D Orthogonal Woven FRP/Concrete Bridge Deck. (Under the direction of Dr. Sami Rizkalla).

In recent years, glass fiber reinforced polymer bridge decks have been considered as an alternative to conventional steel and concrete bridge decking. The research presented in this thesis investigated the behavior of an innovative 3-dimensionally woven bridge deck. The proposed bridge decks were woven at a local textile company, using the 3-D capabilities of the company. Typical decks consisted of two skins of E-glass fabric, and each skin consisted of two fabric layers. The fabric was woven with warp, weft, and vertical z-yarns. Additional z-yarns were used to form a longitudinal joint between the skins. Balsa wood cores were inserted between the skins and the entire deck was vacuum infused with an epoxy resin system.

The research included fabrication of two deck panels with appropriate shear connectors to provide composite action with the top concrete slab. The study included an investigation of the behavior of three types of shear connector configurations. Modeling of the behavior is based on the test results of the measured material properties. These experiments included tensile coupon experiments, fiber volume fraction by burn-off method, tensile experiments of the steel reinforcement, and compressive strength of the concrete to define the complete stress-strain relationship of the concrete using concrete cylinders. Predictions of the behavior were based on simple flexural member behavior and finite element analysis using ANSYS computer program. A U.S. patent is currently filed for the proposed innovative bridge deck panel.

Fabrication and Behavior of 3-D Orthogonal Woven FRP/Concrete Bridge Deck

by

Charles Miller Johnson

A thesis submitted to the Graduate Faculty of
North Carolina State University
in partial fulfillment of the
requirements for the Degree of
Master of Science

CIVIL ENGINEERING

Raleigh

March 15, 2006

APPROVED BY:

Dr. Sami Rizkalla (Chair)



Dr. James Nau



Dr. Emmett Sumner



to Hiram, Rita, John, Margaret, and Brooke

Biography

Charles Miller Johnson was born in Winston-Salem, North Carolina on October 12, 1981. He is the son of John Hiram and Rita Miller Johnson. He has one brother, John. Charles graduated from North Forsyth High School in Winston-Salem in 2000. He received his Bachelor of Science degree in Civil Engineering from North Carolina State University, graduating valedictorian in the spring of 2004.

The author worked on an undergraduate research project for Dr. Amir Mirmiran and Dr. Yutian Shao entitled “Plastic Shrinkage of TechFab, LLC Carbon Grid”. He interned one summer as an assistant to a superintendent for John S. Clark Construction Co. in Winston-Salem. He interned for two summers with Calloway, Johnson, Moore, & West, an Architectural/Engineering firm in Winston-Salem in 2003 and 2004.

Charles Johnson continued his education at North Carolina State University with the pursuit of a Masters of Science degree in Civil Engineering beginning in the fall of 2004. He served as a Teaching Assistant for the Structural Analysis and Matrix Structural Analysis courses. He was inducted into Chi Epsilon Civil Engineering Honor Fraternity and Tau Beta Pi Engineering Honor Fraternity. His graduate studies focused on Structural Engineering and Mechanics and research involved the application of 3-D woven composites. Upon graduation he will work at City Structures D&P, Inc. in Lewisville, North Carolina.

Acknowledgments

The author would like to thank the following people:

Dr. Sami Rizkalla, committee chair, who is one of the most distinguished structural engineers I will ever know. He is also one of the most approachable friends in the profession. I am grateful for the privilege to learn from his classes and appreciate his encouragement and the pride he takes in his research.

Dr. Emmett Sumner, committee member, whose sincere interest in the project and engineering knowledge were invaluable. I value his down to earth style and appreciate his time.

Dr. Jim Nau, committee member, whom I can sincerely call a friend. I appreciate his fellowship, kind words, and faith in my engineering capabilities.

Mr. Tarek Mohamed, graduate student and partner for this thesis. Tarek and I worked simultaneously on both theses and I would never have completed this project without him. He constantly forged ahead, educated me about textile composites, and encouraged me to always do my best.

Dr. Vernon Matzen, NCSU professor, from whom I took three classes and was a teaching assistant for two classes. Dr. Matzen's passion for engineering and ability to present complex material in a manner such that it seems "trivial" make him one of my greatest influences in structural engineering.

Dr. Mansour Mohamed, 3TEX founder and Chief Science Operator, whose experience and knowledge of composites and weaving was a priceless resource. Dr. Mohamed invented the weaving technology used and was supportive of this new application.

Mr. Bob Schartow, 3TEX infusion supervisor, from whom I learned everything I know about the infusion process. Bob was always approachable, concerned about the success of the project, and an encouraging friend.

Mr. Patrick Duke, 3TEX weaving and manufacturing supervisor, who helped primarily with the weaving aspects of the project, but also went out of his way to provide tools, time, and discuss insight into each phase of the fabrication process.

Mr. Brian Birdsall, Carolina Sunrock, who generously arranged the donation of materials used in this project and provided insight into concrete mix designs.

Mr. Jerry Atkinson, Constructed Facilities Laboratory Technician, who shared his expertise in general construction and laboratory testing helping me to finish the project.

Dr. Russell Gorga, NCSU Textiles professor, for his knowledge of composites and approach to research.

Mr. Tim Mumford, NCSU Textiles Synthetic Filament Lab Manager, for his cordiality and the use of his furnace for the fiber volume fraction tests.

Ms. Jan Pegram, NCSU Textiles Physical Testing Laboratory Manager, for use of the lab equipment and facilities.

Mr. Jahmaal Tillman, former undergraduate student, for his work ethic, his pride in the quality of the project, and his camaraderie.

Mr. Jerry Bridges, Mr. Michael Cropper, Mr. Mina Dawood, Mr. Jason Patrick,

Mr. John David Vickery, Mr. Zhenhua Wu, NCSU graduate students, for their practical insight, uncanny ability to get things done, willingness to listen and provide advice, and inspiration to be a true engineer.

National Science Foundation, project sponsor, for funding the previous and current 3-D orthogonal woven GFRP bridge deck research at NC State.

Table of Contents

LIST OF TABLES.....	ix
LIST OF FIGURES.....	x
CHAPTER 1. INTRODUCTION.....	1
1.1 OBJECTIVES	2
1.2 SCOPE OF PROJECT	2
CHAPTER 2. LITERATURE REVIEW	4
2.1 FRP BRIDGE DECK	4
2.2 CODES AND DESIGN GUIDELINES	6
2.3 FABRICATION.....	7
2.4 TYPES OF FRP BRIDGE DECKS	9
2.5 CONNECTIONS	14
2.6 CONSTRUCTABILITY AND PRACTICALITY	16
2.7 MODELING	18
2.8 COST EFFICIENCY	21
2.9 PREVIOUSLY CONDUCTED RESEARCH.....	22
2.10 IMPROVEMENTS IN CURRENT DESIGN	22
2.11 CONCURRENT RESEARCH.....	23
2.12 WEAVING PROCESS	24
2.13 RESIN INFUSION SYSTEMS	25
CHAPTER 3. FABRICATION	37
3.1 DESIGN CONCEPT	37
3.2 DESIGN SPECIFICATIONS OF THE DECK	39
3.3 3WEAVE® FABRICATION PROCESS	39
3.4 WEAVING PROCEDURE.....	41
3.5 WOVEN PREFORM DESIGN.....	43
3.6 PROPERTIES OF PANEL SKINS	43
3.7 INFUSED COMPOSITE PROPERTIES	44
3.8 FABRICATION OF TEST SPECIMENS.....	45
3.9 SHEAR CONNECTOR ASSEMBLY	45
3.10 DECK ASSEMBLY.....	47
3.11 SHEAR CONNECTOR INFUSION SETUP	49
3.12 DECK INFUSION SETUP.....	51
3.13 VACUUM BAGGING	52
3.14 INFUSION.....	54
3.14.1 <i>Infusion of Shear Connectors</i>	55
3.14.2 <i>Infusion of Deck 1</i>	55
3.14.3 <i>Infusion of Deck 2</i>	55
3.15 POSTCURING PROCESS	56
3.16 DEMOLDING.....	57
3.17 TEST SAMPLES.....	58
3.18 STEEL REINFORCEMENT OF THE SHEAR CONNECTOR SPECIMENS.....	60
3.19 STEEL REINFORCEMENT OF THE CONCRETE DECK	60
3.20 SHEAR CONNECTOR SPECIMENS.....	61
3.21 FORMWORK FOR DECKS.....	62
3.22 CONCRETE MIX DESIGN AND PROCESS	62
3.23 PLACEMENT OF CONCRETE	63
3.24 CURING	64
3.25 REMOVAL OF SHEAR CONNECTOR FORMWORK	64
3.26 CUTTING OF CAST SHEAR CONNECTOR SAMPLES	64

3.27 FABRICATION OF THE SHEAR TEST SPECIMENS	65
CHAPTER 4. EXPERIMENTAL PROGRAM.....	90
4.1 CONCRETE STRENGTH.....	90
4.2 PROPERTIES OF THE REINFORCING STEEL	92
4.3 FIBER VOLUME FRACTION OF GFRP SKINS.....	93
4.4 TENSILE STRENGTH OF GFRP SKINS.....	94
4.5 FLEXURAL STRENGTH OF GFRP SKINS.....	96
4.6 SHEAR CONNECTOR TEST	97
4.7 BRIDGE DECK TEST SETUP	101
4.8 DECK INSTRUMENTATION.....	102
4.9 LOADING CYCLE.....	103
4.10 TEST RESULTS OF DECK 1	104
4.11 TEST RESULTS OF DECK 2.....	106
CHAPTER 5. ANALYSIS AND DISCUSSION	135
5.1 BEAM ANALYSIS APPROACH	136
5.1.1 Deck 1.....	136
5.1.2 Deck 2.....	142
5.2 PREDICTION OF THE FLEXURAL RIGIDITY OF THE DECK	145
5.2.1 Deck 1.....	146
5.2.2 Deck 2.....	150
5.2.3 Discussion.....	151
5.3 FINITE ELEMENT APPROACH	153
5.3.1 Assumptions.....	153
5.3.2 Mathematical Model.....	156
5.3.3 ANSYS Modeling	157
5.3.4 Factors Affecting the Finite Element Modeling	157
5.3.5 Convergence Study.....	157
CHAPTER 6. CONCLUSIONS	163
6.1 SUMMARY AND CONCLUSIONS	163
6.2 FUTURE WORK	165
6.2.1 Connections	165
6.2.2 Resin Formulation.....	166
6.2.3 Strength of Joints.....	166
6.2.4 Fatigue Testing.....	167
6.2.5 Shear Properties.....	167
6.3 PROPOSED THIRD GENERATION BRIDGE DECK	167
6.4 OUTLOOK.....	169
APPENDICES.....	171
APPENDIX A. WEAVING CALCULATIONS	172
APPENDIX B. QUIKRETE MSDS.....	177
APPENDIX C. ALCAN BALTEK CONTOURKORE Balsa CORE TYPICAL MECHANICAL PROPERTIES	180
APPENDIX D. GROOVED MACHINING (GP) TO END GRAIN Balsa DATA SHEET	182
APPENDIX E. ADVA 100 DATA SHEET	183
APPENDIX F. JEFFCO EPOXY SYSTEM DATA SHEET	185
APPENDIX G. HYBON 2022 E-GLASS FIBER PROPERTIES.....	187
APPENDIX H. STEEL REINFORCEMENT TEST DATA	189
APPENDIX I. TENSION TEST OF GFRP SKINS	192
APPENDIX J. FOUR-POINT BENDING DATA OF GFRP SKINS	197
APPENDIX K. SHEAR CONNECTOR STUDY	202
CITED REFERENCES	215

List of Tables

TABLE 3.1. DIMENSIONS OF SAMPLE OF 1 FT. OF 1 SKIN (2 LAYERS OF FABRIC).	67
TABLE 3.2. PROPERTIES OF SAMPLE.	67
TABLE 3.3. CALCULATED AVERAGE NUMBER OF Z-YARNS AND WEIGHT CHARACTERISTICS OF SKIN.	67
TABLE 3.4. DECK PROPERTIES PRIOR TO INFUSION.	67
TABLE 3.5. INFUSION SUMMARY.....	68
TABLE 3.6. CONCRETE MIX DESIGN.	68
TABLE 4.1. CONCRETE CYLINDER COMPRESSION TEST RESULTS.	108
TABLE 4.2. STEEL REINFORCEMENT TENSION TEST RESULTS.	108
TABLE 4.3. FIBER VOLUME FRACTION RESULTS.	109
TABLE 4.4. GFRP SKIN TENSION COUPON RESULTS.....	109
TABLE 4.5. GFRP SKIN FOUR POINT BENDING RESULTS.	110
TABLE 4.6. SHEAR CONNECTOR STUDY RESULTS.	110
TABLE 4.7. DECK 1 DEFLECTIONS AT AASHTO EQUIVALENT WHEEL LOAD CLASSIFICATIONS.	111
TABLE 4.8. DECK 1 STRAINS AT PEAK LOAD.	111
TABLE 4.9. DECK 2 DEFLECTIONS AT AASHTO EQUIVALENT WHEEL LOAD CLASSIFICATIONS.	111
TABLE 4.10. DECK 2 STRAINS AT 1 ST PEAK LOAD.	111
TABLE 5.1. DECK 1 TRANSFORMED SECTION PROPERTIES.	161
TABLE 5.2. DECK 1 PARALLEL AXIS THEOREM PROPERTIES.	161
TABLE 5.3. DECK 2 TRANSFORMED SECTION PROPERTIES.	162
TABLE 5.4. DECK 2 PARALLEL AXIS THEOREM PROPERTIES.	162
TABLE 5.5. FINITE ELEMENT ANALYSIS RESULTS COMPARISON.	162
TABLE K.1. VERTICAL FLANGE SHEAR CONNECTOR FAILURE PROGRESSION.	202
TABLE K.2. RECTANGULAR CORE SHEAR CONNECTOR FAILURE PROGRESSION.	202
TABLE K.3. TAPERED CORE SHEAR CONNECTOR FAILURE PROGRESSION.	203

List of Figures

FIGURE 2.1. STRUCTURALLY DEFICIENT REINFORCED CONCRETE BRIDGE DECK, WINSTON-SALEM, NC.	26
FIGURE 2.2. PULTRUSION PROCESS FROM NELSON (2005).....	26
FIGURE 2.3. TRANSONITE® PANELS WITH 3-D FIBER INSERTIONS (2006).....	27
FIGURE 2.4. VACUUM INFUSION PROCESS BY FIBER-TECH (2006).....	27
FIGURE 2.5. GEOMETRY OF DIFFERENT 3-D WOVEN CROSS SECTIONS BY CHOU ET AL. (1989).....	28
FIGURE 2.6. DURASpan® PANELS USED ON SR655 BY MOSES (2005).....	28
FIGURE 2.7. SANDWICH PANEL CONSTRUCTION.....	29
FIGURE 2.8. FILAMENT WOUND PROCESS USED BY SHEHATA ET AL. (2005).....	29
FIGURE 2.9. HYDECK HYBRID FRP-CONCRETE BRIDGE DECK (2005).....	30
FIGURE 2.10. SALEM AVENUE BRIDGE INSTALLATION OF FRP PANELS, HENDERSON (2006).....	30
FIGURE 2.11. GFRP DECK TO CONCRETE GIRDER CONNECTION, HENDERSON (2006).....	31
FIGURE 2.12. GFRP DECK TO STEEL GIRDER CONNECTION, HENDERSON (2006).....	31
FIGURE 2.13. DURASpan® PANEL INSTALLATION ON GREENE COUNTY BRIDGE, HENDERSON (2006).....	32
FIGURE 2.14. UNIT CELL OF 3-D ORTHOGONAL WOVEN PREFORM BY GU (1994).....	32
FIGURE 2.15. STRUCTURE OF 3-D ORTHOGONAL WOVEN FABRIC BY GU (1994).....	33
FIGURE 2.16. ASSEMBLY OF UNIT CELL FOR MODELING BY CARLSON (1995).....	33
FIGURE 2.17. OPTIMAL CROSS-SECTION BY PARK ET AL. (2005).....	34
FIGURE 2.18. 3-D WOVEN TRUSS CONFIGURATION BY NORTON (2004).....	34
FIGURE 2.19. CONCEPTUAL ILLUSTRATION OF DECK CROSS-SECTION WITHOUT SHEAR CONNECTORS.....	35
FIGURE 2.20. CONCEPTUAL MODEL OF 3-D ORTHOGONAL WOVEN GFRP COMPOSITE BRIDGE DECK.....	35
FIGURE 2.21. 3TEX IMAGE OF 3WEAVE® WEAVING PROCESS. (2004).....	36
FIGURE 3.1. DECK PREFORM ASSEMBLY.....	69
FIGURE 3.2. SHEAR CONNECTOR PREFORM ASSEMBLY.....	70
FIGURE 3.3. 3WEAVE® LOOM SETUP.....	71
FIGURE 3.4. RODS AND WEIGHTS TO INDUCE TENSION ON WARP AND Z-YARNS.....	71
FIGURE 3.5. HARNESSES AND YARNS ON 3WEAVE® LOOM.....	72
FIGURE 3.6. REED BEAT-UP FOLLOWED BY SYSTEM TAKE-UP.....	72
FIGURE 3.7. RAPIER SYSTEM TO INSERT FILLING YARNS.....	73
FIGURE 3.8. SELVAGE HOLD PRIOR TO INSERTION.....	73
FIGURE 3.9. HARNESSES PRIOR TO SWITCHING.....	74
FIGURE 3.10. HARNESSES AFTER SWITCHING.....	74
FIGURE 3.11. SKIN PREFORM WOVEN ON 3WEAVE® LOOM.....	75
FIGURE 3.12. 3-D ORTHOGONALLY WOVEN SKIN WITH Z-JOINTS.....	75
FIGURE 3.13. STAPLING OF FABRIC FLAP TO WOODEN CORES ON SHEAR CONNECTORS.....	76
FIGURE 3.14. SHEAR CONNECTOR PREFORM.....	76
FIGURE 3.15. BOTTOM SKIN OF DEMO DECK WITH WOOD SPACERS.....	77
FIGURE 3.16. BOTH SKINS OF DEMO DECK WITH WOOD SPACERS.....	77
FIGURE 3.17. INSERTION OF BOTTOM LAYER OF Balsa CORES INTO DECK PREFORM.....	78
FIGURE 3.18. FOLDING OF SKINS AT OUTER CELLS.....	78
FIGURE 3.19. Balsa INSERTS IN DEMO DECK.....	79
FIGURE 3.20. ASSEMBLED DECK PREFORM.....	79
FIGURE 3.21. SHEAR CONNECTOR FABRIC PLACED ATOP DECK PREFORM.....	80
FIGURE 3.22. INFUSION SETUP OF FLANGE SHEAR CONNECTOR.....	80
FIGURE 3.23. CONNECTION TO RESIN INLET.....	81
FIGURE 3.24. DECK 1 PREFORM PRIOR TO INFUSION.....	81
FIGURE 3.25. DECK PREFORM UNDER VACUUM PRIOR TO INFUSION.....	82
FIGURE 3.26. PRE-HEATING PREFORM USING ELECTRIC BLANKET.....	82
FIGURE 3.27. MIXING OF EPOXY AND HARDENER.....	83
FIGURE 3.28. TOTAL WET-OUT OF DECK 1.....	83
FIGURE 3.29. DECK 1 ON INFUSION TABLE INSIDE OVEN.....	84
FIGURE 3.30. THREE CONFIGURATIONS OF SHEAR CONNECTORS.....	84
FIGURE 3.31. DECK FORMS WITH STEEL SHRINKAGE REINFORCEMENT.....	85

FIGURE 3.32. SHEAR CONNECTOR FORMWORK WITH PVC PIPE INSERTS.....	85
FIGURE 3.33. PVC PIPE INSERTS SEALED WITH DUCT TAPE IN SHEAR CONNECTOR FORMWORK.....	86
FIGURE 3.34. RODDING OF CONCRETE CYLINDERS.....	86
FIGURE 3.35. SCREEDING OF DECK 2.....	87
FIGURE 3.36. CURING OF DECK 2.....	87
FIGURE 3.37. REMOVAL OF SHEAR CONNECTOR FORMWORK.....	88
FIGURE 3.38. STEEL PLATES AND RODS PRIOR TO BONDING TO SHEAR SAMPLES.....	88
FIGURE 3.39. COMPLETED FABRICATION OF VERTICAL FLANGE SHEAR CONNECTOR SPECIMEN.....	89
FIGURE 4.1. CONCRETE COMPRESSION TEST.....	112
FIGURE 4.2. CONCRETE STRESS-STRAIN TEST SETUP PRIOR TO LOADING.....	112
FIGURE 4.3. FAILURE OF CONCRETE CYLINDER.....	113
FIGURE 4.4. CRUSHED CONCRETE CYLINDER.....	113
FIGURE 4.5. BATCH 1 MEASURED STRESS VS. STRAIN AT 28 DAY STRENGTH.....	114
FIGURE 4.6. BATCH 2 MEASURED STRESS VS. STRAIN AT 28 DAY STRENGTH.....	114
FIGURE 4.7. SETUP OF STEEL REINFORCEMENT TENSION TEST.....	115
FIGURE 4.8. NECKING OF STEEL REINFORCEMENT AT FAILURE.....	115
FIGURE 4.9. STEEL REINFORCEMENT TENSION TEST RESULTS.....	116
FIGURE 4.10. SUBMERSION OF FRP SAMPLE TO DETERMINE TOTAL VOLUME.....	116
FIGURE 4.11. COMPOSITE SPECIMENS IN CERAMIC CUP PRIOR TO BURN-OFF.....	117
FIGURE 4.12. FABRIC REMNANTS FROM MATRIX BURN-OFF TEST.....	117
FIGURE 4.13. TENSILE FRP COUPON TEST.....	118
FIGURE 4.14. TESTING OF TENSION COUPONS.....	118
FIGURE 4.15. WARP DIRECTION TENSILE COUPON TEST RESULTS.....	119
FIGURE 4.16. FILLING DIRECTION TENSILE COUPON TEST RESULTS.....	119
FIGURE 4.17. FOUR POINT BENDING TEST SETUP FOR WARP DIRECTION SKIN.....	120
FIGURE 4.18. WARP DIRECTION FOUR POINT BENDING TEST OF SKIN.....	120
FIGURE 4.19. FAILURE OF WARP DIRECTION FOUR POINT BENDING TEST.....	121
FIGURE 4.20. BRITTLE FAILURE OF FILLING SPECIMEN.....	121
FIGURE 4.21. LOAD VS. DISPLACEMENT FOR WARP DIRECTION FOUR POINT BENDING SPECIMEN.....	122
FIGURE 4.22. LOAD VS. DISPLACEMENT FOR FILLING DIRECTION FOUR POINT BENDING SPECIMEN.....	122
FIGURE 4.23. WARP DIRECTION FOUR-POINT BENDING RESULTS.....	123
FIGURE 4.24. FILLING DIRECTION FOUR-POINT BENDING RESULTS.....	123
FIGURE 4.25. SHEAR CONNECTOR TEST SETUP.....	124
FIGURE 4.26. FAILURE OF SHEAR CONNECTOR SPECIMEN.....	124
FIGURE 4.27. STRESS VS. STRAIN FOR ALL VERTICAL GFRP FLANGE SHEAR CONNECTOR SPECIMENS.....	125
FIGURE 4.28. STRESS VS. STRAIN FOR ALL RECTANGULAR WOOD CORE SHEAR CONNECTOR SPECIMENS.....	125
FIGURE 4.29. STRESS VS. STRAIN FOR ALL TAPERED WOOD CORE SHEAR CONNECTOR SPECIMENS.....	126
FIGURE 4.30. STRESS VS. STRAIN FOR ALL SHEAR CONNECTOR SPECIMENS.....	126
FIGURE 4.31. DECK 1 INSTRUMENTATION AT SUPPORT.....	127
FIGURE 4.32. STRING POTENTIOMETERS ATTACHED TO TENSION SIDE OF DECK.....	127
FIGURE 4.33. DECK 1 PRIOR TO LOADING.....	128
FIGURE 4.34. DECK 1 DURING LOADING CYCLE.....	128
FIGURE 4.35. DECK 1 PRIOR TO FAILURE.....	129
FIGURE 4.36. CONCRETE SHEAR FAILURE AND DELAMINATION OF DECK 1.....	129
FIGURE 4.37. DECK 1 AFTER FAILURE.....	130
FIGURE 4.38. CONCRETE CRACKS AT MID-SPAN OF DECK 1.....	130
FIGURE 4.39. DECK 1 CONCRETE SHEAR FAILURE AT SHEAR CONNECTOR.....	131
FIGURE 4.40. DECK 1 LOAD VS. DISPLACEMENT.....	131
FIGURE 4.41. DECK 1 LOAD VS. STRAIN.....	132
FIGURE 4.42. DECK 2 CONCRETE DELAMINATION AND PERMANENT DEFORMATION.....	132
FIGURE 4.43. DECK 2 SHEAR CONNECTOR FAILURE AND CONCRETE DELAMINATION.....	133
FIGURE 4.44. DECK 2 LOAD VS. DISPLACEMENT.....	133
FIGURE 4.45. DECK 2 LOAD VS. STRAIN AT 1 ST PEAK LOAD.....	134

FIGURE 5.1. ASSUMED GEOMETRY OF DECK CROSS-SECTION.	136
FIGURE 5.2. STRAIN AND STRESS VARIATIONS OVER CROSS-SECTION.	137
FIGURE 5.3. MATHEMATICAL MODEL FOR DECK 1.	156
FIGURE 5.4. MATHEMATICAL MODEL FOR DECK 2.	156
FIGURE 5.5. SIDE VIEW OF DECK 1 SYMMETRY AND ANTISYMMETRY CONDITIONS.	159
FIGURE 5.6. DECK 1 DEFLECTED SHAPE WITH 0.25 INCH MESH SIZE.	159
FIGURE 5.7. SIDE VIEW OF DECK 2 SYMMETRY AND ANTISYMMETRY CONDITIONS.	160
FIGURE 5.8. ISOMETRIC VIEW OF DECK 2 WITH 0.25 INCH MESH.	160
FIGURE A.1. SLAB MODEL ASSUMED FOR RULE OF MIXTURES.	176
FIGURE A.2. DETERMINATION OF Z-YARN PACKING FACTOR.	176
FIGURE H.1. BAR 1 STRESS VS. STRAIN CURVE.	189
FIGURE H.2. BAR 2 STRESS VS. STRAIN CURVE.	189
FIGURE H.3. BAR 3 STRESS VS. STRAIN CURVE.	190
FIGURE H.4. BAR 4 STRESS VS. STRAIN CURVE.	190
FIGURE H.5. BAR 5 STRESS VS. STRAIN CURVE.	191
FIGURE H.6. BAR 6 STRESS VS. STRAIN CURVE.	191
FIGURE I.1. WARP TENSION SPECIMEN 1.	192
FIGURE I.2. WARP TENSION SPECIMEN 2.	192
FIGURE I.3. WARP TENSION SPECIMEN 3.	193
FIGURE I.4. WARP TENSION SPECIMEN 4.	193
FIGURE I.5. FILLING TENSION SPECIMEN 5.	194
FIGURE I.6. FILLING TENSION SPECIMEN 6.	194
FIGURE I.7. FILLING TENSION SPECIMEN 7.	195
FIGURE I.8. FILLING TENSION SPECIMEN 8.	195
FIGURE I.9. FILLING TENSION SPECIMEN 9.	196
FIGURE J.1. FILLING FOUR POINT BENDING SPECIMEN 1.	197
FIGURE J.2. FILLING FOUR POINT BENDING SPECIMEN 2.	197
FIGURE J.3. FILLING FOUR POINT BENDING SPECIMEN 3.	198
FIGURE J.4. FILLING FOUR POINT BENDING SPECIMEN 4.	198
FIGURE J.5. FILLING FOUR POINT BENDING SPECIMEN 5.	199
FIGURE J.6. FILLING FOUR POINT BENDING SPECIMEN 6.	199
FIGURE J.7. FILLING FOUR POINT BENDING SPECIMEN 7.	200
FIGURE J.8. FILLING FOUR POINT BENDING SPECIMEN 8.	200
FIGURE J.9. FILLING FOUR POINT BENDING SPECIMEN 9.	201
FIGURE J.10. FILLING FOUR POINT BENDING SPECIMEN 10.	201
FIGURE K.1. VERTICAL FLANGE SPECIMEN 1 (V1) LOAD VS. POT DISPLACEMENT.	204
FIGURE K.2. VERTICAL FLANGE SPECIMEN 2 (V2) LOAD VS. POT DISPLACEMENT.	204
FIGURE K.3. VERTICAL FLANGE SPECIMEN 3 (V3) LOAD VS. POT DISPLACEMENT.	204
FIGURE K.4. RECTANGULAR SPECIMEN 1 (R1) LOAD VS. POT DISPLACEMENT CURVE.	205
FIGURE K.5. RECTANGULAR SPECIMEN 2 (R2) LOAD VS. POT DISPLACEMENT CURVE.	205
FIGURE K.6. RECTANGULAR SPECIMEN 3 (R3) LOAD VS. POT DISPLACEMENT CURVE.	205
FIGURE K.7. TAPERED SPECIMEN 1 (T1) LOAD VS. POT DISPLACEMENT CURVE.	206
FIGURE K.8. TAPERED SPECIMEN 2 (T2) LOAD VS. POT DISPLACEMENT CURVE.	206
FIGURE K.9. TAPERED SPECIMEN 3 (T3) LOAD VS. POT DISPLACEMENT CURVE.	206
FIGURE K.10. VERTICAL FLANGE SPECIMEN 1 (V1) STRESS VS. STRAIN CURVE.	207
FIGURE K.11. VERTICAL FLANGE SPECIMEN 2 (V2) STRESS VS. STRAIN CURVE.	207
FIGURE K.12. VERTICAL FLANGE SPECIMEN 3 (V3) STRESS VS. STRAIN CURVE.	207
FIGURE K.13. RECTANGULAR SPECIMEN 1 (R1) STRESS VS. STRAIN CURVE.	208
FIGURE K.14. RECTANGULAR SPECIMEN 2 (R2) STRESS VS. STRAIN CURVE.	208
FIGURE K.15. RECTANGULAR SPECIMEN 3 (R3) STRESS VS. STRAIN CURVE.	208
FIGURE K.16. TAPERED SPECIMEN 1 (T1) STRESS VS. STRAIN CURVE.	209

FIGURE K.17. TAPERED SPECIMEN 2 (T2) STRESS VS. STRAIN CURVE	209
FIGURE K.18. TAPERED SPECIMEN 3 (T3) STRESS VS. STRAIN CURVE	209
FIGURE K.19. VERTICAL FLANGE SPECIMEN 1 (V1) FAILURE MODE	210
FIGURE K.20. VERTICAL FLANGE SPECIMEN 2 (V2) FAILURE MODE	210
FIGURE K.21. VERTICAL FLANGE SPECIMEN 3 (V3) FAILURE MODE	211
FIGURE K.22. RECTANGULAR SPECIMEN 1 (R1) FAILURE MODE.....	211
FIGURE K.23. RECTANGULAR SPECIMEN 2 (R2) FAILURE MODE.....	212
FIGURE K.24. RECTANGULAR SPECIMEN 3 (R3) FAILURE MODE.....	212
FIGURE K.25. TAPERED SPECIMEN 1 (T1) FAILURE MODE.....	213
FIGURE K.26. TAPERED SPECIMEN 2 (T2) FAILURE MODE.....	213
FIGURE K.27. TAPERED SPECIMEN 3 (T3) FAILURE MODE.....	214

Chapter 1. Introduction

The earliest bridges used by humans were fallen trees spanning across rivers or gorges. Over time, humans tried to mimic nature by cutting down trees and arranging rocks to create their own bridges made of supports and beams. The ancient Romans constructed bridges to transport soldiers and chariots with the invention of the arch and a new building material, cement.

In the 1500's, the Incans constructed the first suspension bridges made from rope. During the 1700's, timber bridges were developed extensively in Europe. The invention of wrought iron during the Industrial Revolution in the 1800's allowed construction of truss-like bridges. However, the tensile strength of wrought iron was very limited to respond to the demands to increase loads required by locomotives and automobiles. The discovery of the Bessemer process to form a new material, steel, with higher tensile strength allowed construction of much larger bridges.

The design of more economical bridges made from readily available materials is still a goal of current societies. Since the 1960's, one particular construction material has been developed significantly: fiber reinforced composites. By definition, composite material is made of two or more distinct components. Traditionally, composites consist of fibers encased in a more flexible, protective matrix binder. The fibers provide the majority of the strength while the matrix holds the composite together. The fibers can be long or short, and oriented randomly, aligned, or woven according to desired properties. For several hundred years, humans have applied this concept of fiber reinforcement. Various civilizations reinforced mud with straw or other natural fibers in their houses. The modern advancement of fiber reinforced composites was initially developed for

aerospace applications, owing to the lightweight and high-performance characteristics. Over the years, other industries have developed their own fiber reinforced composites, including structural applications.

With an increasing population's reliance upon the automobile, demands on bridge performance have increased. In addition, the concrete and steel bridges built in the early 1900's are deteriorating. With reduced manufacturing costs and better defined material characteristics, fiber reinforced composites have become an attractive alternative for certain structural applications in which dead load, construction time, or life cycle costs are of high importance. Some applications include wrapping of concrete and steel structures, corrosion resistant reinforcing bars, and bridge deck.

1.1 Objectives

The research presented in this thesis investigates the fabrication, behavior, and modeling of innovative fiber reinforced composite bridge deck. The objectives of this thesis were (1) to tailor a 3-dimensional weaving process to bridge deck applications, (2) to weave the fabric preforms and fabricate a composite bridge deck, (3) to characterize the material properties of the individual components and the behavior of the entire bridge deck structural system, and (4) to simulate the behavior using basic engineering principles and finite element analysis.

1.2 Scope of Project

This thesis will review the current knowledge and development of FRP bridge decks in Chapter 2. An in-depth account of the fabrication of the deck panels and the shear connector samples is provided in Chapter 3. The experimental program is outlined in Chapter 4 and provides summaries of the test results. Analyses using three different

approaches to predict the deck behavior are described in Chapter 5. The thesis concludes in Chapter 6 with the recommendations based upon the current work and the author's vision for future work needed to better understand the material and optimize the bridge deck design.

Chapter 2. Literature Review

The deterioration of bridge infrastructure has encouraged researchers to investigate glass fiber reinforced polymer bridge deck for more than a decade. Design criteria for decks are currently being implemented into the first standards for use by practicing engineers. Several methods of deck fabrication are available for different types of deck. Each deck type is designed with suitable connections and has different issues regarding constructability. Modeling of deck behavior has been a useful tool to optimize performance and improve cost efficiency. In addition to these topics, previous research related to the current deck design, the improvements made for the current design, concurrent research, and the 3-D weaving process are discussed in this chapter.

2.1 FRP Bridge Deck

Use of glass fiber reinforced polymer (GFRP) bridge deck has been recently investigated as an alternative to conventional steel and reinforced concrete bridge decks. Some of the advantages of GFRP include corrosion resistance and a high strength-to-weight ratio, resulting in a significant reduction of the dead load. Various demonstration projects have been constructed, with bridge spans reaching 10 m. (Keller 2003)

Over half of the existing bridges in the United States were built before 1940. As of 2003, 27.1 percent (160,570) of the nation's bridges were classified as "structurally deficient or functionally obsolete." Thirty percent of North Carolina's bridges fit in these classifications. A "structurally deficient" bridge is closed or restricted to light vehicles due to deterioration. A "functionally obsolete" bridge has outdated design features and cannot sustain current traffic volumes and intended vehicle weights. According to the ASCE Infrastructure Report Card 2005, repair of deficient or obsolete bridges will cost

more than \$9.4 billion per year for 20 years to eliminate the current deficiencies. The cost to prevent backlog of deteriorated bridges from increasing will cost an additional \$7.3 billion. (ASCE 2005) These bridges are deemed deficient due to poor deck conditions and lack of load ratings. (Alampalli et al. 2003) An example of a structurally deficient bridge is shown in Figure 2.1. This bridge is the Interstate 40-Business bridge which crosses Liberty St. in downtown Winston-Salem, NC. The bridge is ranked as the worst bridge in the state for the fifth year in a row by AAA (2006) and is exposed to ever-increasing traffic volumes. It was built in 1955 and is scheduled to be replaced in 2011. One of the numerous structural deficiencies is the corroded steel reinforcement which expands and causes spalling of the concrete cover.

The average life of most bridges in the United States is 68 years, whereas the life of bridge decks is only 35 years. In some extreme regions in the Midwest and locations where extensive deicing salts are used, the life of decking can be limited to 10 years. The maintenance and repair of the decking systems is costly. In Wisconsin, bridge deck replacement accounts for 75-90% of annual maintenance costs with the exclusion of painting. (Karbhari et al. 2001)

A primary advantage of using FRP bridge decks for rehabilitation is the significant reduction of the dead load, which could be achieved by replacing conventional decks with lightweight GFRP. By decreasing the dead load, the allowable live load can be increased. In many cases these advantages allow older, deficient bridges to be brought up to meet current code requirements. (Bakis et al. 2002) Fiber composites are also attractive when lower weight translates to higher seismic resistance. (Davey et al. 2001)

2.2 Codes and Design Guidelines

In the United States, the American Association of State Highway and Transportation Officials (AASHTO) provides standard ratings for bridge deck performance. Choice of design equivalent wheel loads varies by locale and intended use. Some of the recent research adopted the AASHTO HS30 wheel load rating in design and examination of the structural performance of FRP decks. The equivalent wheel load of 32 kips is much larger than the wheel load of the HS20 and HS25 used for many current bridges. Therefore, these higher performance requirements may allow use of FRP bridge deck for upgrading existing bridges to accommodate HS30 for future demands. (Williams et al. 2003) Some investigators who published the design of these bridges using HS25 are Aref et al. (2005), Turner et al. (2004), and Alampalli et al. (2003)

Live load deflection limits for bridge deck are not currently specified by AASHTO. The vertical deflection limit of the span/800 ($L/800$) is applied to bridge girders; however, this value is intended to limit vibration and is strict for bridge deck. Comparisons have been made to other materials, such as timber ($L/425$), to suggest limits between $L/800$ and $L/360$. (Williams et al. 2003) Jeong et al. recommend the deflection limit of $L/800$ for current design with FRP deck, but indicated that this value is very conservative. (2003)

Other guidelines specified by AASHTO include moment distribution factors for design. Turner et al. found that for bridges having girder spacing less than the width of a truck (6 ft), the AASHTO distribution factors for concrete decks are appropriate for GFRP decks. For larger spacings, a reserve moment capacity should be incorporated. (2004)

The incorporation of FRP into codes and the production of standard design guidelines are currently in progress and expected to follow the completion of several National Cooperative Highway Research Program (NCHRP) projects. However, this process is slow due to the variety of the properties of bridge decks produced by several manufacturers. To date, deck manufacturers have been providing the guidelines for their own specific product to engineers. The absence of a design standard for FRP bridge deck is slowing the gaining of acceptance by practicing engineers. (Park et al. 2005)

2.3 Fabrication

Glass fiber reinforced polymer bridge decks are produced by saturating dry fiber performs with a liquid resin system. When the resin cures, it forms a solid protective layer which holds the fibers in place. There are several methods available for resin infusion of FRP decks. These include pultrusion, Resin Transfer Molding (RTM), Vacuum Assisted Resin Transfer Molding (VARTM), Resin Film Infusion (RFI), and Seeman Composite Resin Infusion Molding Process (SCRIMP). The major factors affecting the selection of the production method are the fiber architecture, cost, quality control, and infusion time.

Pultrusion is well-known to be the most cost effective method for fabricating FRP products. Pultrusion is a process in which fibers are drawn in one direction, which is in the case of decking, the direction of the span of the deck. The resin impregnates the fibers just prior to drawing as shown in Figure 2.2. (Nelson 2005) Advanced pultrusion techniques by manufacturers such as Martin Marietta Composites insert fibers in orthogonal directions to the longitudinal fibers at specified intervals as shown in Figure 2.3. One disadvantage of pultrusion fabrication is that a percentage of the fibers may be

damaged or misaligned during to the drawing process. Today, pultrusion is the most common commercial process used for fabrication of FRP bridge deck due to its economical benefits. (Bakis et al. 2002)

Resin Transfer Molding involves placing a dry fabric preform in a two-part mold. The mold is compacted to create a desired fiber volume fraction. The resin is injected into the mold and cured at a specified temperature. Once cured, the composite is removed from the mold. Due to high costs for molding, this process is not as common for large structural components. (Loos 2003)

The Vacuum Assisted Resin Transfer Molding process is similar to RTM except that it uses a vacuum bag for infusion. The dry preform is placed on an infusion table and covered with an airtight vacuum bag as shown in Figure 2.4. Liquid resin impregnates the dry fabric preform using vacuum pressure to assist flow through the thickness direction. This method also uses a highly permeable resin flow distribution medium to assist flow in the plane of the composite. The VARTM process is very effective in limiting voids and resin waste, caused by “racetracking,” since the preform is well-confined. (Loos 2003)

Resin Film Infusion is also similar to RTM except that it uses a hot-melt resin film under the preform instead of a liquid resin to impregnate the dry preform. The fiber volume fraction is achieved by adjusting the compacting pressure which infuses the preform. The resin flow in this method is generally through the thickness, shortening the flow distance compared to other methods. (Loos 2003)

The United States Navy patented a variation of vacuum infusion called Seeman Composite Resin Infusion Molding Process. In addition to the vacuum pressure, this

method uses a non-stick peel ply directly against the preform and a high permeability flow distribution medium to facilitate resin flow. Another enhancement for wetting out the fabric is by creating grooves in the surface of the core material. Grid-like channels allow the resin to flow more easily through the preform and also provide a better bond between the preform and the core. For small thicknesses of preform and spacing of grooves, the use of the microgroove channels has been shown to infuse large components significantly faster than use of the high permeability flow medium. (Karbhari et al. 2001)

The goal of any infusion process is to allow the infused fibers to provide the resistance to flexure and create longitudinal stiffness while the core provides depth, resists buckling of the fibers, and increases the shear stiffness. Typical problems facing composites manufacturers are: inadequate shear stiffness of core materials, inadequate bearing at supports, poor performance under localized loads, and inability to provide anchorage points for fixing accessories. (Davey et al. 2001)

High manufacturing costs have limited use of composites for various applications. New fabrication techniques are constantly being developed in an attempt to lower labor and material costs.

2.4 Types of FRP Bridge Decks

The selection of FRP deck type is based on various influences. The fiber architecture, designed with unidirectional fibers versus 2-D or 3-D fabrics should be based on desired performance. Uniaxial composites achieve the highest volume fractions and the best properties in the axial direction. However, the transverse strength is less than 2-D and 3-D composites. Takatoya et al. drew a comparison between 2-D and 3-D composites. The 3-D specimens failed 6 percent lower in tension and 13 percent lower in compression

than 2-D composites. However, the 3-D composites were 10 and 13 percent higher than 2-D specimens in open-hole tensile strength and compressive strength. For compressive strength after impact, the 3-D composites were up to 47 percent higher than 2-D. While the in plane properties of 2-D composites are generally superior to 3-D, the out of plane property enhancement of 3-D composites makes them the preferred choice for many structural composites. (Takatoya et al. 2004) The through thickness reinforcement provided by 3-D composites eliminates the possibility of delamination commonly exhibited in pultruded bridge decks.

The composites bridge deck industry is still in the developing stage to produce many types of FRP decks. Nevertheless, many types of deck have been already optimized and are now commercially available. During 1996 to 2004, 58 GFRP decked bridges were constructed in the United States. Various configurations of bridge deck have been designed and are currently manufactured. Unidirectional fibers are pultruded in one dimension to create a fiber bridge deck with a constant cross-section. Bi-directional weaving for sandwich panels consists of two skins with two-dimensional interlacing fibers separated by a lightweight core. Both of these types of decks are currently commercially available. The research in this thesis explores a new generation of prefabricated GFRP woven bridge decks which provides fiber reinforcement in three orthogonal directions. There are several types of 3-D weaving processes. Some examples of 3-D weaving are shown in Figure 2.5. The 3-D weaving process used in this project, 3Weave®, is the first type of weaving shown in Figure 2.5.

Each of these fiber arrangements allow for different deck designs. The various deck types include pultruded panels, sandwich panels, filament wound decks, adhesively bonded tubes, and hybrid FRP-concrete panels.

Pultruded deck panels have been developed by many manufacturers. The DuraSpan® panels, produced by Martin Marietta Composites, were used recently for SR655 bridge in Landrum, South Carolina as shown in Figure 2.6. Use of GFRP bridge deck panels reduced the weight of the existing concrete deck from 96 psf to 19 psf using the same deck thickness. The deck was topped with a 2 in. asphalt wearing surface. This is one of the longest and widest spanning bridges ever built with FRP decking. It has the greatest known girder-to-depth ratio of the deck system, with 8 ft. girder spacings and a 7.7 in. thick deck. These dimensions are similar to conventional reinforced concrete deck. The deck was monitored and performed well. The measured strains were less than 2% of the ultimate strain and ranged from 5-10% of specified permissible strains under service loading. Ultimate strains of the FRP material were: 0.0078 in the longitudinal direction and 0.0132 in the transverse direction. (Turner et al. 2004)

Another type of pultruded deck investigated by Davey et al. consists of fibers pultruded around PVC pipes. The PVC pipe created circular voids in the cross-section to save on material used to produce the deck. Other than cost, the benefits of the deck include strong web to flange connections and performance in the transverse direction similar to castellated beams. (Davey et al. 2001)

Sandwich panels consist of two layers of fabric separated by a lightweight core as shown in Figure 2.7. Sandwich panel construction involves two general types of cores which are honeycombed and foam. These panels are supported by concrete or steel

abutments. (Zhou et al. 2005) Hardcore Composites, Inc. produced the sandwich panels investigated by Aref et al. These panels contained a two-way web core matrix with skins of E-glass fibers infused with a vinyl ester resin. (2005)

Another sandwich panel application was the first use of FRP bridge deck for repair of truss bridges was in Wellsburg, New York. The FRP decking was chosen to replace the deteriorated reinforced concrete deck. The FRP deck weighed 80 percent less than the concrete deck, allowing an increase of the live load capacity. The deck consisted of an E-glass sandwich design with foam cores, vacuum infused with a vinyl ester resin. The panels were also manufactured by Hardcore Composites. Both the top and bottom skins consisted of eight plies providing a total thickness of 15 mm per skin. The stresses in the composite were conservatively designed to reach 20 percent of ultimate and the deflection was limited to $L/800$. Observation of the behavior of the deck showed that no composite action developed between the deck and the superstructure, and that the joints between panels did not completely transfer load. The investigators proposed a separate study to determine if a combination of service loads and environmental exposure weaken the panels. (Alampalli et al. 2003)

The filament winding process is one of the oldest and most inexpensive forms of automated composite production. As described by the CRC Press (2006), the technique is based on the winding of continuous rovings (yarns) around a form core. The rovings are wetted with a resin just prior to winding. The tension on the rovings, number of wound layers, and pattern of winding determine the strength of the composite. Williams et al. (2003) experimented with triangular filament wound tubes bonded together by top and bottom GFRP plates. The corners of the tubes were rounded to minimize stress

concentrations from the winding process. Such tubes are manufactured by Creative Pultrusions and Martin Marietta Composites and have been installed on demonstration projects. The anticipated quick installation times have been realized in the demonstration projects with installation times of 5.5 and 8 hours respectively for the two types of core sections. Williams et al. (2003) observed that the filament wound decks were capable of supporting an AASHTO HS30 design truck load and meeting a live load deflection limit of $L/360$. The filament wound deck panel is shown in Figure 2.8.

Hybrid panels attempt to take advantage of both the tensile strength of FRP and the compressive strength of concrete. Commercial hybrid panels are pultruded and provide a stay-in-place formwork for the concrete as shown in Figure 2.9. The concrete serves the dual purpose of compression reinforcement and wearing surface. Hybrid panels are typically cast-in-place, providing a continuous concrete surface over adjacent panels. Due to the increased complexity of these panels over the all-FRP panels, the required fieldwork is increased. (Reising et al. 2004)

Another important selection in the design of FRP panels is the wearing surface. Traditional concrete and steel decks inherently provide a durable concrete topping to withstand impact and wearing damage from traffic loading. FRP is sensitive to the sun's ultraviolet rays, so special care must be taken to avoid degradation of structural properties. Epoxy polymer overlays have been used as alternative wearing surfaces to Portland cement concrete and asphalt concrete; however, the results were very mixed. (Aref et al. 2005) The epoxy coatings eliminate bond and thermal expansion concerns between concrete and FRP, but have been shown to be susceptible to flaws (voids) causing delamination. Such delamination can totally ruin FRP panels. For this reason,

thin concrete toppings, 1 to 2 in. thick, are preferred by some engineers due to their enhanced durability while limiting the additional weight. Depending on the design of the deck system, the additional compressive strength of the concrete can be incorporated into the design.

Other chemical additives which are mixed into the resin prior to infusion can help achieve desired performance characteristics. Aluminum Trihydrate has been used along with resin to act as a flame retardant, releasing water and preventing fire spread or damage to composites. (Kumar et al. 2003) Other additives are used to self-heal the composites. Tiny spherical capsules of uncured epoxy and hardener can be dispersed into the resin prior to infusion. When cracks propagate in the matrix, the capsules are broken. The epoxy and hardener seep into the cracks, mix together, and cure, sealing the crack.

2.5 Connections

A challenge of any bridge deck design is to create adequate connections. These connections can be especially challenging for GFRP decks due to the potential damage to the fibers. The three types of connections for composites as classified by the Eurocomp Design Code and Handbook are: primary joints, secondary structural joints, and non-structural connections. The primary joints transfer the strength and stiffness for the entire life of the structure. The secondary structural joints are joints which when failed, result in only localized failures. The non-structural connections exist mainly to protect the product against the environment. (Zhou et al. 2005)

The two most common methods of joining FRP bridge deck panels are adhesive bonding and mechanical fasteners. Adhesive bonding provides high strength and corrosion resistance. Adhesive bonding is more easily installed and has shown better

performance for component level connections. Adhesive bonding does require more intricate deck fabrication. The adhesives are typically made of epoxy and polyurethane, which show slightly non-linear elastic behavior. Polyurethane adhesives expand to fill joint gaps entirely, but have lower strength and durability than epoxies. (Zetterberg et al. 2001) The adhesive bonding of one GFRP connection for the Salem Avenue Bridge in Dayton, Ohio is shown in Figure 2.10. Mechanical fastening may be perceived as more reliable and facilitates disassembly. Mechanical fastening requires tightening bolts to a specific torque, but not over-tightening to cause damage to the deck. (Zetterberg et al. 2001) Mechanical fasteners are easier to disassemble, but have many drawbacks including stress concentrations due to cutting of fibers and increased installation time and labor costs.

Panel-to-panel connections are commonly either bonded splicing connections or mechanically fixed. For the bonded splicing connections, adjacent panel skins are reduced to half thickness minus a gap for the adhesive at the panel-to-panel joints. The mechanical connections use small bolts at small spacings to prevent against bearing and tear out failures. (Zhou et al. 2005)

Two generic types of overlaps are made for panel-to-panel joints: single overlap and double overlap. The double overlap joints provide nearly twice the strength of the single overlap due to increased resistance to local bending moments. The double overlap would seemingly be the joint of choice. However, special care must be taken when shipping and handling the deck. If the skin overlap used for adhesive bonding or mechanical fastening were to be damaged, the entire panel would likely have to be discarded. Therefore, the more durable but lower strength single overlap is more suitable

for FRP joints. Regardless of the type of joint selected, stringent tolerances on joint fabrication must be kept in order to ensure constructability. A typical overlap distance for joints is 40 mm for adhesively bonded and 50 mm for bolted joints. One suggestion by Zetterberg et al. for mechanically fastened joints is to use prefabricated strips with bolts already inserted. These bolts would be inserted through predrilled holes in the decking. (2001)

Other types of connections include panel-to-girder connections. A typical panel-to-girder connection is shown in Figure 2.11 for concrete girders and Figure 2.12 for steel girders.

2.6 Constructability and Practicality

Proponents of FRP deck construction have cited one of the prime benefits as decreased installation costs and time. In order for these benefits to be realized, the manufacturer must design the panels to be easily and safely handled and installed using conventional construction techniques. The installation of the DuraSpan® panels on the Greene County Bridge is shown in Figure 2.13. (Henderson 2006) The challenges of FRP deck installation is to protect the panels during shipping and handling and to allow for simple installation with conventional construction equipment. One of the most in-depth investigations into the current state of FRP deck construction was completed by Reising et al. These researchers conducted one of a limited number of “showcase projects” on the Salem Avenue Bridge in Dayton, Ohio. The original pair of three-lane, five-span bridges was constructed in 1951 with 20 cm thick reinforced concrete deck cast atop six built-up stringers. The reinforced concrete deck, which had deteriorated over the years, was replaced in 2002 with four types of GFRP panels supplied by four different

manufacturers. The project was an assessment by the Ohio Department of Transportation for the constructability, performance, and feasibility of FRP composite decks. (2004)

The four decks consisted of a pultruded hexagon/double trapezoid interlocking tubing bonded with an adhesive (FRP1), a rectangular foam cell core fabricated using VARTM infusion process (FRP2), a low-density corrugated core sandwich panel fabricated using hand lay-up (FRP3), and a pultruded GFRP hybrid deck, with a 20 cm thick layer of concrete and reinforced with GFRP reinforcing bars (FRP4). (Reising et al. 2004)

Although the main focus of the study was not to examine manufacturing processes, several problems were related to poor quality control of the panels. Water leakage and excess resin in tongue and groove connections translated into constructability problems. The main constructability issues encountered were in the connection between panels, in handling and storage of the panels, and in creating adequate supports for the panel-to-girder connections. When using tongue-and-groove joints, sufficient lateral pressure must be applied on the panels to ensure good adhesion. In addition to the construction challenges, design flexibility is significantly reduced with the use of prefabricated panels with standard widths and thicknesses. (Davey et al. 2001)

Other issues, such as the regular inspection of FRP structures, can be particularly difficult to address. The structures are just as likely to degrade from the inside out as they are the outside in. Fatigue damage is not visually identifiable, so it is necessary that strains are limited so that fiber and matrix cracking do not occur under service conditions. (Turner et al. 2004)

It is well documented that FRP exposure to moisture and extreme thermal conditions can adversely affect the properties of the composite. Until recently, this was overcome by over-designing the properties to compensate for degradation. However, in order for the composites to be cost effective, more research is needed to understand these effects. Freeze-thaw cycles present the possibility for matrix micro-cracking, fiber to matrix debonding, and changes in mechanical properties. (Karbhari 2004)

One of the most challenging concerns hindering more widespread GFRP bridge deck usage is service life. GFRP applications have developed over the last 20 years, and bridge deck applications have been explored carefully only in recent years. Due to the lack of long term performance data, GFRP bridge deck has not yet been proven to satisfy current 50-year design life requirements. Although the 50-year service life cannot be confirmed, it can be simulated, but importantly with some uncertainty.

2.7 Modeling

A useful tool for FRP deck development is computer modeling using finite element software. Models must first be calibrated and verified by experimental results. The modeling of composite structures can be complex. Modeling of individual fibers in a matrix has occurred only on a very small scale. For 3-D composite structural applications, this technique becomes extremely computationally expensive and impractical. The simulation of a 3-D woven structure with finite elements was conducted by Gu (1994). A typical unit cell is shown in Figure 2.14. The cell is composed of fibers in the warp, weft, and thickness directions which are represented as separate blocks of each constituent. The geometric proportions of the constituents in the unit cell correspond to the proportions of each in the actual composite. The void in the unit cell

represents the total voids in the composite, including air bubbles and contaminants. The fabric which the unit cell represents is shown in Figure 2.15. Carlson (1995) examined a similar approach. She modeled subcells which, when assembled, presented a repeatable unit cell capable of representing a continuous composite structure as shown in Figure 2.16.

After calibration, finite element models can then be used to perform parametric studies to optimize the material usage for desired performance characteristics. Park, et al. performed an optimization of a pultruded FRP deck which altered parameters of thickness of the upper and lower flange, thickness of the web, slope angle of the web, height of the deck, and spacing between webs. The goal was to minimize the volume of FRP required for fabrication. The optimal cross-section is shown in Figure 2.17. Park et al. then fabricated this optimal design and tested the deck in fiber direction flexure, transverse flexure, web buckling, and overall prototype behavior. The results of the flexure test produced a rigidity less than 50% of the calculated, which is accredited to the rigidity of the joint between the web and flange. This joint is where most of the failures occurred in the pultruded deck. (Park et al. 2005)

Shell elements have been used to model FRP for laminate structures. Eight-noded solid elements have been used for concrete supports and neoprene pads. (Aref et al. 2005)

Material characteristics of composites are highly directionally dependent. Long continuous fibers increase strength in one direction compared to the other two orthogonal axes. One commonly accepted modeling technique for composites is the unit cell approach. The finite element method is a cost-effective way for modeling large scale components. In this method, the individual components, fiber and matrix, are modeled

for a small volume in order to generate one effective set of material properties for a homogenized composite. To date, no full scale finite element model has been reported which models individual yarns. (Lee et al. 2004)

Fiber reinforced polymer composites are sensitive to flaws, which are difficult to model individually using finite element software. Fiber misalignment, irregular spacing of yarns, and damage to fibers affect the material properties of the composites. Woven composites rely on tension in the yarns and a uniform compaction to provide consistency in the yarn spacing. Uneven spacing causes variations in the fiber volume fraction and thus, the material properties. The filler yarns are usually more susceptible to waviness during weaving since they are not tensioned and the warp yarns are. There is more waviness in a lightly compacted fabric than a highly compacted fabric. (Lee et al. 2004)

Defects and irregularities are commonly accounted for in finite element models using a “knockdown factor.” This factor is a reduction applied to material properties, such as modulus of elasticity or shear modulus. Another advantage of finite element modeling is the ability to calculate all nine constants of orthogonal woven composites, as compared to only three which can be obtained by actual experiment. (Lee et al. 2004)

He et al. used finite element models to simulate the behavior of one type of sandwich panel manufactured by Hardcore Composites and infused by the SCRIMP method. The face skins are E-glass plies which enclose a foam filled core composed of isocyanate. The foam core is wrapped in E-glass fibers. The resin used for infusion is a vinyl ester. Panels are joined together using a longitudinal shear key. (He et al. 2003)

An optimization design procedure by He et al. lists the thickness of the web core as the most important factor controlling stiffness. This factor was shown to be more important

than the thickness of the FRP skins and number of webs, both transverse and longitudinal. The deck was designed using a deflection limit of span/800 and subjected to AASHTO HS25 service I loading condition. The optimization was based on a genetic algorithm. As computer memory and processing speeds continue to increase, some full-scale modeling of individual fibers may become feasible. However, it will still be important to simplify models to limit modeling time and computational costs using techniques like the unit cell approach.

2.8 Cost Efficiency

In much of the construction industry, the most important selection criterion is cost. Due to the current high initial cost of FRP decks compared to conventional steel and reinforced concrete, the use of these decks could be more costly for new bridge construction. However, use of FRP for deck rehabilitation and replacement projects is highly attractive to reduce dead load and installation time. (Turner et al. 2004)

At this point, bridge decks are cost effective only if certain intangible benefits justify the initial cost or if new lower cost materials significantly lower the material cost. Since the 1970's, epoxy and vinyl ester production processes have been optimized to minimize cost. Little margin exists for cost reduction to produce these materials. For standard short term bridges, FRP will not be feasible until major breakthroughs occur to greatly reduce the cost of raw materials or the energy it takes to process the materials. One opportunity is the combination of FRP with other materials, such as FRP bridge deck on a steel or concrete bridge. (Nystrom et al. 2003)

2.9 Previously Conducted Research

The current research is the second investigation of the behavior of 3-D orthogonal woven fabrics at North Carolina State University (NCSU). The previous phase of the project was completed at NCSU by Taylor Norton (2004). His research consisted of the fabrication and testing of three truss-like GFRP bridge decks, one of which is shown in Figure 2.18.

2.10 Improvements in Current Design

The objectives of the current design were to: (1) maximize the depth and stiffness of the deck given a maximum width of 19.5 inches (the width of the selected weaving machine), (2) achieve a total depth of FRP of 4 inches, (3) enhance the shear performance of the deck by providing overlapping continuous shear webs, (4) enhance the bond of the balsa to the FRP by using grooved balsa, (5) prohibit withdrawal of the z-yarns at the joints by making the joints sufficiently wide, and (6) design an easier to fabricate panel with a constant cross-section which could be used for any span. The deck design consists of two skins of fabric. Both skins contain two layers of fabric, one of which is cut along the joint and folded vertically to form a shear web. Balsa cores are inserted in-between the skins. A sketch of the deck cross-section is shown in Figure 2.19. A conceptual 3-D model of the deck design is shown in Figure 2.20 with the concrete topping cut away to expose the tapered GFRP shear connectors. The tapered shear connectors are designed to ensure an adequate bond between the concrete and the GFRP panel so that the components act compositely. The shear connector fabric is similar to the deck fabric, but the axis of the warp fibers is oriented 90° from the axis of the warp fibers of the deck.

This variation permits the z-joints to be oriented in the same direction as the shear connectors.

2.11 Concurrent Research

The other study of 3-D woven bridge deck, which is currently in progress at NCSU by Mohamed (2006), investigates the behavior of similar deck panels without the use of shear connectors or concrete topping. Selected test results of this study are also reported in his thesis. The study considers the effect of the number of z-yarns at the joint, compared an epoxy and vinyl ester for infusion, and considered two different shear span-to-depth ratios. The research aims to isolate the behavior of the decks without the concrete and explore the possibility of replacement of the concrete with only an epoxy wearing layer.

All decks were loaded in three point bending. The first deck was a 4 in. x 18 in. x 60 in. panel with a four foot clear span. The second deck was the same dimensions as the first; however, it contained double the z-yarns at each joint. The dimensions of the third deck were 4 in. x 18 in. x 9 ft. This deck also had 12 z-yarns per joint and was tested with a clear span of 7 ft.

A separate study compared the performance of sandwich panels infused with a vinyl ester (AME 6000) and the same epoxy used in this research. The vinyl ester system was studied due to its easier infusion characteristics, such as lower viscosity, and ability to self-cure without the use of an oven. However, it should be noted that the vinyl ester has lower mechanical properties than the epoxy.

2.12 Weaving Process

The 3-D weaving process used in this research is known as 3Weave® and was developed at 3TEX, Inc. This 3-D orthogonal weaving process provides many advantages over traditional 2-D weaving. Faster resin infusion, lower crimp (bending of fibers), and variable thickness are some of the benefits provided by 3-D weaving. One important benefit of 3-D weaving incorporated in the current design is the ability to join layers of fabric by weaving them together. Two separate layers of fabric are stitched together in the vertical direction.

The fibers oriented in the warp direction (also referred to as the x-direction or 1-direction) provide the primary resistance in the span direction of the deck. The fiber orientations are shown in Figure 2.21. The fibers inserted orthogonally to the warp yarns are the filling yarns (also referred to as y-direction or 2-direction yarns). These fibers are woven in the same horizontal plane as the warp yarns and provide transverse resistance. The warp and filling yarns do not interlace, or cross in an over-under pattern as is the case for 2-D weaving. Instead, they are held together by the through thickness yarns. These yarns are called the z-yarns (also referred to as through thickness or 3-direction yarns), which improve damage resistance. The most useful advantage of 3-D weaving over unidirectional fibers and 2-D fabrics pertaining to the bridge deck application is the ability to create joints between layers of fabric. Vertical joints woven with the z-yarns attach separate layers of fabric to form one skin. According to Gu (1994), the optimal fiber volume fraction of the z-yarns is 2.8 percent. Higher volume fractions do not benefit mechanical properties. This 3-D weaving strengthened the joint adjacent to the

shear webs compared to unidirectional or 2-D weaving, eradicating the common problem of delamination.

2.13 Resin Infusion Systems

Two resin infusion systems are most commonly used for bridge deck applications: vinyl ester and epoxy. Vinyl ester resin is a mixture of methacrylated epoxy compounds and styrene. Styrene is the reactive diluent and the vinyl ester is the cross-linking agent.

Vinyl ester systems contain 20-60 percent styrene by weight. (Karbhari 2004) Vinyl ester systems infuse much quicker than epoxy systems due to lower viscosity. The chemical reaction of the vinyl ester with the hardener is an exothermic process allowing the resin to self-cure in ambient conditions. Vinyl esters require much less hardener (~2%) than epoxy (~30%). In general, epoxies have better bond characteristics than vinyl esters. The modulus of elasticity and ultimate strength of epoxies are higher than those of vinyl esters. An epoxy resin infusion system, Jeffco 1401/21-4101/21, was chosen for the current research due to its anticipated better properties than vinyl ester. The epoxy resin was comparable to typical vinyl esters in per pound cost, but was more expensive overall due to the higher percentage of hardener. The current design relies on the bond of the infused system so that the filling yarns at the z-joints do not pull out, separating the top and bottom skins.

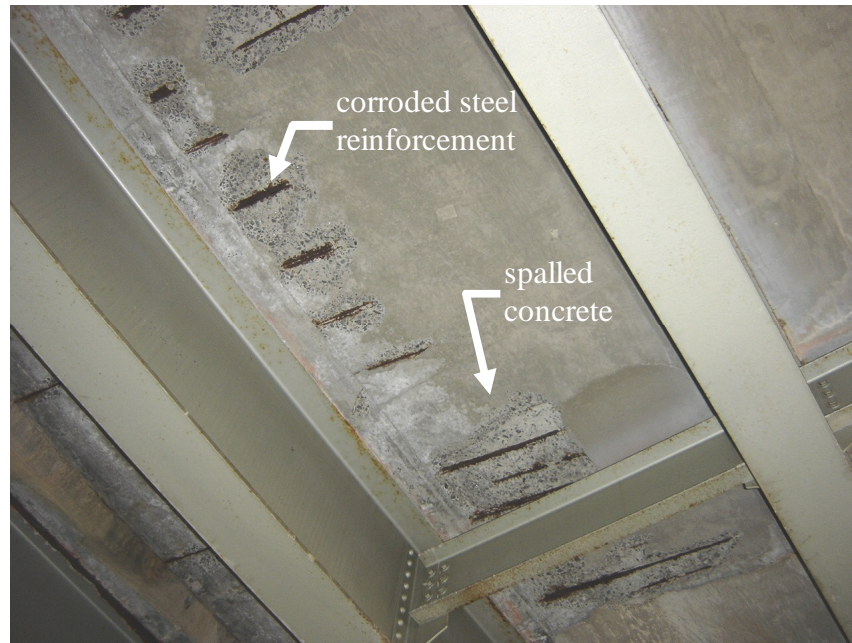


Figure 2.1. Structurally deficient reinforced concrete bridge deck, Winston-Salem, NC.



Figure 2.2. Pultrusion process from Nelson (2005).



Figure 2.3. Transonite® panels with 3-D fiber insertions (2006).

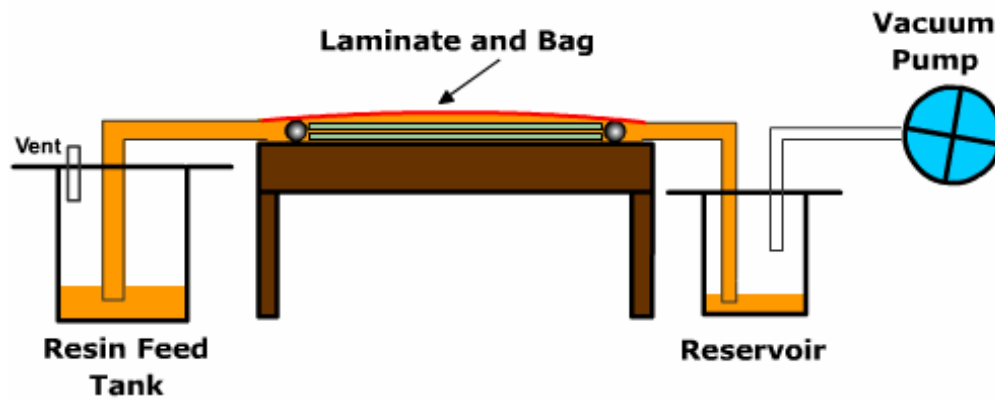


Figure 2.4. Vacuum infusion process by Fiber-Tech (2006).

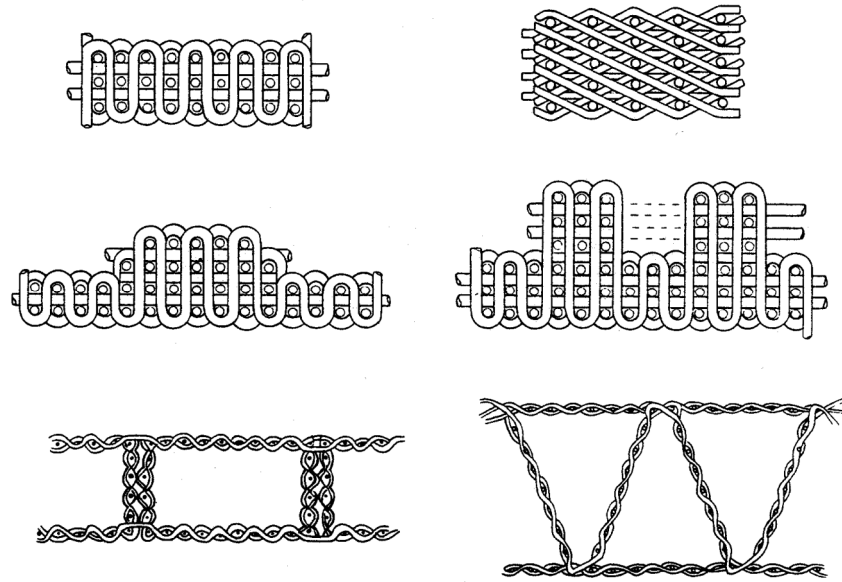


Figure 2.5. Geometry of different 3-D woven cross sections by Chou et al. (1989).

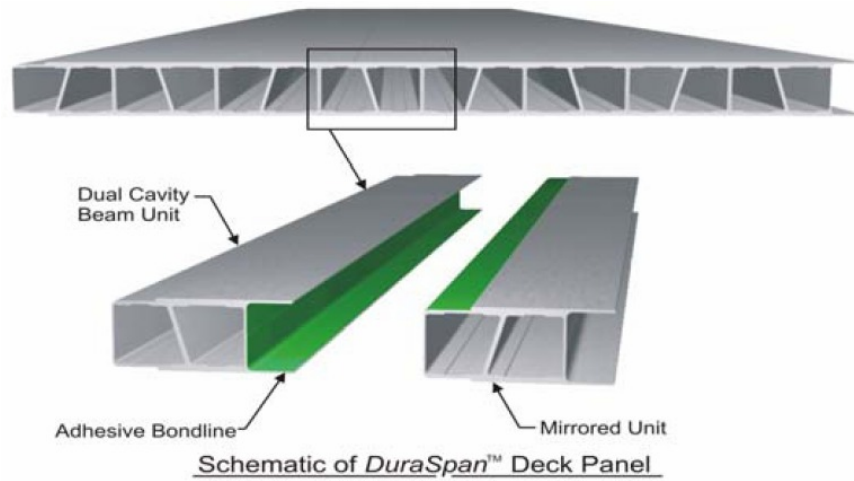


Figure 2.6. DuraSpan® panels used on SR655 by Moses (2005).



Figure 2.7. Sandwich panel construction.

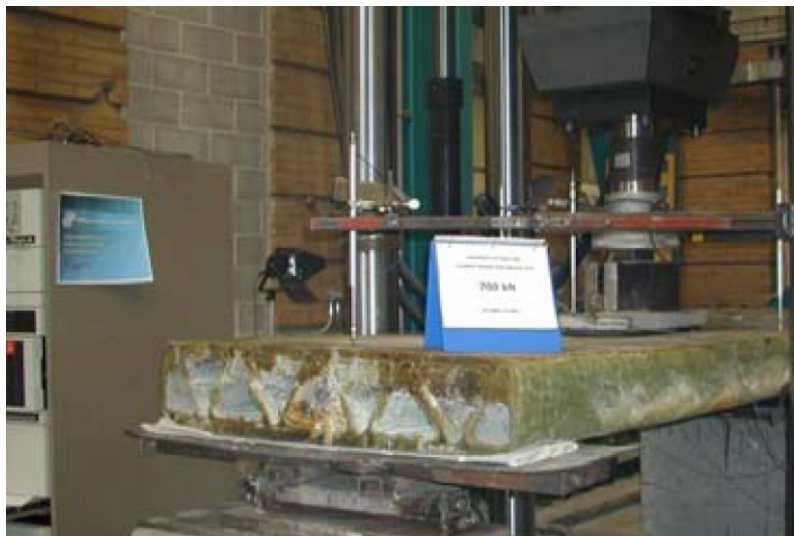


Figure 2.8. Filament wound process used by Shehata et al. (2005)

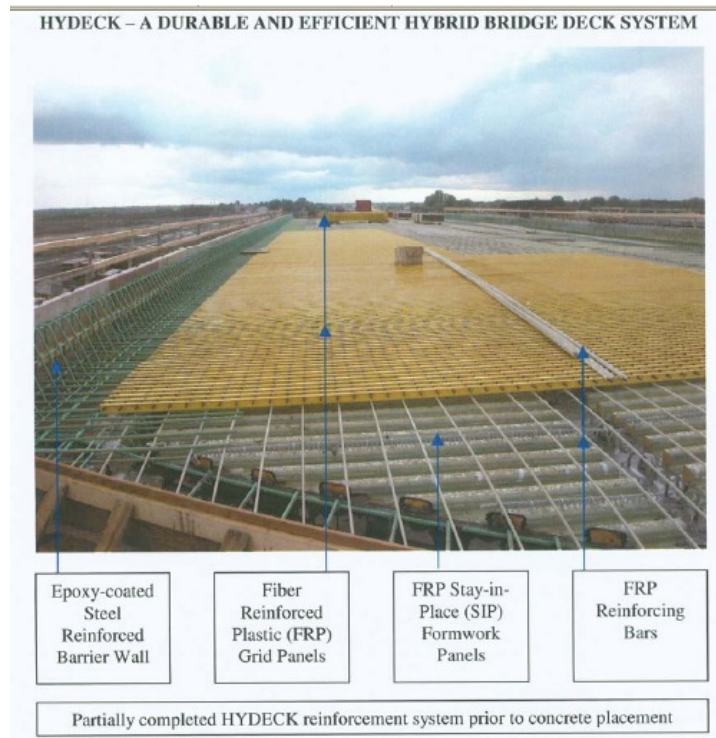


Figure 2.9. Hydeck hybrid FRP-concrete bridge deck (2005).



Figure 2.10. Salem Avenue Bridge installation of FRP panels, Henderson (2006).

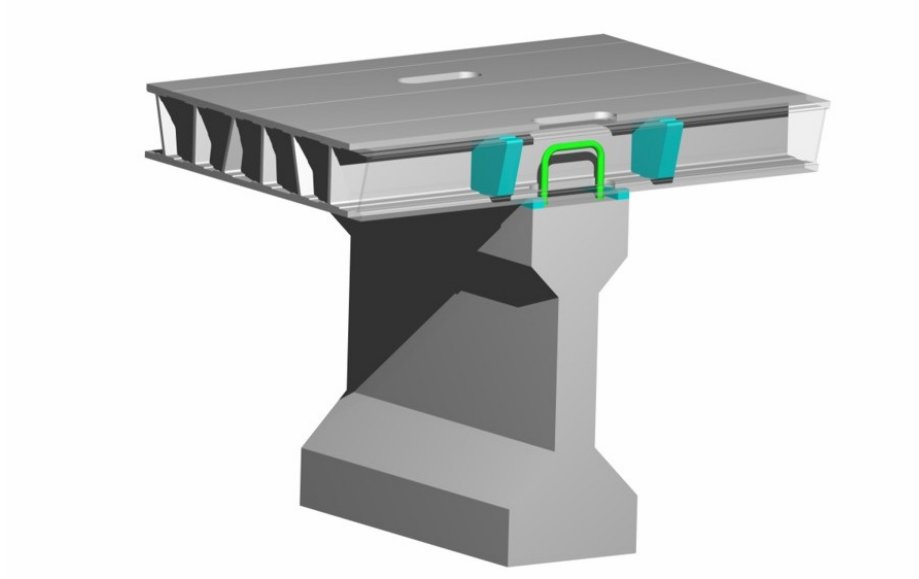


Figure 2.11. GFRP deck to concrete girder connection, Henderson (2006).

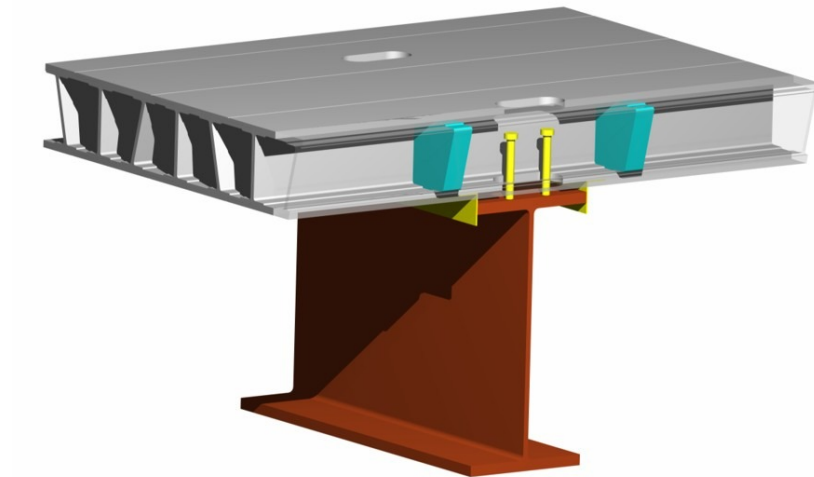


Figure 2.12. GFRP deck to steel girder connection, Henderson (2006).



Figure 2.13. DuraSpan® panel installation on Greene County Bridge, Henderson (2006).

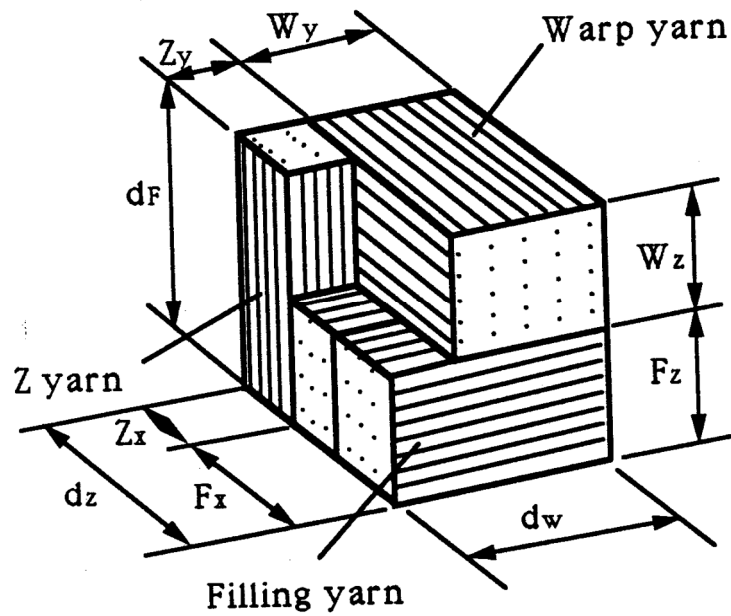


Figure 2.14. Unit cell of 3-D orthogonal woven preform by Gu (1994).

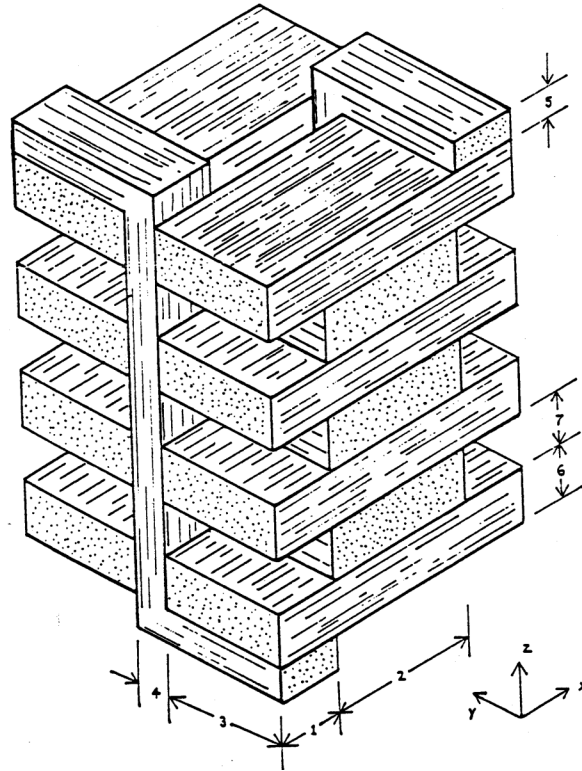


Figure 2.15. Structure of 3-D orthogonal woven fabric by Gu (1994).

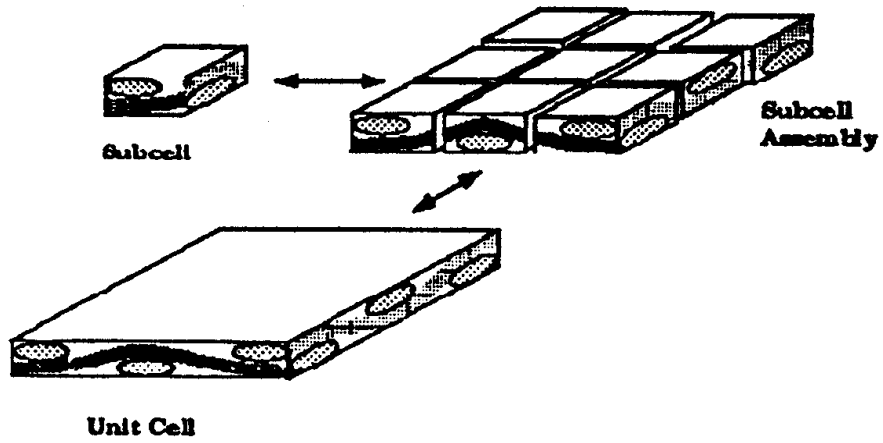


Figure 2.16. Assembly of unit cell for modeling by Carlson (1995).

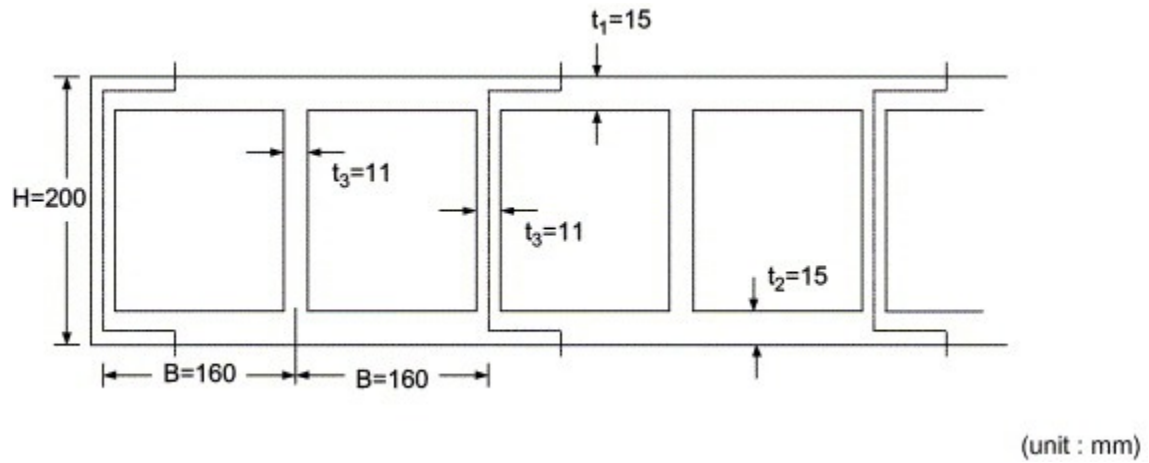


Figure 2.17. Optimal cross-section by Park et al. (2005).

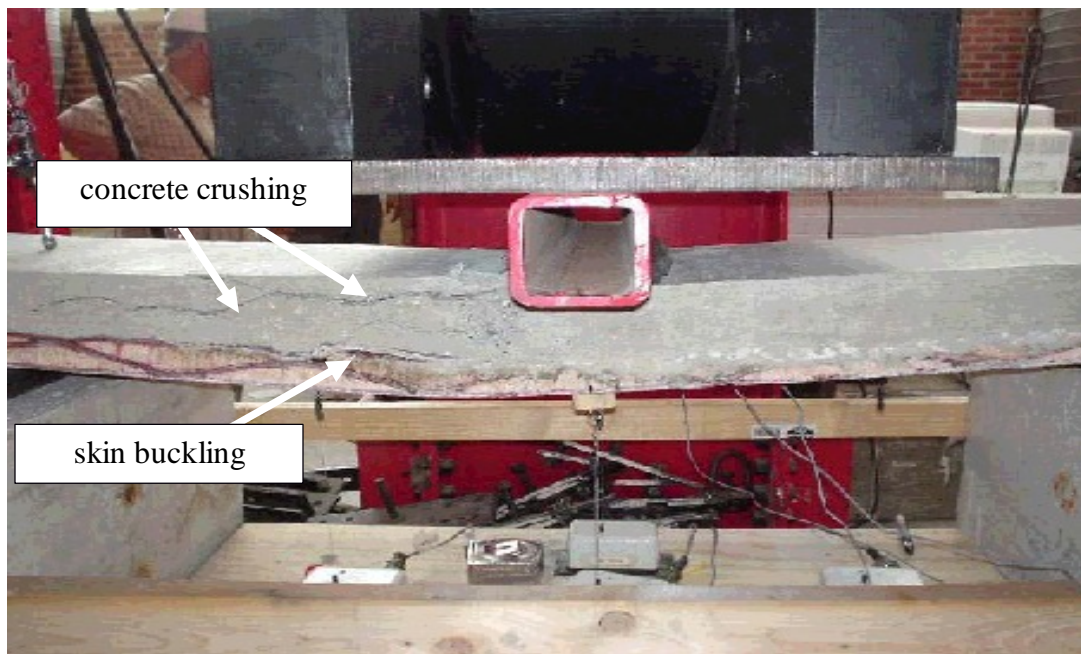


Figure 2.18. 3-D woven truss configuration by Norton (2004).

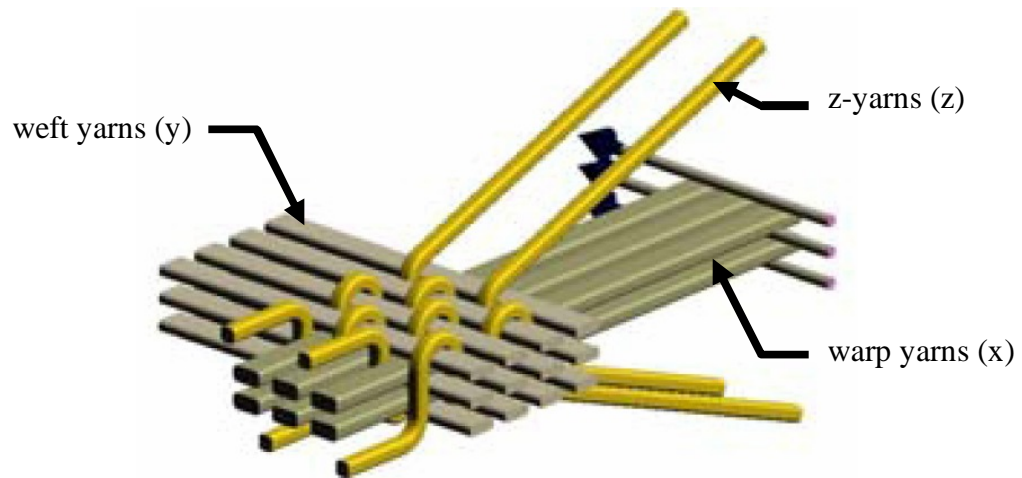


Figure 2.21. 3TEX image of 3Weave® weaving process. (2004)

Chapter 3. Fabrication

This chapter illustrates the fabrication process of the 3-D woven bridge deck and shear connector specimens examined in this thesis. The 3-D fiber architecture and production of the fabric preforms are discussed. The innovative 3Weave® process as tailored to the bridge deck design, the assembly of the entire preforms, and the vacuum infusions using an epoxy resin system are discussed.

3.1 Design Concept

The bridge deck considered in this research was manufactured from 3-D orthogonally woven E-glass fabric skins. The concept of this deck is to create two sheets of fabric, or skins, separated by a considerable distance to increase the inertia. One skin is the bottom surface and the other skin is the top surface of the panel. The bottom fabric skin provides the primary tension resistance when loaded in flexure. The top skin creates a large surface area to which the shear connector fabrics can be attached. Since FRP is relatively weak in compression, a thin concrete topping is used to increase the compression resistance and to provide a wearing surface at the same time. The shear connectors are provided to ensure composite action between the FRP deck and the top concrete layer. The bottom and top skins are linked together by full-height overlapping webs of fabric. The webs are designed to transfer shear between the two FRP skins.

One benefit of the 3Weave® process used to weave the skins is the ability to reinforce joints with yarns in the thickness direction. Each skin is woven as two separate layers of fabric. The two layers of fabric for one skin are joined by 1 in. wide joints spaced 4.85 in. from center-to-center. The joints are created by stitching in the vertical

direction. These dimensions are imposed by the availability of the 3Weave® machine at 3TEX, Inc. without major modifications.

The concept of the fabrication of one deck panel is illustrated in Figure 3.1 (a)-(f). The first step is to weave two identical skins on a 3Weave® loom. The cross-section of one typical skin is shown in (a). Once both the top and bottom skins have been woven, one layer of fabric from each skin is cut alongside each joint in the warp direction, or span direction, of the deck, as shown in (b). This results in flaps of fabric which are folded upward (c) to form a 90° angle to the uncut layer of fabric at each joint shown in (d). Next, the top skin is flipped upside down so that the flaps point downward at each joint and is placed on top of an identically created bottom skin (e). The flap from the top and the flap from the bottom overlap to produce a full-depth overlapping web. These webs have sufficient bond area to prohibit delamination between the top and bottom webs. Grooved balsa cores are inserted in the open cells between the webs (f) to keep the webs vertical until infusion and to transfer shear between the skins. These cores are notched to allow for fit up due to the extra thickness of the second layer of fabric at the joints. Any excess fabric including the filling loops is trimmed following infusion.

A similar type of skin is produced for the shear connectors and is illustrated in Figure 3.2 (a)-(f). The difference in case of the shear connector fabric, shown in (a), compared to the deck fabric is that the number of yarns in the filling direction is halved. However, instead of cutting one layer of fabric at the joints, the cut is made at the midpoint between adjacent joints as shown in (b). A trapezoidal-shaped wooden core is inserted on top of the joint (c) and one flap of fabric for each shear connector is wrapped tightly around the wood (d). The fabric flap is stapled to the wood to hold it in place (e).

Then, the remaining flaps are wrapped tightly around each core insert and over the previous flap. These flaps are also stapled into place (f). The complete shear connector fabric containing four shear connectors apiece is placed on top of the deck with the z-joints of the shear connectors perpendicular to the z-joints in the deck. The entire deck system is infused with a thermosetting epoxy resin. Concrete is then cast atop the infused deck to serve as a wearing surface, provide compression resistance, and hinder buckling of the skins. The concrete is cast with a mesh of ¼ in. steel deformed bars to resist shrinkage and provide confinement for the concrete cast in-between the shear connectors.

3.2 Design Specifications of the Deck

The goal of this research was to produce three decks. The first demonstration deck (Demo Deck) was a 2 ft. long and used as a pilot specimen. This deck was not tested as intended. However, it was used to investigate the viability of the design concept prior to the comprehensive experimental study in which the process is repeated. The first test deck (Deck 1) was 5 ft. to allow 6 in. bearing length at the support for testing purposes. The length of the second test deck (Deck 2) was 9 ft. and tested with a clear span of 7 ft. The nominal depth and width of each deck was 4 in. and 18 in. respectively. The depth of the shear connectors was 1 in. high, embedded in a 2 in. concrete topping.

3.3 3Weave® Fabrication Process

The fabric of the FRP bridge decks was produced using 3Weave®, a 3-dimensional weaving technique developed by 3TEX, Inc. All yarns selected for weaving were continuous E-glass HYBON 2022 yarns. These yarns are produced by PPG Industries, Inc. The E-glass (electrical) yarns are one of several types of glass fibers. Other types of glass fibers include S-glass (structural) and C-glass (enhanced corrosion resistance)

fibers. While the S-glass fibers exhibit slightly better mechanical properties, their higher cost cannot usually justify selection over the more economical E-glass.

The size of the yarns is described by the yield, or number of yards of yarn required to produce one pound of material. The warp yarns (x-direction), the largest yarns, required only 103 yards to weigh one pound, whereas the smaller filling yarns (y-direction) required 330 yards/lb, and the thickness yarns (z-direction) were 675 yards/lb. Each z-yarn and warp yarn was wound around a separate cylindrically shaped bobbin prior to weaving. The warp bobbins were loaded on two separate sets of creels. The z-yarns were loaded onto a separate creel situated in-between the two warp creels. The creel setup is shown in Figure 3.3. The yarns from each row on these creels were threaded through an eyelet grid to organize the rows of yarns into an evenly distributed grid. The yarns were then wound around a series of staggered horizontal metal rods. The rods, along with U-shaped metal weights, generated tension in the yarns, keeping the spools from rotating excessively and limiting sagging yarns, as shown in Figure 3.4. The z-yarns were threaded through heddles (parallel wires with eyelets used to separate and guide the z-yarns) which created openings (shedding) between the layers of fabric for the insertion of the filling yarns shown in Figure 3.5. The warp yarns were threaded through tooth-like openings in a metal divider called dents shown in Figure 3.6. Figure 3.7 shows the filling yarns which were inserted from the side of the deck through the sheds using carbon fiber rapiers. Both the warp yarns and filling yarns remained horizontal during the weaving process. Only the z-yarns moved vertically.

3.4 Weaving Procedure

Weaving of the fabric for the preforms was conducted at 3TEX, Inc. The details of the patented 3Weave® process are well-documented by Mohamed et al. (1988). A basic overview of the process as it applied to the bridge deck preform production is discussed in the following section.

A 3TEX QBasic computer program for the 3Weave® loom was modified for this particular deck design. At the start of the process, each command was manually entered into the computer. This allowed the operator to observe various pitfalls in each step of the weaving process. As more weaving was accomplished, adjustments were made to the weaving setup. Some of these adjustments included increasing or decreasing tension on the yarns, adjusting rapier lengths, and spraying the yarns with distilled water to decrease friction. By the end of the project, the weaving process was semi-automatic. Specified stops in the process were setup for the operator to check shedding for rapier insertion and shedding for the filling yarn rod which created the loops. The quickest cycle recorded lasted 20 seconds. On an improved machine, the weaving process could be fully automated, completing one cycle in a matter of seconds. One weaving cycle consisted of the following steps:

Step 1. The four filling yarns were inserted using carbon fiber rapiers with eyelets at the tips. These rapiers were inserted four inches past the edge of the last warp yarn in the fabric. The rapiers were inserted through the opening (shedding) created between the warp yarns and z-yarns. Due to inadequate tension on the z-yarns, these yarns sometimes required manual separation to provide adequate shedding for the rapier insertion.

Step 2. The filling yarns were next secured in place by a metal rod, the selvage hold, which was inserted down between all four yarns, creating a loop in the filling yarns. This process is shown in Figure 3.8.

Step 3. The rapiers retracted to their original position, pulling the filling yarns against the selvage hold and creating double the filling yarns.

Step 4. The six z-harnesses switched. Two z-harnesses switched for the top layer of fabric. The harness above the top layer of fabric warp yarns dropped below the warp yarns and the harness below the warp yarns moved above the warp yarns. The harnesses above and below the bottom layer of fabric similarly switched places. Two z-harnesses created the top layer, two harnesses created the bottom layer, and the remaining two harnesses wove the two layers together at the joints. The harnesses before and after switching are shown in Figure 3.9 and Figure 3.10 respectively.

Step 5. The reed is shown in Figure 3.6. It is similar to a comb and separates the warp yarns at uniform distances and packs together the fabric as it is woven. The reed was brought forward to beat-up (pack together) the new set of filling and z-yarns.

Step 6. The reed retracted, releasing the compressive force on the yarns used to pack together the filling yarns.

Step 7. The reed was brought forward again for a second beat-up and the take-up system pulled the woven fabric forward an additional amount (0.35 in. for the deck fabric, 0.6 in. for the shear connector fabric), pulling more of each warp and z-yarn into the loom. The take-up system is shown in Figure 3.11.

Step 8. The reed retracted again.

Step 9. If necessary, the sagging z-yarns were separated manually from the warp yarns using metal rods to create shedding for the rapiers and the process was repeated.

3.5 Woven Preform Design

One weaving cycle is defined to contain two filling yarns (picks). One pick was produced by the filling insertion, the other by the retraction of the filling yarns by the rapiers. The spacing of the filling yarns in the longitudinal direction was defined by the approximate number of picks per inch (ppi). This was achieved by setting the take-up system, which controlled how far the skin was pulled during each cycle. The only difference in the fiber architecture of the decks versus the shear connectors is the number of filling yarn ppi. The deck skins were taken up 0.35 in. per weaving cycle, producing 6 ppi in the filling direction. The shear connector skins were taken up 0.6 in. per weaving cycle, producing 3 ppi in the filling direction. The skin is shown in Figure 3.12.

For one skin containing two layers of fabric, the warp consisted of 42 yarns per inch, the filling consisted of 48 yarns per inch (four rapiers inserting 12 yarns per inch giving 6 ppi), and the z-direction produced 14 yarns per inch. At the joints, where the two layers of fabric on each skin were woven together, there were an additional 12 z-yarns per joint. The width of the joints was 0.85 in. The average number of z-yarns per inch spread over the total cross-section was 16.67. At the joints, two z-yarns were inserted through the same dent.

3.6 Properties of Panel Skins

The width of the deck preforms were 19.5 in., plus 0.75 in. of filling loops on either edge. However, the skins were trimmed to a width of 18 in. after infusion. Therefore, the following calculations are based upon the final width of 18 in.

The linear weight of the fabric preform was calculated to be 168 oz/yd of skin. The areal weight of the preform was 336 oz/yd² per skin. Thus, with a deck composed of both a top and bottom skin (4 total layers of fabric), the linear weight of the total fabric for a deck was 336 oz/yd (7 lb/ft).

The weight fraction in proportion to the total weight of fabric preform for the warp (0°), filling (90°), and thickness (z) were 0.699, 0.249, and 0.052 respectively. The volume fractions of these yarns compared to the total volume of the composite after infusion were 0.286, 0.103, and 0.021.

3.7 Infused Composite Properties

The average fiber volume fraction is 0.41, determined experimentally and discussed in the next chapter. This value is the basis for the following calculations. The most fundamental theory of composites is the Rule of Mixtures. The Rule of Mixtures is a fundamental model for composite behavior which treats the fiber and matrix as two separate slabs of material attached with a perfect bond capable of full load transfer. The thickness of each slab is proportional to the volume fraction of each constituent. This model is generally a good estimate for a baseline of expected mechanical properties for unidirectional composites in the longitudinal direction of the fibers. The calculations to determine the predicted properties of the composite are found in Appendix A. The predicted results are compared to the experimental results. The geometric properties of the sample are shown in Table 3.1. Predicted weight and volume fractions of the sample are shown in Table 3.2. Properties of the z-yarns are shown in Table 3.3. Actual deck preform characteristics are listed in Table 3.4.

3.8 Fabrication of Test Specimens

After weaving the fabric for the top and bottom skins of the decks, the preform shapes of the decks were assembled. Balsa wood cores were inserted between the top and bottom skins, holding the vertical shear webs in place. The shear connector and deck assemblies are discussed in the following sections.

3.9 Shear Connector Assembly

All the shear connector specimens were produced using the same fiber arrangement as the deck skins, except with half as many picks per inch. By halving the number of picks per inch, weaving time was cut in half and the fabric could be more easily folded to the desired shape.

Three different shear connector configurations were fabricated for the shear connector study. The first design consisted of vertical flanges, two per z-joint. These specimens were formed by first cutting the top layer of fabric parallel to the joint at a distance of 1 inch from the nearest edge of each joint, as shown in Figure 3.12. The fabric was glued with Duro Super Glue prior to cutting to minimize yarn fibrillation. The top skin of fabric was then folded upward 90° to form a vertical flange. The specimens measured 12.5 in. in the warp direction by 19.5 in. in the weft direction and contained four joints each. This produced a total of eight vertical flanges, two per joint.

The second configuration was formed using pine wood core inserts to form four rectangular-shaped shear connectors. The unit weight of the wood as determined by weighing a known volume of shear connector wood was 33.88 lb/ft³. First, a 2x4 was cut to the dimensions of approximately 5/8 in. x 7/8 in. x 12.5 in. to allow for the shaping of the fabric. Next, the fibers at the midpoint between the joints were glued using Super

Glue to minimize the fibrillation of the yarns after cutting. The top layer of fabric was cut along the glued seam. The wood cores were inserted and then the fabric was wrapped tightly around the cores. The overlap of the fabric wrapped around the wooden cores was approximately $\frac{1}{2}$ in. The fabric preform was stapled using a staple gun with approximately ten $\frac{9}{16}$ in. staples along the top edge of each core to hold it in place until infusion. The pine wood was denser and did not form as good of a bond with the fabric compared to the perforated balsa. However, a necessary function of the core inserts in this case was to serve as a form for the fabric. The pine wood was harder than balsa and less susceptible to withdrawal of staples. The total height from the top surface of the shear connector to the top of the uncut skin was 1 in., similar to the vertical flange design.

The third shear configuration was formed using pine wood inserts to form four trapezoidal-shaped shear connectors. These connectors flared out at the top to resist uplift of the concrete at the shear connectors. This feature was not provided by the other two designs. However, this design was not as practical for large thicknesses of fabric for which bending of the fabric at acute angles would become difficult and damaging to the fibers. Similar to the rectangular shear connectors, a pine core was ripped from a 2x4 on a table saw but at approximately 27° from the vertical instead of completely vertical. The width of the core varied linearly from $\frac{3}{4}$ in. at the base to $1\frac{1}{4}$ in. at the top. The fabric was again glued, then cut at the midpoints between the joints and then folded tightly around the core. The first layer of fabric was stapled to the core as shown in Figure 3.13. Next, fabric on the opposite side was wrapped over the previous layer and stapled. The fabric was stapled in place with $\frac{9}{16}$ in. staples. The overlap of fabric was a minimum of

3/8 in. and the total height from the top surface of the shear connector to the top of the uncut skin was 1 in. An assembled shear connector preform is shown in Figure 3.14.

3.10 Deck Assembly

The flanges and webs of the deck were fabricated using two skins produced on the 3Weave® loom. Both skins were identically woven. Upon completion of weaving, the decks warp yarns were glued using Super Glue to inhibit fiber fibrillation along the line to be cut. The seam of glue was placed on one layer of each skin only, located between the second and third warp yarn parallel to the z-joint. The glue seams were all located on the same side of each joint. A rounded wooden block was inserted into the gap between the two layers of fabric to create separation between the two layers of fabric. One layer of fabric was cut along the glued seam using a utility knife along a metal straightedge. One fabric skin is shown in Figure 3.15 after cutting along the z-joint. The wooden inserts shown in this figure are for demonstration purposes.

Next, the balsa core inserts were shaped. Patterns were created for the notched cross-section to ensure proper fit-up prior to shaping the balsa. The patterns are inserted on the deck shown in Figure 3.16. Due to lack of availability of 4 in. thick cores, two 2 in. cores were stacked on top of each other and bonded together using an epoxy resin. The interior balsa cores were ripped on a table saw to the appropriate width, 4.5 in. The balsa cores in the outermost cells were ripped to a width of 2 in. In order to conform to the shape of the fabric skins, the balsa had to be notched at each z-joint. This notch was created by two perpendicular cuts on the table saw, one 1/8 in. deep and one 1 in. deep. This notch accounted for the thickness of the z-joint.

The outer balsa cores were bonded using Jeffco epoxy resin infusion system. A hand application of the epoxy resin using a paintbrush was used to saturate the interface between the two layers of balsa. The epoxy was cured at room temperature and pressure was applied during curing via various steel plates and other weights.

Several methods were evaluated for assembly of the fabric skins and balsa cores. The concept of assembly was first investigated on a 2 ft. long demonstration deck (Demo Deck). This deck is shown in Figure 3.17 with the top and bottom skins held in place with wood spacers. For Deck 1, (the 4 ft. span deck) the 4 in. thick cores could be inserted from the end of the deck, with both skins of fabric already in place. However, for longer decks, the friction between the balsa and the fabric resulted in damage to the balsa wood and allowed for movement of the webs. This also prevented the use of a chopped strand mat, a commonly used layer of randomly oriented glass fibers which could have enhanced the bond between the balsa and the fabric. The method of choice for assembly consisted of first inserting the bottom layer of the interior balsa cores onto the bottom skin. Next, the top skin was added, starting from one side and inserting the webs down into the gaps between the balsa core and the webs of the bottom skin. With both skins in place, the top layer of balsa cores was inserted from the end of the deck. The maximum length of balsa core available was 4 ft., so the pieces used were 1 ft. and 4 ft. long for each Deck 1 cell, and two 4 ft. and one 1 ft. long pieces for each half cell in Deck 2.

Once the interior balsa cores were inserted, the webs on either side were fastened, tying the top and bottom skins together. The skins were pulled tightly and 9/16 in. staples were inserted through both webs into the balsa cores to hold the skins in place, as

shown in Figure 3.18. A close-up of one complete cell is shown in Figure 3.19. After stapling both sides, the exterior 2 in. wide bonded balsa cores were inserted, as shown in Figure 3.20. These cores were held in place prior to infusion using duct tape.

Three shear connector panels were placed on the top of the deck, each with 4 wooden core inserts to provide a total of 12 shear connectors at 4.85 in. on-center. Figure 3.21 shows the end of Deck 2 with the shear connectors placed on top. Each shear connector preform measured 17 in. in the warp direction by 19.5 in. in the filling direction. The angle of slope from the vertical for the flanges was approximately 27° prior to infusion. Had folding the fabric been any more difficult, a warp yarn could have been left out at the fold to make the shaping of the fabric easier. The areal weight of the shear connectors without wood cores was 150.84 oz/yd^2 . This average value was obtained by weighing 5 shear connector fabric sheets, then dividing by the total area of each piece, including the loops, formed during weaving.

Approximately 1.5 in. was left at the end of each deck without shear connector fabric. However, this area would be beyond the outside of the support, if not trimmed prior to testing. Also, a 1.5 in. edge distance from the edge of the shear connector to the edge of the deck was used. This was also trimmed to an approximate edge distance of 0.5 in.

3.11 Shear Connector Infusion Setup

The shear connector preforms were infused on a steel table. The surface of the table was first cleaned with acetone and then waxed and buffed to provide a smooth, level surface for infusion. The infusion setup for the flange configuration is shown in Figure 3.22. A sheet of 1/8 in. thick High Density Polyethylene (HDPE) was placed underneath the shear

connectors, extending approximately 4 in. past the end of the fabric on all four sides. The HDPE sheet was used to provide for easier cleanup and demolding and was a better insulator than the steel table top, which would have acted as a heat sink.

Next, a strip of tacky tape from Composites One was adhered to the table with the paper backing still intact on the upward side of the tape. The tape was placed on the table, 4 in. to 6 in. from the edge of the preform. Next, a layer of peel ply was cut to fit over the entire exposed surface of the preform. A layer of flow medium was taped to the top of the peel ply to assist the resin flow in the warp direction. The infusion occurs as much as three times faster in the filling direction than the warp due to the lower fiber volume fraction in the filling direction, so the flow medium was needed to attempt to wet out all edges of the preform simultaneously. The only difference between the infusion setup of the flange configuration versus the wooden insert configurations was the use of Ultra High Molecular Weight Polyethylene (UHMW) in the flange configuration, as shown in Figure 3.23. The flanges required a form to hold the fabric vertically in place prior to infusion. The self-lubricating UHMW was cut into blocks, 1 in. thick in-between joints and 13/16 in. thick at the joints. The UHMW was removed after infusion.

A ½ in. diameter spiral tubing was also placed on top of the flow medium to assist resin flow in the warp direction. The spiral tubing was also taped down around the perimeter of the preform to serve as the outlet for excess resin and to create a uniform vacuum around the perimeter. At the exits in the vacuum bag, spiral outlet tubing was wound around a solid ½ in. tubing within the vacuum bag. The solid tubing would carry the excess resin from the spiral tubing to a disposal container inside the vacuum pump. Next, a white breather cloth was placed in 1 in. wide strips, linking the edge of the

preform to the outlet spiral tubing. The breather cloth allowed unwanted air bubbles exiting the preform to flow easily, but was more resistant to resin flow.

The resin inlet tube was a ½ in. diameter tube inserted through the vacuum bag to an inlet connection placed underneath the vacuum bag. The inlet connection was held in place on top of the spiral tubing during vacuuming and is shown in Figure 3.23. Under a slight vacuum, the air leaks in the bag due to damage or improper seals were identified audibly and sealed manually using tacky tape.

3.12 Deck Infusion Setup

The decks were infused on a 4 ft. x 10 ft. sheet of UHMW. The UHMW was selected for the infusion table surface due to its superior abrasion and thermal resistance compared to the HDPE and steel. The entire infusion setup is shown in Figure 3.24. First, the 1 in. thick UHMW table was cleaned. Next, a 1/8 in. HDPE sheet was placed underneath the deck for protection of the surface and easy cleanup. Slits were cut at three points along the length of the deck, cutting off the filling loops and two warp yarns to make room for duct tape. Next, the peel ply was cut to length. The peel ply was wrapped on top of the deck, oriented in the warp direction of the deck so to provide more infusion assistance in the warp direction. Duct tape was attached at the slits in the deck, wrapped around the deck in the filling direction to serve as a clamping and confining force to hold the side balsa cores in place and tighten the webs until the vacuum bag could be pulled tight. These slits would be trimmed off after infusion. The duct tape had to be taped to itself to ensure that it would not slip off of the self-lubricating HDPE sheet.

Red flow medium was cut and wrapped over the shear connectors to assist the flow of the resin. The rectangular-shaped flow medium was wrapped over the shear

connectors and stopped 2 in. from the edges so that the resin was required to flow some distance on its own. This was to prevent “racetracking”, or flow of resin quickly around the perimeter of the preform straight to the outlet tubes, creating significant waste and possibly exhausting the resin supply. The flow medium stopped at the midpoint of the endmost shear connectors as shown in Figure 3.25. This left the resin to flow down the last shear connector and horizontally to the end of the preform. Angled strips of flow medium were placed at each of the four corners on the top to assist in the wet-out of the corners. These strips were held in place by duct tape.

Spiral tubing was placed on top of the flow medium along the centerline of the deck in the warp direction. The tubing was split into a y-shape at either end of the deck to assist wet-out of the corners on top of the flow medium angled strips. These are the locations to which the resin must flow the farthest. This y-connection was formed by wrapping another spiral tube around the longitudinal spiral tubing. The resin inlet tube was a ½ in. diameter tube inserted through the vacuum bag to an inlet connection placed underneath the vacuum bag. The inlet connection was held in place on top of the spiral tubing during vacuuming. The air gaps were identified audibly and sealed manually using tacky tape.

3.13 Vacuum Bagging

The vacuum bag was cut to a length two times the length of the deck. The bag was produced on an 8 ft. wide roll, of which 20 in. of width was trimmed before bagging so that bag could be more easily kept square. Skewed bagging could cause highly tensioned seams or wrinkles in the bag that even large pleats could not remedy. After cutting the bag, the tacky tape was applied to the UHMW. The sticky side of the tape was stuck to

the table with the backing still intact. The tape was offset approximately 3 in. from the edge of the deck on all sides.

White breather cloth was cut in 1 in. strips and placed 1 in. from the edge of the deck on all sides, as shown in Figure 3.25. This cloth slowed the resin, transferred air bubbles easily, and slowly carried excess resin to the outlet tube. The breather cloth was also cut in 1 in. wide strips, approximately 2 in. long and placed perpendicular to the perimeter strips. One end of the cloth was placed at the edge of the balsa and the other on the perimeter strips of breather. This served as a link between the preform and the perimeter breather strips. The breather was taped to the table every 2 ft. to hold it in place during bagging and vacuuming. The perimeter breather was placed slightly closer to the preform at the corners of the deck so that there was better vacuum (less slack in the bag) at these hard to wet-out points.

Next, the spiral tubing and inlet connection were resituated on top of the deck. Vertical pleats were formed in the vacuum bag at each corner, and two extra along the long sides to provide enough slack in the bag so that it could be pulled tightly over the shear connectors. The height of each pleat was approximately 12 in.

A clamp was placed on the resin inlet tube and the vacuum was activated through the outlet tube. Under a slight vacuum of 2 in. of Mercury or less (~1 psi), the bag was arranged by hand so that the flow medium was tucked tightly under each shear connector and the slack was pulled to the top of the shear connector. Under full vacuum, any additional slack required for each shear connector would come from these locations above the individual shear connectors. A total of 27 in. of Mercury head (~13 psi) was maintained for the entire vacuum infusion process.

3.14 Infusion

Prior to infusion, each preform was preheated for 2 hours using an electric heating blanket shown in Figure 3.26 to elevate the preform temperature to at least 80°F. The resin was mixed in a flexible plastic liner in a 5-gallon bucket. The weight of the empty bucket was zeroed on a scale and the appropriate amount of epoxy was weighed out. After zeroing the weight reading again, the hardener was poured into the epoxy bucket while on the scale to monitor the hardener weight, which was proportioned in a ratio of 100 parts epoxy to 30 parts hardener by weight.

Each batch of resin was mixed mechanically using an epoxy drill bit mixer extension on a variable speed DeWalt drill shown in Figure 3.27. The resin was stirred for six minutes per batch at as high of a speed as possible without creating obvious additional air bubbles. The resin was allowed to sit for 10 minutes before infusion to allow air bubbles to surface.

After mixing and vacuuming, the first batch of resin was placed on the infusion table at the inlet tube, creating a pressure head. The inlet tube was inserted into the resin and the clamp removed. The resin flowed through the preform as designed, shown in Figure 3.28. Upon complete wet-out of the preform, the inlet and exit tubes were both clamped to maintain vacuum overnight. Each specimen was postcured overnight for 18 hours with a heating blanket. At the end of 18 hours, the surface of the specimens was still tacky and required additional postcure with an oven. Specific notes on each infusion are given in the following sections.

3.14.1 Infusion of Shear Connectors

The first shear connector specimen with the vertical flanges achieved wet out at the perimeter in two minutes. The red flow medium and HDPE allowed the resin to flow very quickly. The path of the resin followed the spiral tubing to the flanges to the base layer of fabric. Due to the uniform covering of the specimen with flow medium, the four corners of the base layer of fabric took considerably longer to wet out. Total wet out was achieved in 31 minutes.

The second shear connector infusion involved simultaneous infusion of the rectangular shaped and tapered shear connector specimens. Although the area to be infused was larger than the vertical flange shear connectors, the time for complete wet out was reduced to 28 minutes. Not as much “racetracking” or excess exiting of resin occurred since the flow medium was stopped at least 4 in. from each edge.

3.14.2 Infusion of Deck 1

The epoxy resin for Deck 1 was mixed in two equal weight batches. The total time for complete wet out of infusion was 33 minutes. The inlet tube connection was pulled tightly against the preform by the vacuum. After resituating the inlet tube, the resin flowed freely and complete wet out was achieved.

3.14.3 Infusion of Deck 2

The epoxy resin for Deck 2 was mixed in two batches. Within fifteen seconds of vacuuming the first batch, the resin had flowed halfway to the left end of the deck. Due to a combination of the vacuum bag being pulled into one outlet tube and into the spiral tube at three locations along the length, the infusion took longer than should have been necessary. After 5 minutes, the left inlet was clamped off since the right side was not

pulling resin as quickly. When approximately half of the first batch of resin was used, the second batch was poured into the batch 1 bucket so that no additional air bubbles were introduced. Deck 2 achieved total wet-out in 35 minutes. At this time, both the inlet and outlet tubes were clamped to hold the vacuum and then the vacuum pump was turned off. The results of the infusion process are shown in Table 3.5.

3.15 Postcuring Process

Jeffco infusion system 1401-21/4101-21 Slow requires 4-6 hours of postcure for development of maximum strength properties. In order to achieve elevated temperatures, an extension to an existing oven was constructed at 3TEX. The doors from an existing oven were removed and a box-shaped extension was constructed to contain the entire length of the deck.

The walls of the extension consisted of R4 Styrofoam insulation board. The foam board was fabricated with a tongue-and-groove connection. Air gaps between the floor and oven were sealed with a flexible blue Styrofoam seal to inhibit heat loss. The frame consisted of SPF No. 2 wood, nominally 2x3's and 2x4's. At each of the four corners, two legs were attached to provide support for the corner columns. The entire system was built to be easily disassembled for storage in four pieces.

An infusion table was created to allow for quality infusion of the 9 ft. specimens. The table consisted of a wide flange steel frame with a 1 in. thick sheet of UHMW continuously spanning 2 spans to provide a rigid surface for infusion shown in Figure 3.29. The table was mounted with wheels to roll directly into the existing oven equipped with an exhaust system and blower.

In order to monitor the temperature during postcure, thermometers were inserted through holes drilled at various locations in the Styrofoam walls. Due to air leaks in joints on the oven extension, it was observed that an oven temperature setting of 160°F was necessary to ensure a minimum 150°F temperature throughout the oven. The decks were postcured at 150°F for four hours according to manufacturer's instructions.

3.16 Demolding

Following post-cure, each specimen was demolded from the infusion table. First, the inlet tube was cut such that no resin remained in the inlet tube. Next, an air hose was inserted into the inlet tube and air was pumped into tube, inflating the vacuum bag and separating it from the infused specimen. The vacuum bag and tacky tape were pulled up from the table.

Use of UHMW for the vertical flange shear connector specimens created a smooth surface at the top of the fabric where the vacuum bag pressed the plastic against the top surface. As a result, the texture resembled that of the peel ply, which was infused in direct contact with the fabric. Removal of the peel ply was difficult for the vertical flange specimen due to the accumulation of resin on the outside of the peel ply and flow medium.

The cured decks were easily delaminated from the infusion table by lifting up one corner of the infusion table at a time, bending the plastic such that the rigid infused deck separated from the flexible table. Next, the peel ply was removed by cutting slits in the ply and manually stripping the ply off the deck. The excess cured resin on the infusion table was cleaned using a metal scraper and the residual tacky tape was cleaned with acetone and paper towels. In order to minimize damage to the vacuum infusion

components, the peel ply, tubing, breather cloth, flow medium, tacky tape, and vacuum bag were disposed of after each infusion. Only the infusion table and inlet connection were reused for subsequent infusions.

3.17 Test Samples

Each specimen was trimmed after infusion to create a uniform specimen suitable for testing and modeling, neglecting edge effects. Following infusion, some breather cloth, peel ply, flow media, and vacuum bag were still attached around the edges to the sample, encased in excess resin. The filling loops left over from the weaving process also needed to be trimmed in order to ensure the presence of warp yarns uniformly in the remaining cross-section.

All decks and shear connectors were cut using a wet stone cutting saw. The shear connectors were initially cut around the perimeter to provide a flat edge for the concrete formwork. The three replicates from each shear connector configuration were not cut until after the concrete was cured. The three shear connector configurations cut to size for concrete placement are shown in Figure 3.30.

The infusion process resulted in rough edges of cured excess resin extending beyond the filling loops. This resin was attached to the deck after demolding. In order to create a uniform cross-section for the decks, the edges of the decks were trimmed. The first step in cutting was to create a support system for the decks. A level surface on either side of the saw table was built to support the long decks. The decks were placed on top of the 1/8 in. thick HDPE sheets to prohibit damage from scraping on the table and to facilitate sliding the decks across the table of the saw. The first cut on the decks was to create one straight edge by trimming one side of the deck. Two methods were

investigated for aligning the deck on the saw table: visual alignment using a reference edge of the table and alignment using a laser projected onto a 90° framing square. The laser projection was not as effective as the visual alignment due to the inability to find a flat reference surface parallel to the blade. The laser level could not be placed against the blade due to the height of the decks and therefore was placed against the blade cover. The blade cover was not exactly straight and caused variation in alignment each time the deck was moved. Visual alignment using the edge of the table provided a straighter surface with variations in width less than 1/16 in. at any cross-section along the length. The maximum length of a saw cut on the guide was approximately three feet at a time before the motor was turned off, the deck was slid further through the saw, the deck realigned, and then cut again.

The first cut removed only the excess resin, no balsa. The second cut involved the same process on the opposite side of the deck. Following these two cuts, the straighter of the two cuts was determined. Next, a guide fence made of wooden 4x4's, 2x4's and plywood was clamped to the table and tested to ensure a uniform, accurate cut. The straightest side of the deck was placed against the fence and approximately 3/4 in. was trimmed off of the opposite side. After cutting along the entire length of the deck, the deck was rotated 180°. A sheet of 3/4 in. plywood was laid vertically against the fence to trim an additional 3/4 in. off the remaining side. This brought the final width of the deck to 18 in.

The ends of the deck were trimmed last. A framing square was placed against the balsa on the sides of the deck at each end, a straight line marked, and the deck was cut to length. The final length of Deck 1 was 61.5 in. and the final length of Deck 2 was 106.5

in. No additional cutting would be required for the decks following the placement of concrete.

3.18 Steel Reinforcement of the Shear Connector Specimens

Shrinkage reinforcement was used in the concrete layer surrounding the shear connectors in each specimen. The reinforcement consisted of two $\frac{1}{4}$ in. diameter deformed bars in the longitudinal direction and eight $\frac{1}{4}$ in. diameter deformed bars in the transverse direction. Two of the transverse bars were eliminated as the specimens were cut to length. The longitudinal bars were placed directly on top of the shear connectors and the transverse bars were tied with rebar ties to the underneath of the longitudinal bars. The transverse bars were tied against the side of the shear connectors so as to provide some bearing on the shear connectors and to create confinement for the concrete between the shear connectors. The longitudinal bars were placed 2 in. apart, leaving $\frac{1}{2}$ in. concrete on both sides.

3.19 Steel Reinforcement of the Concrete Deck

The shrinkage reinforcement used in the composite decks consisted of a mesh of $\frac{1}{4}$ in. diameter deformed bars shown in Figure 3.31. The longitudinal bars were spaced 4 in. on-center, leaving 1 in. concrete cover on either side. The longitudinal bars were placed directly on top of the shear connectors. The transverse bars were placed on either side of each shear connector and were tied underneath the longitudinal bars with rebar ties. The transverse bars functioned as shrinkage reinforcement, confinement for the concrete below the top of the shear connectors, and also provided some bearing on the shear connectors.

3.20 Shear Connector Specimens

The wooden formwork used for concrete placement atop the three shear connector configurations consisted of SPF nominal 2x4's. The 2x4's were ripped to actual cross-section dimensions 1.5 in. x 2.25 in. The wood was cut to length according to the perimeter dimensions of the infused shear connector specimens. The inside dimensions of the formwork were approximately 12.5 in. x 19.5 in. as shown in Figure 3.32. The wood was fastened at each corner with two 2.5 in. long screws. A form release agent, Durogard, was sprayed onto the wood surface to facilitate disassembly after the placement of concrete.

An additional form was constructed to create cylindrical voids in the concrete in which bolts were to be inserted for the shear tests. For each shear specimen, a 1 in. x 1.5 in. x 22 in. strip of wood was cut. The first strip served as a pattern for the rest of the wooden strips. The pattern wooden strip was drilled with four 13/16 in. diameter holes at the midpoint between each z-joint in the shear specimens. The pattern was clamped on top of each succeeding specimen on the drill press. All holes in succeeding specimens were aligned using the holes in the pattern. The 13/16 in. hole diameter corresponded to the outside diameter of nominal ½ in. inside diameter PVC pipe. The wooden strips were screwed into the shear connector formwork with 2.5 in. long screws. A 0.5 in. thick wooden shim was inserted in-between the shear connector formwork and the wooden strips. The purpose of the shim was to create a gap between the finished surface of the concrete and the underneath of the wooden strips large enough for a trowel to place the concrete.

The ½ in. PVC pipe was cut to lengths of 5 in. Both ends of the pipe were covered with duct tape to prevent concrete from infiltrating the pipe during casting. The PVC pipe was coated in Durogard form release immediately before casting to facilitate removal after concrete curing. The pipe was inserted into the holes in the wooden strips to complete the formwork for the shear connector specimens. One PVC pipe insert is shown in Figure 3.33.

3.21 Formwork for Decks

The wooden formwork for the decks consisted of nominal 2x8's which were ripped on a table saw to actual cross-sectional dimensions of 1.5 in. x 6.5 in. The wood was placed around the perimeter of both decks and rested on a flat surface. The side pieces were attached to the end pieces with four 2.5 in. long screws at each corner. A silicone seam was caulked on the formwork at the interface of the GFRP and concrete to prevent splintering of the formwork during disassembly and to serve as a watertight seal. The 2 in. of wood exposed to the concrete was sprayed with a form release agent, Durogard, to facilitate disassembly.

3.22 Concrete Mix Design and Process

The concrete mix was designed with the aid of the Portland Cement Association's design manual (Kosmatka et al. 2002) The coarse aggregate used for the mix was 78M, a 3/8 in. nominal maximum size of aggregate gradation. The Portland cement used was Quikrete Portland Cement Type I/II. A superplasticizer from W.R. Grace Construction Products, ADVA 100, was used to increase slump and workability. The water to cement ratio was 0.35 for a target compressive strength of 7000 psi.

The fine and coarse aggregate were batched prior to casting and covered with plastic to retain Saturated Surface Dry (SSD) condition. The Portland cement and water were batched immediately before casting. The components were separated into two equally weighted batches. In order to maximize workable time, the fine aggregate and coarse aggregate were mixed in a concrete mixer prior to hydration. Once a uniform mix was achieved, the Portland cement was added followed by 1/3 of the water. The main purpose of this water was to keep the Portland cement powder from spreading in the air while mixing. After mixing, the remaining water was added. The superplasticizer was added as needed to achieve a target slump of 5 in. to 7 in. for easy placement. A total of 10 mL of ADVA 100 superplasticizer were added to batch 1. Due to the residual moisture from batch 1, batch 2 required no superplasticizer to achieve a comparable workability. A slump test was performed for both batches according to ASTM C143 (2005). The slump for batch 1 was 6.5 in. The slump for batch 2 was 5.5 in.

3.23 Placement of Concrete

The concrete was placed in two batches. The first batch was used for the three shear connector forms and for the 5 ft. deck. The second batch was used for the 9 ft. deck. After placing the concrete in the form, the specimens were vibrated vertically on a shake table for approximately 10-15 seconds shown in Figure 3.41. The concrete surface was screeded with a block of wood shown in Figure 3.42.

A total of 13 concrete cylinders were cast. Seven cylinders from batch 1 and six cylinders from batch 2 were made. The cylinders remained in the form and were covered with a plastic cap until the time of testing. Compressive strength tests were performed at

7, 14, and 28 days. In addition, three cylinders from each batch were tested to develop the stress versus strain diagram for modeling purposes.

3.24 Curing

Immediately following placement of the concrete, the concrete surface was covered with a plastic sheet shown in Figure 3.43. The sheet was sealed to the formwork with duct tape. The plastic sheet contained the bleed water. Approximately 6.5 hours after the completion of placement, the decks had achieved a set suitable for curing with burlap. The plastic covering was removed, saturated burlap sheets were placed directly on the finished concrete surface, and the plastic was resealed over the burlap. The burlap was rewetted after 16 hours and remained on the deck for 6 additional days, rewetted as needed. The shear test specimens were not covered with burlap due to impracticality caused by the PVC pipe inserts. The shear specimens were, however, covered with plastic sheets to contain the moisture.

3.25 Removal of Shear Connector Formwork

The screws fastening the formwork together were unscrewed and the side wooden pieces were removed. The PVC pipes were clamped with vise grips and removed manually with a combined twisting and upward pulling motion as shown in Figure 3.44. The duct tape which sealed the bottom of the tubes from the fresh concrete was removed using a needle with a hooked end, leaving a void for the bolts as in Figure 3.45.

3.26 Cutting of Cast Shear Connector Samples

By casting each specimen of each configuration together, the required formwork was reduced and the concrete was more easily vibrated. After curing of the concrete specimens, the specimens were cut to size. First, a line was drawn on the concrete

surface through the centerline of the bolt holes along the length of each specimen.

Another line was marked on the table of the saw, offset 1.5 in. from the edge of the saw blade. The centerline of each specimen was aligned with the 1.5 in. offset to ensure this remaining amount of material after the first cut. All samples were cut to 1.5 in. on one side only. Next, a wooden 2x8 was clamped to the table offset 3 in. from the saw blade edge to serve as a guide fence. The saw blade then trimmed each specimen to the same width, 3 in. The specimens were cut to length while clamped in a vise grip. Although each specimen was originally designed to contain four shear connectors giving a total length of 19 in., the specimens were trimmed to 15.5 in. and three shear connectors due to height restrictions of the test setup. The top surface of each specimen was ground flat using a grinder to create a level surface suitable for attaching the steel plates with an epoxy.

3.27 Fabrication of the Shear Test Specimens

In order to distribute the applied load uniformly, $\frac{3}{4}$ in. steel plates were attached to the top and bottom faces of the shear samples. From the end of each shear plate, a 35° angled tip was cut, sharper than the 45° in the support to allow for easy fit-up and free rotation of the shear plates. The plates were fabricated with $\frac{3}{4}$ in. diameter holes at the locations of the voids left in the concrete. One 5 in. long, $\frac{3}{4}$ in. diameter threaded rod was screwed into each hole to reduce the tendency of the top layer of concrete above the shear connectors to delaminate. The rods were threaded through the plates until in contact with the GFRP surface. In this manner, the rods provided some bearing on the concrete confined by the shear connectors. The plates containing the rods for the shear samples are shown in Figure 3.46.

After cleaning the plates, a two part epoxy resin system, SikaDur, was mixed according to manufacturer's specifications. The cured resin has a shear strength of 6000 psi. The liquid resin was applied with a brush to the bottom steel plate and to the bottom surface of GFRP to ensure adequate bond. The shear specimen was placed on top of the bottom plate and braced on all sides to prevent lateral sliding during curing. Next, the epoxy was applied to the top concrete surface. The holes in the concrete for the rods were nearly filled with resin in an effort to ensure total bond of the rods to the concrete. The top plate, including the rods, was painted with resin and inserted into the rod holes. Assorted weights were placed on top of the top plate to ensure contact between the concrete and the plates during curing.

Table 3.1. Dimensions of sample of 1 ft. of 1 skin (2 layers of fabric).

Width (y)	18	in
Length (x)	12	in
Packing increase factor (z)	1.68	
V_f (fiber vol. fraction)	0.41	

Table 3.2. Properties of sample.

	yarns per in.	yarns per joint	Total length of yarns (in)	Yield (yd/lb)	Weight (oz/in)	Weight for Area (oz)	w (weight fraction)	w (sum z's)	V (vol. fraction)
Warp	42	--	9072	103	0.004315	39.146	0.687		0.344
Filling	48	--	10368	330	0.001347	13.964	0.245		0.123
z (yarns)	14	--	4896	675	0.000658	3.224	0.057	0.068	0.034
z-joint	--	12	979.2	675	0.000658	0.645	0.011		
Total						56.978			

Table 3.3. Calculated average number of z-yarns and weight characteristics of skin.

Avg. z-yarns/in	16.67
Areal wt. (oz/yd ²)	341.87
Linear wt. (oz/yd)	170.93

Table 3.4. Deck properties prior to infusion.

	Length (in)	Vol. Balsa (ft ³)	Balsa Wt. (lbs)	Total Wt. Fabric (lbs)	Weight Deck Preform Without Shear Connectors (lbs)	Total Wt. Infused (excluding concrete) (lbs)
Deck 1	61.5	2.354	22.127	36.501	58.6	106.5
Deck 2	106.5	4.076	38.318	63.210	101.5	178.1

Table 3.5. Infusion summary.

Specimen	Actual weight prior to infusion (lbs)	Epoxy Weight (lbs)	Hardener Weight (lbs)	Time of Infusion (minutes)	Post Cure Time (hrs)	Notes
8 Vertical GFRP Flaps with UHMW Spacers	5.25	4.04	1.21	31	18	Air leak at inlet prevented faster infusion. Total wet-out occurred within 2 minutes.
4 Square Boxes with Pine Core Inserts	6.46	--	--	28	18	Cured with heating blanket
4 Tapered connectors with Trapezoidal Pine Core Inserts	6.44	--	--	28	18	Cured with heating blanket
Deck 1	--	19.50 20.50	5.85 6.12	33	18/4	Cured four hours in oven
Deck 2	--	19.68 25.32 25.32	5.99 7.60 7.60	35	18/4	Cured four hours in oven

Table 3.6. Concrete mix design.

	Water (lb)	Super-plasticizer (mL)	Portland Cement (lb)	Coarse Aggregate (lb)	Fine Aggregate (lb)
Batch 1	32.0	10	92.6	111.0	130.0
Batch 2	32.0	0	92.6	111.0	130.0

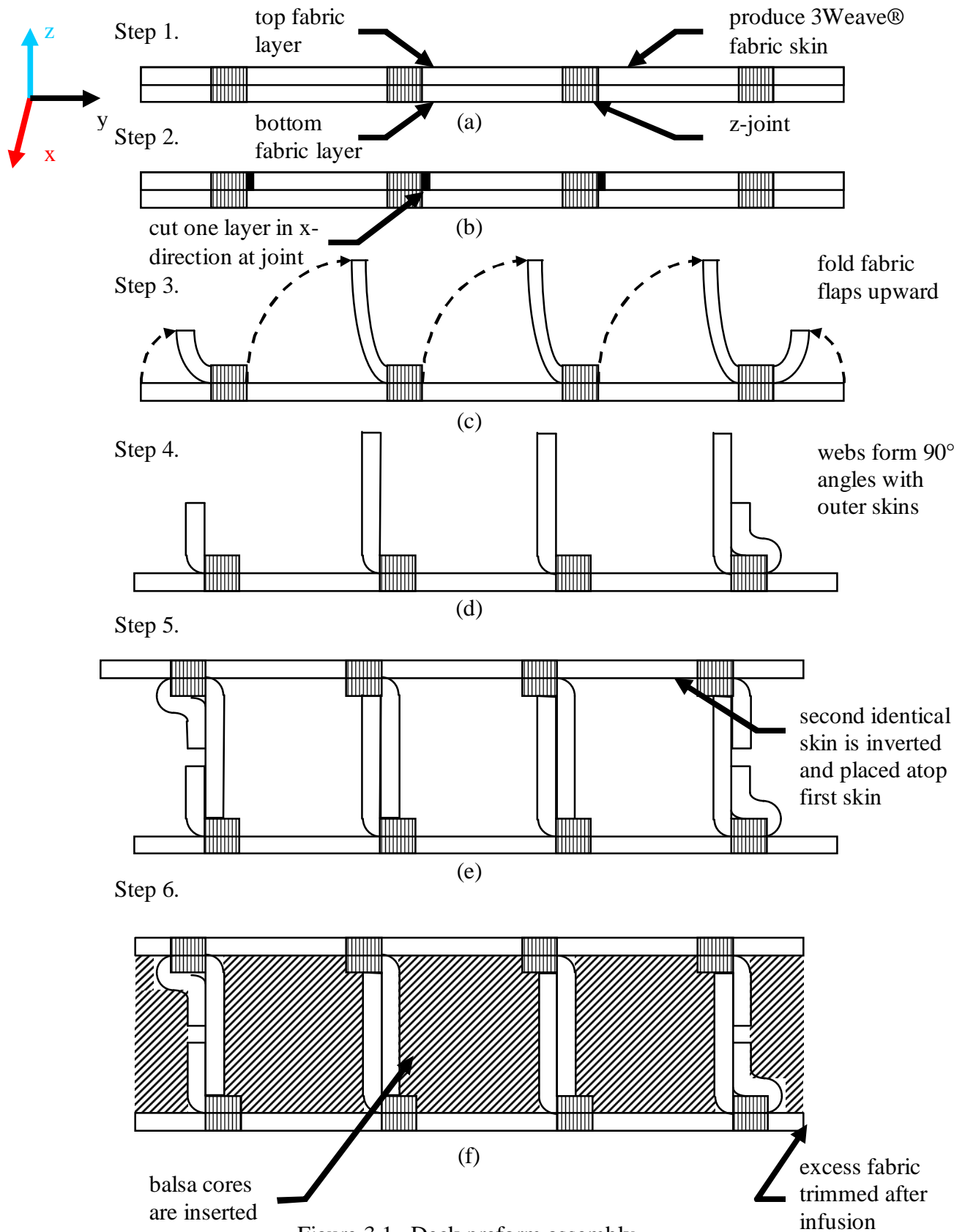


Figure 3.1. Deck preform assembly.

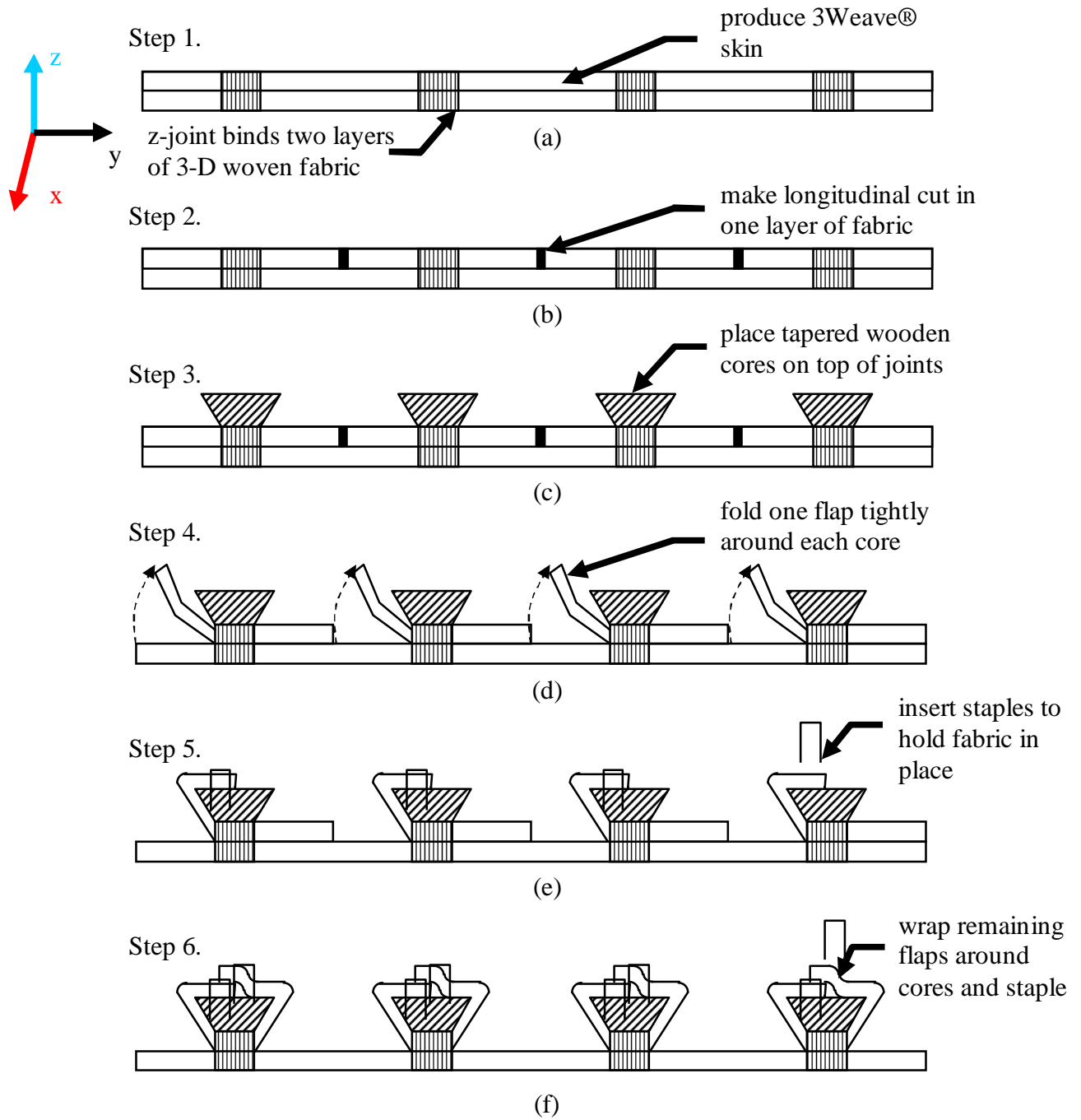


Figure 3.2. Shear connector preform assembly.

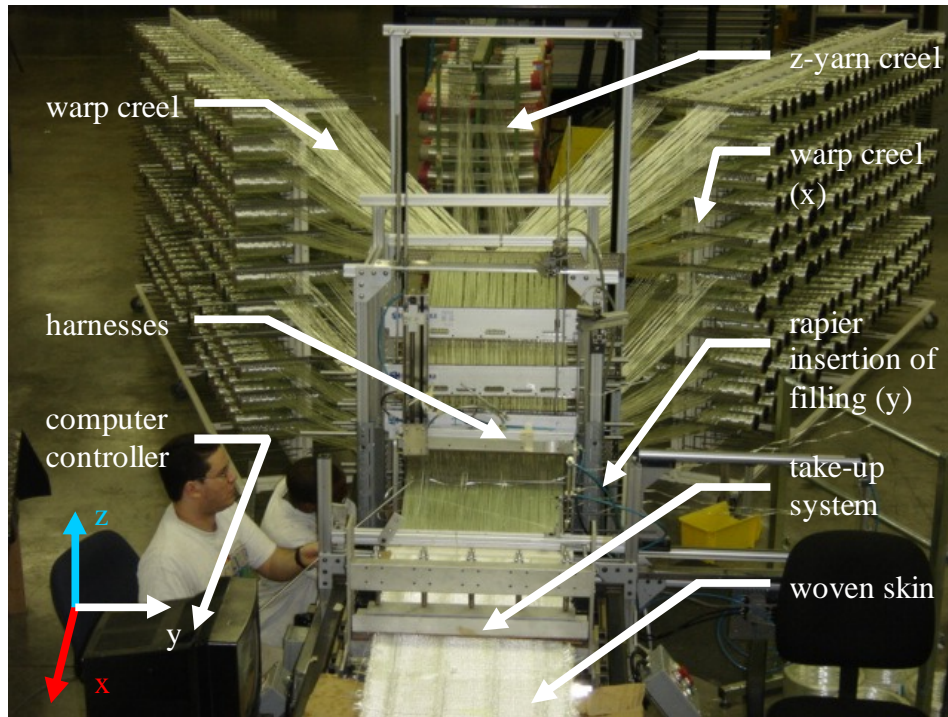


Figure 3.3. 3Weave® loom setup.

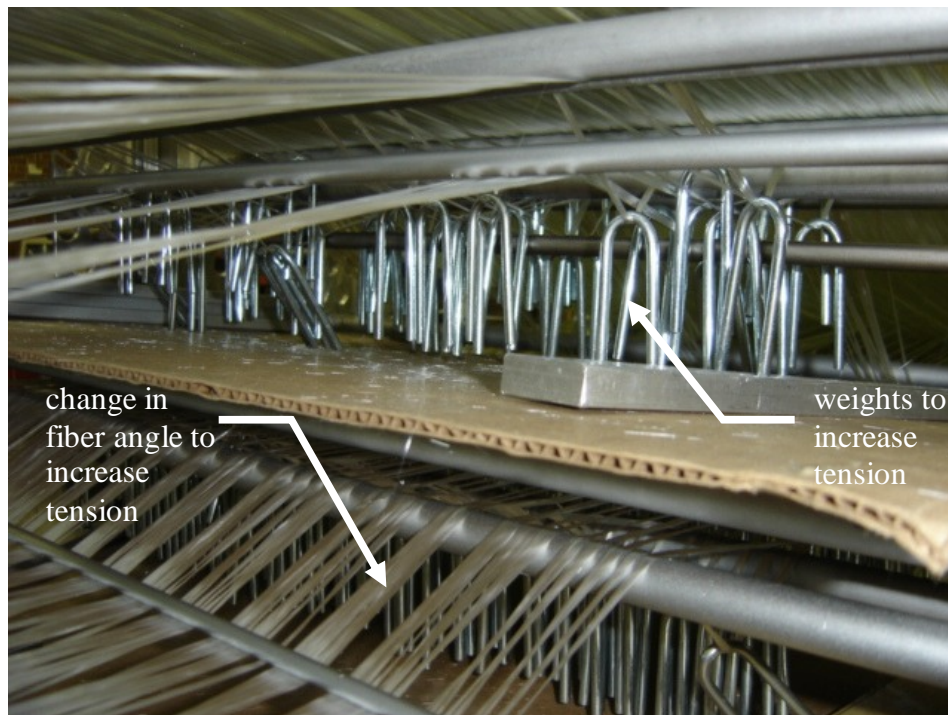


Figure 3.4. Rods and weights to induce tension on warp and z-yarns.

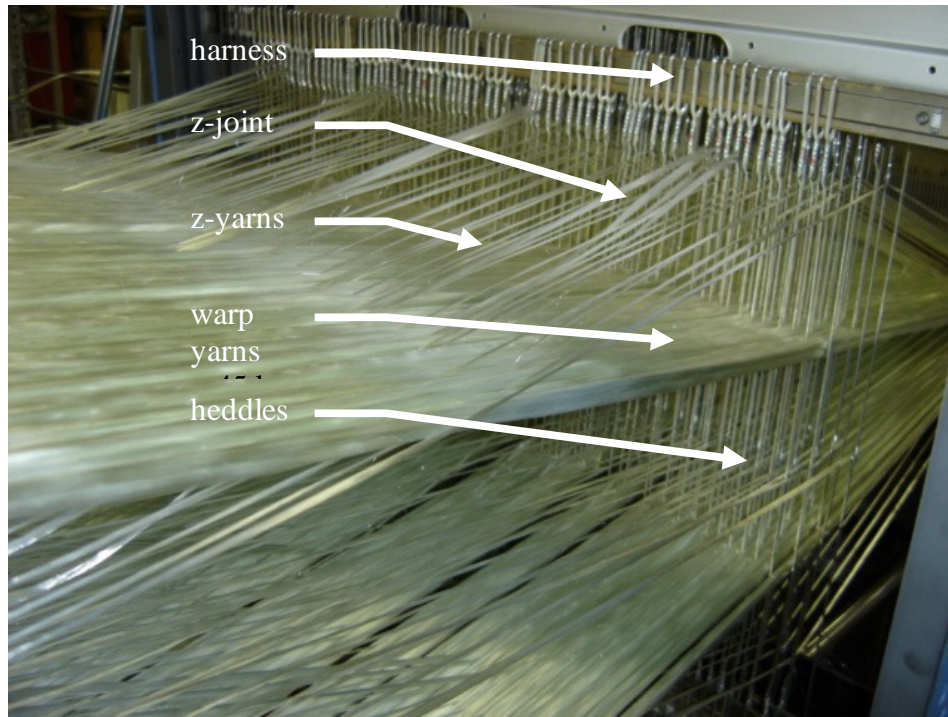


Figure 3.5. Harnesses and yarns on 3Weave® loom.



Figure 3.6. Reed beat-up followed by system take-up.



Figure 3.7. Rapier system to insert filling yarns.

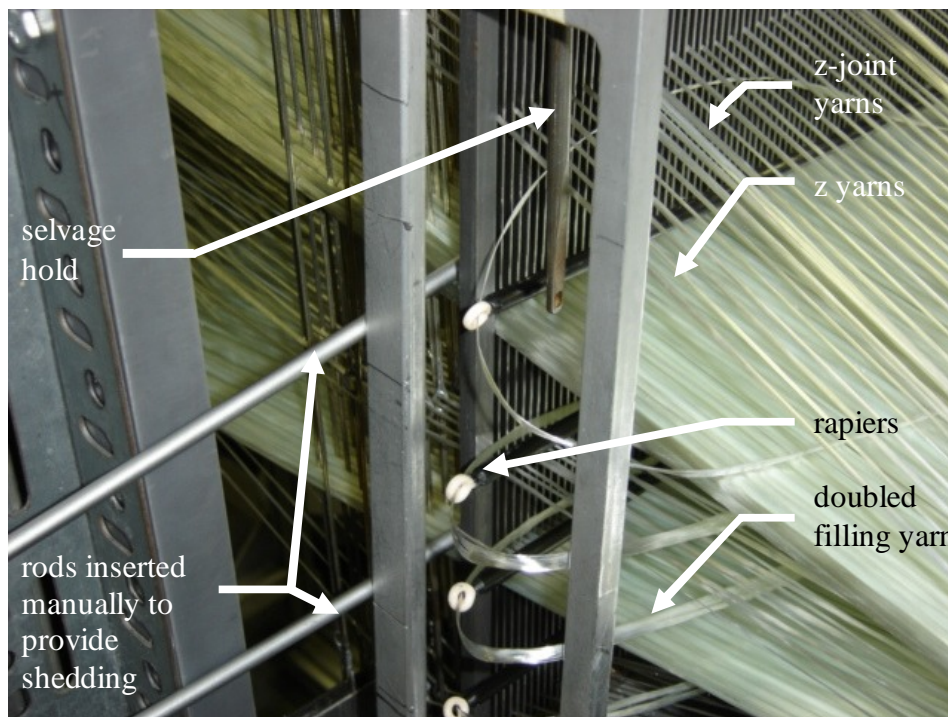


Figure 3.8. Selvage hold prior to insertion.



Figure 3.9. Harnesses prior to switching.



Figure 3.10. Harnesses after switching.

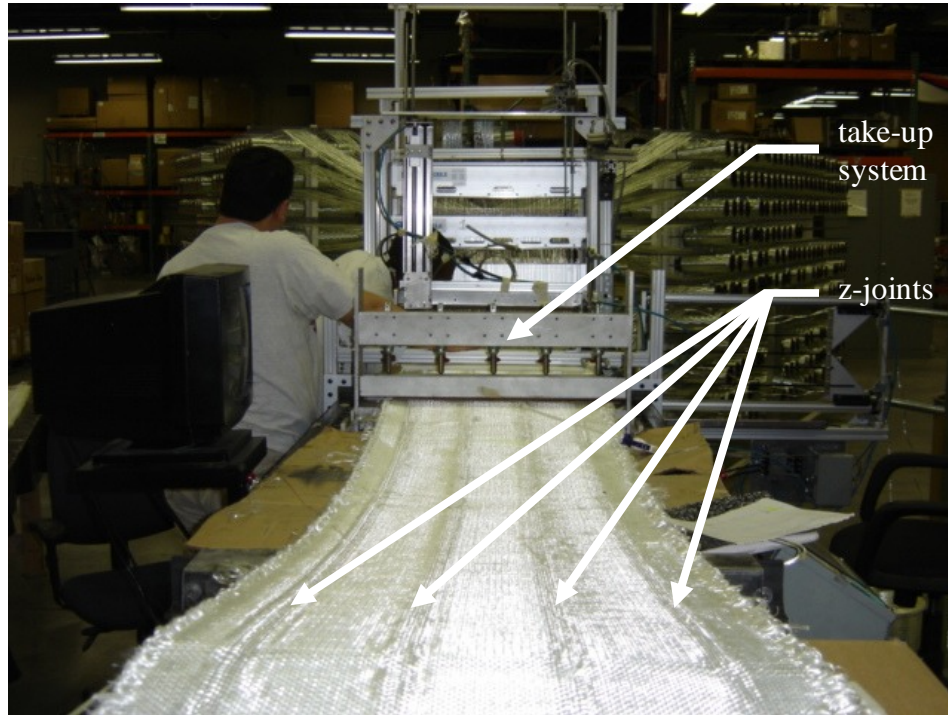


Figure 3.11. Skin preform woven on 3Weave® loom.

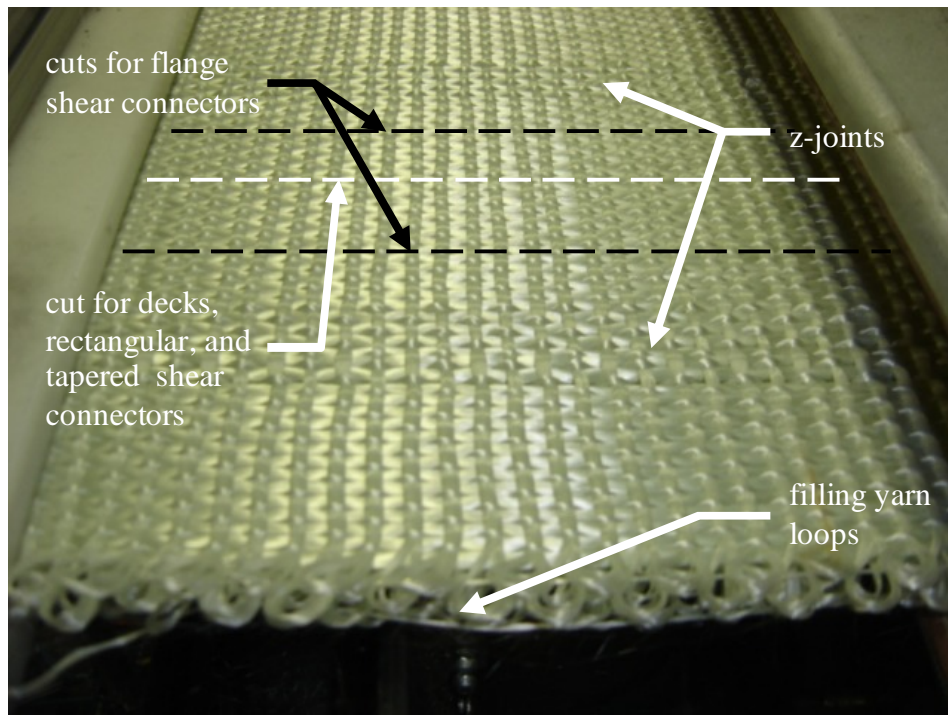


Figure 3.12. 3-D orthogonally woven skin with z-joints.



Figure 3.13. Stapling of fabric flap to wooden cores on shear connectors.

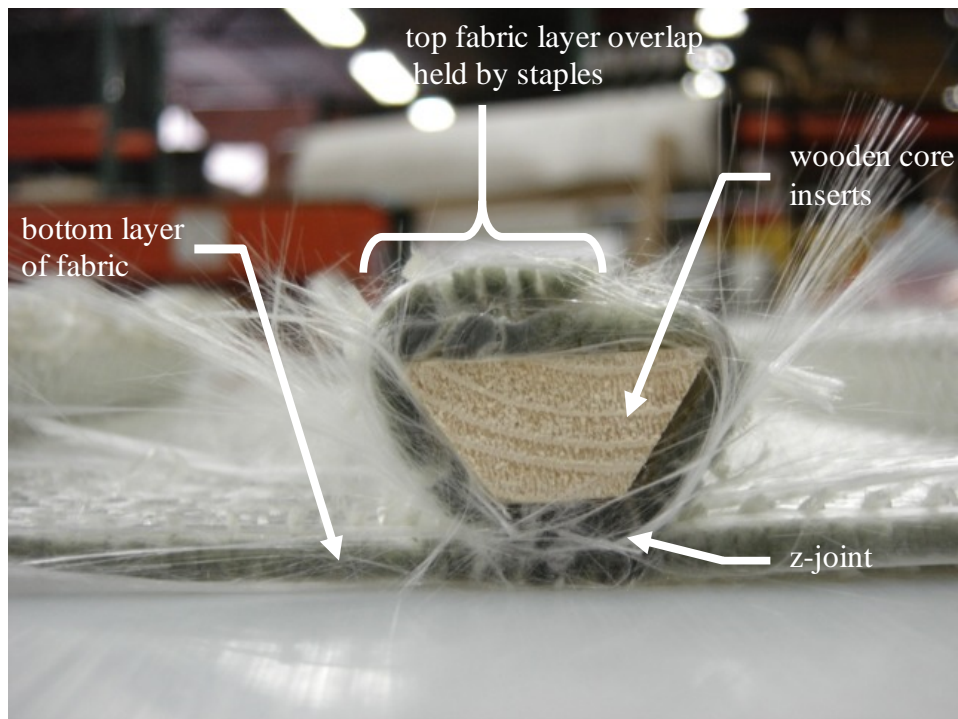


Figure 3.14. Shear connector preform.

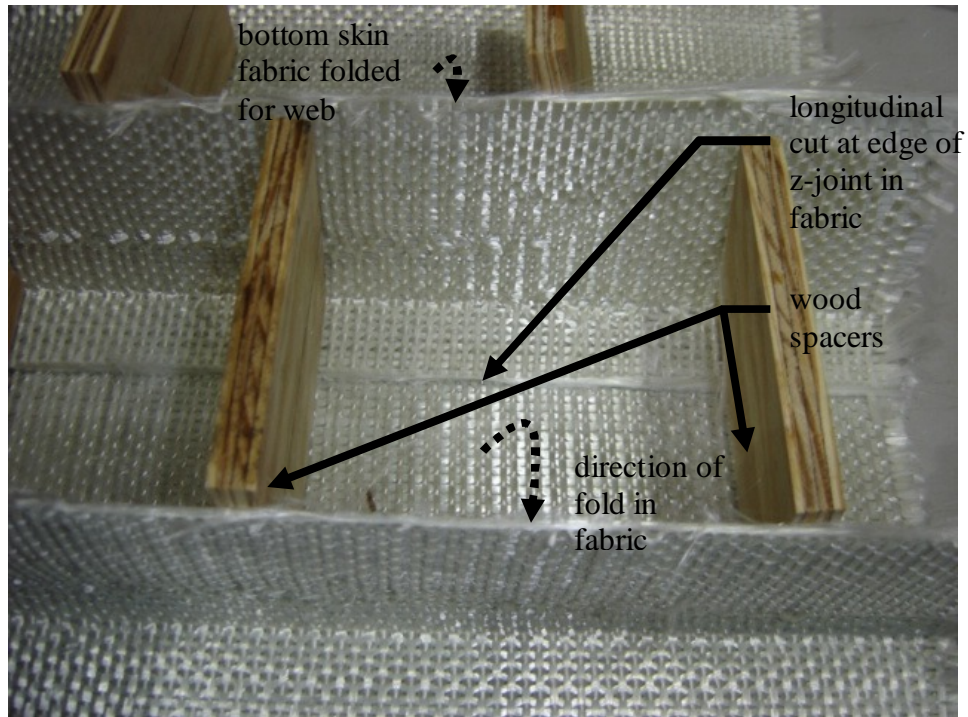


Figure 3.15. Bottom skin of Demo Deck with wood spacers.

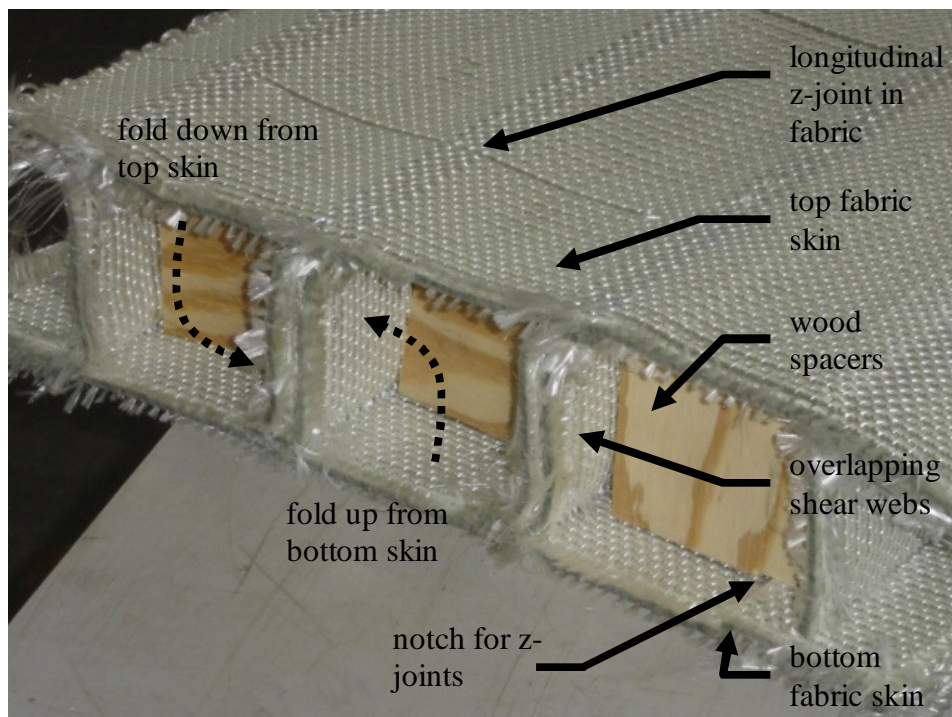


Figure 3.16. Both skins of Demo Deck with wood spacers.

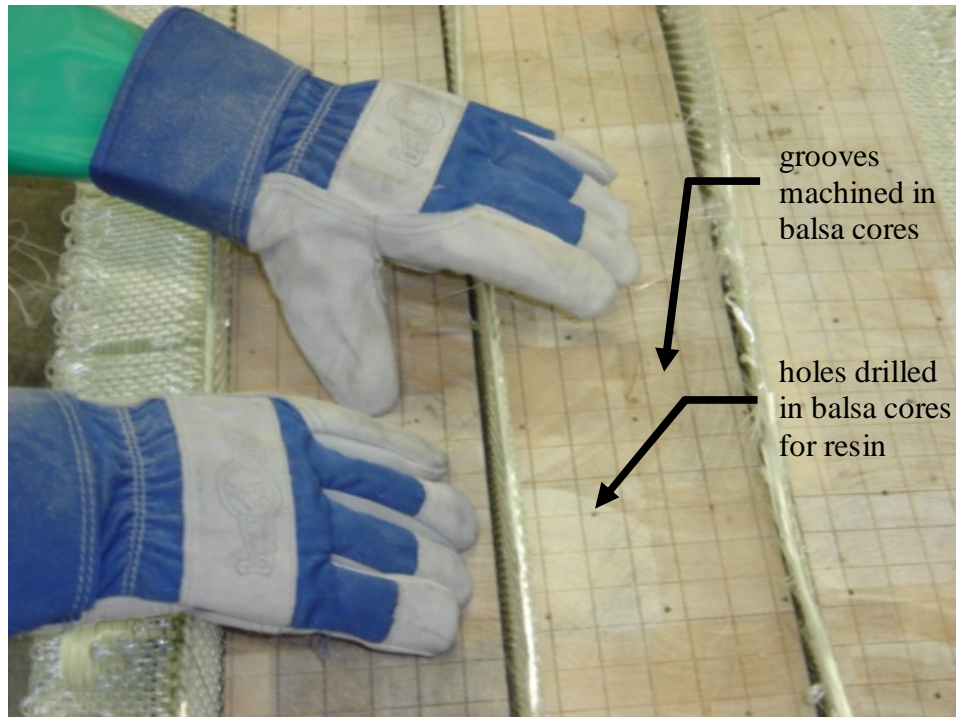


Figure 3.17. Insertion of bottom layer of balsa cores into deck preform.

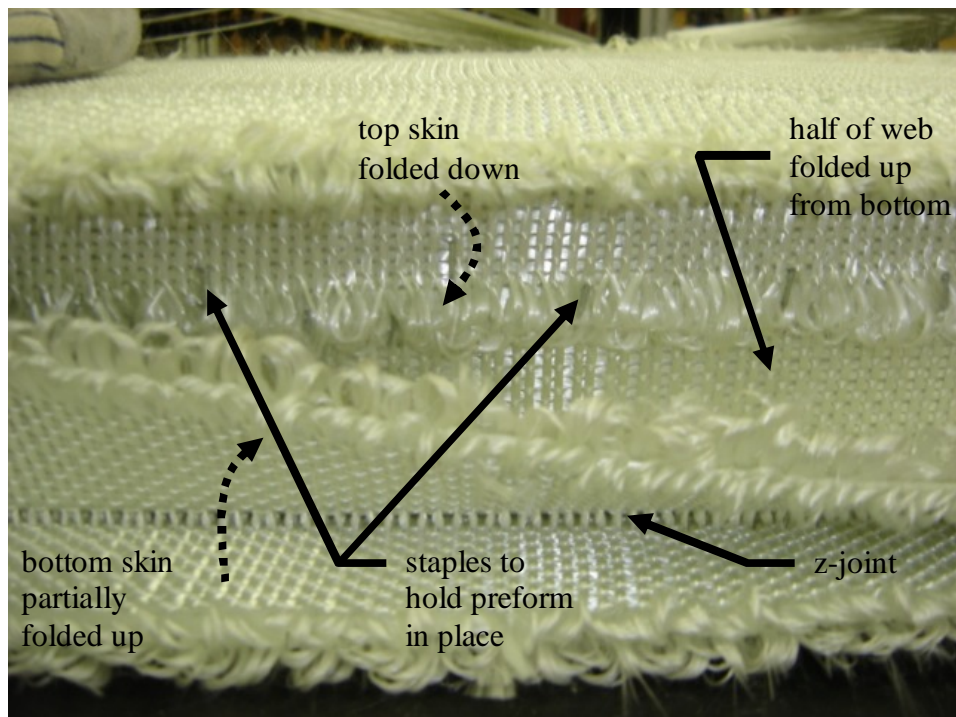


Figure 3.18. Folding of skins at outer cells.



Figure 3.19. Balsa inserts in Demo Deck.

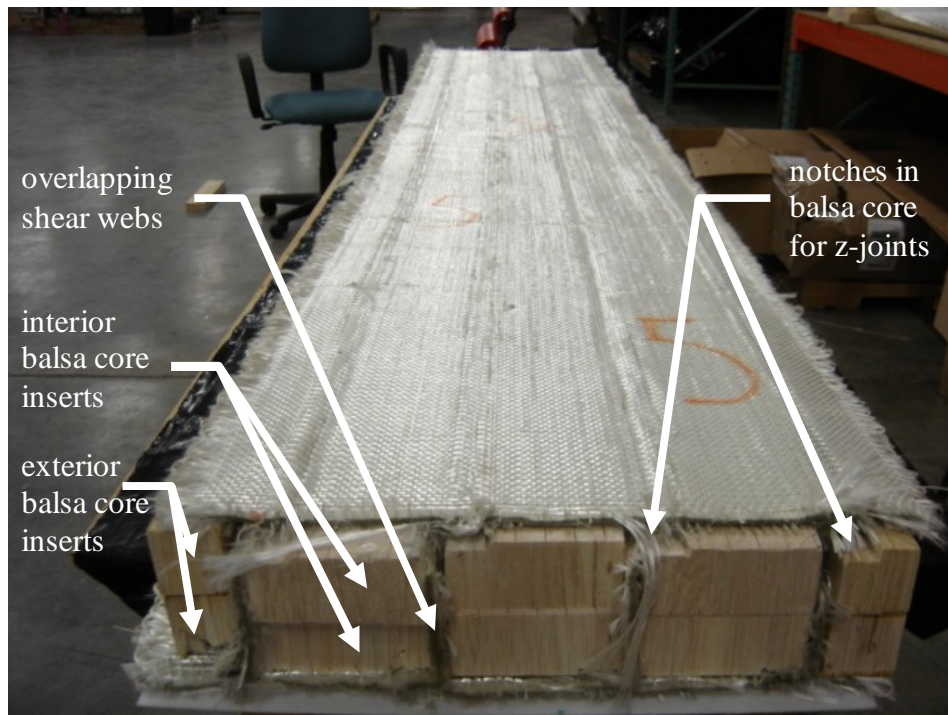


Figure 3.20. Assembled deck preform.

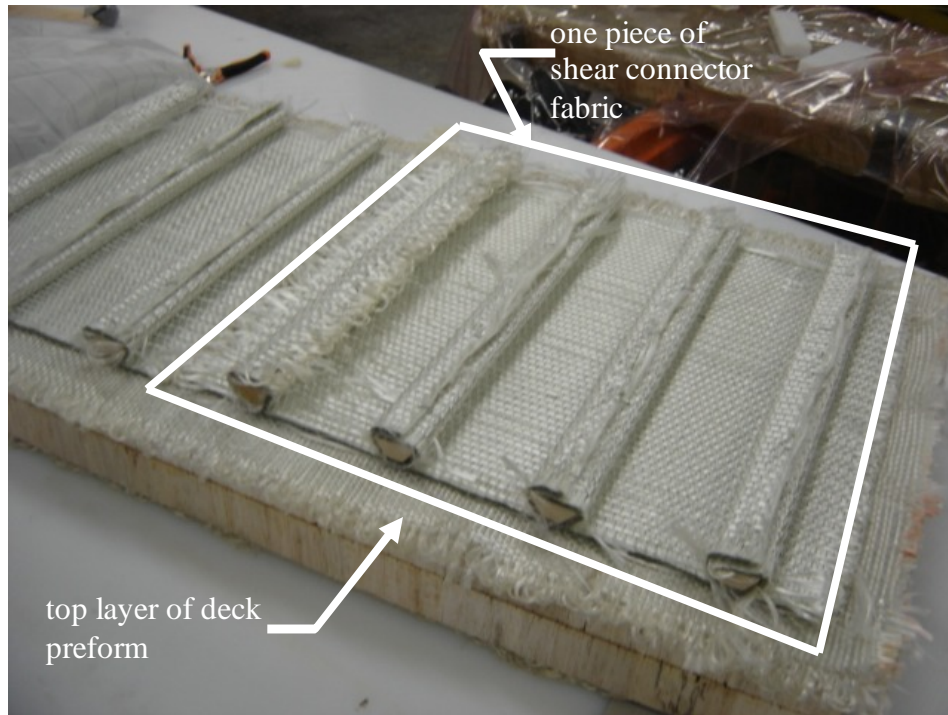


Figure 3.21. Shear connector fabric placed atop deck preform.

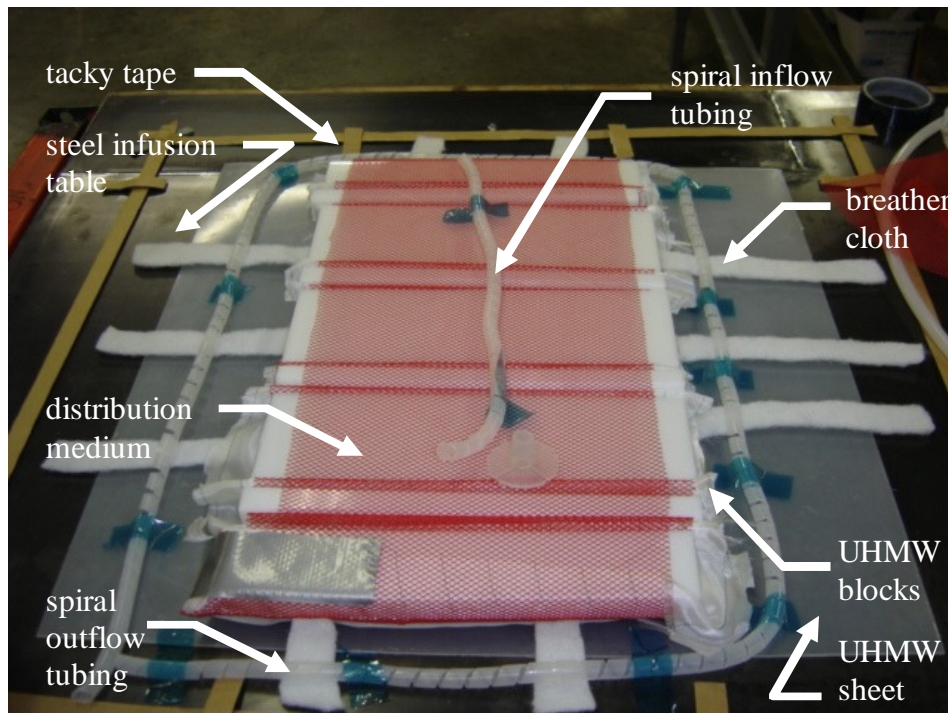


Figure 3.22. Infusion setup of flange shear connector.

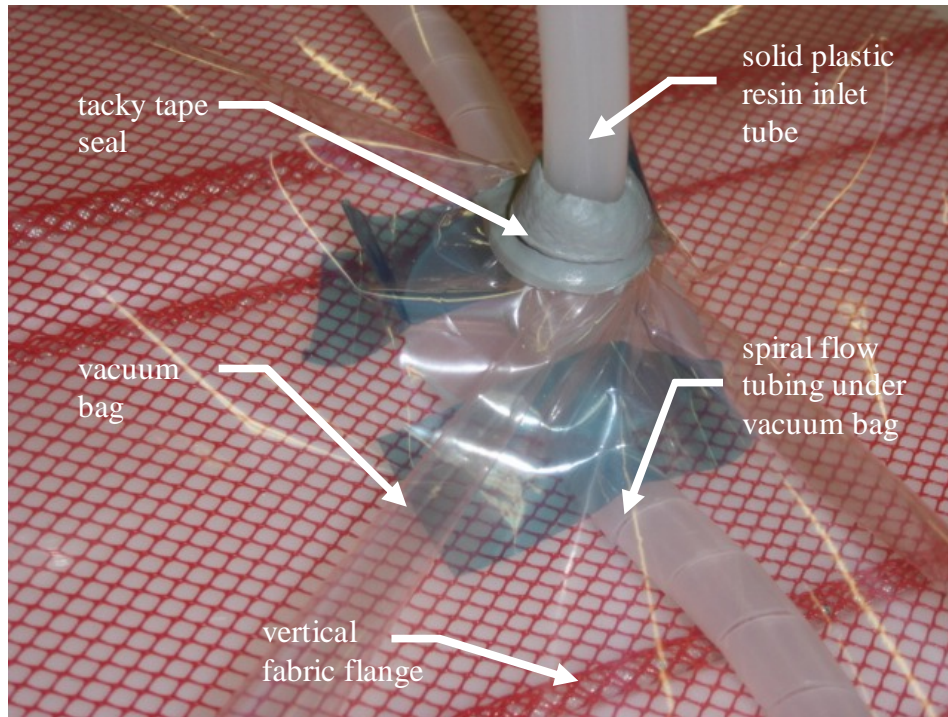


Figure 3.23. Connection to resin inlet.

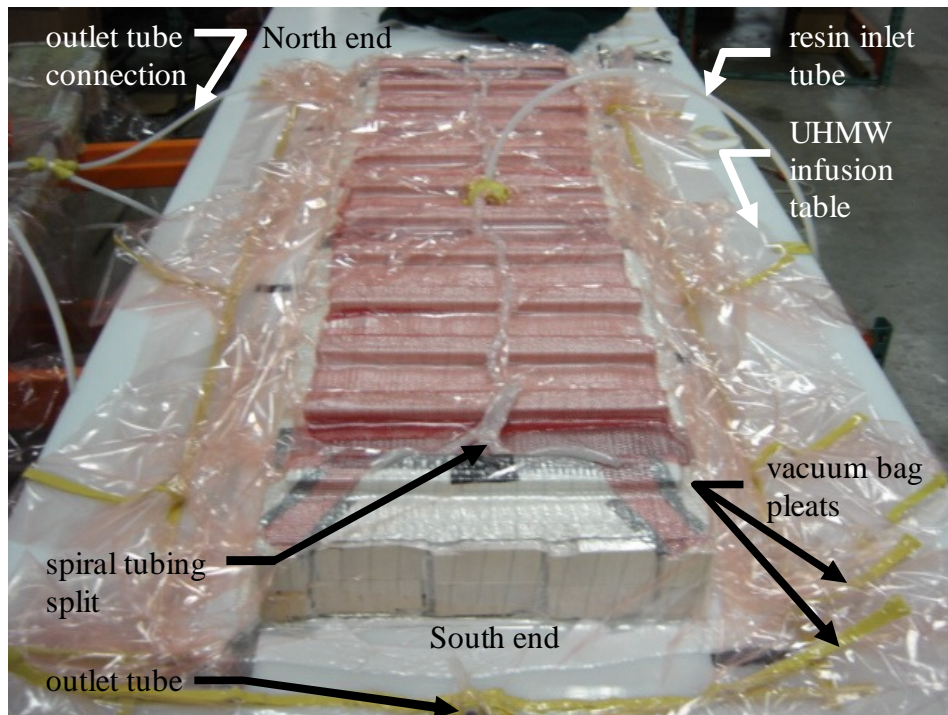


Figure 3.24. Deck 1 preform prior to infusion.

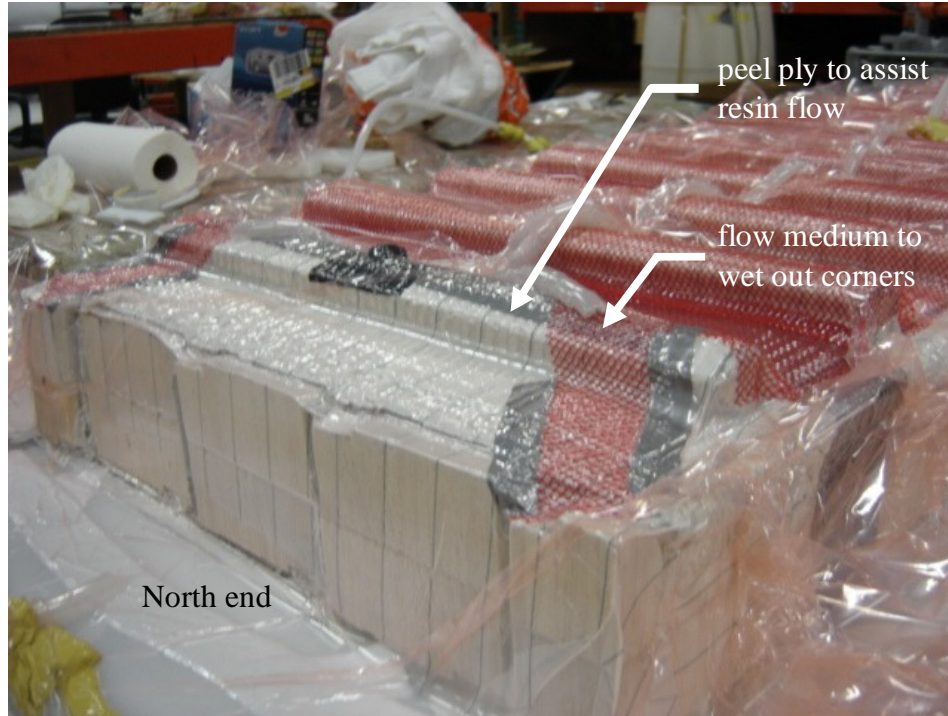


Figure 3.25. Deck preform under vacuum prior to infusion.



Figure 3.26. Pre-heating preform using electric blanket.



Figure 3.27. Mixing of epoxy and hardener.

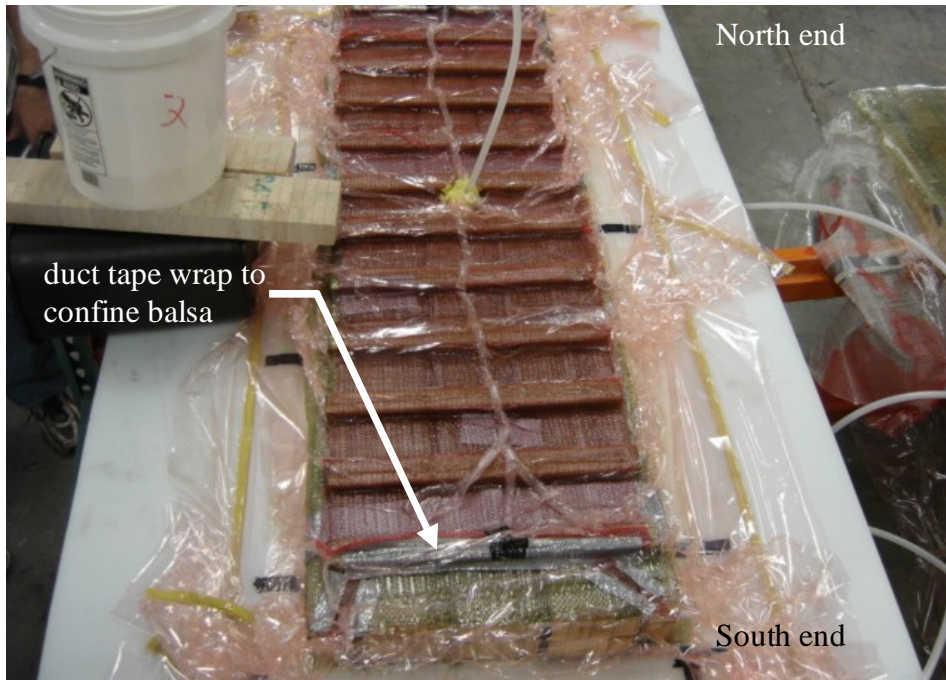


Figure 3.28. Total wet-out out of Deck 1.

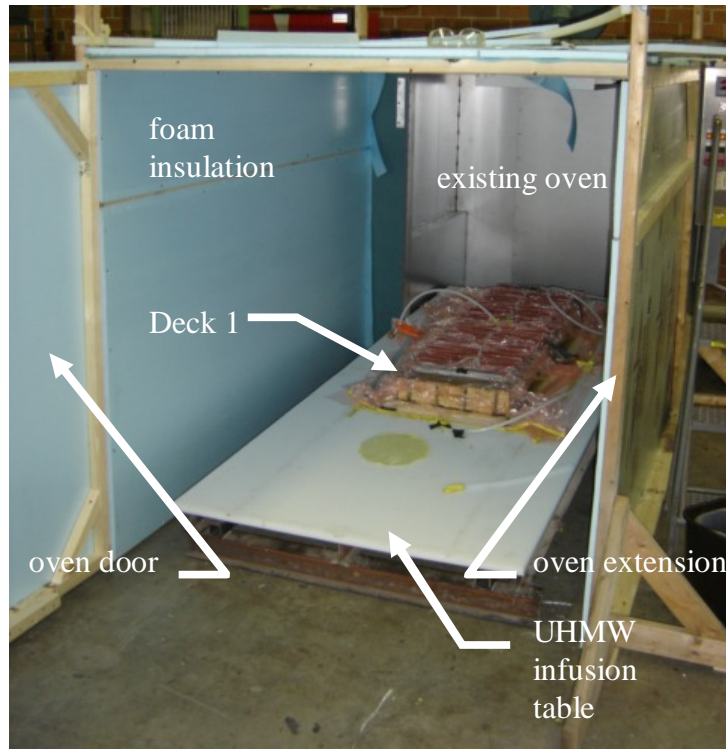


Figure 3.29. Deck 1 on infusion table inside oven.

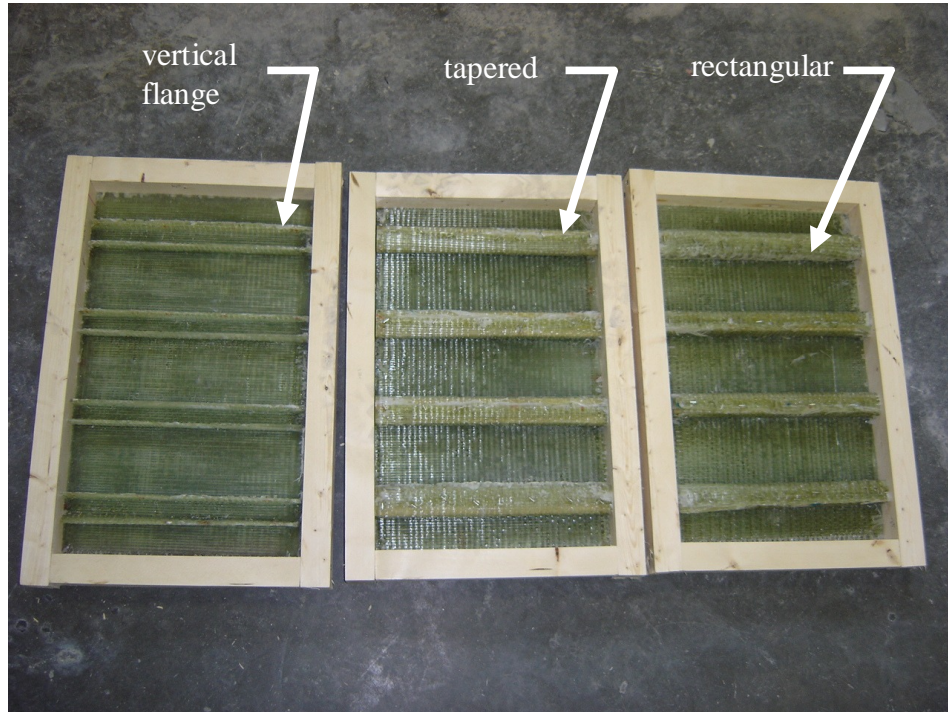


Figure 3.30. Three configurations of shear connectors.

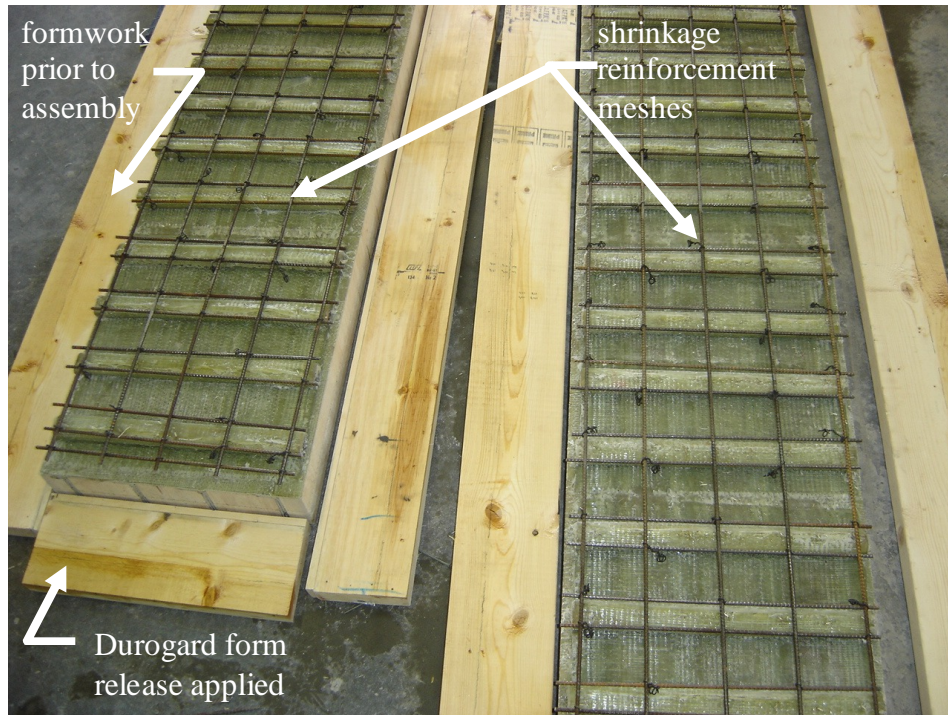


Figure 3.31. Deck forms with steel shrinkage reinforcement.



Figure 3.32. Shear connector formwork with PVC pipe inserts.

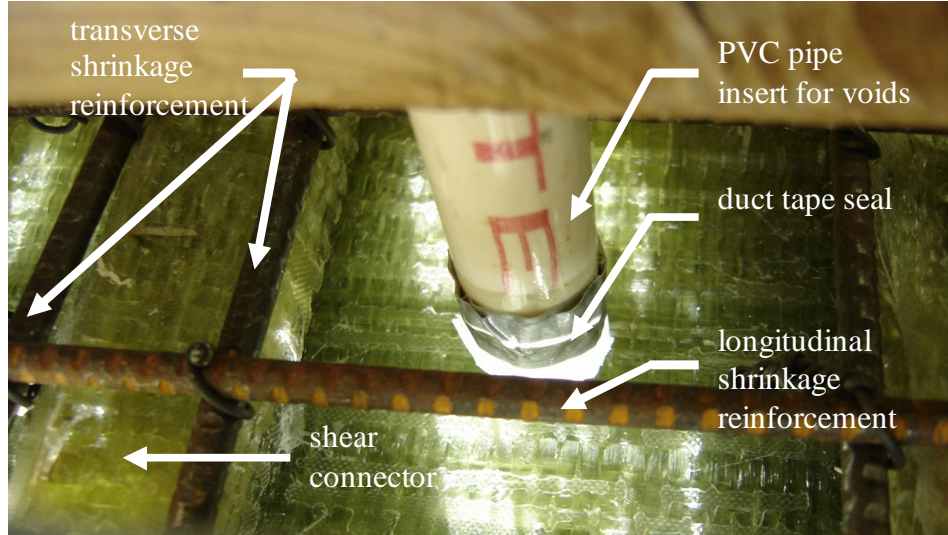


Figure 3.33. PVC pipe inserts sealed with duct tape in shear connector formwork.

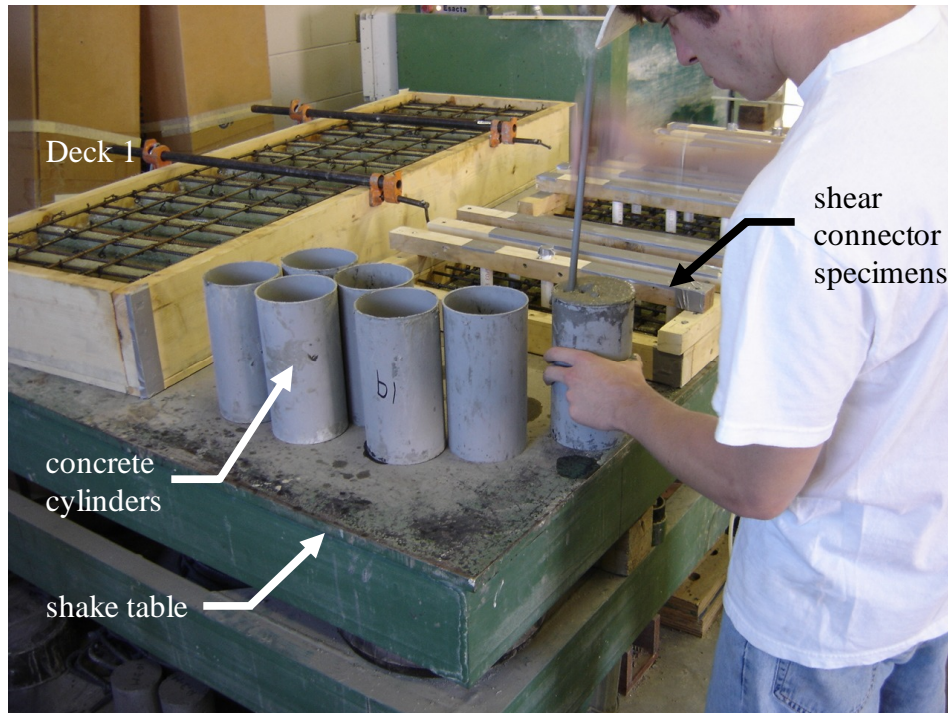


Figure 3.34. Rodding of concrete cylinders.



Figure 3.35. Screeding of Deck 2.



Figure 3.36. Curing of Deck 2.



Figure 3.37. Removal of shear connector formwork.



Figure 3.38. Steel plates and rods prior to bonding to shear samples.



Figure 3.39. Completed fabrication of vertical flange shear connector specimen.

Chapter 4. Experimental Program

The material properties of the decks were characterized by a variety of tests on materials obtained from actual decks. These tests included compressive strength tests of concrete cylinders, steel reinforcement tensile tests, fiber volume fraction tests, GFRP skin tensile coupon tests, and four-point bending of the GFRP skins. In addition, three configurations of shear connectors were tested. The two deck panels were tested in three-point bending to examine their structural behavior under the effect of a load simulating the effect of an equivalent AASHTO truck load. The test setup, instrumentation, and notes on the observed behavior are provided in this chapter. At the end of each test description, commentary on the results is provided with a discussion of how the results compare to the predicted values.

4.1 Concrete Strength

The compressive strength of the concrete used in the decks was determined from concrete cylinders cast from the same batches as those used for the top concrete layer acting in composite action with the GFRP deck. The 4 in. x 8 in. concrete cylinders were tested in a compression machine shown in Figure 4.1 at an age of 7, 14, and 28 days in accordance with ASTM C 39 (2005). The cylinders were capped with neoprene padded plates and the maximum load was recorded to determine the ultimate compressive strength, f'_c . The load was applied using a loading rate of 35 psi/sec. In addition, three cylinders from both batches were tested immediately after testing of the deck to develop the full stress vs. strain curve at the time of testing of the decks. The ends of these cylinders were grinded to level the surfaces rather than capping with neoprene pads. The test setup included two circular metal rings attached to the cylinders at a fixed distance apart, 4.998 in., in the

height direction of the cylinder as shown in Figure 4.2. Four one inch long linear motion transducers were mounted to an aluminum bar. The bar was attached to the top ring and allowed the transducers to press against an angle mounted to the bottom ring to measure the relative displacement of the rings. These cylinders were also initially loaded at an approximate rate of 35 psi/sec. However, the descending portion of the stress vs. strain curve was obtained by maintaining the machine stroke rate after reaching the peak load. The displacement measured by the four transducers was recorded and divided by the gage length, 4.998 in., to compute the strain. The area calculated from the measured diameter and the machine load were used to calculate the compressive stress. The modulus of elasticity for the cylinders was calculated from the stress-strain curves using ASTM C 469 (2002).

All of the compression cylinders exhibited, as expected, uniform concrete crushing, except for one cylinder from the second batch. This cylinder failed prematurely due to its uneven surface. The results of all cylinder tests are tabulated in Table 4.1. The 7-day strength of the cylinders was 74% of the 28 day strength (f'_c) for both batches. This is slightly higher than the ACI estimate (Lew et al. 1978) of 70% at 7 days. The 14 day strength is 88% of f'_c for batch 1 and 85% of f'_c for batch 2. These strength values compare closely with the ACI estimate at 14 days is 88% of f'_c . The failure of a typical cylinder from the strength test is shown in Figure 4.3 and the typical failure of a cylinder from the elastic modulus cylinders is shown in Figure 4.4.

The cylinders tested to determine the elastic modulus were also used to develop the full stress-strain relationship of the concrete. The ASTM standard for the determination of the elastic modulus of the concrete, ASTM C 469, states that the

calculation of the modulus of elasticity should be the slope of the line between two points on the stress vs. strain curve. The first point is at a strain of 0.00005 and the second point is at 40 percent of the maximum stress. The stress vs. strain curves for batch 1 and batch 2 are shown in Figure 4.5 and Figure 4.6, respectively. The average maximum compressive stress for batch 1 was 8174 psi and for batch 2 was 8836 psi. The average modulus of elasticity for batch 1 was 3313 ksi and for batch 2 was 3937 ksi. The predicted elastic modulus according to ACI 318-02 (2002) uses the recommends the value $57000\sqrt{f'_c}$. The predicted values are 5153 ksi for batch 1 and 5358 ksi for batch 2. The measured values are only 64% and 73% of the predicted using the ACI estimate for batch 1 and batch 2, respectively. This is expected as the ACI estimate tends to overestimate the elastic modulus of concrete.

4.2 Properties of the Reinforcing Steel

Tension tests of the steel bars used to reinforce the concrete topping were performed according to ASTM A 370 (2005). Six samples of the ¼ in. diameter steel reinforcing bars used for shrinkage reinforcement in the deck were tested in tension. The specimens were cut to 24 in. lengths and clamped at both ends in the MTS machine. The strain was measured using an extensometer with a 2 in. gage length attached at the mid-height of each specimen as shown in Figure 4.7. The specimens were loaded to failure in tension at a load rate of 0.001 in/sec. The modulus of elasticity and stress vs. strain curves were developed.

The tension tests of the steel reinforcement similar to the bars embedded in the concrete topping of the decks provided useful data. Due to the high susceptibility of the bars to buckling in compression, compression tests could not be easily conducted. Citing

the linear isotropic elastic properties of steel, the compression properties are assumed to be the same as the tension.

The tensile failure of one bar is shown in Figure 4.8. The results of each test are shown in Table 4.2 and plots of all specimens are shown in Figure 4.9. Three of the bars failed prematurely due to excessive deformation induced by the clamping forces.

Therefore, these samples were not factored in the average of the ultimate strains. The extensometer pin was not removed at the beginning of testing sample 1; therefore, the yield strain of this sample is not representative of the behavior and was not included in the average yield strain calculation. With these exceptions, material properties were based on an average of all tests. The average modulus of elasticity was 31330 ksi, the yield stress was 80.9 ksi, the stress at the ultimate load was 86.3 ksi, and the strain at the ultimate load was 0.0226. Individual plots for each specimen are located in Appendix H.

4.3 Fiber Volume Fraction of GFRP Skins

The fiber volume fraction was determined according to the matrix burnoff test presented in ASTM D 3171 (2004). The volumes of the GFRP skin samples were first measured by submersion in water shown in Figure 4.10. Also, the dimensions of the specimens were measured with digital calipers to calculate the volume. The weights of the samples were recorded prior to testing. The samples were then placed in ceramic mugs as shown in Figure 4.11 and placed in a Thermolyne 6000 furnace. The furnace temperature was elevated to 400°C over the period of one hour, remained constant at 400°C for four hours, and then allowed to cool for one hour. The elevated temperature used in this test, 400°C, is well above the glass transition temperature, T_g , for the epoxy. Therefore, the elevated temperature completely burned off the cured thermosetting resin, leaving only the woven

E-glass fabric, as shown in Figure 4.12. The weight of the remaining glass fibers was recorded. Using the density of the fibers and matrix provided by the manufacturer and the measured weight fractions of each, the fiber volume fraction of the entire composite was calculated. The fiber volume fraction, f , is expressed by Hull and Clyne (1996) as:

$$f = \frac{w_f / \rho_f}{w_f / \rho_f + w_m / \rho_m}$$

where w_f is the weight fraction of the fiber, w_m is the weight fraction of the matrix, ρ_f is the density of the fiber, and ρ_m is the density of the matrix. The results are shown in Table 4.3. The average fiber volume fraction was 0.41. This fraction is typical for vacuum infusion processes. The nature of the infusion process draws excess resin downward and toward the vacuum outlet, creating a lower fiber volume fraction than typical pultrusion specimens, which typically range from 0.55 to 0.65.

4.4 Tensile Strength of GFRP Skins

The tensile properties of the GFRP skins were investigated in a tensile coupon study. The modulus of elasticity and stress-strain diagrams were developed in accordance with ASTM D 3039 (2006). Samples from both the warp and filling direction were tested. The test specimens were cut from actual deck specimens to nominal dimensions of 0.2 in. thick x 1 in. wide x 12 in. long. Actual measurements, taken using digital calipers, were used for calculations. Aluminum grips were attached with an epoxy to the ends of tensile coupons and loaded on an MTS machine as shown in Figure 4.13. The constant load rate was 0.001 in/sec. An extensometer with a gage length of 2.0 in. was used in order to calculate tensile strain.

The tensile modulus of the GFRP skins was determined with good precision. However, the tensile strength properties were not well-determined. Inadequate bearing area of the aluminum tabs attached to the samples prevented proper clamping of the specimens in the hydraulic wedge grips. An adequate clamping force could not be achieved prior to crushing of the skins in the grips. This prevented full development of the tensile stress in the coupons. Only one specimen did not fail prematurely within the grips. This sample exhibited a failure stress of 66 ksi in the warp direction. The testing of one sample is shown in Figure 4.14.

The stress and strain results, along with the failure modes of each specimen are listed in Table 4.4. The average modulus of elasticity in the warp direction was 3430 ksi with a maximum recorded stress of 66 ksi. The average modulus of elasticity in the filling direction was 1650 ksi with a maximum recorded stress of 10.2 ksi. The maximum strain observed was 0.0215 in the warp direction and 0.0126 in the filling, well below the ultimate fiber strain of 0.035. Assuming a linear relationship to failure, the average elastic modulus is multiplied by the expected ultimate fiber failure strain to give an expected failure stress of 120 ksi in the warp direction and 58 ksi in the filling direction. The stress vs. strain curves are shown for the warp direction in Figure 4.15 and for the filling direction in Figure 4.16. These plots also include a linear best fit line to determine the modulus of elasticity. However, the varying number of data points per specimen skews the accuracy of this estimate. Although these elastic modulus values are similar to the average values, the average modulus of elasticity represents a better approximation due to the equal influence of each data set. Plots for individual specimens are shown in Appendix I.

4.5 Flexural Strength of GFRP Skins

The flexural properties of the GFRP skins were tested in accordance with ASTM D 6272. A total of 10 flexural specimens were cut from deck panels. Half of the specimens were cut along the warp direction and half were cut from filling direction. Each specimen measured approximately 0.2 in. thick x 1 in. wide x 5 in. long. Actual measurements using digital calipers were used for calculations. The specimens were tested on an MTS machine as shown in Figure 4.17. The specimens were simply supported with a span of 3.25 in. The two loading points were located at the quarter-spans, 0.8125 in. from the nearest support and loaded at a constant rate of 0.001 in/sec. The mid-span displacement was recorded using a 1 in. linear motion transducer shown in Figure 4.18.

The flexural behavior of the GFRP skins showed results comparable to the tensile property tests. The elastic modulus for the samples was calculated in two ways: (1) over the entire linear response region; and (2) from 0 to 20% of the maximum stress. The elastic modulus was 13% lower using the entire linear region for the warp direction and 5% lower for the filling direction due to some permanent deformation after 20% of the maximum stress. Although each failure was brittle, only two filling direction specimens fractured into two separate pieces. This shows some added ductility due to the presence of the z-yarns which remain intact after cracking of the matrix or fracture of the warp yarns. Failure of one warp specimen is shown in Figure 4.19 and brittle fracture of one filling specimen is shown in Figure 4.20. Some specimens exhibited multiple peaks in loading as the matrix cracking progressed. Plots for one warp direction and one filling direction specimen are shown in Figure 4.21 and Figure 4.22, respectively. These plots show the linear regression lines for the elastic modulus determination up to 20 percent of

the maximum stress and over the entire elastic region. The failure occurred under the loading points for all specimens. Summaries of the results are shown in Table 4.5. Plots of stress vs. strain are shown for all warp specimens in Figure 4.23 and for all filling specimens in Figure 4.24. Similarly to the tension data, a linear regression is fitted to the linear portion of the graph, but is not as good as an average of the five specimens. Plots of each specimen are given in Appendix J.

The ASTM standard calculates the elastic modulus based on the bending moment on the sample and the section modulus. However, this neglects the fact that the elastic modulus of FRP is lower in compression than tension. Bending causes both compression and tension, so the calculated modulus in this ASTM standard should be somewhere in-between elastic modulus predicted by the pure compression and pure tension tests. The elastic modulus is lower in the warp direction (3462 ksi) than from the tension coupons (3430 ksi) as expected, but the filling direction modulus (3646 ksi) is higher than from the tension tests (1650 ksi). The unexpected increase in modulus is possibly due to the densely-packed warp yarns which enhance the compression zone in bending.

4.6 Shear Connector Test

The structural behavior of three GFRP shear connector configurations previously described in the fabrication chapter were investigated to compare the structural behavior. Three replicates of each configuration were tested, giving a total of nine specimens. The first configuration was the vertical flange shear connectors (V1, V2, and V3). The second configuration was the rectangular core shear connectors (R1, R2, and R3). The third configuration was the tapered shear connectors with a wooden core insert (T1, T2, T3). Since no ASTM standard is currently available for testing of a GFRP shear

connector, this experiment was specially designed for a GFRP-to-concrete shear connector specimen. The test setup is similar to the setup for shear testing of FRP sandwich cores described in ASTM C 273 (2000).

The specimens were loaded on an MTS machine. The test fixture is designed to have the line of the load action pass through diagonally opposite corners of the specimens, preventing eccentricity on the specimen. The specimens are supported at the bottom by a circular plate with a $\frac{1}{4}$ in. deep groove, angled at 45° . The top support fixture was suspended from the MTS crosshead. The top fixture contained an assembly of plates which also included a grooved support. The support block was attached to the support system using a $\frac{3}{4}$ in. diameter pin. The tapered edges of the steel plates were inserted in the grooved steel plates, allowing rotation of the specimen. The angle of tilt from the vertical of the steel plates was recorded. As the MTS machine compressed, the compression force was transferred through the plate, creating a shear force on the concrete. An opposing shear force was created at the interface of the other steel plate and the GFRP fabric. The shear connector test setup is shown in Figure 4.25.

Two safety features were implemented to control the brittle failure. The green rope tied to the top threaded rod in each specimen secured one steel plate to the top crosshead. Duct tape was wrapped loosely around both plates, holding them together. The tape would not be tensioned unless a brittle failure due to debonding of the steel plates or delamination of the concrete topping occurred. The rate of machine stroke was set at of 0.001 in/sec and the specimens were loaded until the load dropped below 50% of the peak load. The machine load was recorded.

The instrumentation was designed to capture the relative displacement between the top and bottom surfaces of the specimen. The steel plates are assumed rigid compared to the concrete and GFRP. Two ½ in. linear motion transducers were used to find an average value of the relative displacement. These transducers were clamped to a magnetic base. The magnetic base was attached to the surface of one steel plate, while the transducers rested against a metal angle attached to the other plate.

The first shear test encountered a bond problem. The test specimen, V1, exhibited a brittle debonding of the steel plate from the GFRP surface. The applied load was approximately 25 kips, well below the load required to create a 6000 psi shear stress listed as the maximum by the manufacturer of the adhesive. It was noted that all the epoxy adhesive remained attached to the GFRP at debonding, showing that the weakest bond was to the steel plate. In response, the steel plates attached to the GFRP face of each of the first set of specimens were removed. The plates were cleaned using a wire brush and sandblasted to roughen the surface. The epoxy adhesive on the GFRP surface was sanded and roughened using a file and low grit sandpaper. The plates were sandblasted prior to each subsequent test to ensure an adequate bond.

The machine load was converted to a load aligned with the epoxy bond from the steel plates to the specimens using the measured angle of tilt, θ . The difference in these two forces is small due to the small angle of tilt of the specimen. Nevertheless, all loads listed in the results are converted to components aligned with the specimen, not the measured machine load. The shear strain is calculated as the ratio of the relative displacement of the steel plates to the thickness of the shear connector specimens. The relative displacement between the steel plates is small prior to concrete cracking after the

peak load. The displacement after cracking or debonding of the concrete topping is more easily identified as shown in Figure 4.26. A summary of the selected shear connector test results is shown in Table 4.6. Details of the progressive failure of the vertical flange, rectangular core, and tapered core specimens are given in Appendix K. Plots of the shear stress vs. shear strain for all the vertical flanges, the rectangular cores, and tapered cores, are shown in Figure 4.27, Figure 4.28, and Figure 4.29 respectively. The data from all nine shear specimens is compiled in Figure 4.30. Complete results of the individual specimens are provided in Appendix K, including load vs. relative displacement plots, shear stress vs. shear strain plots, and pictures of the failure of each test specimen.

All specimens exhibited shear cracks in the concrete prior to delamination of the concrete topping. However, the concrete in each specimen did eventually delaminate from the GFRP. The flange shaped connectors maintained the most ductility beyond the peak load. These specimens also reached the highest stresses. Whereas the wood core specimens created weak spots compared to the concrete topping, the vertical flange specimens benefited from equally stiff concrete in-between flanges. The tapered cores provided confinement due to the wedge action provided, but allowed some compression and rotation of the soft core inserts. Tiny air gaps were noted as a result of the infusion process in the wooden core specimens. These gaps created weak points in the specimens. The rectangular shaped connectors provided the least confinement due to the vertical rotation of the soft cores. For these reasons, the vertical flange shear connector configuration seems to be the best choice.

This test also showed the importance of the interface between two dissimilar materials. Several solutions exist. One solution is to roughen the surface of the GFRP

surface. Textured molds or mechanical grating could provide additional roughness to enhance the bond. Another solution is to stagger the location of the shear connectors so that the distance between connectors at any given cross-section is cut in half using the same amount of material. This is slightly more labor intensive, but could be easily done. A third alternative is to use the same shear connector configuration, but space the shear connectors closer together. This is not recommended as the design becomes impractical. A fourth solution is to an epoxy additive in the concrete topping. Commercially available uncured epoxy resin is mixed in with the batched concrete and provides better compatibility at the bond interface. The cost of the epoxy material would increase the overall price of the deck, but the mixing would be done simultaneously with the concrete creating no additional cost. The roughened texture seems to be the most economical solution as the mold process will likely be used to commercialize production. However, if adequate bond still cannot be achieved, the epoxy concrete seems to be the second best choice.

4.7 Bridge Deck Test Setup

Both deck panels were tested using a three-point loading configuration. The load was applied by a 220 kip actuator at mid-span. The panels were supported by concrete blocks measuring 19 in. high x 24 in. deep x 48 in. wide. For Deck 1, the 5 ft. deck, the concrete blocks were placed 5 ft. apart from center to center, symmetrically about the center of the actuator. For Deck 2, the 9 ft. deck, the concrete blocks were placed 7 ft. apart from center to center. The supports were leveled using metal washers. To provide a larger contact area for the supports, Hydrocal was mixed with water in a plastic bag and placed under the perimeter of the concrete blocks. On top of the concrete blocks, 14 in. deep

steel wide flange beams with full depth stiffeners were placed to raise the height of the supports to ensure sufficient stroke of the actuator. These steel wide flange beams were leveled and Hydrocal was placed underneath the edges to provide stability. Neoprene bearing pads 3 in. thick and 4 in. wide were placed on top of the steel beams. The clear span between the pads was 48 in. for Deck 1 and 84 in. for Deck 2.

The loading was transferred from the actuator to the neoprene pad using a 4 in. square HSS tube. The HSS was oriented perpendicular to the span direction of the deck, along the centerline of the actuator. A 1 in. thick by 6 in. wide neoprene pad was centered at the mid-span of the deck to provide a bearing area of 4 in. x 18 in. for the HSS, as shown in Figure 4.31.

4.8 Deck Instrumentation

Five string potentiometers were attached to the tension side of both decks. Three string potentiometers were placed at mid-span; one at the centerline and the other two located 2 in. from either edge of the deck, as shown in Figure 4.32. The other two string potentiometers were placed at the centerline of either quarter-span of the deck. The string potentiometers were attached to plywood blocks and adhered to the underside of the deck using an epoxy. Two potentiometers were placed above the deck at the edge of either neoprene pad support to measure the displacement of the pads, as shown in Figure 4.33. The complete flexure test setup is shown in Figure 4.34.

Two 120.4 Ω electrical resistance FRP strain gages were adhered to the tension side of Deck 1 as shown in Figure 4.32. The surface was sanded and cleaned before attaching the gages with a cyanoacrylate adhesive, CN. One strain gage was oriented along the span direction of the deck, at the centerline of the mid-span. The other strain

gage was also at the mid-span but oriented perpendicular to the first gage in order to determine Poisson's ratio. Two 120 Ω electrical resistance PL-60 concrete strain gages were attached to the top face, the compression side of the deck, as shown in Figure 4.35. The surface was sanded and cleaned prior to attaching the strain gages with a 2-part polyester adhesive, PS. A preliminary layer of adhesive was applied, allowed to cure, and sanded to an even surface. A second layer of epoxy was then applied for the strain gages after 7 hours. One strain gage was in the direction of the span of the deck and offset 6 in. from mid-span to avoid placing it directly underneath the neoprene pad and HSS. This offset between the concrete strain gages and the mid-span is accounted for in calculating the mid-span strain by a simple ratio of the bending moment values at these two locations. This assumes the bending moments are proportional to the strains. The second strain gage was oriented perpendicularly to the first to determine Poisson's ratio in the transverse direction.

The instrumentation for Deck 2 was similar to Deck 1 except that two longitudinal strain gages were applied to both the FRP and concrete. One longitudinal concrete strain gage was offset towards the north side of the mid-span and the other was offset towards the south support.

4.9 Loading Cycle

The load was applied using a stroke controlled actuator for loading and unloading at a rate of 0.1 in/min. The deflections and loads were balanced immediately before testing. The first applied loading cycle was from 0 to 2,000 lbs. Upon reaching this maximum load, the deck was unloaded at the same rate, 0.1 in/min. The subsequent loading cycles were from 0 to the next multiple of 2,000 lbs. This loading cycle was repeated up to

32,000 lbs, which is the equivalent to the approximate AASHTO specification for the HS30 design wheel load classification. After one last unloading cycle, the decks were loaded to failure. The purpose of the loading cycles was to identify any permanent deformation or residual strains accumulated in each cycle.

4.10 Test Results of Deck 1

The first deck tested was Deck 1 with a clear span of 4 ft. At 20% of the maximum load, 13.49 kips, the mid-span deflection was 0.109 in. (L/442). No noticeable permanent deformation occurred up to a load level of 32 kips, as shown in Figure 4.35. The mid-span deflection at this load was 0.325 in. (L/148). At a load of 40 kips, slight cracking of the matrix was audible. The maximum load supported by Deck 1 was 67.5 kips. The mode of failure was a brittle shear failure of the concrete, as shown in Figure 4.36. In addition, the concrete topping delaminated from the deck over the north support and cracking propagated at a 45° angle from the edge of the support. Although the majority of the shear cracking occurred on the north end of the panel as shown in Figure 4.37, minute shear cracks were observed on the right end of the panel. Shear cracks and crushing on the compression side have been traced and are shown in Figure 4.38. The shear connectors did not fail. However, the concrete did delaminate from two of the shear connectors, one of which is shown in Figure 4.39. The panel was unloaded and the FRP exhibited a near fully elastic recovery. The load-displacement plot is shown in Figure 4.40. The average relative (to the supports) mid-span displacement at failure was 0.794 in. (L/61). The quarter span displacements at the peak load were 0.600 in. at the north quarter-span and 0.624 in. at the south quarter-span. The deflections of Deck 1 at various AASHTO equivalent wheel load classifications are given in Table 4.7. Deck 1 is

at the threshold of acceptable serviceability performance for the HS15 AASHTO classification, exhibiting a deflection of 0.155 in. ($L / 310$), which is very close to the recommended value of $L / 360$. However, these deflections are not representative of a full-size panel. The maximum width of deck produced on the selected weaving machine was 18 in. A commercial panel would have a width of approximately 72 in. The effective width of deck resisting an AASHTO truck load is not currently specified for FRP decks. Therefore, the effective width was calculated based on the specification for reinforced concrete decks. The equation given by AASHTO for the effective width, w_d in inches is:

$$w_d = 26 + 6.6S$$

where S is the spacing between supports and is measured in feet. This equation yields an effective width of 52 in. for Deck 1. The deflection is assumed to vary inversely proportional to the effective width. The deflections based on the effective width of a full-size panel are also given in Table 4.7. This consideration shows that the deck meets the strictest serviceability recommendations for the AASHTO HS 30 live load.

The maximum tensile strain of the FRP in the longitudinal direction was 0.0054. The maximum compressive strain of the concrete in the longitudinal direction was 0.0027, which is close to the ultimate value. In the transverse direction, the maximum measured strain in the FRP was 0.0007, while the maximum concrete strain was 0.00034. The load vs. strain plot is shown in Figure 4.41, which shows slight nonlinearity near the peak load. The strain results at the peak load are listed in Table 4.8.

4.11 Test Results of Deck 2

The supports were moved to a clear span of 7 ft. for Deck 2. At 20% of the maximum load, 9.199 kips, the mid-span deflection was 0.226 in. (L/371). No noticeable permanent deformation occurred in Deck 2 up to a load of 32 kips. During the load to failure cycle, the first peak in load occurred at 42.7 kips and a mid-span deflection of 1.185 in. (L/71). The deflection at the north quarter-span was 0.796 in. and the deflection at the south quarter-span was 0.839 in. At this load, some concrete topping delamination occurred near the north support. The second peak in load occurred at 44.5 kips with a mid-span deflection of 1.46 in. (L/58). The deflection at the north quarter-span was 0.981 in. and the deflection at the south quarter-span was 0.994 in. Additional delamination of the concrete topping occurred. The concrete topping on the north end of the deck started to delaminate followed by a shear crack at the quarter-span. The load on the deck was maintained at 40 kips for 1.38 in. of additional deflection beyond the second peak in load. The maximum load occurred at 46.0 kips. At this loading, the mid-span displacement was 2.84 in. (L/30). The north quarter-span deflection was 2.128 in. and the south quarter-span deflection was 1.673 in. At this point, the entire north end of the deck exhibited complete and brittle concrete topping delamination as shown in Figure 4.42. Four of the shear connectors failed in tension and the load dropped to less than 10 kips within seconds as shown in Figure 4.43. When unloaded, the deck was permanently deformed and the deflected shape at shear connector failure was retained. The displacement for all loading cycles is shown in Figure 4.44. The deflections of Deck 2 at various AASHTO equivalent wheel load classifications are given in Table 4.9. Deck 2 was below the recommended serviceability performance, exhibiting 0.401 in. deflection

(L / 209) at the HS15 AASHTO equivalent wheel load classification. The deflections considering the effective width are also given in Table 4.9 and show that the deck is adequate for the AASHTO HS 30 load classification.

All strain gages were damaged prior to ultimate load. Extrapolations of each strain gage were determined up to the first load peak, 42.4 kips. The average maximum tensile strain of the FRP in the longitudinal direction was 0.0047. The average maximum compressive strain of the concrete in the longitudinal direction was 0.002. In the transverse direction, the maximum compressive FRP strain was 0.00074 while the maximum tensile concrete strain was 0.00042. The strain values at the first peak load are shown in Table 4.10 and the load vs. strain plot extrapolated to the first peak load is shown in Figure 4.45. The strains in the deck are still linear for Deck 2 near the peak load. At these same strain levels, the load vs. strain relationship was also linear for Deck 1.

The results indicate that the shear connectors were not totally adequate to achieve the full strength of the material used in the GFRP/concrete deck. Future work should focus on proper design of the shear connectors. Test results indicate that even with the restricted dimensions used for these decks, the use of 3-D woven material has an excellent potential for fabrication of structurally effective bridge deck.

Table 4.1. Concrete cylinder compression test results.

	No.	Days Cured	Max Load (lbs)	Area (in ²)	Elastic Modulus (ksi)	Average Elastic Modulus (ksi)	Max Comp. Strength (psi)	Average Comp. Strength (psi)
Batch 1	1	7	77075	12.6687	--		6084	--
	2	14	90986	12.5837	--		7230	--
	3	28	98140	12.6923	--		7732	7947
	4	28	103908	12.7303	--		8162	
	5	28	91656	12.6167	3914	3313	7265	8174
	6	28	112625	12.5805	2761		8952	
	7	28	105132	12.6576	3264		8305	
Batch 2	1	7	82871	12.7255	--		6512	--
	2	14	94860	12.6135	--		7520	--
	3	28	91043	12.7006	--		7168*	--
	4	28	117806	12.7413	3838	3937	9246	8836
	5	28	96048	12.5734	4434		7639	
	6	28	121478	12.6241	3539		9622	
Avg.						3625		8319

*Denotes premature failure at ends.

Table 4.2. Steel reinforcement tension test results.

No.	Bar Diameter (in)	Elastic Modulus (ksi)	Yield Stress (ksi)	Yield Strain (in/in)	Max Stress (ksi)	Max Strain (in/in)	Location of Failure
1	0.243	31613	80.5	0.00455	85.9	0.0214	Bottom 1/3
2	0.241	30803	79.8	0.00459	84.4	0.0142	Top Grip
3	0.239	32698	83.1	0.00454	89.1	0.0237	Middle 1/3
4	0.242	32042	80.7	0.00452	86.8	0.0227	Middle 1/3
5	0.239	32869	84.4	0.00458	89.9	0.0143	Top Grip
6	0.247	27963	77.0	0.00475	81.7	0.0164	Bottom Grip
Avg.	0.242	31330	80.9	0.00460*	86.3	0.0226**	

* Excludes bar 1 which had extensometer malfunction.

** Includes bars 1, 3, and 4.

Table 4.3. Fiber volume fraction results.

No.	Calculated Initial Volume V_{geom} (in ³)	Measured Composite Mass m_1 (g)	Composite Total Mass m_{T1} (g)	Fabric Mass After Burnoff m_{T2} (g)	Fabric Weight Fraction w_{fm}	Matrix Weight Fraction w_{mm}	Fiber Volume Fraction f
1a	0.0635	38.85	76.65	47.76	0.623	0.377	0.412
1b	0.0613	37.8					
2a	0.0585	34.26	65.34	40.2	0.615	0.385	0.404
2b	0.0593	31.08					
3a	0.0756	39.75	77.94	49.25	0.632	0.368	0.421
3b	0.0605	38.19					
4a	0.0490	37.48	37.48	23.08	0.616	0.384	0.404
Avg	--	--	--	--	0.622	0.379	0.41
ρ_f	0.094	lb/in ³					
ρ_m	0.039827	lb/in ³					

Table 4.4. GFRP skin tension coupon results.

No.	Direction of Loading	Area (in ²)	Maximum Stress (ksi)	Ultimate Strain (in/in)	Modulus of Elasticity (ksi)	Failure Mode
1	warp	0.237	32.3	0.0097	3459	tension in grip
2	warp	0.224	66.0	0.0215	3230	fiber fracture
3	warp	0.197	45.4	0.0133	3734	tension in grip
4	warp	0.267	6.9	0.0022	3286	tab slippage
Avg					3430	
5	filling	0.228	6.1	0.0031	1837	tension in grip
6	filling	0.260	2.4	0.0017	1476	tension in grip
7	filling	0.232	6.1	0.0040	1622	tension in grip
8	filling	0.246	4.5	0.0016	1568	tension in grip
9	filling	0.254	10.2	0.0126	1767	tension in grip
Avg					1650	

Table 4.5. GFRP skin four point bending results.

No.	Specimen Span Direction	Elastic Modulus E (ksi)	Elastic Modulus to 20% Max Stress $E_{20\%}$ (ksi)	Max Stress σ_{max} (ksi)	Strain at Max Stress ϵ_u (in/in)
1	warp	3108	2718	68.3	0.0334
2	warp	2750	3504	63.1	0.0236
3	warp	2904	4048	66.8	0.0218
4	warp	1994	2205	56.5	0.0291
5	warp	2493	2788	60.3	0.0255
Average	--	2650	3053	63.0	0.0267
6	filling	3773	3648	51.3	0.0141
7	filling	5525	6346	70.0	0.0108
8	filling	3248	3522	42.3	0.0132
9	filling	4357	3335	51.6	0.0137
10	filling	4463	4346	50.2	0.0153
Average	--	4273	4239	53.1	0.0134
Overall Average	--	3462	3646	58.0	0.0201

Table 4.6. Shear connector study results.

ID	Height (in)	Width (in)	Length (in)	Max Shear Stress (psi)	Shear Strain at Max Stress (in/in)	Test Angle θ (°)
V1	2.390	3.057	15.513	567.4	0.0106	7.5
V2	2.432	3.030	15.529	515.0	0.0195	6.5
V3	2.434	3.032	15.527	790.8	0.0089	8
V_{avg}	2.419	3.040	15.523	624.4	0.0130	7.3
R1	2.215	3.013	15.569	410.9	0.0046	8
R2	2.260	3.049	15.561	402.7	0.0032	8
R3	2.207	3.030	15.532	422.8	0.0039*	8
R_{avg}	2.227	3.031	15.554	412.1	0.0039	8
T1	2.380	2.986	15.534	421.7	0.0487	7.5
T2	2.371	3.050	15.523	419.4	0.0013	7.5
T3	2.368	3.007	15.570	423.8	0.0030	8
T_{avg}	2.373	3.014	15.542	421.6	0.0177	7.7
Avg	2.340	3.028	15.540	486.0	0.0115	7.7

*Strain at max stress adjusted to average of R1 and R2 due to loss of data prior to max load.

Table 4.7. Deck 1 deflections at AASHTO equivalent wheel load classifications.

	HS 15	HS20	HS25	HS30
Load (kips)	16	22	26	32
Deflection (in)	0.155	0.184	0.218	0.275
L / xxx	310	261	220	175
Effective width (in)	52	52	52	52
Deflection considering effective width (L / xxx)	899	757	638	508

Table 4.8. Deck 1 strains at peak load.

	FRP (X)	FRP (Y)	Concrete (X)	Concrete (Y)
Strain (in/in)	0.00575*	-0.00067	-0.00275*	0.00042

* Strain values are linearly extrapolated due to failure of strain gage readings prior to peak load.

Table 4.9. Deck 2 deflections at AASHTO equivalent wheel load classifications.

	HS 15	HS20	HS25	HS30
Load (kips)	16	22	26	32
Deflection (in)	0.401	0.552	0.656	0.796
L / xxx	209	152	128	106
Effective width (in)	72	72	72	72
Deflection considering effective width (L / xxx)	838	610	513	425

Table 4.10. Deck 2 strains at 1st peak load.

	CY	CXL	CXR	TY	TXF	TXB
Strain (in/in)	0.00047*	-0.00221*	-0.00232*	-0.00079*	0.004920*	0.004488*
Avg. Strain (in/in)	0.00047	-0.00227		-0.00079	0.004704	

*Strain values are extrapolated due to failure of strain gage readings prior to peak load.



Figure 4.1. Concrete compression test.



Figure 4.2. Concrete stress-strain test setup prior to loading.



Figure 4.3. Failure of concrete cylinder.

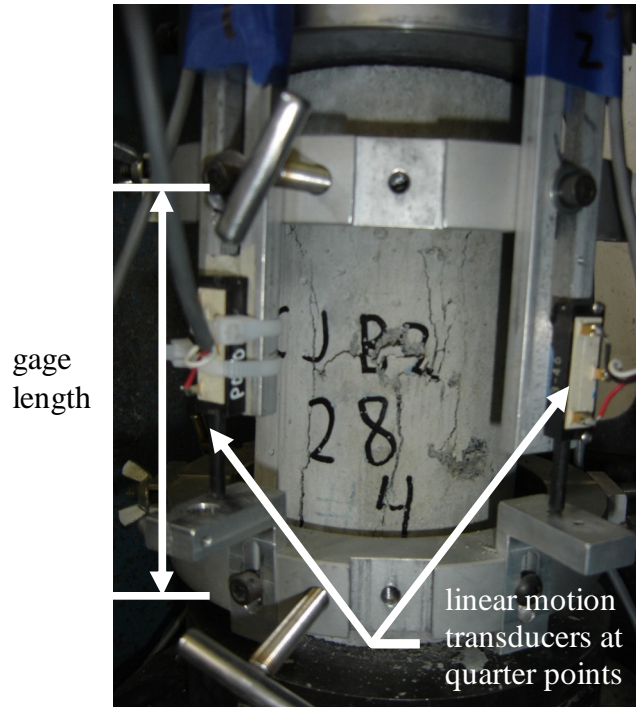


Figure 4.4. Crushed concrete cylinder.

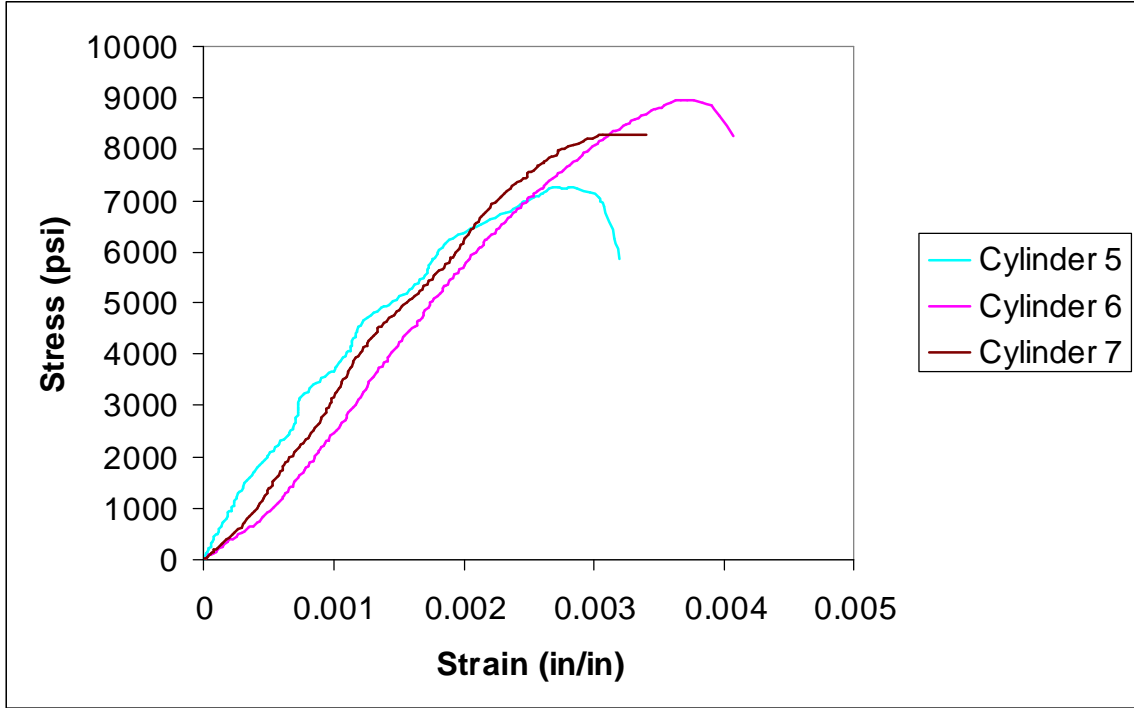


Figure 4.5. Batch 1 Measured Stress vs. Strain at 28 day strength.

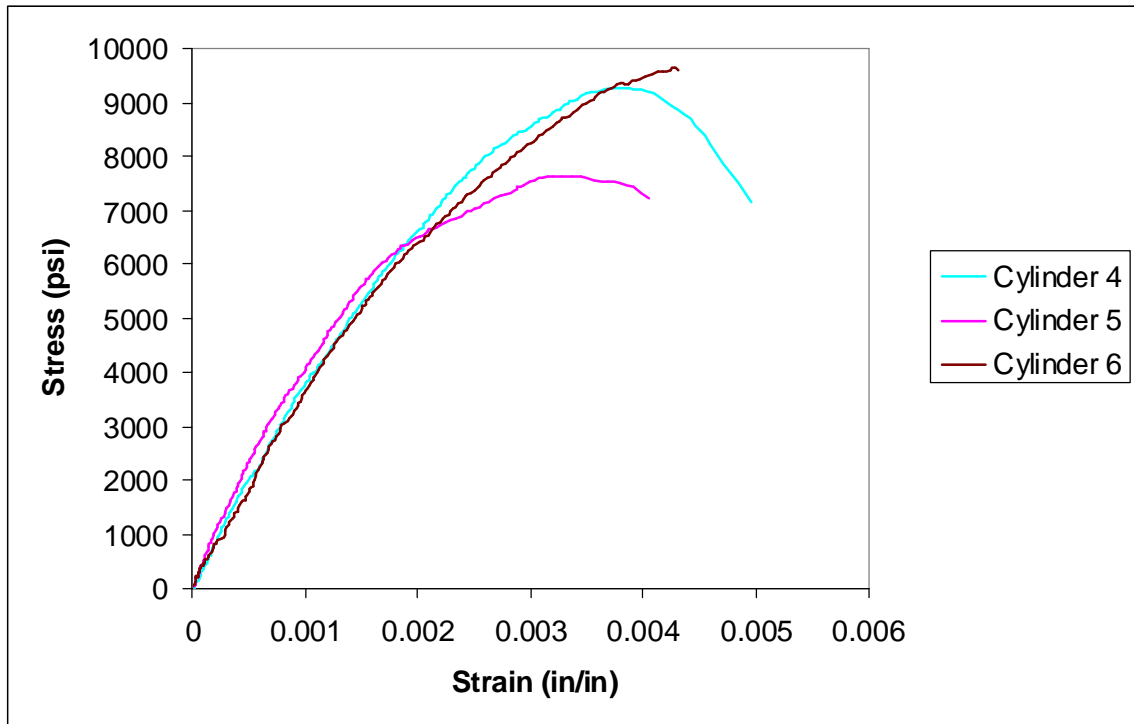


Figure 4.6. Batch 2 Measured Stress vs. Strain at 28 day strength.

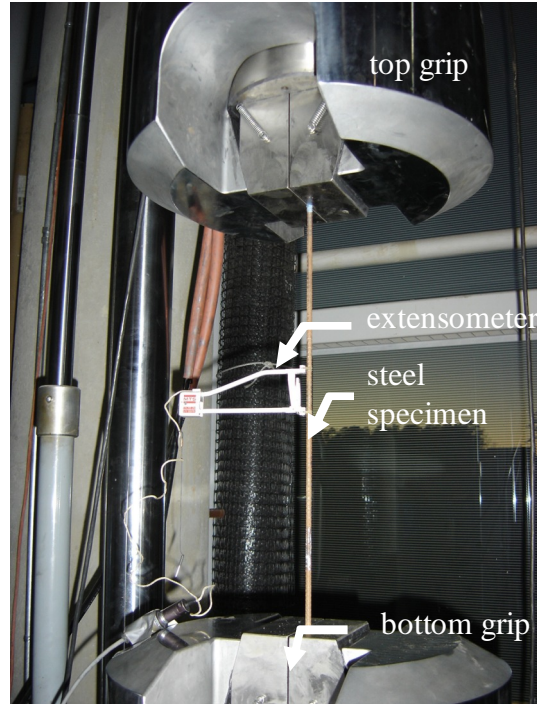


Figure 4.7. Setup of steel reinforcement tension test.



Figure 4.8. Necking of steel reinforcement at failure.

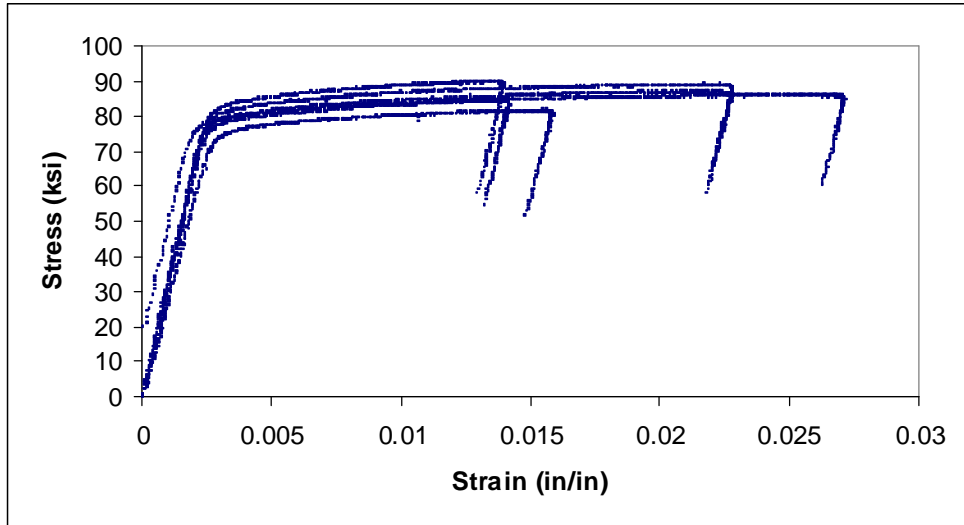


Figure 4.9. Steel reinforcement tension test results.



Figure 4.10. Submersion of FRP sample to determine total volume.



Figure 4.11. Composite specimens in ceramic cup prior to burn-off.



Figure 4.12. Fabric remnants from matrix burn-off test.

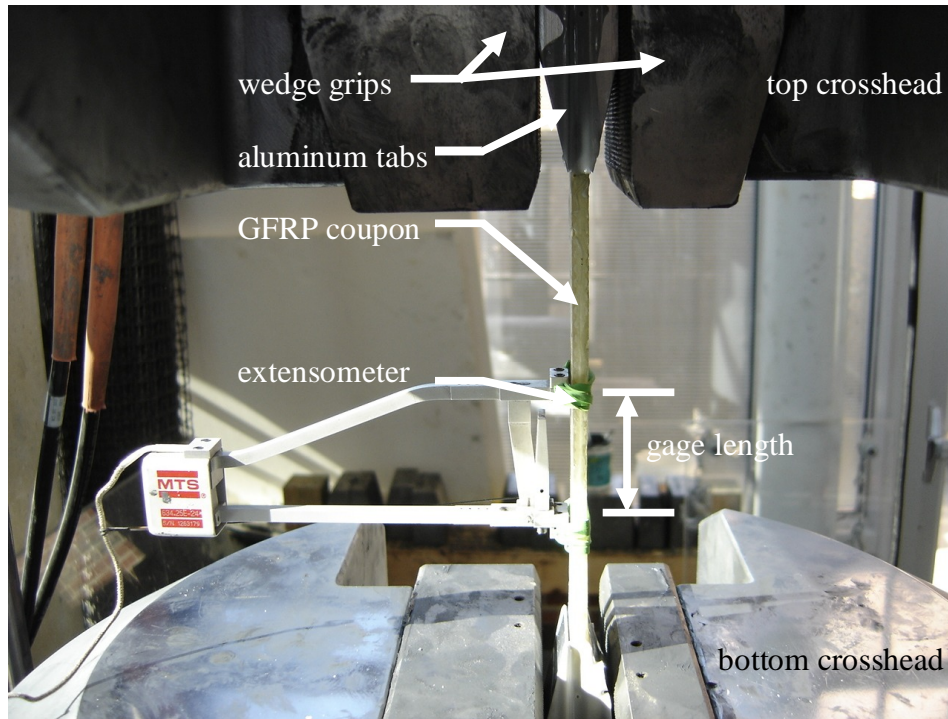


Figure 4.13. Tensile FRP coupon test.

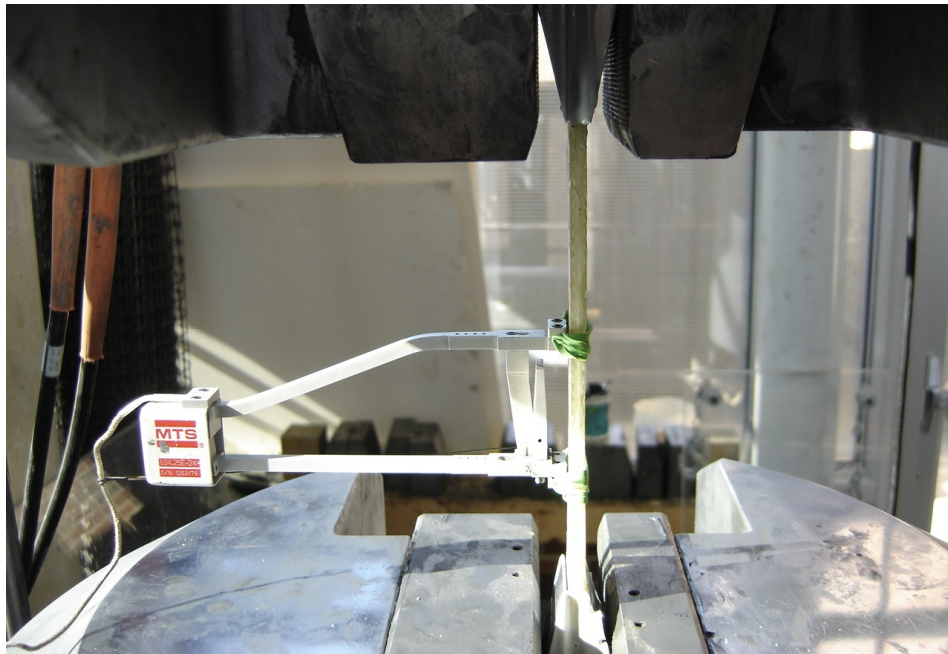


Figure 4.14. Testing of tension coupons.

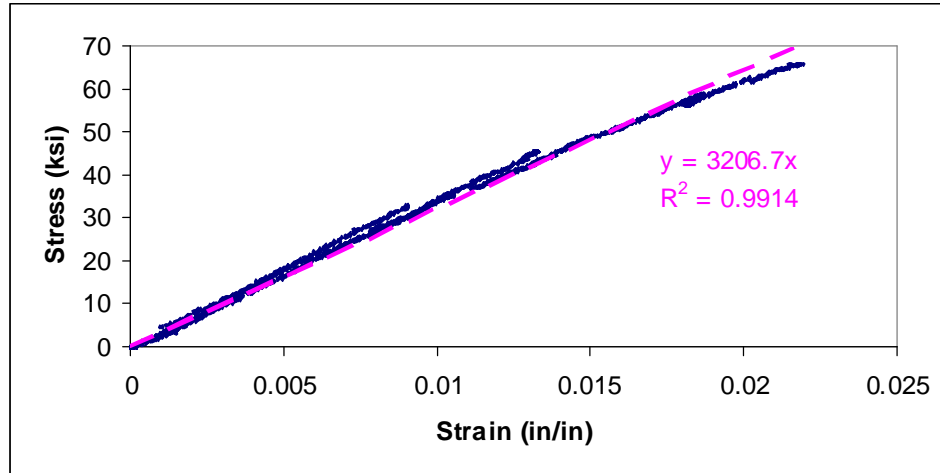


Figure 4.15. Warp direction tensile coupon test results.

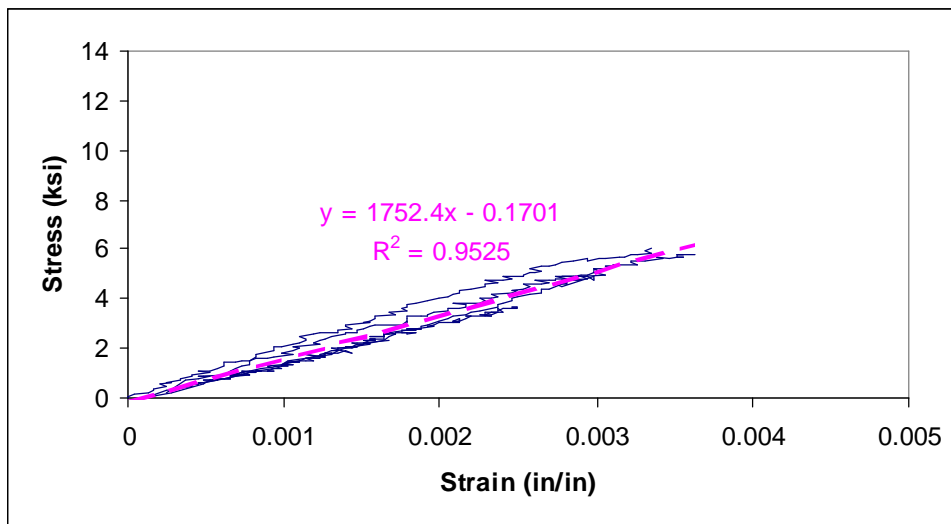


Figure 4.16. Filling direction tensile coupon test results.

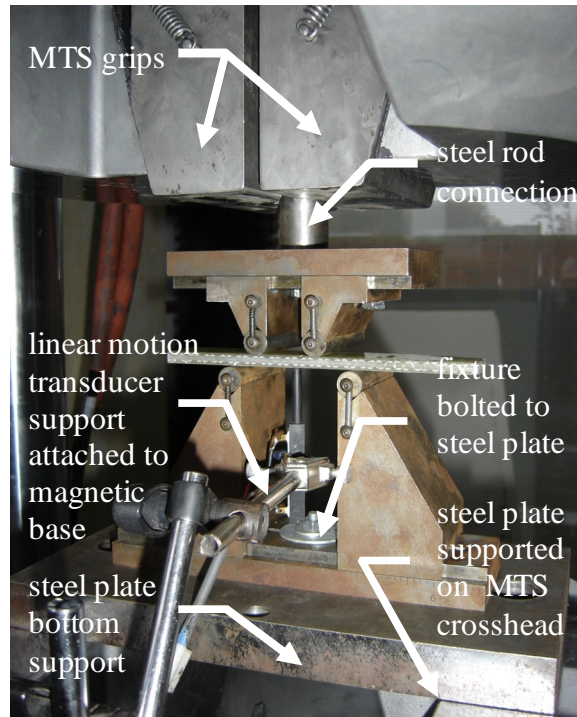


Figure 4.17. Four point bending test setup for warp direction skin.

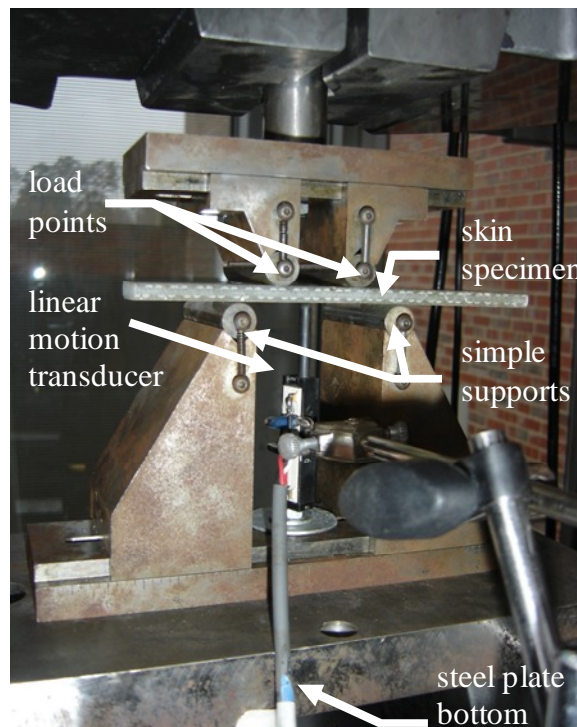


Figure 4.18. Warp direction four point bending test of skin.

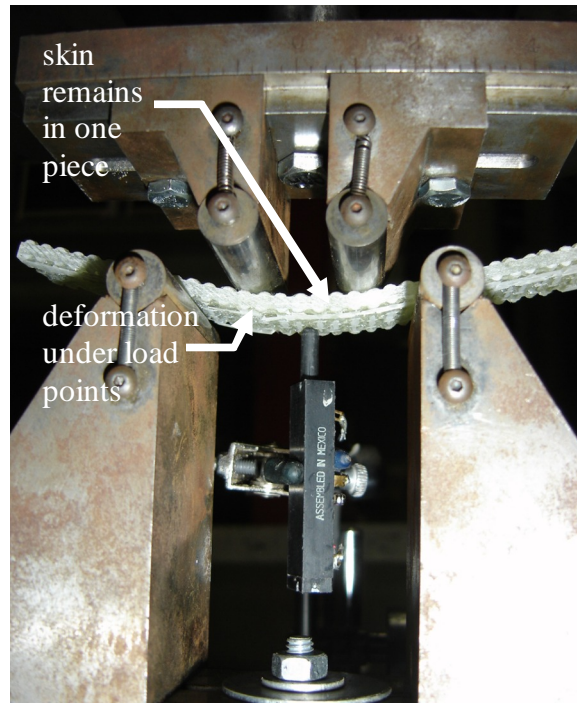


Figure 4.19. Failure of warp direction four point bending test.



Figure 4.20. Brittle failure of filling specimen.

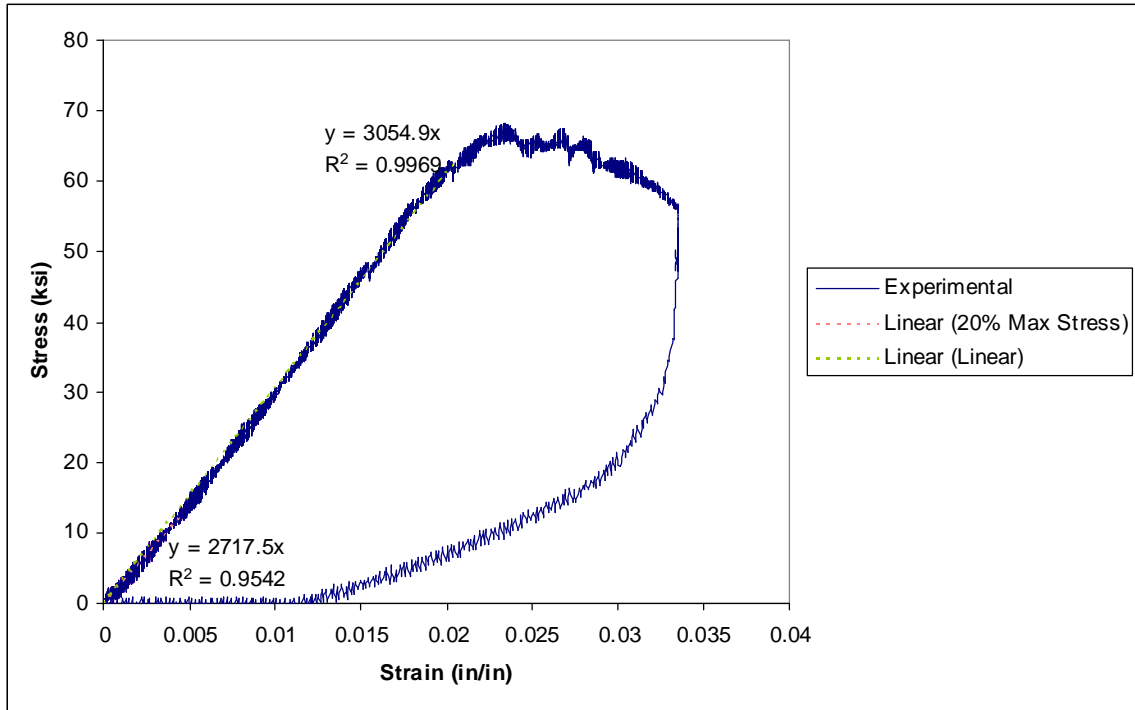


Figure 4.21. Load vs. displacement for warp direction four point bending specimen.

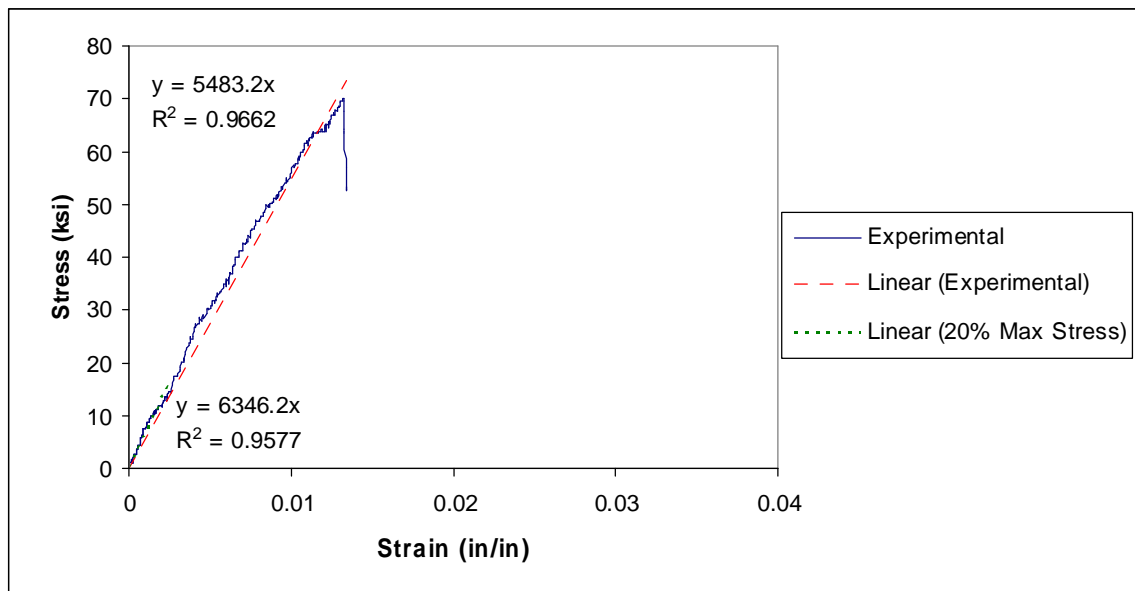


Figure 4.22. Load vs. displacement for filling direction four point bending specimen.

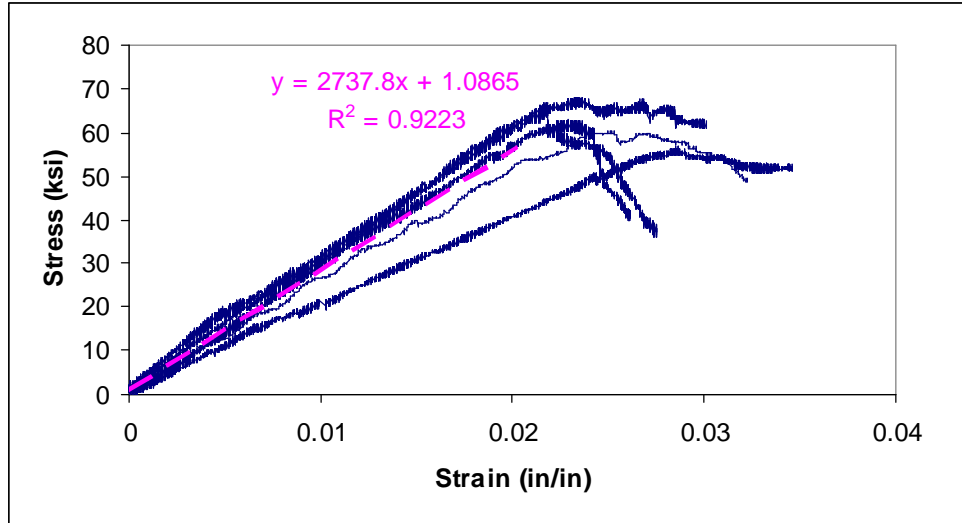


Figure 4.23. Warp direction four-point bending results.

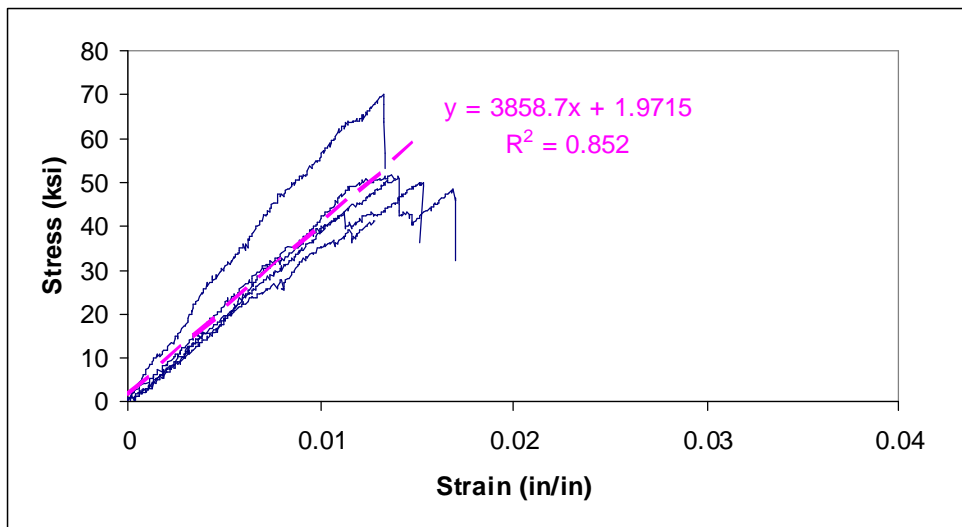


Figure 4.24. Filling direction four-point bending results.

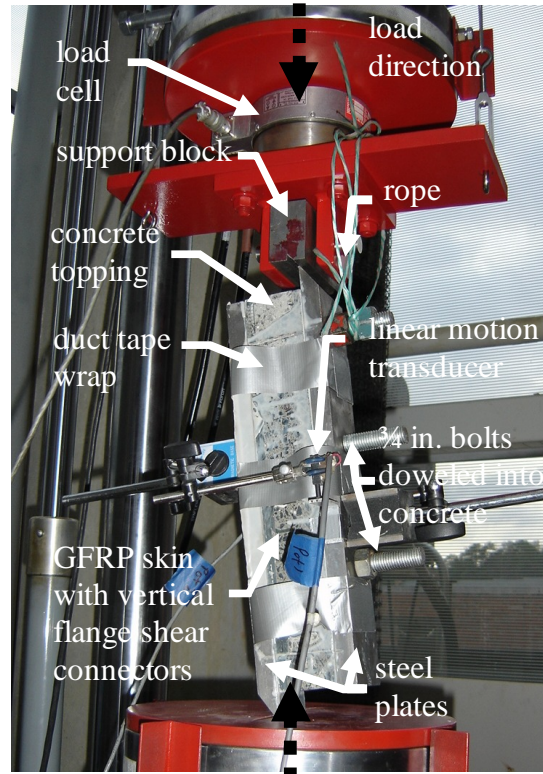


Figure 4.25. Shear connector test setup.



Figure 4.26. Failure of shear connector specimen.

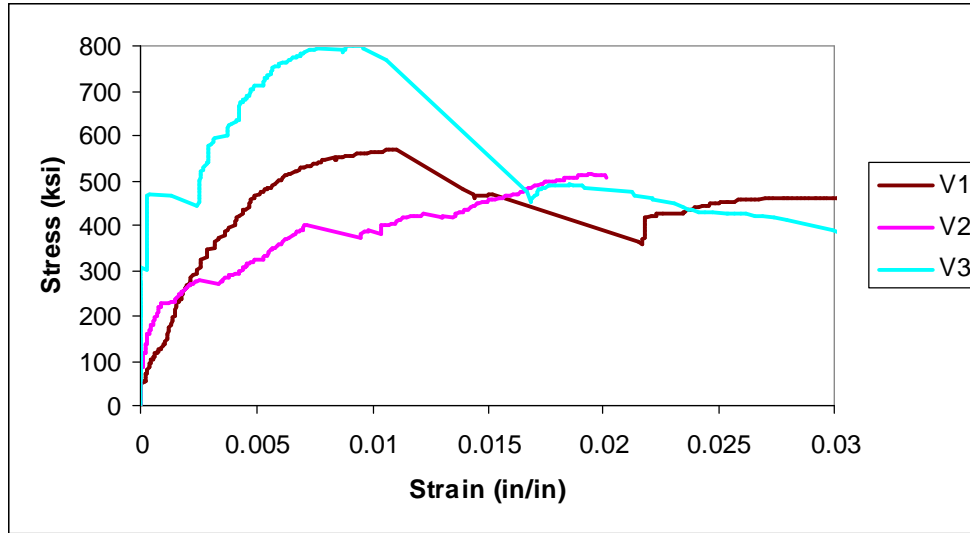


Figure 4.27. Stress vs. strain for all vertical GFRP flange shear connector specimens.

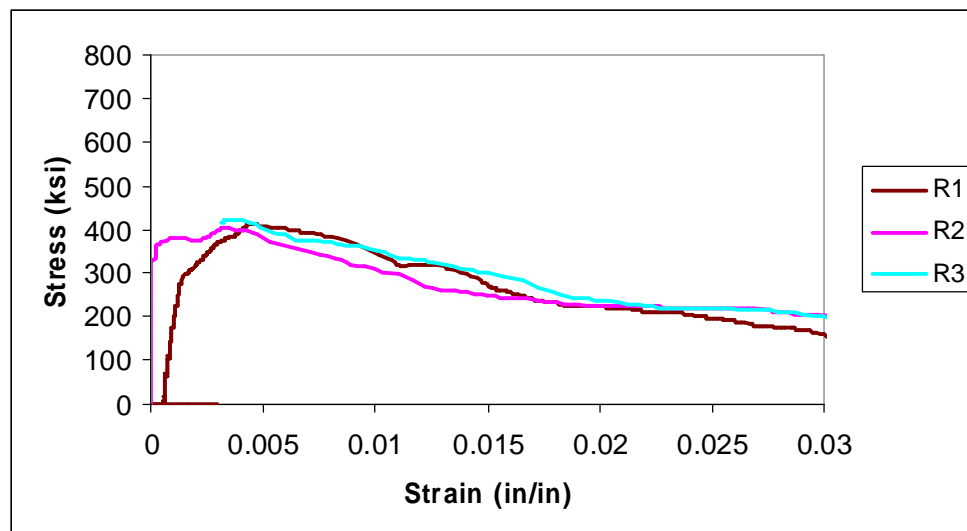


Figure 4.28. Stress vs. strain for all rectangular wood core shear connector specimens.

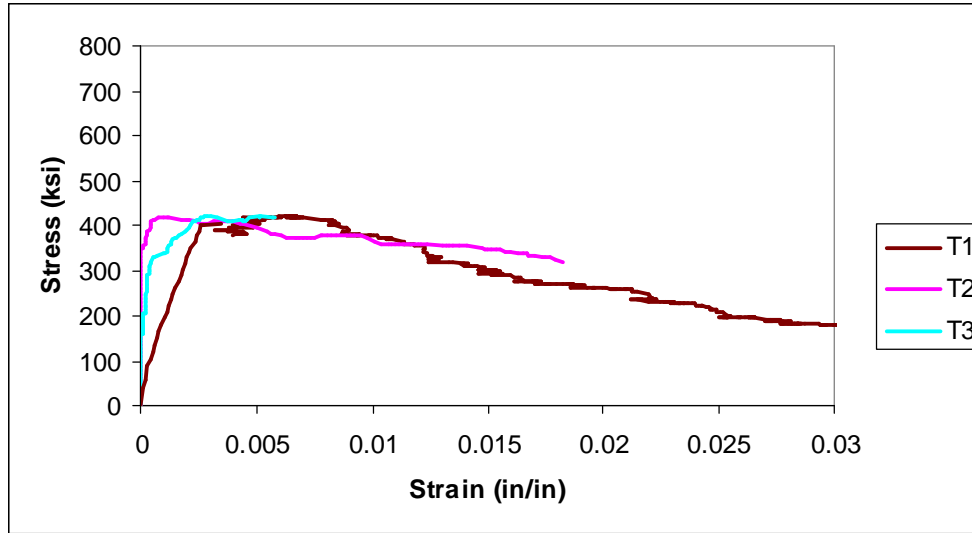


Figure 4.29. Stress vs. strain for all tapered wood core shear connector specimens.

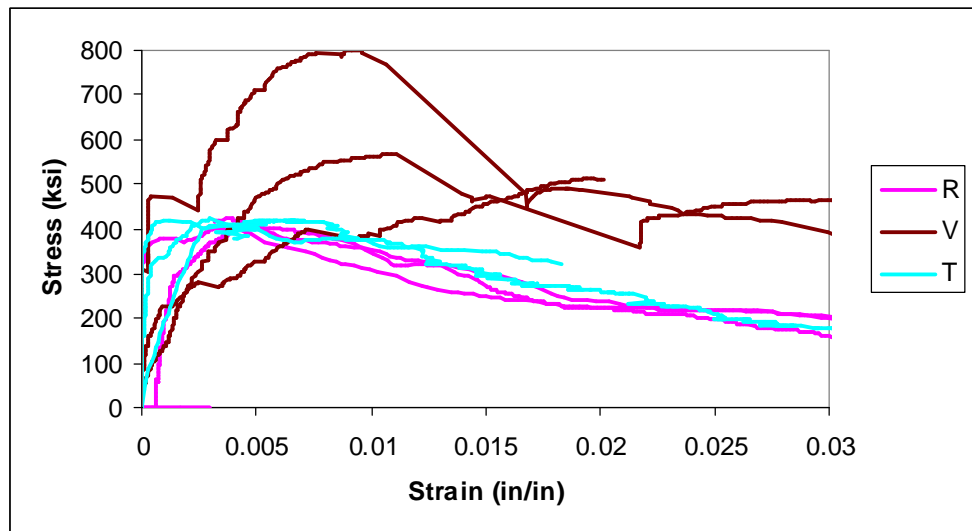


Figure 4.30. Stress vs. strain for all shear connector specimens.

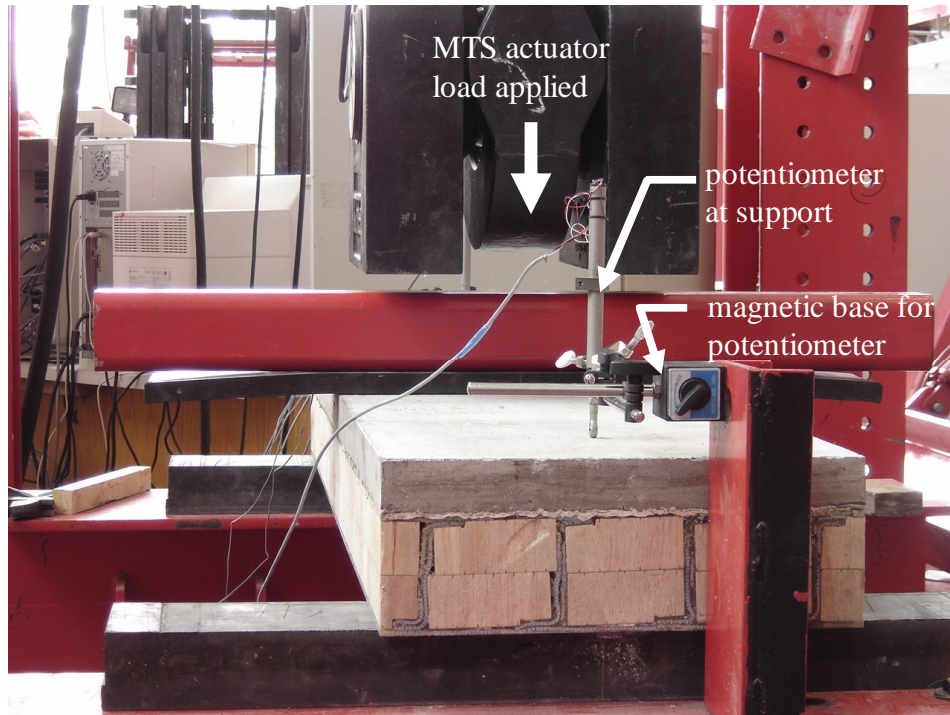


Figure 4.31. Deck 1 instrumentation at support.

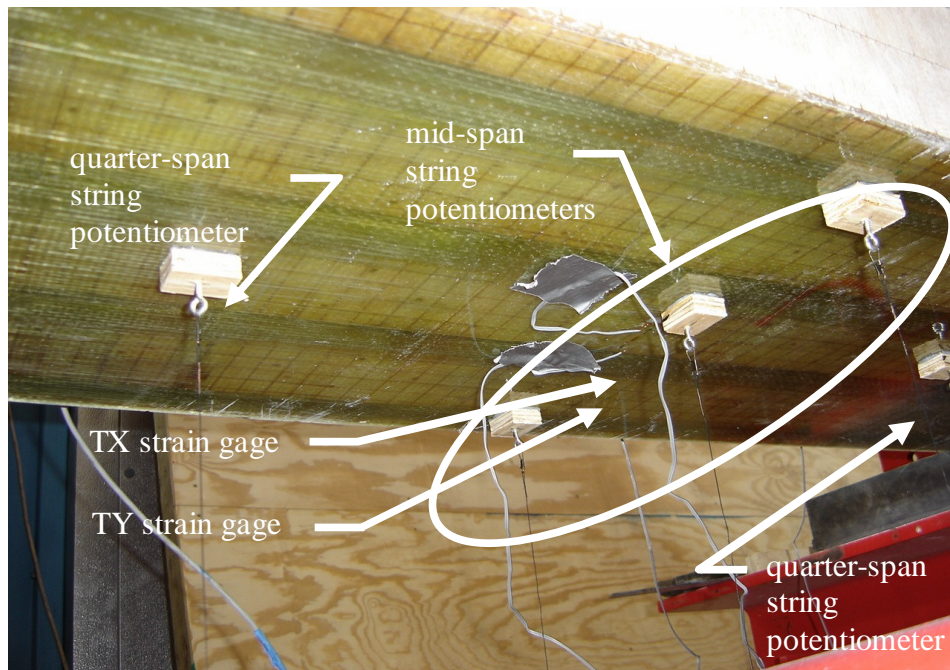


Figure 4.32. String potentiometers attached to tension side of deck.

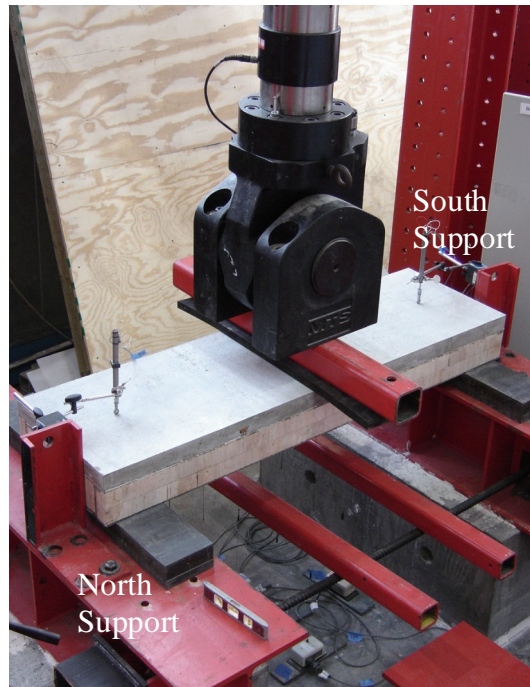


Figure 4.33. Deck 1 prior to loading.

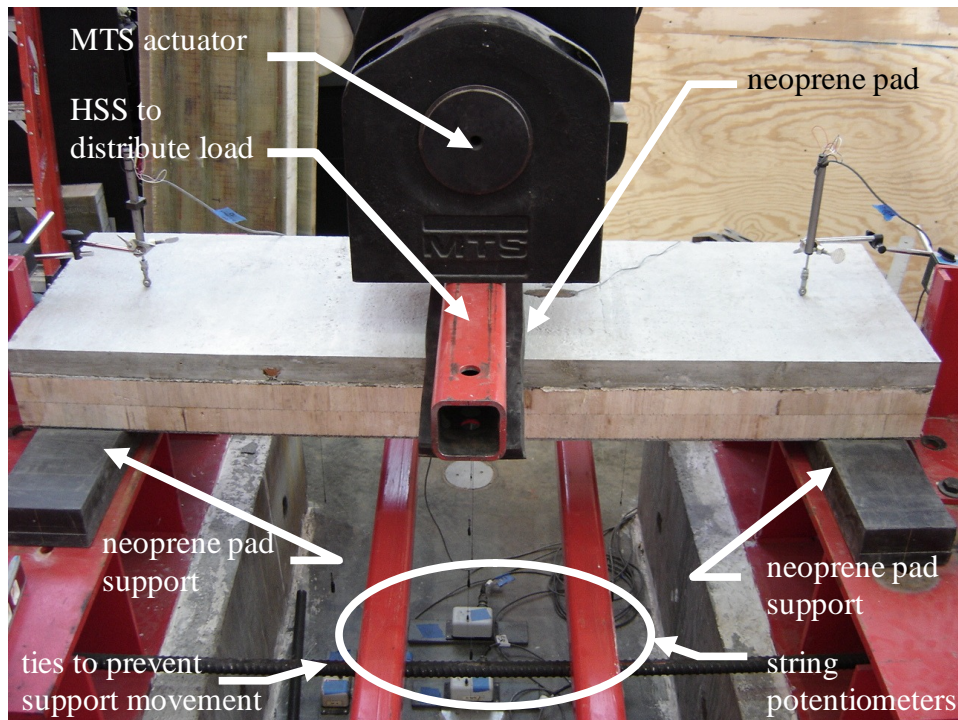


Figure 4.34. Deck 1 during loading cycle.

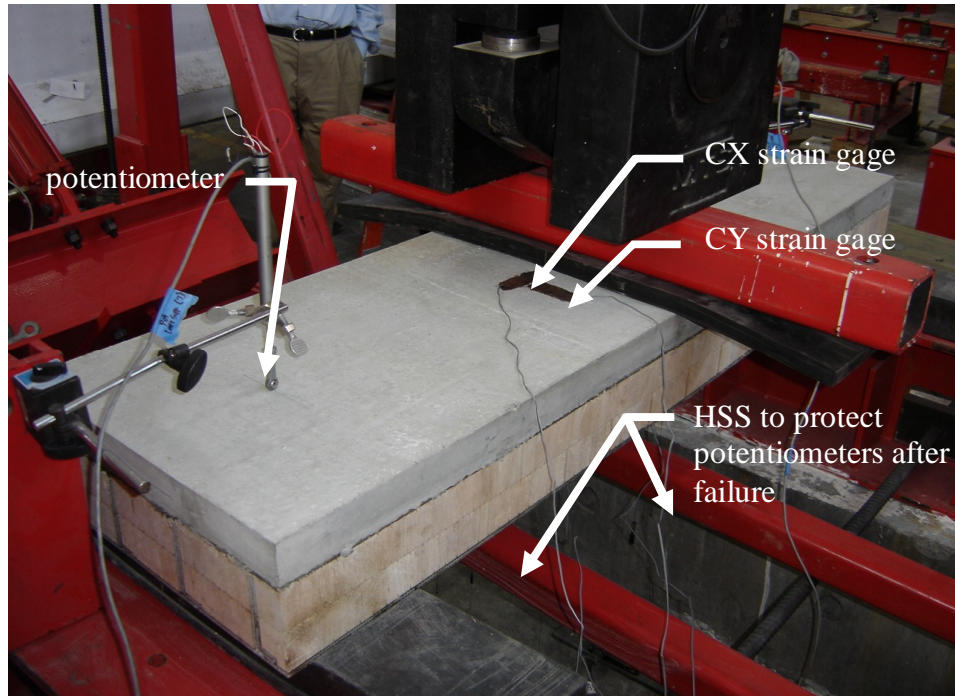


Figure 4.35. Deck 1 prior to failure.

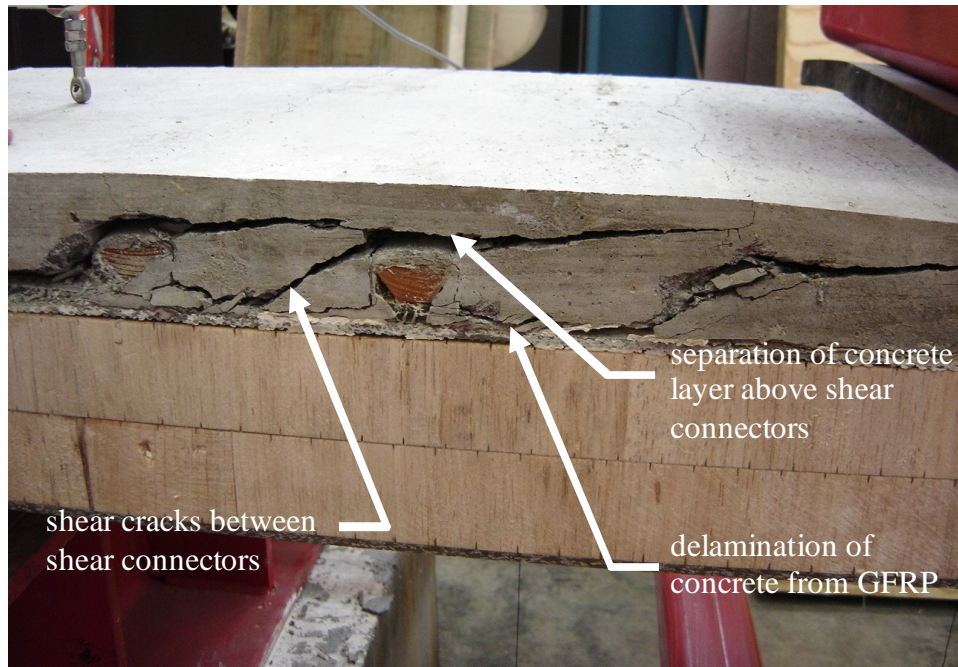


Figure 4.36. Concrete shear failure and delamination of Deck 1.

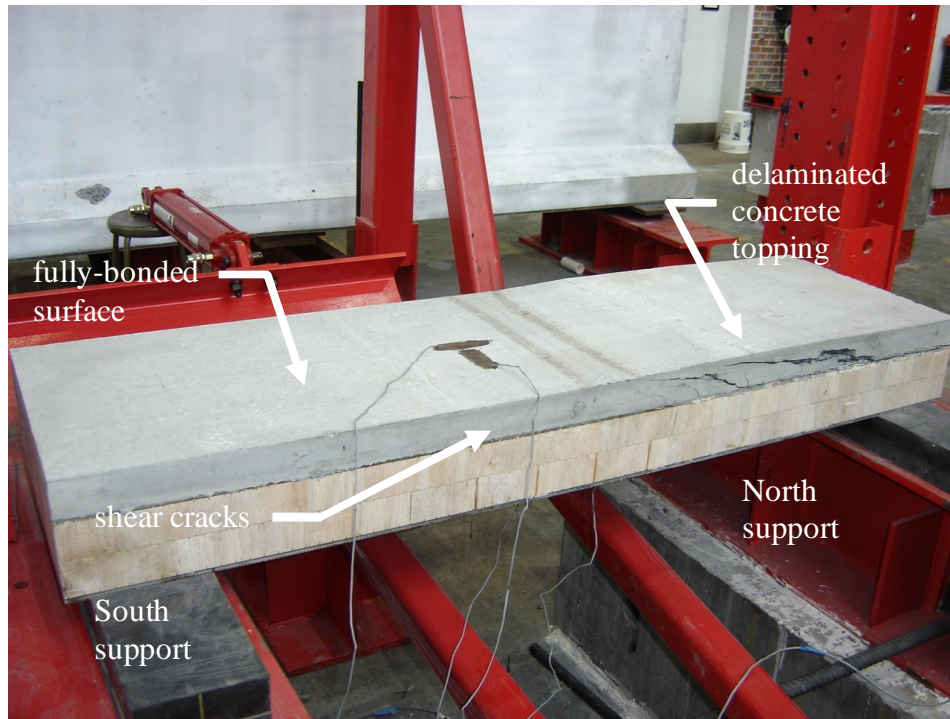


Figure 4.37. Deck 1 after failure.

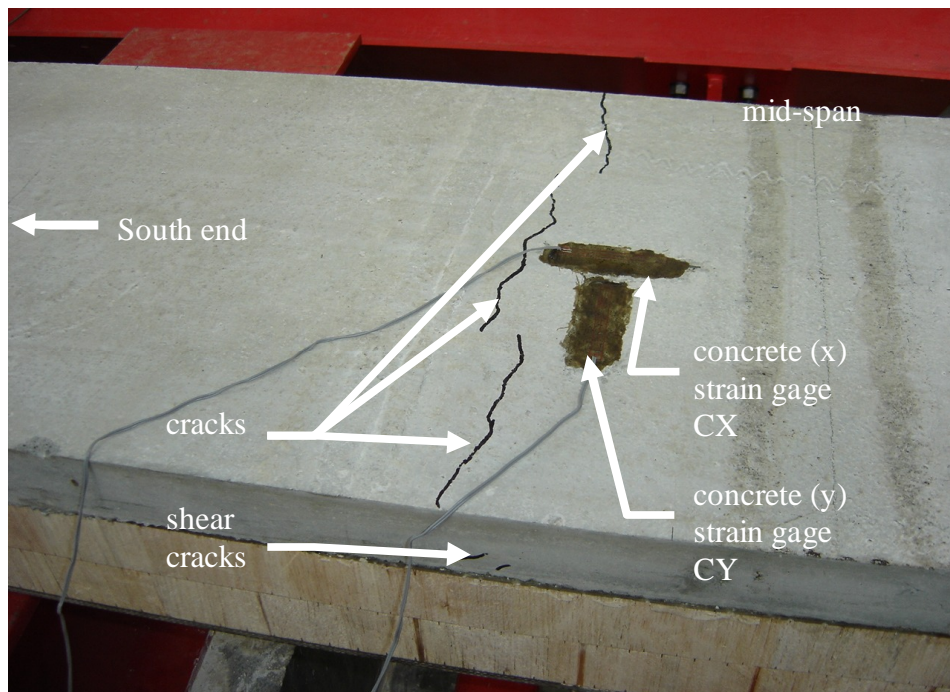


Figure 4.38. Concrete cracks at mid-span of Deck 1.

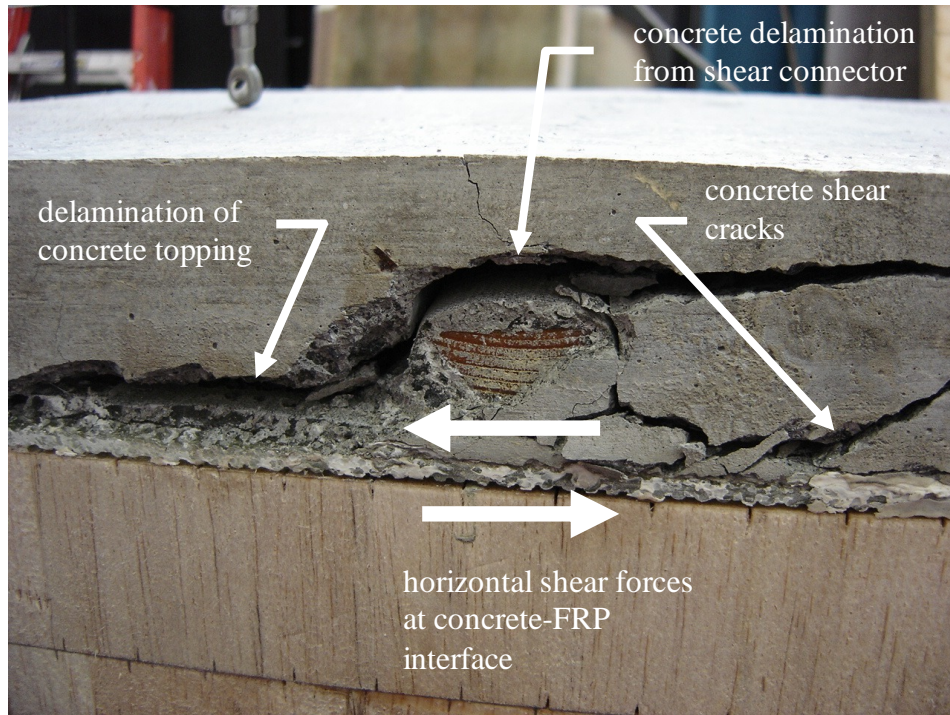


Figure 4.39. Deck 1 concrete shear failure at shear connector.

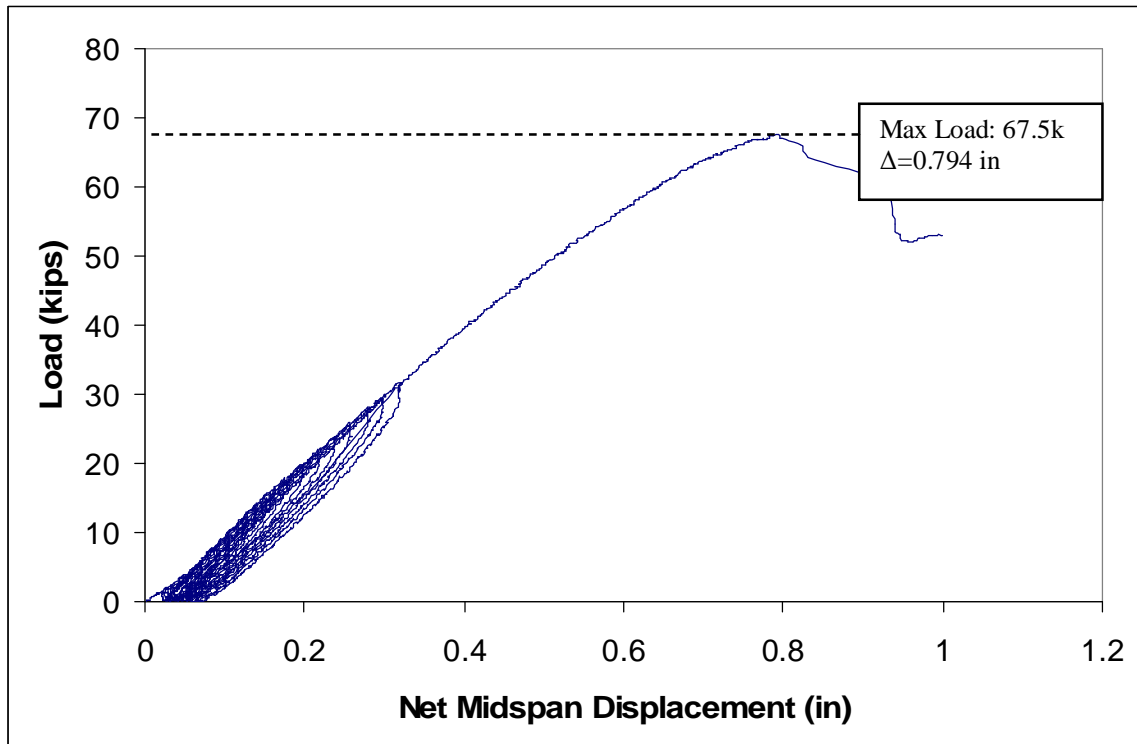


Figure 4.40. Deck 1 Load vs. Displacement.

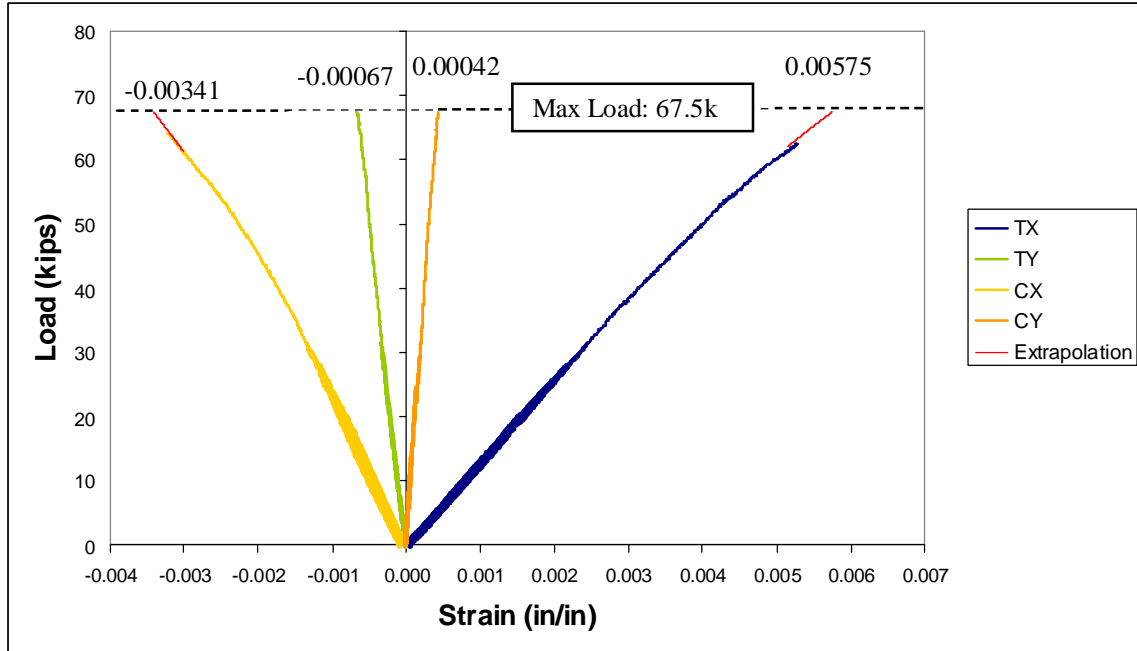


Figure 4.41. Deck 1 Load vs. Strain.

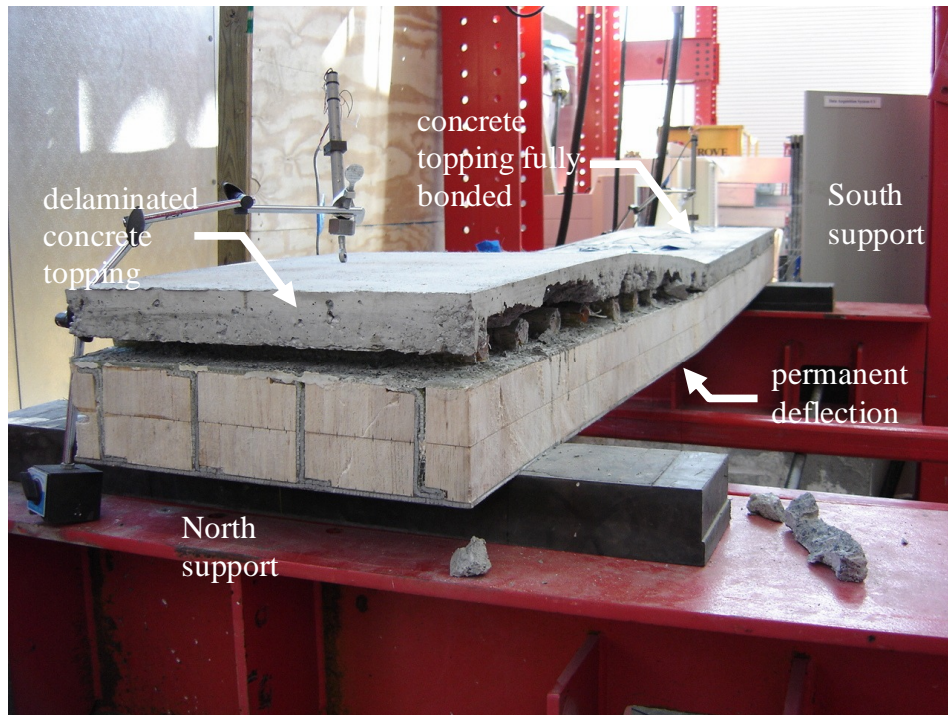


Figure 4.42. Deck 2 concrete delamination and permanent deformation.

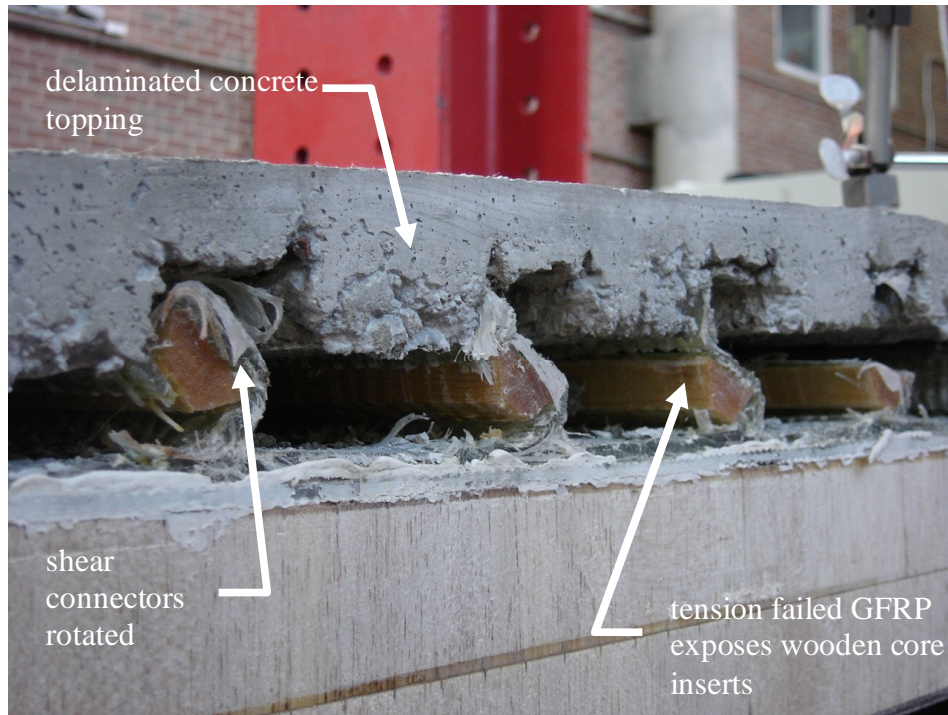


Figure 4.43. Deck 2 shear connector failure and concrete delamination.

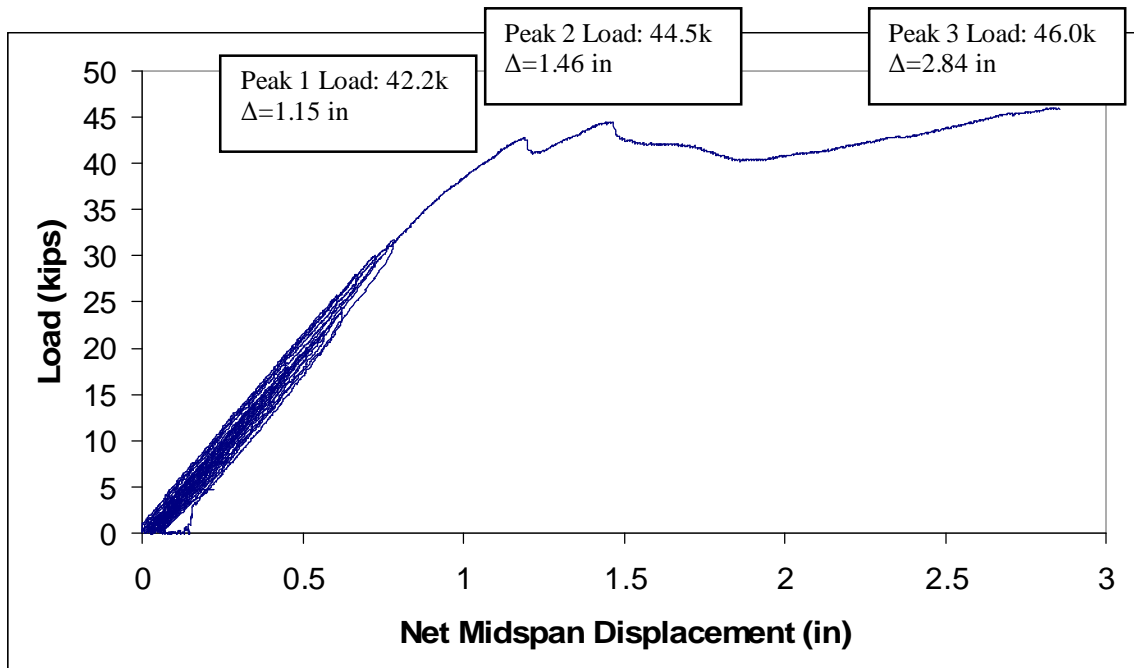


Figure 4.44. Deck 2 Load vs. Displacement.

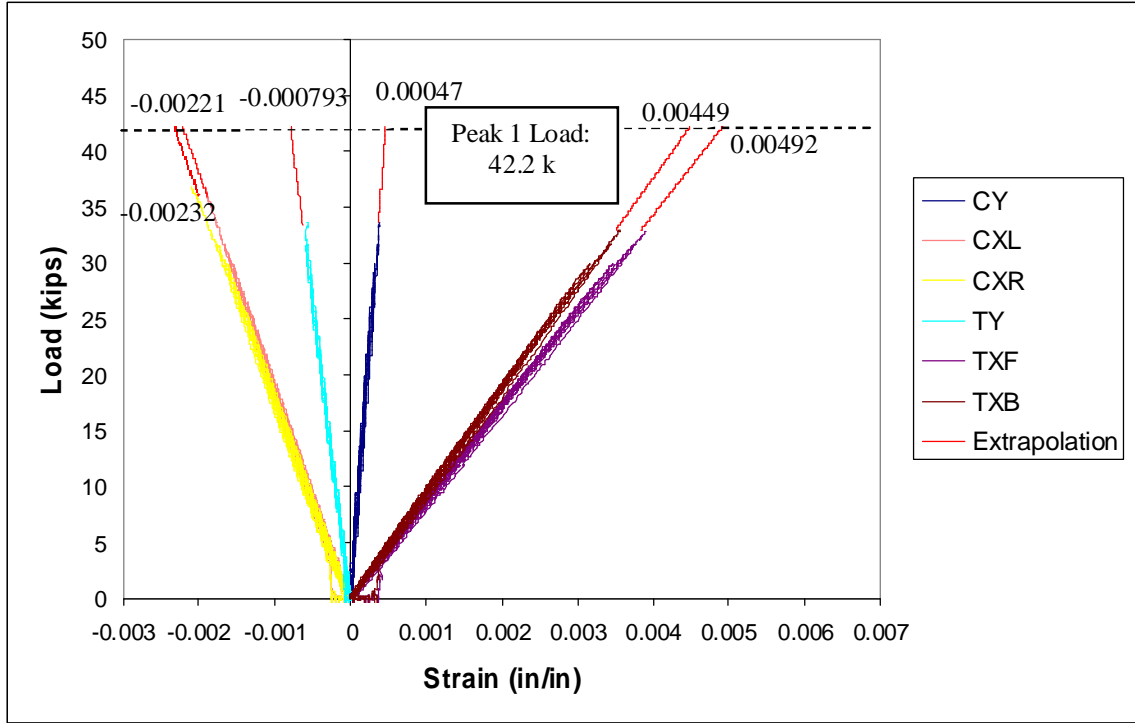


Figure 4.45. Deck 2 Load vs. Strain at 1st Peak Load.

Chapter 5. Analysis and Discussion

This chapter discusses three analysis approaches performed to predict the behavior of the decks: simple beam analysis, calculation of the flexural rigidity, and modeling using finite element analysis. The key assumptions, validity of these assumptions, and differences between predicted and observed test results are described.

Both decks were analyzed using three different approaches. For each approach, the decks were analyzed at 20 percent of the maximum load. This load has been selected since the level is typically used by designers for bridge decks. This large factor of safety accounts for the uncertainty in material properties, the brittle nature of FRP failure, and the susceptibility of glass to creep rupture for sustained loading. The same load was selected to be the maximum load level for testing under cyclic loading conditions. The overall behavior of the deck in this range is linearly elastic.

The first analytical approach was undertaken to predict the applied load corresponding to the maximum strain measured during this loading cycle of the bridge. This analysis is based on satisfying strain compatibility and equilibrium equations. The second approach used the measured deflection to estimate the overall flexural rigidity, EI , for the decks. This approach is based on a transformed section analysis similar to the approach used in any composite material section. The third approach was based on finite element simulation of the bridge deck to predict the behavior using a commercially available software program ANSYS. A discussion of the assumptions in each approach and their validity are provided in the following sections.

5.1 Beam Analysis Approach

This approach assumed a specified strain in the concrete equal to the strain measured by a strain gage attached to the top surface of the concrete, parallel to the span direction. Based on the assumption of plane sections remaining plane after deformation, other strains are determined from equilibrium assuming a linear strain distribution and are compared to measured experimental values. The corresponding stresses are assumed to be linearly proportional to the strain to determine the internal moment capacity at the measured strain selected. The following section illustrates the calculations for the internal moment of Deck 1.

5.1.1 Deck 1

The cross section of Deck 1 is shown in Figure 5.1. All distances shown are in inches.

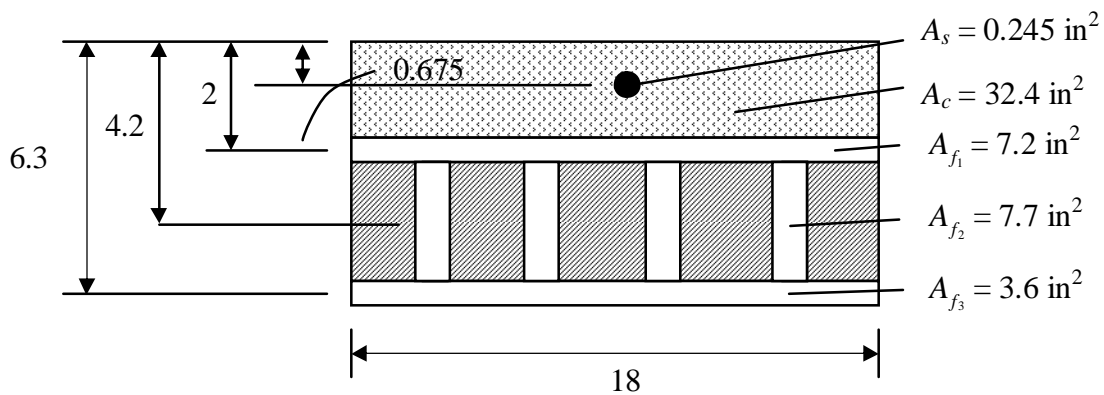


Figure 5.1. Assumed Geometry of Deck Cross-Section.

The initial location of the neutral axis is assumed to be within the GFRP top skin layer. This assumes the upper portion of the top GFRP skin is in compression and the lower portion is in tension. The distance from the top of the concrete topping to the neutral axis is labeled c , as shown in Figure 5.2. Assuming plane sections remain plane, the

following strain and equilibrium diagrams are established. The concrete stress is also assumed to vary linearly. This is considered to be a very close approximation based upon the measured material properties from the concrete cylinder results at the selected strain value. The stress in the balsa cores is also assumed to vary linearly. Based on integration of the stress diagrams at each portion, the internal forces are located at the centroid of each particular area. Through an iterative analysis process, the final location of the neutral axis was found to be within the top GFRP skin.

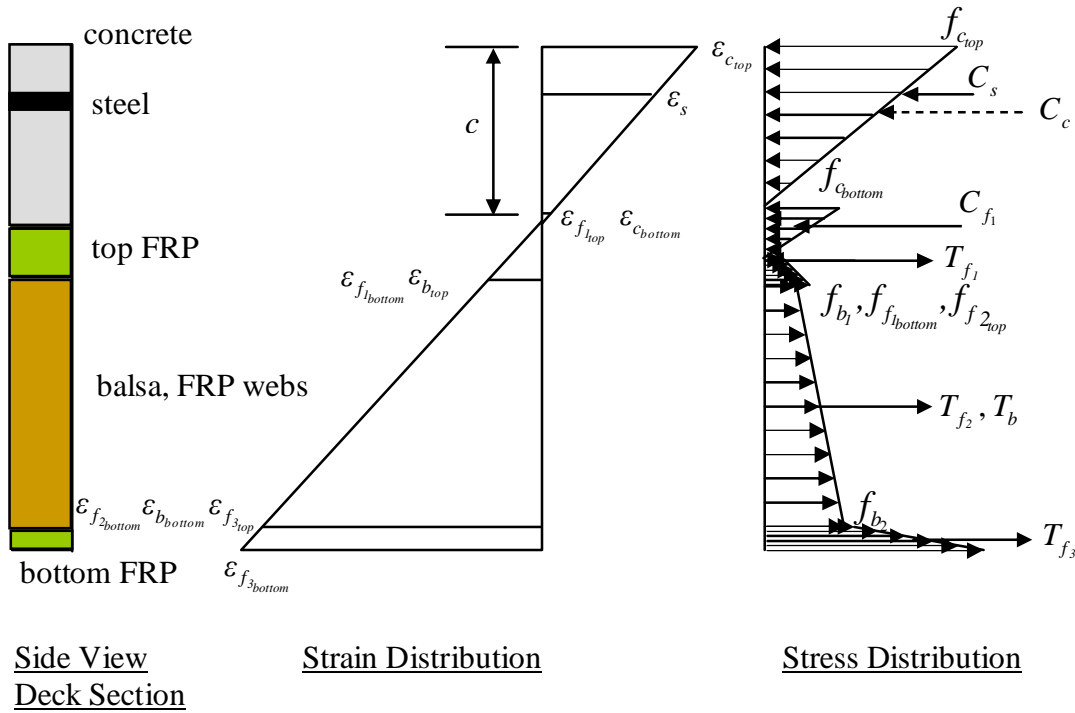


Figure 5.2. Strain and stress variations over cross-section.

From similar triangles on strain diagram:

$$\frac{e_{c_{top}}}{c} = \frac{e_{c_{bottom}}}{c-1.8} = \frac{e_s}{c-0.675} = \frac{e_{f_{1top}}}{c-1.8} = \frac{e_{f_{1bottom}}}{2.2-c} = \frac{e_{f_{2top}}}{2.2-c} = \frac{e_{f_{2bottom}}}{6.2-c}$$

$$= \frac{e_{f_{3top}}}{6.2-c} = \frac{e_{f_{3bottom}}}{6.4-c} = \frac{e_{b_{top}}}{2.2-c} = \frac{e_{b_{bottom}}}{6.2-c}$$

Some simplifications to the above equations may be introduced. For example, the location of the bottom of the concrete coincides with the top of GFRP 1. Assuming a perfect bond between the concrete and the GFRP, the strains must be equal, therefore:

$$\therefore e_{f_{1top}} = e_{c_{bottom}}$$

Similarly for other material boundaries, the following substitutions may be made:

$$e_{f_{1bottom}} = e_{b_{top}} = e_{f_{2top}}$$

$$e_{f_{2bottom}} = e_{b_{bottom}} = e_{f_{3top}}$$

Solving for each strain component in terms of the maximum concrete strain, $e_{c_{top}}$, the strain at each level can be found as the following:

$$e_{c_{bottom}} = \left(\frac{c-1.8}{c} \right) e_{c_{top}}$$

$$e_s = \left(\frac{c-0.675}{c} \right) e_{c_{top}}$$

$$e_{f_{1top}} = \left(\frac{c-1.8}{c} \right) e_{c_{top}}$$

$$e_{f_{1bottom}} = \left(\frac{2.2-c}{c} \right) e_{c_{top}}$$

$$e_{f_{2bottom}} = \left(\frac{6.2-c}{c} \right) e_{c_{top}}$$

$$e_{f_{3bottom}} = \left(\frac{6.4-c}{c} \right) e_{c_{top}}$$

Based on the dimensions of each section and the material properties, the forces at each zone can be determined as follows:

$$C_{c_{rect}} = A_c f_{c_{rect}} = A_c E_c e_{c_{bottom}} = (18)(1.8)(3310) \left(\frac{c-1.8}{c} \right) e_{c_{top}}$$

$$\begin{aligned} C_{c_{triangle}} &= \frac{1}{2} A_c (f_{c_{top}} - f_{c_{bottom}}) = \frac{1}{2} A_c (f_{c_{top}} - E_c e_{c_{bottom}}) \\ &= \left(\frac{1}{2} \right) (18)(1.8) \left[(3310) (e_{c_{top}}) - (3310) \left(\frac{c-1.8}{c} \right) e_{c_{top}} \right] \end{aligned}$$

$$C_s = A_s (E_s - E_c) e_s = (0.245437)(31330 - 3310) \left(\frac{c-0.675}{c} \right) (e_{c_{top}})$$

$$C_{f_1} = \frac{1}{2} A_{f_{1compression}} E_f e_{f_{1top}} = (c-1.8)(18)(3430) \left(\frac{c-1.8}{c} \right) (e_{c_{top}})$$

$$T_{f_1} = \frac{1}{2} A_{f_{1tension}} E_f e_{f_{1bottom}} = (2.2-c)(18)(3430) \left(\frac{2.2-c}{c} \right) (e_{c_{top}})$$

$$T_{f_{2rect}} = A_{f_2} E_f e_{f_{2top}} = (7.7)(3430) \left(\frac{2.2-c}{c} \right) (e_{c_{top}})$$

$$T_{f_{2triangle}} = \frac{1}{2} A_{f_2} E_f (e_{f_{2bottom}} - e_{f_{2top}}) = \left(\frac{1}{2} \right) (7.7)(3430) \left[\left(\frac{6.2-c}{c} \right) - \left(\frac{2.2-c}{c} \right) \right] (e_{c_{top}})$$

$$T_{f_{3rect}} = A_{f_3} E_f e_{f_{3top}} = (3.6)(3430) \left(\frac{6.2-c}{c} \right) (e_{c_{top}})$$

$$T_{f_{3triangle}} = \frac{1}{2} A_{f_3} E_f (e_{f_{3bottom}} - e_{f_{3top}}) = \left(\frac{1}{2} \right) (3.6)(3430) \left(\frac{6.4-c}{c} - \frac{6.2-c}{c} \right) (e_{c_{top}})$$

$$T_{b_{rect}} = A_b E_b e_{b_{top}} = (4)(16.4)(10) \left(\frac{2.2-c}{c} \right) (e_{c_{top}})$$

$$T_{b_{triangle}} = \frac{1}{2} A_b E_b (e_{b_{bottom}} - e_{b_{top}}) = \left(\frac{1}{2} \right) (4)(16.4)(10) \left[\left(\frac{6.2-c}{c} \right) - \left(\frac{2.2-c}{c} \right) \right] (e_{c_{top}})$$

For equilibrium:

$$C = T$$

$$C_{c_{rect}} + C_{c_{triangle}} + C_s + C_{f_1} = T_{f_1} + T_{f_{2_{rect}}} + T_{f_{2_{triangle}}} + T_{f_{3_{rect}}} + T_{f_{3_{triangle}}} + T_{b_{rect}} + T_{b_{triangle}}$$

Using $e_c = 0.00061045$, the depth of the compression zone, c , can be found:

$$c = 1.918 \text{ in.}$$

Therefore the neutral axis nearly coincides with the centroid of the top GFRP skin. Using the correct value of the compression zone, the forces can be determined as:

$$C_{c_{rect}} = 4.046 \text{ k}$$

$$C_{c_{triangle}} = 30.740 \text{ k}$$

$$C_s = 2.721 \text{ k}$$

$$C_{f_1} = 0.137 \text{ k}$$

$$T_{f_1} = 0.779 \text{ k}$$

$$T_{f_{2_{rect}}} = 2.366 \text{ k}$$

$$T_{f_{2_{triangle}}} = 16.808 \text{ k}$$

$$T_{f_{3_{rect}}} = 16.823 \text{ k}$$

$$T_{f_{3_{triangle}}} = 0.393 \text{ k}$$

$$T_{b_{rect}} = 0.059 \text{ k}$$

$$T_{b_{triangle}} = 0.417 \text{ k}$$

The internal moment of the section can be determined by summation about the neutral axis of the section, which is located 1.919 in. below the top concrete surface:

$$\begin{aligned} \sum M_{@NA} = & C_{c_{rect}} (c - 0.9) + C_{c_{triangle}} \left[c - \left(\frac{1}{3} \right) (1.8) \right] + C_s (c - 0.675) + C_{f_1} \left[\frac{2}{3} (c - 1.8) \right] + T_{f_1} \left(\frac{2}{3} \right) (2.2 - c) \\ & + T_{f_{2_{rect}}} (4.2 - c) + T_{f_{2_{triangle}}} \left(2.2 + \frac{2}{3} (4) - c \right) + T_{f_{3_{rect}}} (6.3 - c) + T_{f_{3_{triangle}}} \left(6.2 + \frac{2}{3} (0.2) - c \right) \end{aligned}$$

$$\begin{aligned}
 &+ T_{b_{rect}} (4.2 - c) + T_{b_{triangle}} \left(2.2 + \frac{2}{3} (4) - c \right) \\
 &= 179.95 \text{ k-in} \\
 &= 14.996 \text{ k-ft}
 \end{aligned}$$

The equation for the maximum bending moment for a simply supported beam with a distributed load applied at mid-span is given by AISC (2001) as:

$$M = R_1 \left(a + \frac{R_1}{2w} \right)$$

where

$$R_1 = \frac{wb}{2l} (2c + b)$$

And l is the span of the beam, a is the distance from the left support to the start of the distributed load, b is the width of the load, and c is the distance from the right support to the nearest edge of the distributed load. Solving for w gives 3.912 k/in, so solving for P gives 15.648 kips. To compare to the experimental results, the percent difference between the predicted and measured applied load can be evaluated as:

$$\begin{aligned}
 \text{Percent difference} &= \left| \frac{\text{Measured} - \text{Predicted}}{\text{Measured}} \right| \times 100\% \\
 &= \left| \frac{13.492 - 15.648}{13.492} \right| \times 100\% = 16.0\%
 \end{aligned}$$

Based on the predicted moment, the strain at the bottom of the GFRP, $e_{f_3_{bottom}}$, was also predicted and found to be 0.001426, which is different by 32 percent from the measured value of 0.001078.

The difference may be attributed to the discrepancy of the measured material properties of the GFRP skins, possible stress concentrations, and/or the orientation of the

attached strain gage. Due to material and fabrication constraints, the elastic modulus from the material properties tests were determined from separate decks than those tested for this thesis. Although the fiber architecture and infusion process were identical, the nature of the vacuum infusion process allows limited quality control. Some regions of the skins are wetted with more resin than other regions. As the resin is setting, gravity tends to draw excess resin to the bottom of the deck. For the internal moment of the section to correspond to the external moment due to the applied loads, the required elastic modulus of the GFRP should be equal to 2620 ksi. Using this elastic modulus results in a 33.4% difference in the longitudinal FRP strain. This corresponds to a total fiber volume fraction of 0.45. The warp direction fiber volume fraction required is 0.31 of the entire composite.

5.1.2 Deck 2

The same process is repeated for Deck 2. The first peak load is calculated based on the measured concrete strain, $\varepsilon_{c_{top}}$ of 0.0005236. Similar to Deck 1, the neutral axis lies within the top GFRP skin. All materials are assumed linear elastic up to the selected condition.

$$C_{c_{rect}} = A_c f_{c_{rect}} = A_c E_c e_{c_{bottom}} = (18)(1.8)(3940) \left(\frac{c-1.8}{c} \right) e_{c_{top}}$$

$$C_{c_{triangle}} = \frac{1}{2} A_c (f_{c_{top}} - f_{c_{bottom}}) = \frac{1}{2} A_c (f_{c_{top}} - E_c e_{c_{bottom}})$$

$$= \left(\frac{1}{2} \right) (18)(1.8) \left[(3310)(e_{c_{top}}) - (3940) \left(\frac{c-1.8}{c} \right) e_{c_{top}} \right]$$

$$C_s = A_s (E_s - E_c) e_s = (0.245437)(31330 - 3940) \left(\frac{c-0.675}{c} \right) (e_{c_{top}})$$

$$C_{f_1} = \frac{1}{2} A_{f_1 \text{compression}} E_f e_{f_1 \text{top}} = (c - 1.8)(18)(3430) \left(\frac{c - 1.8}{c} \right) (e_{c_{top}})$$

$$T_{f_1} = \frac{1}{2} A_{f_1 \text{tension}} E_f e_{f_1 \text{bottom}} = (2.2 - c)(18)(3430) \left(\frac{2.2 - c}{c} \right) (e_{c_{top}})$$

$$T_{f_2 \text{rect}} = A_{f_2} E_f e_{f_2 \text{top}} = (7.7)(3430) \left(\frac{2.2 - c}{c} \right) (e_{c_{top}})$$

$$T_{f_2 \text{triangle}} = \frac{1}{2} A_{f_2} E_f (e_{f_2 \text{bottom}} - e_{f_2 \text{top}}) = \left(\frac{1}{2} \right) (7.7)(3430) \left[\left(\frac{6.2 - c}{c} \right) - \left(\frac{2.2 - c}{c} \right) \right] (e_{c_{top}})$$

$$T_{f_3 \text{rect}} = A_{f_3} E_f e_{f_3 \text{top}} = (3.6)(3430) \left(\frac{6.2 - c}{c} \right) (e_{c_{top}})$$

$$T_{f_3 \text{triangle}} = \frac{1}{2} A_{f_3} E_f (e_{f_3 \text{bottom}} - e_{f_3 \text{top}}) = \left(\frac{1}{2} \right) (3.6)(3430) \left(\frac{6.4 - c}{c} - \frac{6.2 - c}{c} \right) (e_{c_{top}})$$

$$T_{b_{\text{rect}}} = A_b E_b e_{b_{\text{top}}} = (4)(16.4)(10) \left(\frac{2.2 - c}{c} \right) (e_{c_{top}})$$

$$T_{b_{\text{triangle}}} = \frac{1}{2} A_b E_b (e_{b_{\text{bottom}}} - e_{b_{\text{top}}}) = \left(\frac{1}{2} \right) (4)(16.4)(10) \left[\left(\frac{6.2 - c}{c} \right) - \left(\frac{2.2 - c}{c} \right) \right] (e_{c_{top}})$$

Based on equilibrium of the section:

$$C = T$$

$$C_{c_{\text{rect}}} + C_{c_{\text{triangle}}} + C_s = T_{f_1} + T_{f_2 \text{rect}} + T_{f_2 \text{triangle}} + T_{f_3} + T_{b_{\text{rect}}} + T_{b_{\text{triangle}}}$$

and using $e_{c_{top}}$ of 0.0005236, the depth of the compression zone, c , for Deck 2 was found

to be 1.816 in., which is located within the top GFRP skin. Using the depth of the

compression zone of 1.816, the internal forces were determined as follows:

$$C_{c_{\text{rect}}} = 0.575 \text{ k}$$

$$C_{c_{\text{triangle}}} = 33.099 \text{ k}$$

$$C_s = 2.211 \text{ k}$$

$$C_{f_i} = 0.002 \text{ k}$$

$$T_{f_1} = 1.315 \text{ k}$$

$$T_{f_{2_{\text{rect}}}} = 2.927 \text{ k}$$

$$T_{f_{2_{\text{triangle}}}} = 15.229 \text{ k}$$

$$T_{f_{3_{\text{rect}}}} = 15.609 \text{ k}$$

$$T_{f_{3_{\text{triangle}}}} = 0.356 \text{ k}$$

$$T_{b_{\text{rect}}} = 0.073 \text{ k}$$

$$T_{b_{\text{triangle}}} = 0.378 \text{ k}$$

Summing the internal forces about the neutral axis, the internal predicted moment,

$M_{\text{predicted}}$, can be calculated as:

$$\begin{aligned} \sum M_{\text{@ NA}} &= C_{c_{\text{rect}}} (c - 0.9) + C_{c_{\text{triangle}}} \left[c - \left(\frac{1}{3} \right) (1.8) \right] + C_s (c - 0.675) + C_{f_i} \left[\frac{2}{3} (c - 1.8) \right] + T_{f_1} \left(\frac{2}{3} \right) (2.2 - c) \\ &\quad + T_{f_{2_{\text{rect}}}} (4.2 - c) + T_{f_{2_{\text{triangle}}}} \left(2.2 + \frac{2}{3} (4) - c \right) + T_{f_{3_{\text{rect}}}} (6.3 - c) + T_{f_{3_{\text{triangle}}}} \left(6.2 + \frac{2}{3} (0.2) - c \right) \\ &\quad + T_{b_{\text{rect}}} (4.2 - c) + T_{b_{\text{triangle}}} \left(2.2 + \frac{2}{3} (4) - c \right) \\ &= 170.0 \text{ k-in} \\ &= 14.17 \text{ k-ft} \end{aligned}$$

For a span of 7.0 ft and a distributed load, w of 2.073 k/in, the total predicted load was found to be 8.29 kips, which is only 9.9 percent different from the measured value, 9.2 kips. The corresponding predicted strain in the bottom GFRP layer was found to be 0.001322, which is about 25 percent different from the measured value of 0.001051. To

satisfy equilibrium and for the internal stresses to correspond to the measured applied load, the analysis indicates that required elastic modulus should be 4770 ksi. Using this elastic modulus results in a 6.6% difference in the FRP strain. This corresponds to a total fiber volume fraction of 0.63. The warp direction fiber volume fraction required is 0.44 of the entire composite.

5.2 Prediction of the Flexural Rigidity of the Deck

This analytical approach used the measured deflections to predict the overall flexural rigidity of the proposed bridge deck. The properties of the deck cross-section are heterogeneous as it is composed of four main materials: concrete, balsa wood, steel, and GFRP. Therefore, Bernoulli Euler Beam Theory and mechanics of materials cannot be applied directly to find an equivalent flexural rigidity, EI . To determine an “equivalent flexural rigidity” for the deck cross-section, the materials must be converted to an equivalent area of one common material. This approach is called a transformed section analysis. The area of each component is scaled by the ratio of the moduli of elasticity of that material to the common material. This ratio is called the modular ratio. Once all areas have been converted to an equivalent area of one material having the same modulus of elasticity, a neutral axis for the entire section and the flexural rigidity can be determined.

For the decks under consideration, all materials were converted to equivalent areas of balsa wood, the most flexible material within the cross-section. The calculations for both decks are shown in the following sections.

5.2.1 Deck 1

The results of the transformed section analysis are shown in Table 5.1 and Table 5.2.

The elastic modulus values are taken from the material properties tests. The modular ratio, n , is the ratio of the elastic modulus of each material to the elastic modulus of the transformed material, balsa. The area, A , is the cross-sectional area of each material in the actual deck. The equivalent balsa area, A_e , converts the area of each material to an area of balsa which would provide an equivalent force contribution.

The equivalent balsa area is found for the concrete as:

$$A_e = nA = (331)(32.4) = 10734 \text{ in}^2$$

However, the case of the steel is slightly different. The steel area is also encompassed within the calculated concrete area. To avoid accounting for the same area twice, the equivalent balsa area for the steel is calculated as:

$$A_e = \left(\frac{E_s}{E_b} \right) A_s - \left(\frac{E_c}{E_b} \right) A_s = (n_s - n_c) A_s = (3133 - 331)(0.245437) = 687.7 \text{ in}^2$$

The moment of inertia of each material about its own neutral axis is shown as I_o . This value is calculated as:

$$I_o = \frac{\pi r^4}{4} \text{ for circular sections where } r \text{ is the radius}$$

This applies to the steel reinforcement only.

$$I_o = \frac{bh^3}{12} \text{ for rectangular sections where } b \text{ is the width and } h \text{ is the height}$$

This equation applies to all other materials used. The moment of inertia of each component is converted to an equivalent balsa moment of inertia using the modular ratio.

The equivalent balsa inertia of the concrete is calculated as:

$$nI_o = (331)(8.748) = 2898 \text{ in}^4$$

The value y in Table 5.1 is the distance from the top of the deck to the centroid of each material. The product $A_e y$ is given as it is used to calculate the neutral axis of the transformed section. The distance from the top of the cross-section to the neutral axis of the transformed section is \bar{y} and is calculated as:

$$\bar{y} = \frac{\sum A_e y}{\sum A_e} = \frac{34211}{17903} = 1.911 \text{ in. from top to neutral axis}$$

The value d given in Table 5.2 is the distance from the neutral axis of the section to the centroid of each component. The value d is calculated as:

$$d = \bar{y} - y$$

The next quantity shown in Table 5.2 is derived from the parallel axis theorem. This term, $A_e d^2$, constitutes the majority of the transformed moment of inertia. According to the parallel axis theorem, the total inertial contribution of each component, I_t , is the sum of the moment of inertia, nI_o , for each component plus the Ad^2 term. The total transformed inertia for the entire cross-section is the sum of all I_t terms.

The flexural rigidity, EI_t , is the product of the elastic modulus of the balsa and the balsa equivalent transformed moment of inertia for the section, I_t :

$$E_b I_t = (55977)(10) = 559766 \text{ k-in}^2$$

The deflection formula for a simply supported beam with a point load applied at the mid-span is derived from Bernoulli-Euler Beam Theory. The predicted deflection, Δ_p , at this state of loading is given as:

$$\Delta_p = \frac{PL^3}{48EI_t} = \frac{(13.4922)(4 \times 12)^3}{(48)(559766)} = 0.0555 \text{ in.}$$

The predicted mid-span deflection at this state of loading for Deck 1 is 48.8 percent different from the measured value of 0.1085 in. To match the measured deflection, the required elastic modulus of the GFRP was found to be 1410 ksi.

The influence of shear deformation should not be neglected in order to accurately predict the behavior of the deck panels. However, no theories have been currently developed which can be applied directly to panels similar to the one under consideration. The sandwich theory assumes the two FRP skins which are separated by a core material are of equal thickness and identical material. The compression skin of the deck in this research consists of both concrete and FRP and the combined thickness of these materials is nine times thicker than the tension skin. Also, the core is not a homogeneous material, as is assumed by the theory. The majority of the volume of the core consists of balsa. The majority of the shear stiffness is assumed to be derived from the continuous overlapping FRP shear webs.

In this section, the sandwich theory is applied to the panels to provide an approximation of the deflections which account for the shear deformation. Some modifications must be made to the deflection equation. The deflection due to shear deformation is given by Allen (1969) as:

$$\Delta_s = \frac{PL}{4AG},$$

where

$$A = \frac{bd^2}{c}$$

and P is the applied load, b is the width of the panel, L is the length of the span, d is the distance between the centerlines of the tension and compression skins, c is the thickness of the core material, and G is the shear modulus of the core.

The modifications to this theory are based on proportioning the shear modulus of the core according to the volume fractions of the GFRP and balsa. The thickness of the compression skin is assumed to be the total thickness of the top skin of GFRP and the concrete. Using these modifications, the theory was used for the following parameters:

$$b = 18 \text{ in}$$

$$d = 5.2 \text{ in}$$

$$c = 4 \text{ in}$$

$$A_c = 32.4 \text{ in}^2$$

$$A_f = 18.5 \text{ in}^2$$

$$A_b = 64.3 \text{ in}^2$$

$$A_{\text{total}} = 115.2 \text{ in}^2$$

$$G_f = 1320 \text{ ksi}$$

$$G_b = 14 \text{ ksi}$$

$$G = \frac{G_f A_f + G_b A_b}{A_f + A_b} = \frac{(1320)(18.5) + (14)(64.3)}{18.5 + 64.3} = 305.8 \text{ ksi}$$

$$A = \frac{bd^2}{c} = \frac{(18)(5.2)^2}{4} = 121.68$$

$$\Delta_s = \frac{PL}{4GA} = \frac{(13.4922)(48)}{4(305.8)(121.68)} = 0.0044 \text{ in.}$$

The total deflection including the contribution from bending and from shear is given by

$$\Delta_{\text{total}} = \Delta_b + \Delta_s = 0.0555 + 0.0044 = 0.0599 \text{ in.}$$

The percent difference between the predicted total deflection including shear deformation and the measured deflection is 44.8 percent. Using the same approach and assuming the all other material properties are constant, the required shear modulus of the core to match the measured is 25 ksi.

5.2.2 Deck 2

The same transformed section analysis was applied to Deck 2. The only differences between Deck 1 and Deck 2 are the elastic modulus of the concrete and the deck span. Table 5.3 shows the transformed section properties and Table 5.4 shows the final results from the parallel axis theorem applied to Deck 2.

The transformed flexural rigidity, EI_t , of the Deck 2 section is 58352 k-in². The state of loading selected is also 20% of the maximum load for Deck 2. The corresponding load was 9.199 kips. The predicted deflection, Δ_p , was calculated as:

$$\Delta_p = \frac{PL^3}{48EI_t} = \frac{(9.199)(7 \times 12)^3}{(48)(58352)} = 0.1947 \text{ in.}$$

The predicted mid-span deflection at this state of loading of Deck 2 is 0.1947 in., which is 14 percent different from the measured value of 0.2262 in. To match the measured deflection, the required elastic modulus of the GFRP should be 2790 ksi.

The same approach to account for the shear deformation as described for the first deck is applied to the second deck. For the given load of 9.199 kips, the predicted deflection due to shear, Δ_s , can be estimated as:

$$\Delta_s = \frac{PL}{4GA} = \frac{(9.199)(84)}{4(305.8)(121.68)} = 0.0052 \text{ in.}$$

The total deflection including the contribution from bending and from shear is given by

$$\Delta_{\text{total}} = \Delta_b + \Delta_s = 0.1942 + 0.0052 = 0.1994 \text{ in.}$$

The predicted deflection, accounting for the shear deformation is about 11.8 percent different from the measured value. Using the same approach and assuming all other material properties are constant to match the measured deflection, the required shear modulus of the core should be 50 ksi.

5.2.3 Discussion

The predicted flexural rigidity of Deck 2 is much more reasonable than for Deck 1. The percent difference for Deck 1 is four times larger than the percent difference of Deck 2. The largest factors for this difference are the higher influence of shear deformation on the shorter span Deck 1, the variation in material properties of the GFRP due to the nature of the vacuum infusion process, and the influence of the seating of the deck on the neoprene pad.

The span-to-depth ratio of Deck 1 is 7.5 compared to the span-to-depth ratio of Deck 2 which is 13. Note that the shear deformation is accounted for, but not with great accuracy. In both cases, the predicted deflection is lower than the experimental. If shear deformation were better quantified, the predicted deflections would increase and more closely approximate the experimental deflections. The approximation of the deflection due to shear deformation using sandwich theory is admittedly crude. The prediction tends to underestimate the shear deformation by assuming that the GFRP shear webs and the balsa cores develop the same shear strain. The bond between these two materials is not perfect and the influence of the slippage is magnified on the first deck which has a smaller shear span-to-depth ratio.

It should also be noted that the shear connectors prevent the assumed solid concrete topping from being a fully accurate representation. Due to the fabrication process, small voids were created between the infused shear connector fabric and the tapered wooden cores. These voids lowered the stiffness of the concrete as the deck was loaded, allowing a higher deflection than if the topping was exclusively concrete as assumed.

The above analysis suggests that the range of the elastic modulus of the 3-D woven GFRP material ranges between 1400 and 3000 ksi.

5.3 Finite Element Approach

The final approach used in this research was based on finite element analysis. The purpose of the finite element model was to compare to the measured results and the hand calculation approaches. The finite element model is expected to account for more intricate modeling including material properties and the geometry of the joints which cannot be easily performed by the simple analysis approach.

5.3.1 Assumptions

There were a number of key assumptions which were made in order to create the finite element model. These assumptions include:

- The shear connectors provide complete composite action. However, it should be mentioned that the shear connectors are not modeled. A solid concrete topping is modeled atop the deck with a thickness of 1.8 in.
- The rigid HSS, or steel tube, used to distribute the load to the wearing surface spanned the entire width of the deck, preventing two-way bending. The load applied through the HSS was modeled as a uniform area load at mid-span, although in reality a higher load was distributed at the edges of the HSS than at the exact mid-span due to the curvature of the deck.
- An essential goal of finite element modeling is to create a convergent model. Concentrated loads or supports cause stress concentrations. Therefore, the simple support conditions could not be modeled with a simple pin and roller condition. The simple supports were indirectly modeled using a symmetry boundary condition at the mid-span and an antisymmetry boundary condition at the support. The symmetry boundary condition allows movement in the vertical direction but

- allows no rotation or lateral movement. The antisymmetry boundary condition allows rotation of the cross-section but prevents movement in the vertical direction. No axial reaction can develop at the antisymmetry plane. The application of the antisymmetry boundary condition essentially imposes a roller support without the consequence of creating a stress concentration. This assumption is not truly valid, but is a rough approximation. This condition ignores crushing of the deck at the support, but the crushing effect is assumed small compared to the deformation due to bending.
- The horizontal layer of fabric from the shear connectors is assumed to cover the entire 18 in. width and entire length of the deck. The actual edge of this fabric was offset from the edge of the deck by up to 0.5 in. However, this fabric was very close to the neutral axis so this assumption has negligible effect on the stiffness of the deck.
 - The pin location for the simply supported boundary conditions is located at the interior face of support. The decks lifted up off the exterior edge of the neoprene pad supports, increasingly towards failure. While the true pin location was somewhere between the middle of the support and the face of support, the difference in displacement is minimal.
 - Perfect bond is attained between concrete and GFRP. This assumption was not valid at failure due to the inability of the GFRP shear connectors to transfer the load from the topping to the deck. However, the goal of this model was to compare elastic behavior, so this assumption was valid for this model.

- Concrete can be modeled as an isotropic material using the elastic modulus from the compressive strength cylinder tests.
- Composite GFRP can be represented by a linear elastic homogeneous material. According to experimental test data for modulus of elasticity, the average experimental value was used. The modulus of elasticity in compression of GFRP would actually be less than the modulus of elasticity for tension, but no separate compression modulus was specified.
- GFRP can be represented as an orthotropic material. Tensile coupon test results were used for the warp and weft direction properties. The z-direction properties are derived in Appendix A.
- Balsa does not contribute significantly to the stiffness of the deck. The primary functions of the balsa were to provide a form for the GFRP during the infusion process, ensure a composite behavior between the two GFRP skins, and prevent buckling of GFRP in compression.

3.3.2 Mathematical Model

The mathematical models for Deck 1 and Deck 2 are shown in Figure 5.3 and Figure 5.4, respectively. The width of the distributed load is modeled. The supports are not modeled over a finite width. Instead, the pin location is assumed at the face of the support.

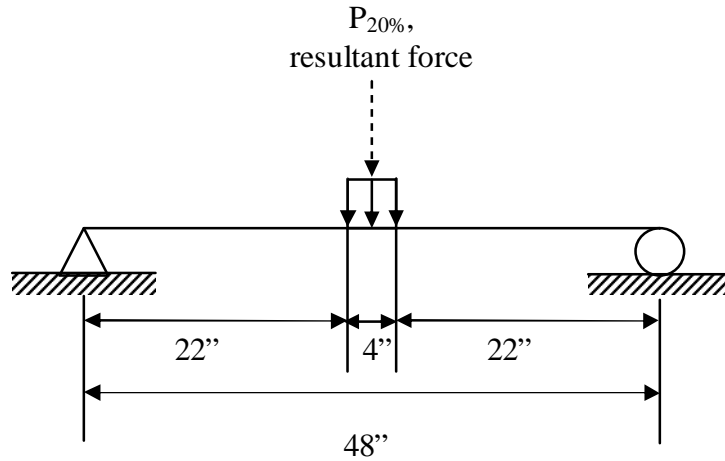


Figure 5.3. Mathematical model for Deck 1.

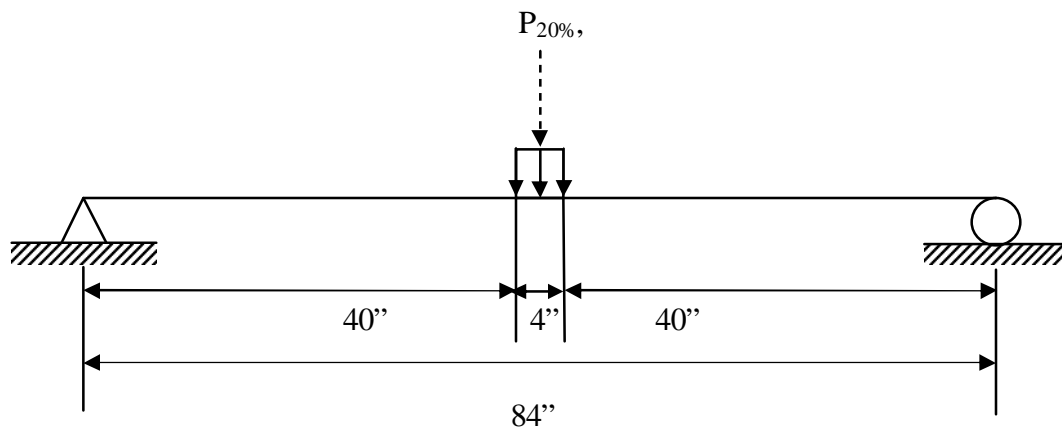


Figure 5.4. Mathematical model for Deck 2.

5.3.3 ANSYS Modeling

The finite element software ANSYS 9.0 was selected for modeling. The finite element type selected to represent each material was SOLID185, an 8-noded brick element with three translational degrees of freedom at each node. The same element type was selected in order to ensure compatibility between elements. A linear elastic analysis was performed to determine the mid-span deflection at 20 percent of the maximum load for both decks. The initial mesh had a characteristic element length of 1 inch wherever possible. For the two subsequent mesh refinements, the element size was reduced by one half.

5.3.4 Factors Affecting the Finite Element Modeling

Prediction of the behavior using the finite element approach could be significantly affected by one or more of the following reasons:

- Inexact measurement of dimensions
- Modeling the concrete topping as a homogeneous layer assuming perfect load transfer, neglecting shear connectors
- Considering the applied load as an evenly distributed load
- Considering the effect of the supports at a point located at the edge of the clear span
- Misalignment and inaccurate location of the strain gages and measuring devices
- Inaccuracy of the measured material properties

5.3.5 Convergence Study

The mesh was adequately refined to achieve convergence of subsequent trials within one percent. The results of the different meshes for these two decks are shown in Table 5.5. Similar to the previous two approaches, the percent difference of the measured deflection

for Deck 1 was 36.5 percent, which is much higher than the 5.9 percent difference for Deck 2. The deflected shape for Deck 1 using a one inch mesh size and a 0.25 inch mesh size are shown in Figure 5.5 and Figure 5.6, respectively. The deflected shape for Deck 2 using a one inch and a 0.25 inch mesh size are shown in Figure 5.7 and Figure 5.8, respectively.

Results of the finite element modeling match the same trend determined by the simple analytical approach. The results suggest that, for typical bridge spans such as the span of 7 ft. used for Deck 2, both analytical approaches can be used fairly well to determine the response. The behavior for short spans, such as for Deck 1, is significantly affected by other factors, such as shear deformation and is complex. Further analysis is required to understand the behavior and is beyond the scope of this thesis. It should be noted also that the behavior is greatly affected by the fabrication process, which was evident in these pilot research specimens and contributed to the large discrepancies obtained from the analytical approaches in comparison to the measured values.

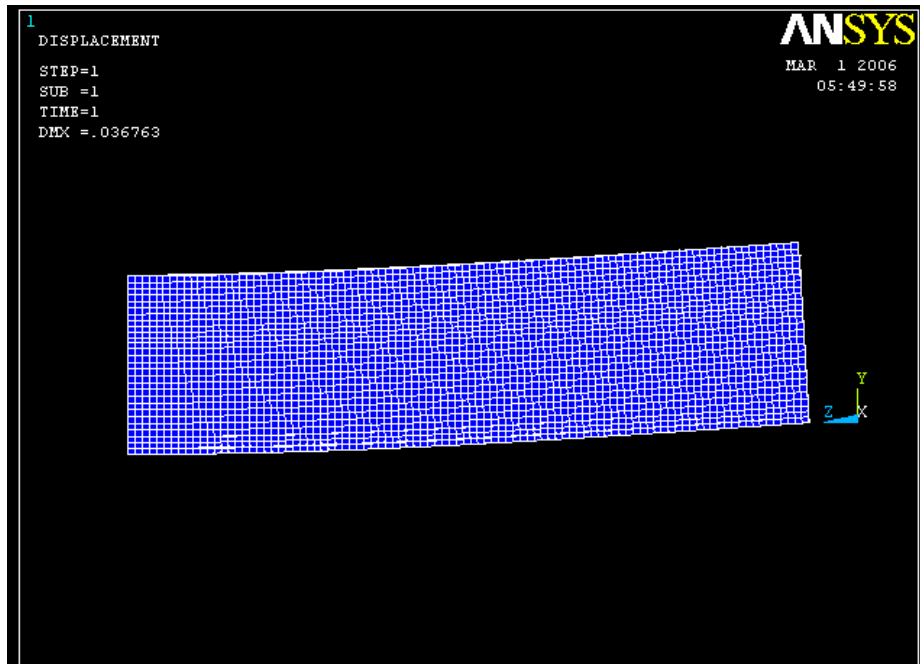


Figure 5.5. Side view of Deck 1 symmetry and antisymmetry conditions.

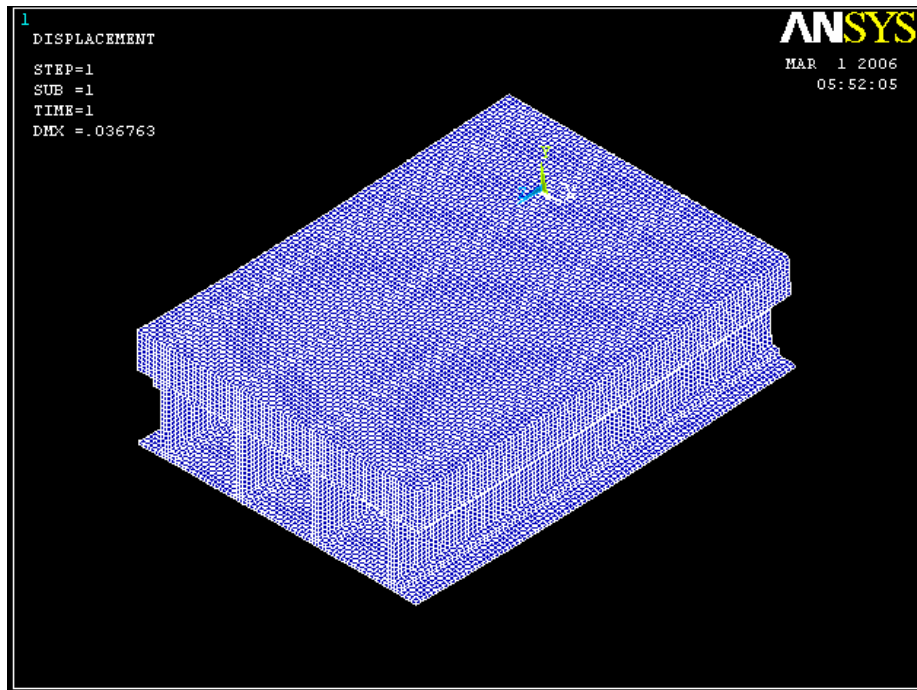


Figure 5.6. Deck 1 deflected shape with 0.25 inch mesh size.

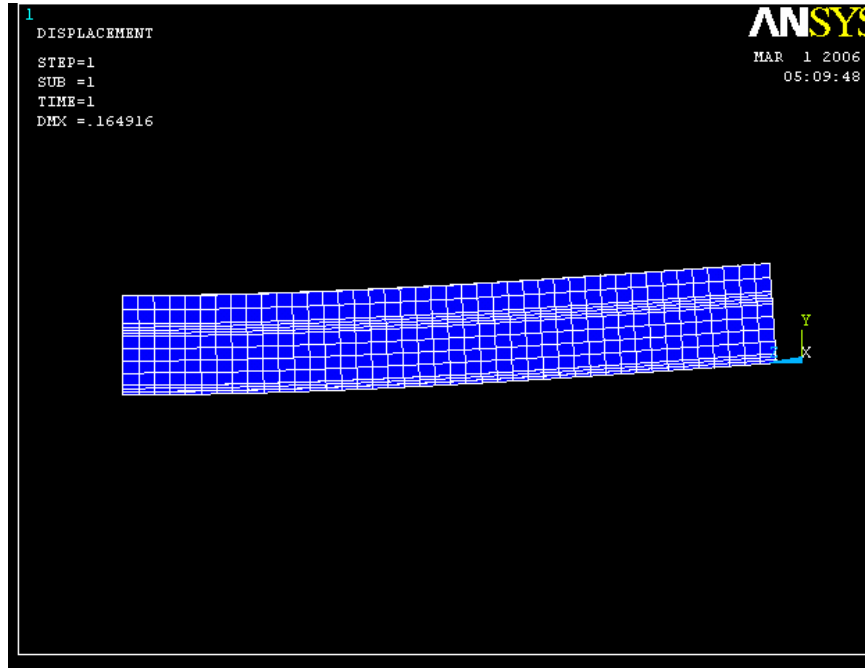


Figure 5.7. Side view of Deck 2 symmetry and antisymmetry conditions.

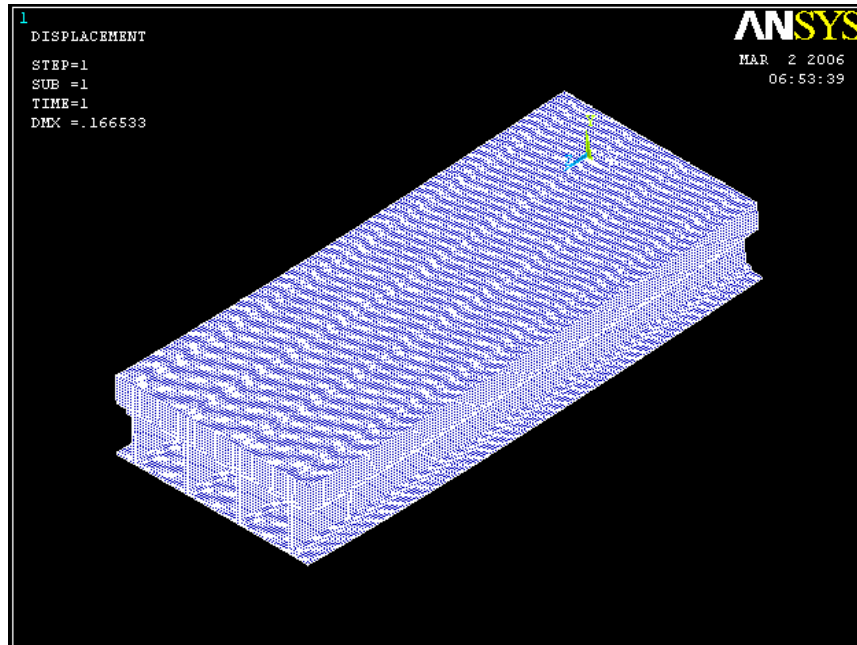


Figure 5.8. Isometric view of Deck 2 with 0.25 inch mesh.

Table 5.1. Deck 1 transformed section properties.

Material	Elastic Modulus E (ksi)	Modular Ratio n	Area A (in ²)	Equivalent Balsa Area A_e (in ²)	I_o (in ⁴)	y from top (in)	$A_e y$ (in ³)
Concrete	3313	331	32.4	10734	8.748	0.9	9661
Steel	31330	3133	0.245437	768	0.00096	0.675	519
Balsa	10	1	65.6	65.6	87.467	4.2	276
FRP1	3430	343	7.2	2470	0.096	2	4939
FRP2	3430	343	7.7	2633	8.533	4.2	11060.3
FRP3	3430	343	3.6	1231	0.012	6.3	7757
Total				17902			34210

Table 5.2. Deck 1 parallel axis theorem properties.

Material	d (in)	Transformed $A_e d^2$ (in ⁴)	Transformed Inertia nI_o (in ⁴)	Total Transformed Inertia I_t (in ⁴)
Concrete	1.011	10971	2898	13870
Steel	1.236	1174	3	1177
Balsa	-2.289	344	87	431
FRP1	-0.089	20	33	52
FRP2	-2.289	13798	297	16724
FRP3	-4.389	23717	4	23721
Total		50024	5953	55976

Table 5.3. Deck 2 transformed section properties.

Material	Elastic Modulus E (ksi)	Modular Ratio n	Area A (in ²)	Equivalent Balsa Area A_e (in ²)	I_o (in ⁴)	\bar{y} from top (in)	$A\bar{y}$ (in ³)
Concrete	3937	394	32.4	12756	8.748	0.9	11480
Steel	31330	3133	0.245437	768	0.00096	0.675	519
Balsa	10	1	65.6	66	87.467	4.2	276
FRP1	3430	343	7.2	2470	0.096	2	4939
FRP2	3430	343	7.7	2641	8.533	4.2	11093
FRP3	3430	343	3.6	1235	0.012	6.3	7779
Total				19935			36085

Table 5.4. Deck 2 parallel axis theorem properties.

Material	d (in)	Transformed $A_e d^2$ (in ⁴)	Transformed Inertia nI_o (in ⁴)	Total Transformed Inertia $nI_o + A_e d^2$ (in ⁴)
Concrete	0.910	10566	3444	14010
Steel	1.135	990	3	993
Balsa	-2.390	375	87	462
FRP1	-0.190	89	33	122
FRP2	-2.390	15084	2927	18011
FRP3	-4.490	24892	4	24896
Total		51996	6499	58495

Table 5.5. Finite element analysis results comparison.

Element Size (in)	Deck 1 displacement (in)	Percent Difference (predicted vs. measured)	Deck 2 displacement (in)	Percent Difference (predicted vs. measured)
1	0.067965	37.4	0.210703	6.9
0.5	0.068662	36.7	0.212271	6.2
0.25	0.068891	36.5	0.212769	5.9
Measured	0.1085	--	0.2262	--

Chapter 6. Conclusions

The initial goals of this research were attained through a comprehensive investigation to examine the feasibility of producing an innovative GFRP bridge deck design using 3-D weaving technology. Although this research is exploratory in nature, the feasibility of 3-D woven GFRP bridge decks has shown great promise. As a result, North Carolina State University and 3TEX, Inc. have begun joint filing for a United States patent for the proposed deck design.

6.1 Summary and Conclusions

The research in this thesis successfully achieved the four objectives stated at the outset. First, the current 3-D weaving process, 3Weave®, was successfully applied to the first viable structural application. These fabrics have been manufactured primarily for marine applications and protective apparel, owing to the fast infusion and excellent out of plane properties provided by the fiber architecture. The most promising feature of this technology was shown to be the ability to strengthen the joint between the shear webs and the face skins. The typical reported failure mode of GFRP bridge decks is a separation of the fibers, which are confined only by resin using the pultrusion process by which current commercial bridge decks are produced. This concern is completely eliminated with the 3-D weaving process. The joints are strengthened with sufficient through thickness reinforcement. This feature comes at the expense of slightly lower mechanical properties in the longitudinal direction. The panels fabricated in this research were constructed with the worst case on the joints, having the fabrics skins fold 90° at the z-joints. Unidirectional panels are unable to maximize the stiffness of the decks by

increasing the depth in this manner, due to the susceptibility of the fibers at the joints to delaminate. This is a landmark development for the application of 3-D woven fabrics.

The second objective was fulfilled by fabricating two deck panels with shear connectors. The fabrication process was very exploratory in nature. The decks were machined with intense labor over a period of nearly twelve months. The weaving loom from which the fabrics were produced was designed for research purposes and is by no means capable of producing fabric in with volume or efficiency needed to create a commercial product. There are commercial looms which can presently weave 3-D fabric in six foot maximum widths, with thicknesses up to two inches. Bridge decks from this material can be mass produced and optimized, but that development will take time and much more research and is beyond the scope of this initial project.

The third objective was to attempt an in-depth characterization of the material properties of the individual components in the bridge deck. Considering the nature of the fabrication process, the basic material behavior was determined with some expected variation. The manufacturing process of the woven fabric can be produced with excellent quality control. As opposed to unidirectional fibers which are liable to shift during the pultrusion process, the 3-D fibers in woven fabrics are confined within a mesh and create a more uniform product. In addition to the measurement of the material properties, predictions of these properties were shown to be surprisingly accurate. The Rule of Mixtures derived for fiber reinforced composite analysis provided a reasonable estimation of material properties.

The analysis of the designed panels is also in the preliminary stages. At this stage, in-depth finite element modeling of the panels could provide only a crude

estimation of the test results. This is due to the limited replication of test samples, the tolerances of dimensions of the samples, quality control of the materials, and lack of other important material parameters yet to be considered. In addition to sophisticated modeling techniques which mimic the observed behavior as closely as possible, there is always a need for researchers to provide simple models for approximations. Well-known analytical techniques including transformed section analysis and basic engineering principles showed to be excellent approximations of the behavior, especially considering the numerous assumptions. If engineers can associate with bridge deck design using analytical techniques with which they are familiar, they should become more comfortable designing with this new material.

6.2 Future Work

This was a successful pilot study on this configuration of bridge deck. However, much research remains to produce a deck panel optimized for cost efficiency, performance, and commercial production.

6.2.1 Connections

Connections were not studied directly in this project due to material constraints. The speculation for the design of these panels is that the panel-to-panel joints would be adhesively bonded with a single overlap layer of FRP. This seems to be the most practical type of connection for a GFRP deck panel, although the through thickness reinforcement of 3Weave® exhibits excellent properties if mechanical fasteners are desired.

6.2.2 Resin Formulation

The resin infusion system used in this research was Jeffco 1401-21/4101-21. It is one of the lower grade epoxy systems commercially available. Its primary applications are for high performance E-glass composites. The epoxy system was chosen for its increased mechanical properties. However, the anticipated higher properties compared to vinyl ester systems are accompanied with some tradeoffs.

In general, epoxy systems are more expensive than vinyl ester systems. For one reason, epoxy systems require about ten times as much hardener as vinyl ester systems. Another advantage of vinyl ester systems is infusibility. The viscosity of vinyl ester is much less than epoxy, allowing for quicker infusion. Also, the reaction between the vinyl ester and catalyst is exothermic, allowing the resin to self-cure. The additional time and cost of maintaining an autoclave as required by some epoxy systems is eliminated. One of the final steps in refining the deck panel design would be to formulate a resin system for this particular bridge deck design. The desired performance would be based upon desired mechanical properties, pot life, viscosity, cost, thermal resistance, and compatibility with concrete.

6.2.3 Strength of Joints

The width of the z-joints was designed to ensure failure of the webs prior to withdrawal of the fibers at the joints. However, the width of the joint necessary to develop full strength of the webs is unknown. It is dependent upon the z-yarns, the properties of the resin, and the web strength. Being able to reduce the width of the joint would allow for an increase in panel depth and thus, an increase in stiffness. A separate study is needed to determine the strength of the joints alone. This could be accomplished by loading the

web and fixing the fabric which contains the z-joint. Once the behavior is well-understood, the width of the joint required to develop a certain web strength could be modeled using finite element software.

6.2.4 Fatigue Testing

All testing in the current research involved static testing. For the three point bending tests, the decks were loaded cyclically to show permanent deformation, but no dynamic testing was performed. One concern for higher magnitudes of dynamic loading is the progressive cracking of matrix and fibers. During static loading, snapping of the fibers and cracking of the matrix was audible and became more frequent as the load approached failure. One concern is that dynamic loading would cause matrix cracks to propagate more quickly or cause additional fiber fracturing, resulting in strength and stiffness degradation. Dynamic loading should be a focal point for future testing.

6.2.5 Shear Properties

One issue regarding the vertical webs is whether or not the fully overlapping webs develop the shear resistance provided by a fabric of the thickness of two adjoined webs. A shear test in accordance with ASTM C273 for FRP panels would provide insight into the shear behavior.

6.3 Proposed Third Generation Bridge Deck

The first generation 3-D woven GFRP bridge deck was the truss configuration studied by Norton (2004). He conducted the first investigation into the 3Weave® fabrication process applied to bridge decks. The current research investigated a totally different design approach, a beam configuration providing continuous shear webs, using the same weaving technology. Neither of these approaches may be ideal. Both approaches

provided valuable insight into refining the process. Drawing on the test results and issues regarding fabrication, a new generation of bridge deck should be considered.

The beam configuration should be retained for the third generation deck. This design should be further developed due to the improved shear resistance and maximized stiffness of the vertical webs. The fabrication process which produces a constant cross-section can be much more easily automated than the truss configuration and can produce deck panels of any desired length. In the current project, the longitudinal cuts in the skins were made adjacent to the z-joints. The benefit of cutting at this location is to maximize inertia for the given width of weaving loom. With a wider loom available, a different deck design could be investigated. The proposed new design should investigate cutting at the midpoint between the webs instead of beside joints. The depth of deck for a certain width between joints would be decreased. However, this would eliminate the need for notching the balsa for the joints. The webs would not necessarily have to remain completely vertical. In the case that the balsa cores were not used or rotted, angled webs would be preferable to provide truss a truss-like mechanism to resist braking forces induced by vehicles traveling perpendicular to the deck span. Also, the danger of the webs pulling out of the joints during handling or insertion of the balsa cores is eradicated because the fibers would be continuous on either side of the z-joint.

The concrete topping is an important feature of the bridge deck design that should be retained. The topping serves the dual purpose of added compressive resistance and protective layer for the GFRP. The main concerns of the concrete topping are the bond to the GFRP and the increased material weight. The bond can be enhanced by using a textured mold during the infusion process or by machining after the resin is cured. Epoxy

admixtures which are batched with fresh concrete are becoming more commonly used to improve the bond. Although this alternative would increase the material cost, no additional cost is induced by labor or machining. The weight of the concrete topping can be minimized by using a thinner layer or specifying lightweight concrete.

The shear connectors that should be considered for a third generation deck must be more easily manufactured and provide better resistance. The vertical flange configuration performed the best of the three configurations selected for study. This configuration allows double the height of the other two configurations and develops the tensile properties of the FRP. The flanges rotate as the horizontal shear is applied, increasing the tension resistance. A possible improvement upon this design would be to create a flat head at the top of the flange by folding the fabric horizontally. The head would further engage the concrete and could be easily molded with the fabric preform.

The vacuum infusion process is best suited for specialized, small volumes of fabric. This process can be continued during the exploratory stages of the bridge deck design, but is not practical or economical for mass production. One proposed solution is to draw the 3-D woven fabric through a mold which forces the fabric into a desired cross-section. The fabric is wetted as it is drawn through a bath of resin and is cured as one continuous process. This is similar to the fabrication process used to pultrude unidirectional panels and would be much more economical for high volume production. This could also eliminate the need for balsa wood core inserts, saving in material costs.

6.4 Outlook

This project is a giant step in realizing the potential of 3-D woven fabrics for structural applications. Future development will be dependent on funding for research to improve

manufacturing methods vital to efficient production and analytical studies to optimize the material usage. In time, these panels can be developed into an attractive alternative to conventional steel and concrete bridge decks.

Appendices

Appendix A. Weaving Calculations

The following calculations apply the Rule of Mixtures described by Hull and Clyne (1996) to the composite used in this project. The Rule of Mixtures is based on equilibrium and strain compatibility and was derived to predict the elastic constants for unidirectional composites. The slab model is illustrated in Figure A.1. The total amount of fibers in a unit block is amassed into one solid block of fiber material with a thickness, t_f , proportional to the total fiber volume fraction, f . The remainder of the block is composed of solid matrix material with a thickness, t_m , proportional to the volume fraction of the matrix. The ultimate strains according to manufacturers' data sheets for the fibers shown in Appendix G and matrix shown in Appendix F are:

$$e_f = 0.035 < e_m = 0.0745$$

∴ The composite is fiber limited, i.e., the fibers fail first

Deformations in the warp (x) and filling (y) are considered isostrain conditions. Through the thickness direction (z), the deformation is considered isostress. The Rule of Mixtures based on the slab model gives the following elastic constants for the warp, filling, and thickness directions:

$$E_x = E_y = E_m(1-f) + E_f f$$

$$E_x = (465\text{ksi})(1-0.41) + (10500\text{ksi})(0.41)$$

$$E_x = 4580 \text{ ksi}$$

$$E_x = E_y = 4580 \text{ ksi}$$

$$E_z = \left[\frac{f}{E_f} + \frac{(1-f)}{E_m} \right]^{-1}$$

$$E_z = \left[\frac{f}{E_f} + \frac{(1-f)}{E_m} \right]^{-1}$$

$$E_z = \left[\frac{0.41}{10500\text{ksi}} + \frac{(1-0.41)}{465\text{ksi}} \right]^{-1}$$

$$E_z = 765 \text{ ksi}$$

For the strong direction, strain compatibility is assumed for fiber and matrix:

$$\sigma_x = E_m \varepsilon(1-f) + E_f \varepsilon f, \text{ where } e = e_f$$

$$\sigma_x = (465\text{ksi})(0.035)(1-0.41) + (10500\text{ksi})(0.035)(0.41)$$

$$\sigma_x = 160 \text{ ksi}$$

Assuming isostress condition, composite fails in lower strength material (the matrix).

$$\sigma_z = \sigma_m = 10.3 \text{ ksi}$$

However, these predicted values do not accurately represent the composition of 3-D woven fabrics. The majority of the composite stiffness in any particular direction is a product of the amount of continuous fibers having longitudinal axes aligned in that particular direction. Therefore, a refinement to the rule of mixtures is to use the fiber volume fraction corresponding to each direction.

However, for the thickness direction, only a portion of the z-fibers are aligned in the z-direction at any given point. The z-fibers undulate above and below both the warp and weft yarns. Therefore, a packing factor, P, representing a unit length of the composite in the warp direction compared to the length of the straightened length of z-yarns is used, decreasing the fiber volume fraction in the z-direction.

This factor is determined as:

$$P = \left(1 - \frac{L_z}{L} \right)$$

where L_z is the total length of the straightened z-fibers for a length of composite L in the warp direction. This factor was determined experimentally by measuring the length of a piece of 3-D woven fabric in the warp direction, extracting and straightening the z-yarns, and measuring the straightened length. A straightened z-yarn from the woven fabric is shown in Figure A.2. The packing factor was determined to be 0.6.

These calculations are shown below:

$$f = 0.41$$

$$f_x = (0.687)(f) = 0.282$$

$$f_y = (0.245)(f) = 0.100$$

$$f_z = (0.057)(f)(P) = 0.014$$

$$E_x = E_m(1 - f) + E_f f_x$$

$$E_x = (465 \text{ ksi})(1 - 0.41) + (10500 \text{ ksi})(0.282)$$

$$E_x = 3240 \text{ ksi}$$

$$E_y = E_m(1 - f) + E_f f_y$$

$$E_y = (465 \text{ ksi})(1 - 0.41) + (10500 \text{ ksi})(0.100)$$

$$E_y = 1320 \text{ ksi}$$

The z-direction now provides an isostrain condition due to the z-fibers:

$$E_z = E_m(1 - f) + E_f f_z$$

$$E_z = (465 \text{ ksi})(1 - 0.41) + (10500 \text{ ksi})(0.014)$$

$$E_z = 420 \text{ ksi}$$

Similarly for the stresses:

$$\sigma_x = E_m \epsilon (1 - f) + E_f \epsilon f_x, \text{ where } e = e_f$$

$$\sigma_x = (465 \text{ ksi})(0.035)(1 - 0.41) + (10500 \text{ ksi})(0.035)(0.282)$$

$$\sigma_x = 113 \text{ ksi}$$

$$\sigma_y = E_m \epsilon (1 - f) + E_f \epsilon f_y, \text{ where } e = e_f$$

$$\sigma_y = (465 \text{ ksi})(0.035)(1 - 0.41) + (10500 \text{ ksi})(0.035)(0.100)$$

$$\sigma_y = 46 \text{ ksi}$$

$$\sigma_z = E_m \epsilon (1 - f) + E_f \epsilon f_z, \text{ where } e = e_f$$

$$\sigma_z = (465 \text{ ksi})(0.035)(1 - 0.41) + (10500 \text{ ksi})(0.035)(0.023)$$

$$\sigma_z = 18 \text{ ksi}$$

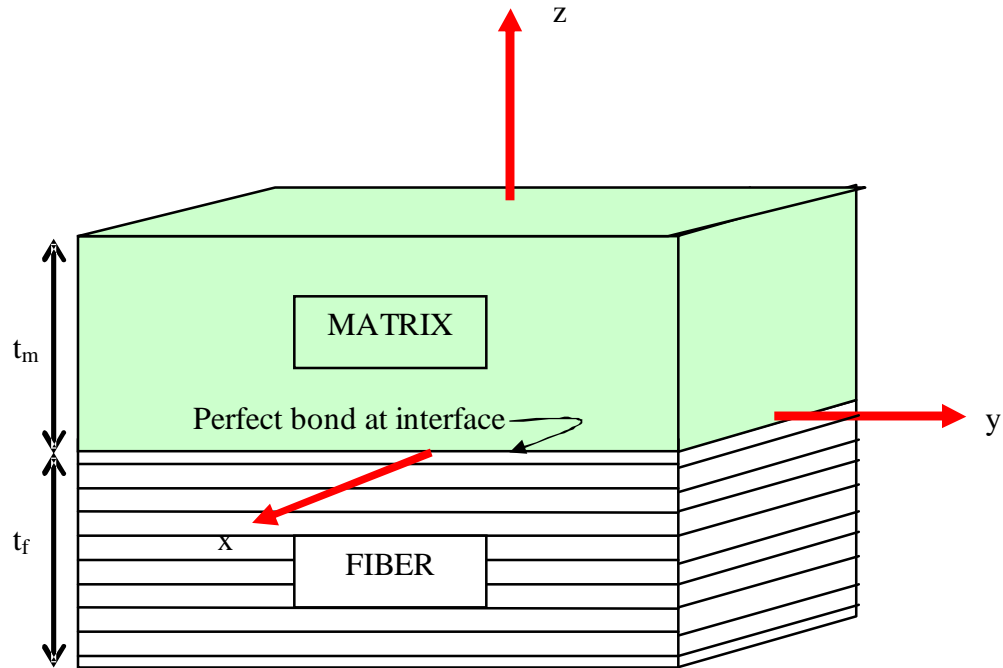


Figure A.1. Slab model assumed for Rule of Mixtures.



Figure A.2. Determination of z-yarn packing factor.

Appendix B. Quikrete MSDS


Material Safety Data Sheet
[OSHA 29 CFR 1910.1200]

The QUIKRETE® Companies
 One Securities Centre
 3490 Piedmont Road, Suite 1300
 Atlanta, GA 30329

Emergency Telephone Number
 (770) 216-9580

Information Telephone Number
 (770) 216-9580

Revision: July 2003

MSDS K

SECTION I: PRODUCT IDENTIFICATION

Product Types: QUIKRETE® DRY PACKAGED PORTLAND CEMENT BASED PRODUCTS (SERIES 5)

<u>QUIKRETE® Product Name</u>	<u>Code #</u>	<u>QUIKRETE® Product Name</u>	<u>Code #</u>
QUIKRETE® PORTLAND CEMENT	1124	QUIKRETE® MASONRY CEMENT	1125-70
QUIKRETE® PORTLAND/LIME CEMENT	1124-06 1125-21	PORTLAND/POZZOLAN CEMENT	1118-35
PLASTIC CEMENT	2121	GROUT-TYPE A	1585-04

(ALSO APPLIES TO OTHER SPECIALTY PORTLAND OR MASONRY CEMENTS)

SECTION II - HAZARDOUS INGREDIENTS/IDENTITY INFORMATION

Hazardous Components	CAS No.	PEL (OSHA) mg/M ³	TLV (ACGIH) mg/M ³
Portland Cement	65997-15-1	5	5
May contain:			
Silica Sand, crystalline	14808-60-7	<u>10</u> %SiO ₂ +2	0.05 (respirable)
Pulverized Limestone	01317-65-3	5	5
Fly Ash	68131-74-8	5	5
Gypsum	10101-41-4	5	5
Lime	01305-62-0	5	5

Although these products contain no intentionally added Silica, they may contain small amounts of silica occurring as natural impurities in the other raw materials.

Other Limits: National Institute for Occupational Safety and Health (NIOSH). Recommended standard maximum permissible concentration=0.05 mg/M³ (respirable free silica) as determined by a full-shift sample up to 10-hour working day, 40-hour work week. See NIOSH Criteria for a Recommended Standard Occupational Exposure to Crystalline Silica.

SECTION III - PHYSICAL/CHEMICAL CHARACTERISTICS

Appearance: Gray to gray-brown colored powder. Some products available in white and other colors.
Specific Gravity: 2.6 to 3.15 **Melting Point:** >2700°F **Boiling Point:** >2700°F
Vapor Pressure: None **Vapor Density:** None **Evaporation Rate:** None
Solubility in Water: Slight **Odor:** None



QUIKRETE® MATERIAL SAFETY DATA SHEET

page # 2

Product Types: QUIKRETE® DRY PACKAGED PORTLAND CEMENT BASED PRODUCTS (SERIES 5)

MSDS K

SECTION IV - FIRE AND EXPLOSION HAZARD DATA

Flammability: Noncombustible and not explosive.

SECTION V - REACTIVITY DATA

Stability: Stable.**Incompatibility (Materials to Avoid):** Material when mixed with water will react with Aluminum and other alkali and alkaline earth elements liberating hydrogen gas.**Hazardous Decomposition or By-products:** None**Hazardous Polymerization:** Will Not Occur.**Condition to Avoid:** Keep dry until used to preserve product utility.

SECTION VI - HEALTH HAZARD DATA

Route(s) of Entry: Inhalation, Skin, Ingestion**Acute Exposure:** Product becomes alkaline when exposed to moisture. Exposure can dry the skin, cause alkali burns and effect the mucous membranes. Dust can irritate the eyes and upper respiratory system. Toxic effects noted in animals include, for acute exposures, alveolar damage with pulmonary edema.**Chronic Exposure:** Dust can cause inflammation of the lining tissue of the interior of the nose and inflammation of the cornea. Hypersensitive individuals may develop an allergic dermatitis.**Carcinogenicity:** Since portland cement and blended cements are manufactured from raw materials mined from the earth (limestone, marl, sand, shale, etc.) and process heat is provided by burning fossil fuels, trace, but detectable, amounts of naturally occurring, and possibly harmful, elements may be found during chemical analysis. Under ASTM standards, portland cement may contain 0.75 % insoluble residue. A fraction of these residues may be free crystalline silica. Respirable crystalline silica (quartz) can cause silicosis, a fibrosis (scarring) of the lungs and possibly cancer. There is evidence that exposure to respirable silica or the disease silicosis is associated with an increased incidence of Scleroderma, tuberculosis and kidney disorders.**Carcinogenicity Listings:**

NTP:	Known carcinogen
OSHA:	Not listed as a carcinogen
IARC Monographs:	Group 1 Carcinogen
California Proposition 65:	Known carcinogen

NTP: The National Toxicology Program, in its "Ninth Report on Carcinogens" (released May 15, 2000) concluded that "Respirable crystalline silica (RCS), primarily quartz dusts occurring in industrial and occupational settings, is *known to be a human carcinogen*, based on sufficient evidence of carcinogenicity from studies in humans indicating a causal relationship between exposure to RCS and increased lung cancer rates in workers exposed to crystalline silica dust (reviewed in IAC, 1997; Brown *et al.*, 1997; Hind *et al.*, 1997)**IARC:** The International Agency for Research on Cancer ("IARC") concluded that there was "*sufficient evidence* in humans for the carcinogenicity of crystalline silica in the forms of quartz or cristobalite from occupational sources", and that there is "*sufficient evidence* in experimental animals for the carcinogenicity of quartz or cristobalite." The overall IARC evaluation was that "crystalline silica inhaled in the form of quartz or cristobalite from occupational sources is *carcinogenic to humans* (Group 1)." The IARC evaluation noted that "carcinogenicity was not detected in all industrial circumstances or studies. Carcinogenicity may be dependent on inherent characteristics of the crystalline silica or on external factors affecting its biological activity or distribution of its polymorphs." For further information on the IARC evaluation, see IARC Monographs on the Evaluation of carcinogenic Risks to Humans, Volume 68, "Silica, Some Silicates." (1997)

Product Types: QUIKRETE® DRY PACKAGED PORTLAND CEMENT BASED PRODUCTS (SERIES 5) MSDS K

Signs and Symptoms of Exposure: Symptoms of excessive exposure to the dust include shortness of breath and reduced pulmonary function. Excessive exposure to skin and eyes especially when mixed with water can cause caustic burns as severe as third degree.

Medical Conditions Generally Aggravated by Exposure: Individuals with sensitive skin and with pulmonary and/or respiratory disease, including, but not limited to, asthma and bronchitis, or subject to eye irritation, should be precluded from exposure. Exposure to crystalline silica or the disease silicosis is associated with increased incidence of scleroderma, Tuberculosis and possibly increased incidence of kidney lesions.

Chronic Exposure: Dust can cause inflammation of the lining tissue of the interior of the nose and inflammation of the cornea. Hypersensitive individuals may develop an allergic dermatitis. (May contain trace (<0.05 %) amounts of chromium salts or compounds including hexavalent chromium, or other metals found to be hazardous or toxic in some chemical forms. These metals are mostly present as trace substitutions within the principal minerals)

Medical Conditions Generally Aggravated by Exposure: Individuals with sensitive skin and with pulmonary and/or respiratory disease, including, but not limited to, asthma and bronchitis, or subject to eye irritation, should be precluded from exposure.

Emergency First Aid Procedures:

Eyes: Immediately flush eye thoroughly with water. Continue flushing eye for at least 15 minutes, including under lids, to remove all particles. Call physician immediately.

Skin: Wash skin with cool water and pH-neutral soap or a mild detergent. Seek medical treatment if irritation or inflammation develops or persists. Seek immediate medical treatment in the event of burns.

Inhalation: Remove person to fresh air. If breathing is difficult, administer oxygen. If not breathing, give artificial respiration. Seek medical help if coughing and other symptoms do not subside. Inhalation of large amounts of portland cement require immediate medical attention.

Ingestion: Do not induce vomiting. If conscious, have the victim drink plenty of water and call a physician immediately.

SECTION VII - PRECAUTIONS FOR SAFE HANDLING AND USE

If spilled, use dustless methods (vacuum) and place into covered container for disposal or use if not contaminated or wet. Use adequate ventilation.

Waste Disposal Method: The packaging and material may be land filled; however, material should be covered to minimize generation of airborne dust. This product is not classified as a hazardous waste under RCRA or CERCLA.

SECTION VIII - CONTROL MEASURES

DO NOT BREATHE DUST. In dusty environments, the use of an OSHA, MSHA or NIOSH approved respirator and tight fitting goggles is recommended. Local exhaust can be used, if necessary, to control airborne dust levels. The use of barrier creams or impervious gloves, boots and clothing to protect the skin from contact is recommended. Following work, workers should shower with soap and water. Precautions must be observed because burns occur with little warning -- little heat is sensed.

WARN EMPLOYEES AND/OR CUSTOMERS OF THE HAZARDS AND REQUIRED OSHA PRECAUTIONS ASSOCIATED WITH THE USE OF THIS PRODUCT.

NOTE: The information and recommendations contained herein are based upon data believed to be correct. However, no guarantee or warranty of any kind, express or implied, is made with respect to the information contained herein. We accept no responsibility and disclaim all liability for any harmful effects which may be caused by exposure to silica contained in our products.

Appendix C. Alcan Baltek Contourkore Balsa Core Typical Mechanical Properties




Data Sheet / Issue 09/05 / Replaces Issue 03/05

BALTEK® SL SELECTED DENSITY END-GRAIN BALSA

Description	End-grain balsa core with tightly controlled densities for better management of design properties. Seed selection, advanced farming techniques and special processing are used to grow a better grade of raw material. It has excellent mechanical properties, and is compatible with all types of resins and manufacturing processes. By improving on all the advantages and characteristics of standard balsa, it is ideally suited as core material for sandwich structures where extreme performance and weight savings are critical. All while being a renewable resource.
Applications	<ul style="list-style-type: none"> • Marine hulls, decks, bulkheads, superstructures, interiors • Road and Rail floors, walls, roof panels, body panels, interiors, front-ends, side skirts • Wind Energy rotor blades, spinners, nacelle covers, generator housings • Aircraft floor panels, galley carts, interior partitions, cargo pallets, containers, general aviation (sport aircraft) parts • Defense naval vessels, containers, cargo pallets, tactical shelters • Industrial Containers, tanks, covers, impact limiter, skis, snowboards, wakeboards, canoes, kayaks
Characteristics	<ul style="list-style-type: none"> • extremely high strength and stiffness to weight ratios • tight density control to $\pm 8 \text{ kg/m}^3$ ($\pm 1/2 \text{ lb/ft}^3$) of average • ecological product (renewable resource) • excellent fire performance • wide operating temperature range (-212°C to +163°C, -414°F to +325°F) • excellent fatigue resistance • good sound and thermal insulation • high impact strength • good moisture resistance
Processing	<ul style="list-style-type: none"> • contact molding (hand/spray) • resin injection (RTM) • adhesive bonding • compression molding • pre-preg processing (up to 180°C, 355°F) • vacuum infusion

APPENDICES



Data Sheet / Issue 09/05 / Replaces Issue 03/05

Typical properties for BALTEK® SL			SL.45	SL.56	SL.67	SL.78	SL.89	SL.910	SL.1011	SL.1112	SL.1213	SL.1314	SL.1415
Apparent nominal density	ASTM C 271	kg/m ³	81	96	112	128	143	161	175	188	212	220	236
		lb/ft ³	5.1	6.0	7.0	8.0	8.9	10	10.9	11.7	13.2	13.7	14.7
Compressive strength perpendicular to the plane	ASTM C 365	N/mm ²	5.1	6.6	8.2	10.0	11.7	13.9	15.77	17.52	20.9	22.1	24.6
		psi	736	943	1182	1450	1703	2019	2288	2541	3238	3209	3562
Compressive modulus perpendicular to the plane	ASTM C 365	N/mm ²	1610	2047	2552	3113	3641	4299	4854	5376	6397	6750	7471
		Psi	233466	296029	370205	451483	528118	623526	703999	779699	927835	978936	1083614
Tensile strength perpendicular the plane	ASTM C 297	N/mm ²	6.2	7.6	9.1	10.7	12.2	14.0	15.54	16.9	19.6	20.5	22.3
		Psi	897	1097	1318	1556	1773	2036	2253	2454	2837	2967	3229
Tensile modulus perpendicular the plane	ASTM C 297	N/mm ²	1897	2241	2612	2997	3342	3750	4079	4378	4940	5127	5601
		psi	275169	325101	378833	434735	484667	543826	591587	635006	716417	743564	797828
Shear strength	ASTM C 273	N/mm ²	1.8	1.8	2.2	2.5	2.8	3.14	3.4	3.7	4.2	4.4	4.7
		psi	225	267	313	361	405	456	498	536	607	631	679
Shear modulus	ASTM C 273	N/mm ²	97	107	120	135	149	169	186	204	241	255	286
		psi	14026	15555	17386	19524	21653	24478	27025	29570	36006	37032	41441
Thermal conductivity at room temperature	ASTM C 177	W/m.K	0.042	0.049	0.054	0.060	0.064	0.068	0.071	0.074	0.078	0.080	0.082
		BTU.in/ft ² .h. ^o F	0.292	0.335	0.375	0.411	0.439	0.489	0.491	0.509	0.541	0.551	0.589
Dimensions	width	mm	609.6	609.6	609.6	609.6	609.6	609.6	609.6	609.6	609.6	609.6	609.6
		in	24	24	24	24	24	24	24	24	24	24	24
	length	mm	1219.2	1219.2	1219.2	1219.2	1219.2	1219.2	1219.2	1219.2	1219.2	1219.2	1219.2
		in	48	48	48	48	48	48	48	48	48	48	48
	Plain sheet thickness	mm	5 to 100										
		in	3/16 to 4										
	Contoured** thickness	mm	5 to 50										
		in	3/16 to 2										

Other dimensions, configurations, and closer tolerances upon request **>SL.1314 over 38mm (1 1/2") only available 24" by 24"

The data provided gives approximate values for the nominal density. Due to density variations these values can be lower than indicated above. Minimum values to calculate sandwich constructions can be provided upon request.

Please specify LamPrep (micro-sanded) surface treatment or AL600/10 coating (decreases porosity and increases bond strength) when ordering. Densities greater than SL.67 are available by special order only. Additional lead time and minimum order quantities will apply.

The information contained herein is believed to be correct and to correspond to the latest state of scientific and technical knowledge. However, no warranty is made, either expressed or implied, regarding its accuracy or the results to be obtained from the use of such information. No statement is intended or should be construed as a recommendation to infringe any existing patent.

Alcan Airex AG
 CH-5643 Sins, Switzerland
 Tel: +41 41 789 88 00
 Fax: +41 41 789 88 60
 www.alcanairex.com

Alcan Baltek Corporation
 108 Fairway Court
 Northvale, NJ 07647, USA
 Tel: +1 201 767 14 00
 Fax: +1 201 367 12 01
 www.alcanbaltek.com

ALCAN COMPOSITES

Appendix D. Grooved Machining (GP) to End Grain Balsa Data Sheet

Baltek Product Data Sheet

GPS™

Description:

GPS is a line of new core products specially machined for use with resin infusion technology. GPS makes it possible to infuse laminates without the use of additional flow media or specially-designed molds. Panels are available in rigid sheets (GP) or slit in the long direction to conform to simple curves (GPS).

The resin infusion process allows reinforcements and cores to be assembled dry in the mold. A sealed bag is then placed over the part and vacuum pressure draws resin through the material. This process greatly enhances quality by eliminating voids and results in high-fiber volumes, producing stronger, lighter laminates. Variability due to environment and human error is also reduced, generating part-to-part repeatability and higher production rates with lower rejects. Volatile organic compounds (VOCs) are captured inside the vacuum bag, meeting or exceeding all present and proposed emission regulations. The process is also worker friendly, with no respirators or protective suits required.

The unique configuration of perforations and flow channels in GPS results in a higher infusion rate with an even flow-front. Very large parts may be manufactured in one step, eliminating secondary bonds.

Resin infusion with GPS has further advantages. It eliminates disposable surface or internal-feed resin-distribution media. The dry spots and print-through associated with standard flexible core sheets and the heavy, resin-rich areas left by intra-laminar infusion are also eliminated.

Waste, labor, equipment, and floor space are all significantly reduced, resulting in considerable cost savings for the end user.

GPS is available in any Baltek foam or balsa core product. It's also available in pre-cut custom core kits through our KitKore™ program.

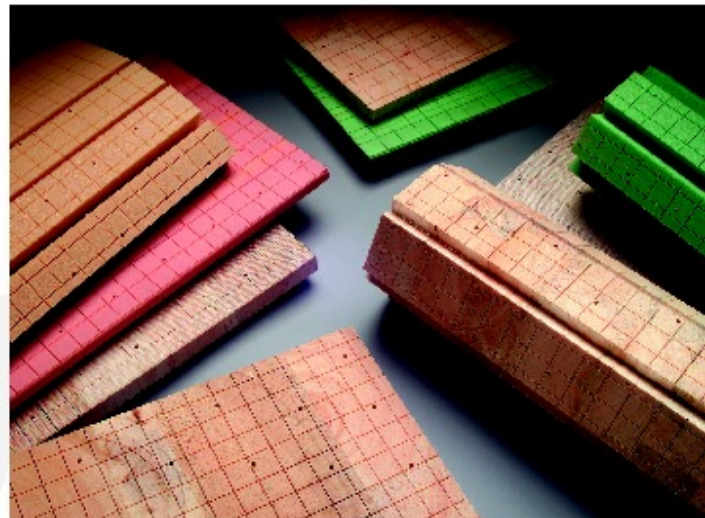
Data File 234

Advantages:

- Lightweight
- Eliminates harmful VOCs
- Saves labor
- Compatible with all types of vacuum and pressure-driven closed-molding processes
- Eliminates secondary bonds
- Reduces print-through
- Speeds production
- Improves quality control
- Exceptional cost effectiveness
- Internationally certified by American Bureau of Shipping, Det Norske Veritas, and Lloyd's Register of Shipping

Applications:

- Marine: hulls, decks, superstructure, interior components, hatches and small parts
- Rail: exterior fairings, floors, walls, doors, roof panels, interior partitions and modules, and monocoque body structures
- Automotive, RV, Bus, Truck: floor panels, roof panels, body panels and monocoque body structures
- Energy Generation: wind turbine blades and nacelles
- Aircraft: floor panels, bulkheads, doors, galley carts, and interior partitions
- Industrial: corrosion resistant tanks, pipes, ductwork and structures
- Architectural: lightweight structures and building panels



Appendix E. ADVA 100 Data Sheet

Concrete

P R O D U C T I N F O R M A T I O N

ADVA® 100

High Range Water Reducer ASTM C 494, Type F

Description

ADVA® 100 Superplasticizer is a high range water-reducing admixture. It is a liquid which has been formulated by the manufacturer for use as received. ADVA 100 Superplasticizer contains no added chloride. ADVA 100 Superplasticizer is formulated to comply with Standard Specification for Chemical Admixtures for Concrete, ASTM C



494, Type F. One liter weighs approximately 1.06 kg (8.8 lbs/gal).

Dispersion

ADVA 100 Superplasticizer is a superior dispersing admixture having a marked capacity to disperse the cement agglomerates normally found in a cement-water suspension. This capability exceeds that of normal water-reducing admixtures, resulting in lower dosages and better control.

Uses

ADVA 100 Superplasticizer produces concrete with extreme workability characteristics for high slump, flowing concrete. It



also allows concrete to be produced with very low water/cement ratios at low or normal slumps.

ADVA 100 Superplasticizer is ideal for use in any concrete where it is desired to keep the water/cement ratio to a minimum and still achieve the degree of workability necessary to provide easy placement and consolidation. ADVA 100 Superplasticizer will also fluidize concrete making it ideal for tremie concreting or other applications where high slumps are desired.

Advantages

1. ADVA 100 Superplasticizer is highly efficient, producing high slump concrete at very low dosage with no loss in strength.
2. ADVA 100 Superplasticizer may be added to concrete mix water for rapid batching.
3. ADVA 100 Superplasticizer provides a superior combination of long slump life with near neutral set time.

GRACE
Construction Products

- ADVA 100 Superplasticized concrete, even at high slump, exhibits little significant segregation in comparison to concrete without a superplasticizer at the same slump.
- ADVA 100 Superplasticizer finishes easily without stickiness, tearing or spotty set characteristics.

Addition Rates

Addition rates of ADVA 100 Superplasticizer can vary with type of application, but will normally range from 195 to 650 mL/100 kg (3 to 10 fl oz/100 lbs) of cement. In most instances the addition of 195 to 325 mL/100 kg (3 to 5 fl oz/100 lbs) of cement will be sufficient. For best results, ADVA 100 Superplasticizer may be added to the initial mix water. At a given water/cement ratio, the slump required for placement can be controlled by varying the addition rate. Should job site conditions require using more than recommended addition rates, please consult your Grace Representative.

Compatibility

In concrete containing ADVA 100 Superplasticizer the use of an air-entraining agent (such as Daravair® 1000 or Darex® II AEA) is recommended to provide suitable air void parameters for resistance against freeze-thaw attack. Please consult your Grace Representative for dosage guidance.

Most Type A water reducers or Type D water-reducing retarders are compatible with ADVA 100 Superplasticizer as long as they are separately added to the concrete. Normally these admixtures are added to concrete before the ADVA 100. Caution should be exercised when using ADVA 100 Superplasticizer together with a retarder, as excessive retardation can occur if the admixture dosages are too high. Pre-testing of the concrete should be performed to optimize dosages and addition times of these admixtures. The admixtures should not contact each other before they enter the concrete.

Packaging

ADVA 100 Superplasticizer is available in bulk, delivered by metered tank trucks, in 1250 L (330 gal) disposable totes, and in 208 L (55 gal) drums.

It will begin to freeze at 0°C (32°F), but will return to full strength after thawing and thorough agitation. Please consult your Grace Representative if this product freezes.

In storage, and for proper dispensing, ADVA 100 Superplasticizer should be maintained at temperatures above 0°C (32°F) and below 55°C (132°F).



Visit our web site at: www.graceconstruction.com

printed on recycled paper

W. R. Grace & Co.-Conn. 62 Whittemore Avenue Cambridge, MA 02140

ADVA, the ADVA logo, Darexair and Darex are registered trademarks of W. R. Grace & Co.-Conn.

We hope the information here will be helpful. It is based on data and knowledge considered to be true and accurate and is offered for the user's consideration, for reference and reflection, but we do not warrant the results to be obtained. Please read all instructions, room conditions or suggestions in conjunction with our conditions of sale, which apply to all goods supplied by us. No statement, room condition or suggestion is intended for any use which would infringe any patent or copyright. W. R. Grace & Co.-Conn., 62 Whittemore Avenue, Cambridge, MA 02140. In Canada, Grace-Canada, Inc., 234 Glenora Road, Whitby, Ontario, Canada L1P 1K2.

This product may be covered by patents or patents pending. Copyright 2002, W. R. Grace & Co.-Conn. DC-02B Printed in U.S.A. 402 FAWP93M

GRACE
Construction Products

Appendix F. Jeffco Epoxy System Data Sheet



EPOXY FORMULATORS

JEFFCO 1401-21/4101-21

5252 Kearny Villa Way
San Diego, California 92123
Tel: 858.576-9900
Fax: 858.576-7093

Epoxy System for Infusion

DESCRIPTION: Multifunctional epoxy and cycloaliphatic-amine blend hardener for high performance composite parts. Two curing agents (4101-21 fast and 4101-21 slow) provide a complete range of working times from 40 minutes to 6 hours, and by blending the curing agents, any point in between. 1401-21 with 4101-21 provides for ample pot life with fast cure development at standard molding temperatures. Jeffco 1401-21 provides good thermal resistance, excellent fatigue and inter-laminar shear strength with rapid wetting of E-glass fiber reinforcements. Jeffco 1401-21 Epoxy Resin is formulated for highly increased E-glass fiber compatibility. Low toxicity, low odor system. No VOC's, 100% solids.

SUGGESTED USES: Resin infused composite rotor blades, other large fiberglass reinforced structures.

SYSTEM LIQUID PROPERTIES:

Viscosity 1401-21 Resin, 77°F	750-900 cps
Viscosity 4101-21 Slow Hardener, 77°F	20 cps
Viscosity of 4101-21 Fast Hardener	50 cps
Mix Ratio, Resin to Hardener	100:30 by weight
Weight Per Gallon, 1401-21 Resin	9.5 - 9.6 lbs.
Weight Per Gallon, 4101-21 Hardener	7.9-8.1 lbs.
Weight per Gallon, Mixed	9.2 lbs
Mixed Viscosity, 77°F	160 cps (slow) / 240 cps (fast)
Mixed Viscosity, 100°F	90 cps (slow) / 130 cps (fast)

GEL TIME RECIPE TABLE: Jeffco 1401-21 Resin, 100 parts, Jeffco 4101-21 as specified, 30 parts:

Gel Time, 150 grams @ 77 °F	Percent of 4101-21 Slow	Percent of 4101-21 Fast
360 minutes	100% (30PHR)	-
160 minutes	90% (27PHR)	10% (3 PHR)
100 minutes	75% (23 PHR)	25% (7 PHR)
70 minutes	60% (18PHR)	40% (12 PHR)
40 minutes	-	100% (30 PHR)

RESIN INFUSION BASICS: Condition epoxy resin and hardener to between 24°C and 38°C (75°F to 100°F) to ensure proper mixed viscosity. Introduce mixed material into part to be infused keeping mold temperature between 35°C and 40°C (95°F to 104°F). Place or position injection ports to introduce material as needed to ensure injection within two hours. Under moderate vacuum, inject material for up to 120 minutes at the above temperature parameters. Once injection is complete, increase mold temperature to between 50°C and 65°C (122°F to 149°F). Hold at this temperature for between 4 and 6 hours. Cure temperatures may be from 50°C to 85°C to accomplish maximum HDT. Optimum cure time(s) versus temperature(s) will depend on parameters such as part thickness or size.

APPENDICES

REINFORCEMENT TYPES: Jeffco 1401-21 Epoxy Resin is specially formulated for highly increased compatibility with E-glass reinforcements. For carbon fiber laminates, Jeffco 1401-14 Epoxy Resin should be used. When using E-glass / carbon fiber hybrid fabrics or reinforcements, Jeffco 1401-16 Epoxy Resin is recommended. All three Epoxy Resins are compatible and recommended with Jeffco 4101 series Epoxy Hardener(s). Please refer to the specific Jeffco Epoxy Resin product bulletin for more information.

ADVANTAGES OF JEFFCO 1401-21 EPOXY RESIN: As discussed previously, Jeffco 1401-21 Epoxy Resin is formulated to improve the intimate bond between the epoxy resin and E-glass fiber reinforcements. This formulation technique results in increased physical properties as follows:

- ◆ Fiber Pull-Out Strength
- ◆ Tensile Strength and Modulus
- ◆ Flexural Strength and Modulus
- ◆ Compressive Strength
- ◆ Impact Resistance
- ◆ Inter-Laminar Shear Strength

Of equal, if not greater significance is the retention of the above properties after exposure to heat, cycle fatigue, water, expected adverse environmental reagents such as salt spray, acid rain, etc. The formulation of Jeffco 1401-21 Epoxy Resin results in minimal degradation of the cured composite's physical properties as compared to epoxy resin systems not containing the proprietary formulation constituents of Jeffco 1401-21 Epoxy Resin. Similar results with carbon reinforced composites are obtained with Jeffco 1401-14 Epoxy Resin and carbon / E-glass hybrids with Jeffco 1401-16 Epoxy Resin.

The benefit to the composite fabricator is obvious and clear: Increased product life and confidence!

CURED PHYSICAL PROPERTIES OF COMPOSITE: A-260 unidirectional E-glass (epoxy compatible rovings) with Jeffco 1401-21 Epoxy Resin and 4101-21 Epoxy Hardener (70:30 glass to resin ratio). Cure schedule – 2 hours at 35°C (infusion) / 4 hours at 65°C (basic cure) / 2 hours at 85°C (final cure).

Property	Result	Test Method
Tensile Strength	83,000 psi	ASTM D 638
Tensile Modulus	5,250,000 psi	ASTM D 638
90° Tensile Strength	6.05 ksi	ASTM D 3039
In-Plane Shear Strength (4 plies ±45°)	9.14 ksi	ASTM D 3518
Flexural Strength	86,000 psi	ASTM D 790
Flexural Modulus	2,490,000 psi	ASTM D 790
Izod Impact	44.5 ft/lb/in	ASTM D 256-A
Water Absorption	0.09%	ASTM D 570
Barcol Hardness	64	Jeffco Products

CURED PHYSICAL PROPERTIES OF NEAT RESIN: Jeffco 1401-21 Epoxy Resin, 100 parts, Jeffco 4101-21 Epoxy Hardener, 30 parts. 2 hours at 35°C (infusion) + 4 hours at 60°C (basic cure)

Property	Result	Test Method
Tg (DSC)	194°F (90°C)	IPC-TM-650, 2.4.25
Shore D Hardness	90D	Jeffco Products
Tensile Strength	10.30 Ksi	ASTM D 638
Ultimate Elongation	7.4 -7.5%	ASTM D 638
Tensile Modulus	465 Ksi	ASTM D638
Ultimate Compressive Strength	14,500 psi	Sandia Labs Method
Flexural Strength	18.65 Ksi	ASTM D 790
Flexural Modulus	430 Ksi	ASTM D 790

Supplied in 5 Gallon Pails, 55 Gallon Drums, 250 Gal IBC's, Combination Bulk Tanker (4,000 Gals).
Curing agent(s) may be ordered as premixed blends in larger quantities.

Appendix G. Hybon 2022 E-Glass Fiber Properties.



TECHNICAL DATA SHEET
Hybon® 2022 Roving

Application: *Hybon® 2022 Roving is a single end roving for filament winding and weaving/knitting applications and is made of electrical (E) glass fiber. This roving is compatible with polyester, vinyl ester, epoxy, and phenolic resin systems. Hybon® 2022 Roving is designed for applications that require maximum wet-out and wet-out consistency, together with good abrasion resistance and processing characteristics. It is suitable for applications such as piping in oil-field CO₂ gathering systems and pressure cylinders.*

- Provides strand hardness without sacrificing rapid and complete wet-out
- Excellent payout and package transfer
- Low resin demand during processing
- Excellent package transfer efficiency through the use of an outer adhesive film
- Supported by PPG's extensive technical resources
- Product is manufactured in conformance to ISO 9002 requirements

PRODUCT DESCRIPTION

Type of Fiber	E-Glass (ASTM D578-98, paragraph 4.2.2)												
Type of Sizing	Silane												
Roving Yields, nominal ± 7% (yd/lb)	103	206	218	225	250	288	330	413	450	675	827	1200	1800
Tex, nominal ± 7% (g/km)	4800	2400	2275	2200	1985	1722	1500	1200	1100	735	600	413	276
Fiber Diameter, nominal	T	MN	MN	T	M	LM	Q	MN	MN	K	K OR MN	K OR MN	K
Micrometers, µm	24	17	17	24	16	15	20	17	17	13	13 OR 17	13 OR 17	13
Percent of Sizing (by wt. of glass)	.55	.55	.55	.55	.55	.55	.55	.55	.55	.55	.55	.55	.55

PACKAGING & PALLETIZING DATA

Packaging Option 1:

- Yields: 103, 206, 413 & 827
- 48 packages/pallet
- Pallet weight: 980 kg
- Package weight: 20.4 kg

Packaging Option 2:

- Yields: 218, 225, 250, 288, 330, 450, 675, 1200 & 1800
- 60 packages/pallet
- Pallet Weight: 1,225 kg
- Package Weight: 20.4 kg

Storage: These products should be stored at room temperature and at a relative humidity of 65% +/- 10%. To avoid problems with humidity or static electricity, the glass product should be conditioned in the working area prior to use.

Caution: To avoid the possibility of potential injury, maintain column stability by limiting pallet stacking to two high as noted on individual shipping container.

APPENDICES

Specific Gravity (bare fiber)

2.59 g/cm³

For commercial fiber glass products with sizing (binder), specific gravity and density are reduced by 0.02 g/cm³ and 0.0007 lb/in³ respectively for each one percent by weight of sizing application.

Density (bulk), 0.094 lb/in³

2.63 g/cm³

Tensile Strength, @ 50% Relative Humidity 72 °F

200 - 300 x 10³ psi

1380 - 2070 MPa

Modulus of Elasticity

10.5 x 10⁶ psi

72.45 Gpa

Elastic Recovery

100%

Elongation at break

3 - 4%

Poisson's Ratio

0.22

Linear Coeff. of Thermal Expansion (25 - 300 °C)

2.8 - 3.3 x 10⁻⁶ in/(in °F)

5.0 - 6.0 x 10⁻⁶ cm/(cm °C)

Thermal Conductivity (bulk)

0.6 - 0.7 btu/(hr-ft °F) @ 72 °F

0.0025 - 0.003 cal/(sec-cm °C) @ 22 °C

Specific Heat (bulk)

0.197 btu/(lb °F) @ 72 °F

0.197 cal/(g °C) @ 22 °C

Softening Point

1540 °F

838 °C

Dielectric Constant

6.7 @ 106 Hz & 72 °F (22 °C)

Index of Refraction @ 550 nanometers

1.559

Ultraviolet transmission

opaque

Hardness (moh scale) (bulk)

6.5

Appendix H. Steel Reinforcement Test Data

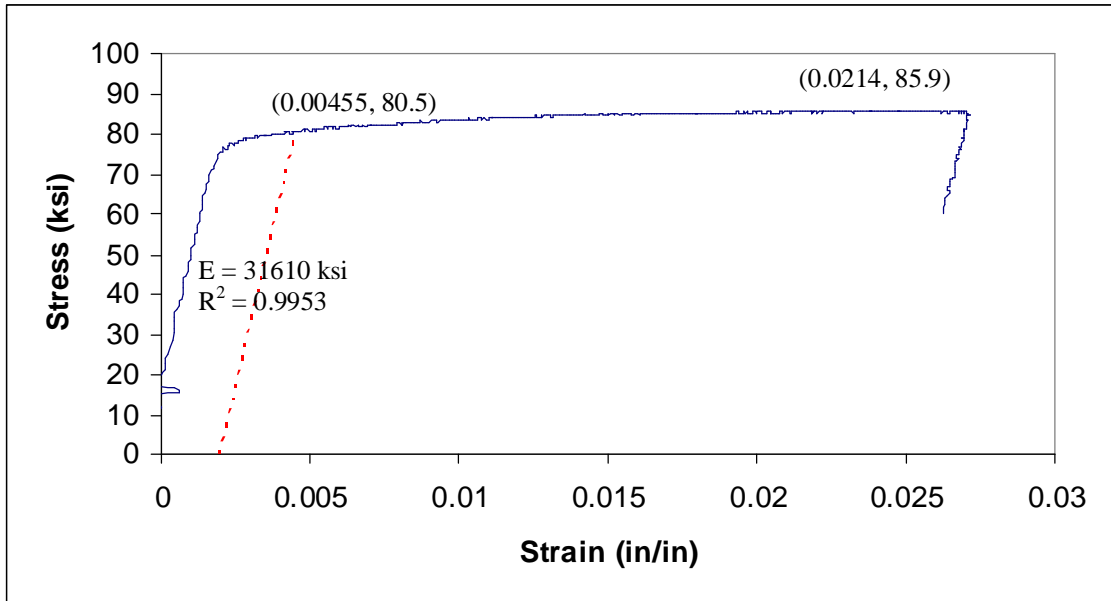


Figure H.1. Bar 1 stress vs. strain curve.

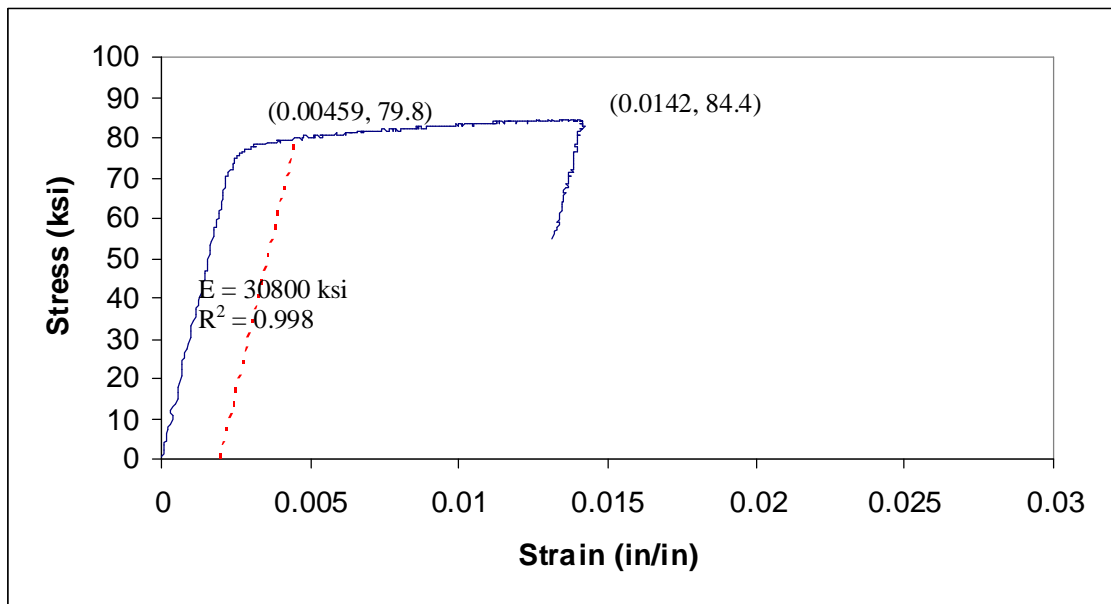


Figure H.2. Bar 2 stress vs. strain curve.

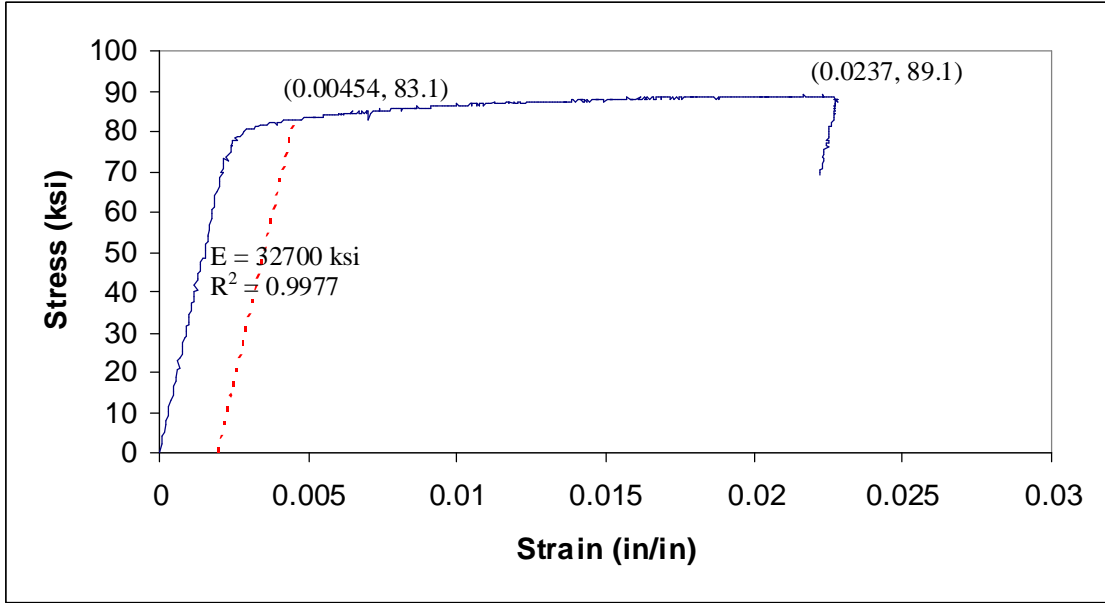


Figure H.3. Bar 3 stress vs. strain curve.

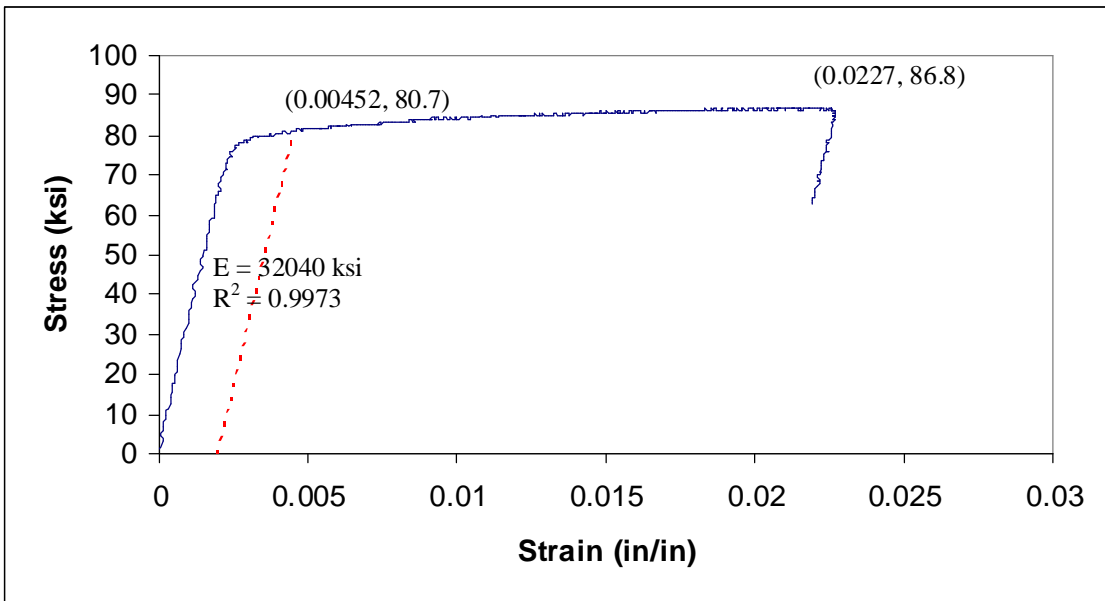


Figure H.4. Bar 4 stress vs. strain curve.

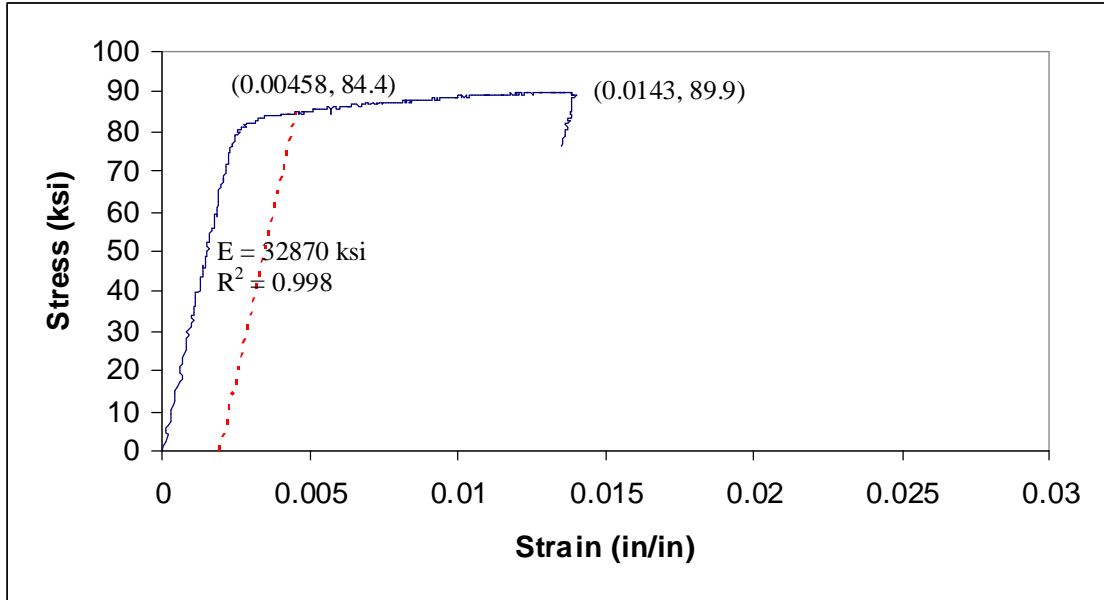


Figure H.5. Bar 5 stress vs. strain curve.

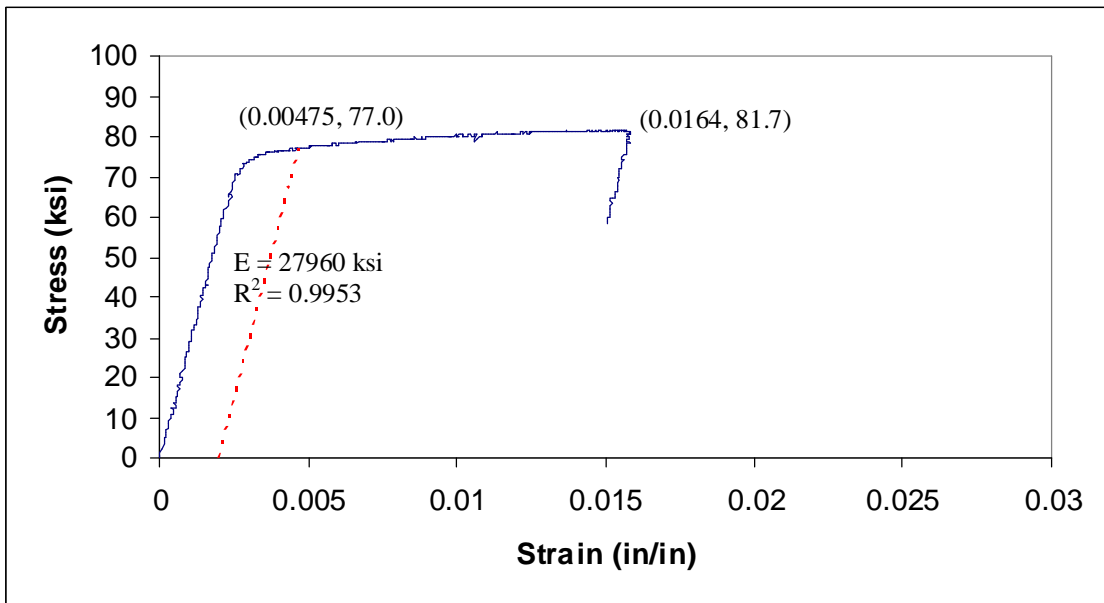


Figure H.6. Bar 6 stress vs. strain curve.

Appendix I. Tension Test of GFRP Skins

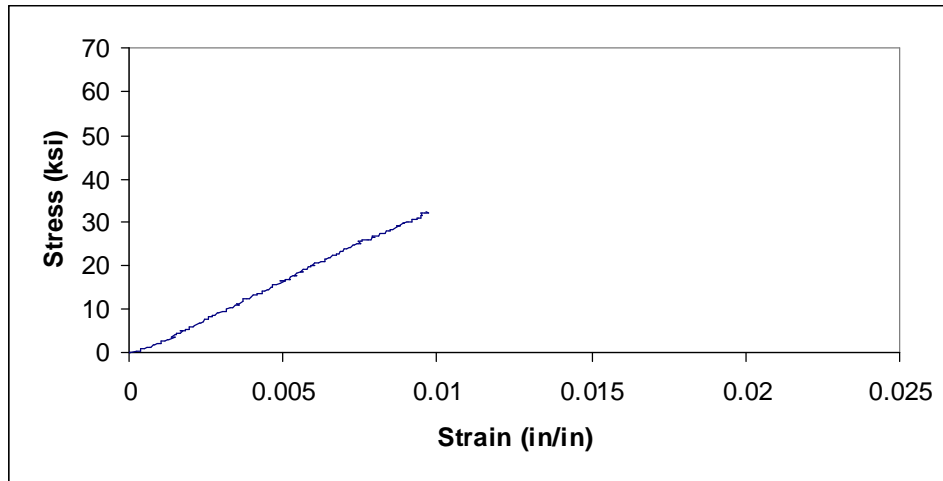


Figure I.1. Warp tension specimen 1.

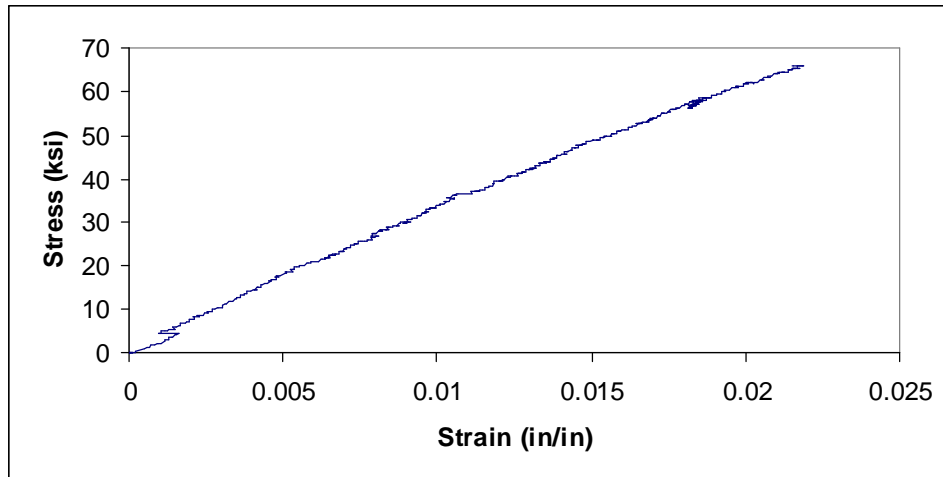


Figure I.2. Warp tension specimen 2.

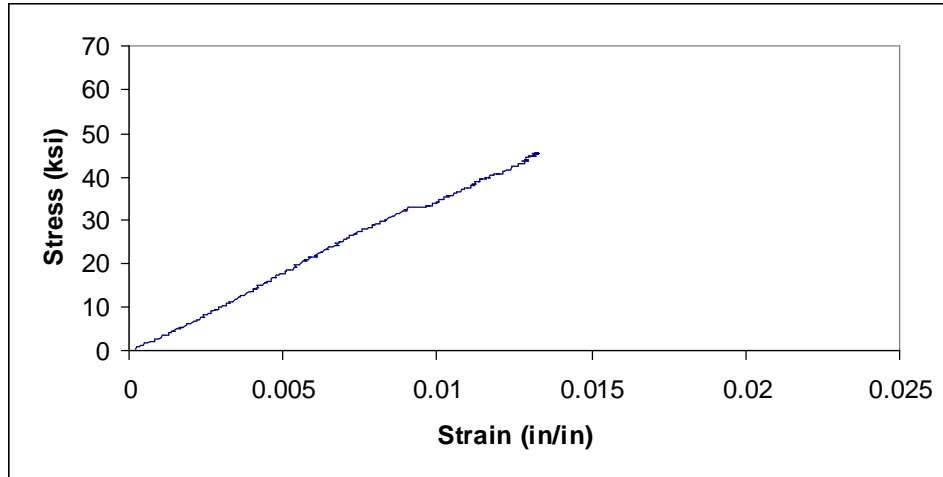


Figure I.3. Warp tension specimen 3.

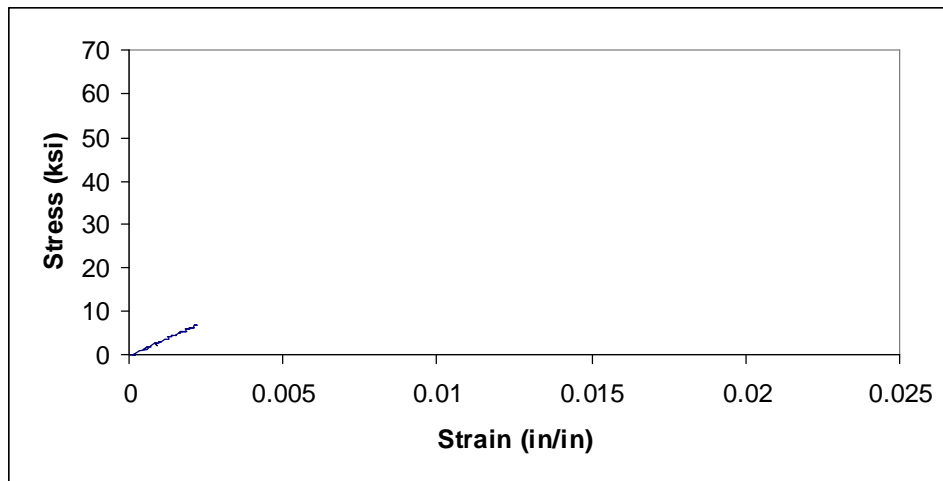


Figure I.4. Warp tension specimen 4.

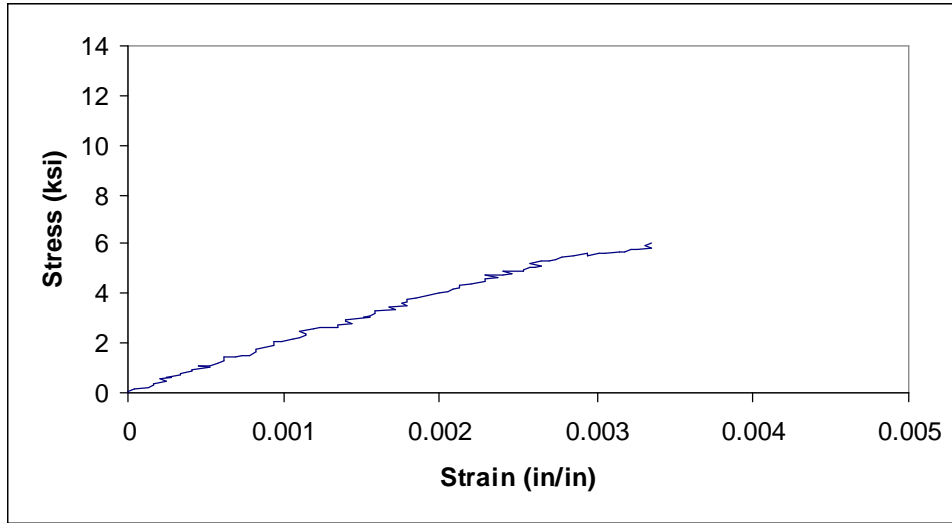


Figure I.5. Filling tension specimen 5.

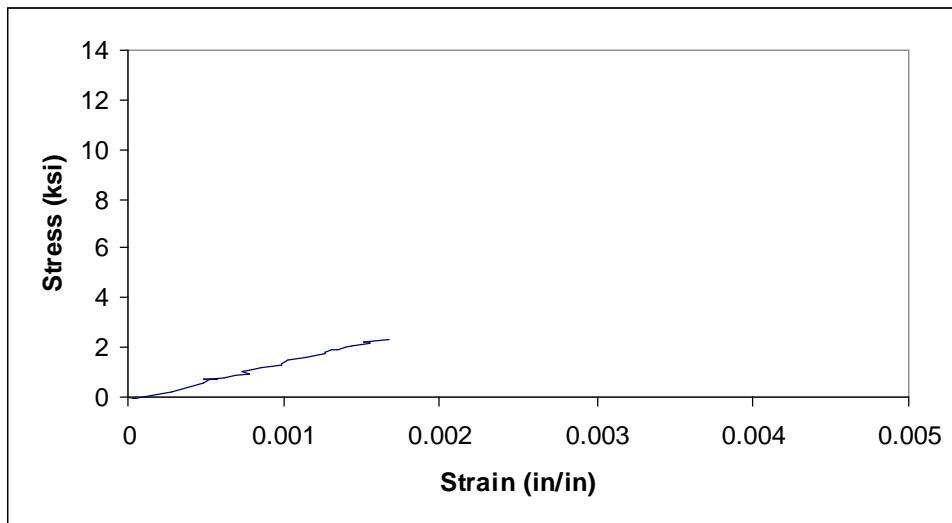


Figure I.6. Filling tension specimen 6.

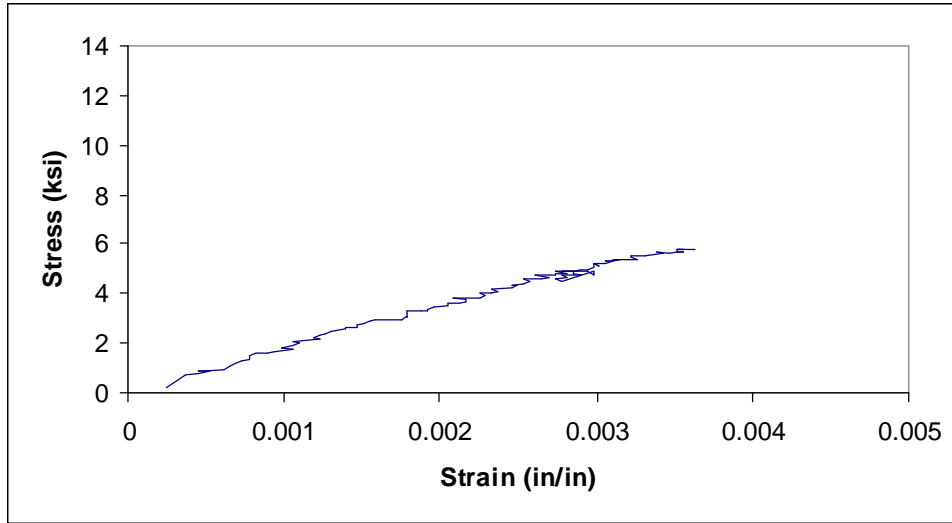


Figure I.7. Filling tension specimen 7.

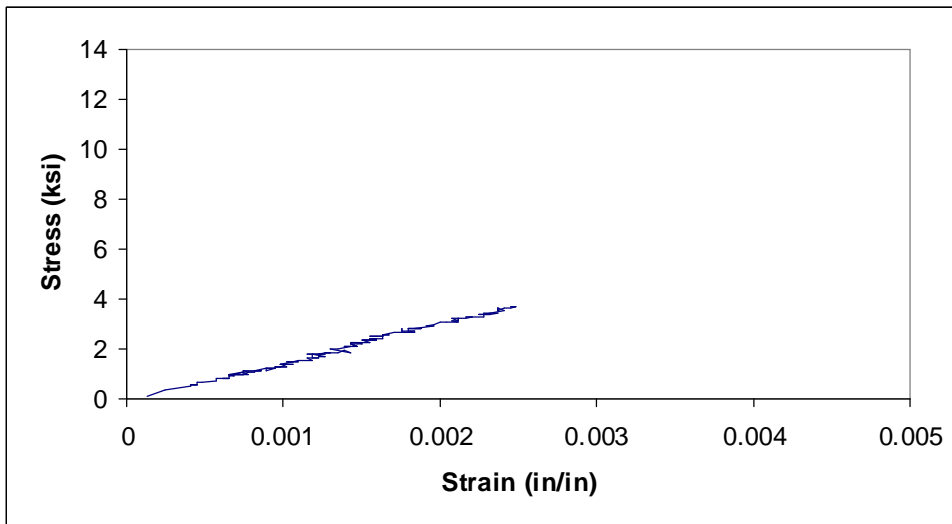


Figure I.8. Filling tension specimen 8.

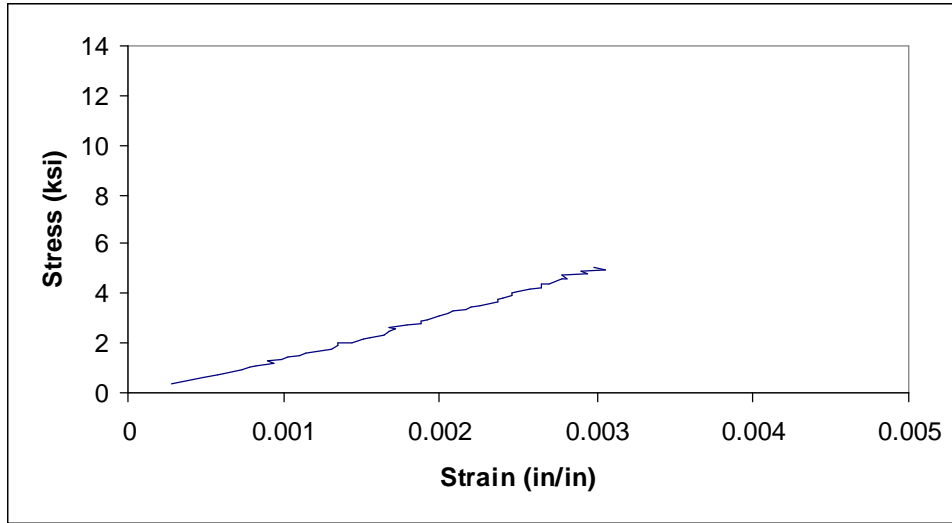


Figure I.9. Filling tension specimen 9.

Appendix J. Four-Point Bending Data of GFRP Skins

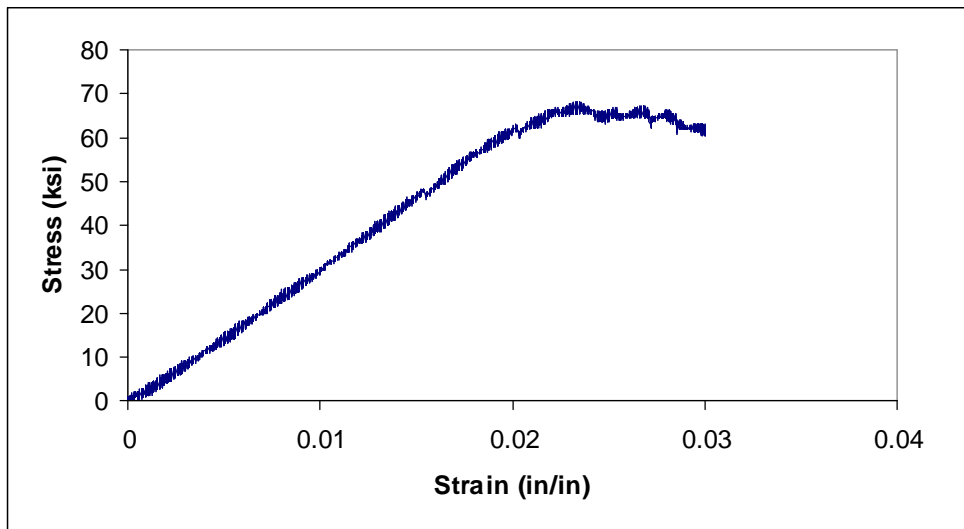


Figure J.1. Filling four point bending specimen 1.

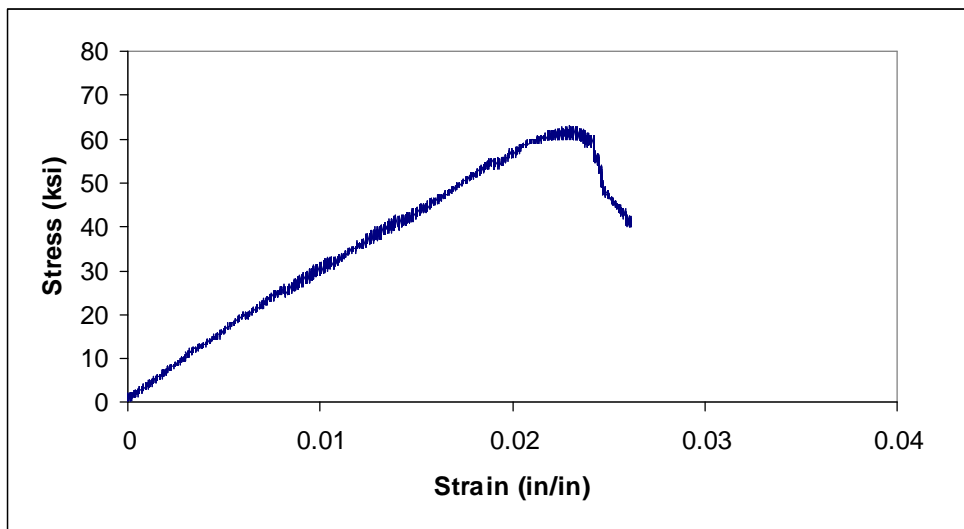


Figure J.2. Filling four point bending specimen 2.

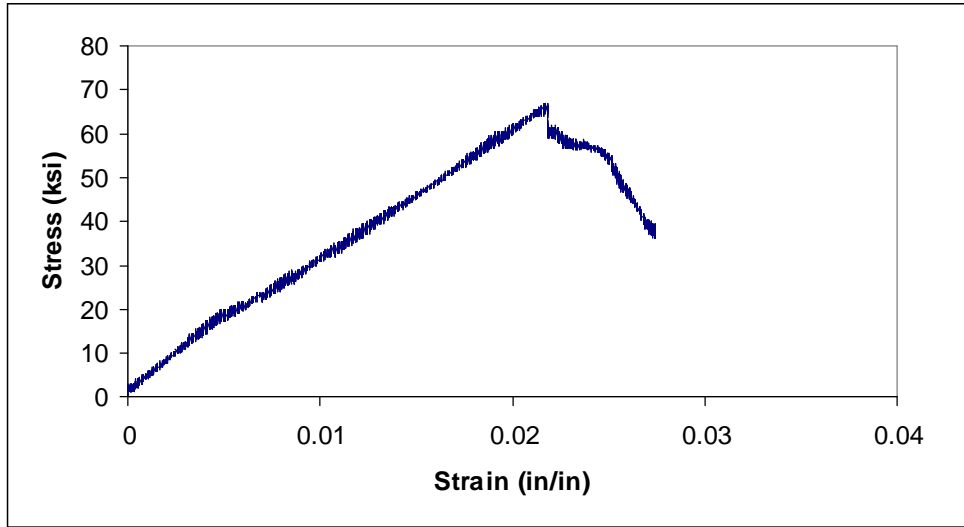


Figure J.3. Filling four point bending specimen 3.

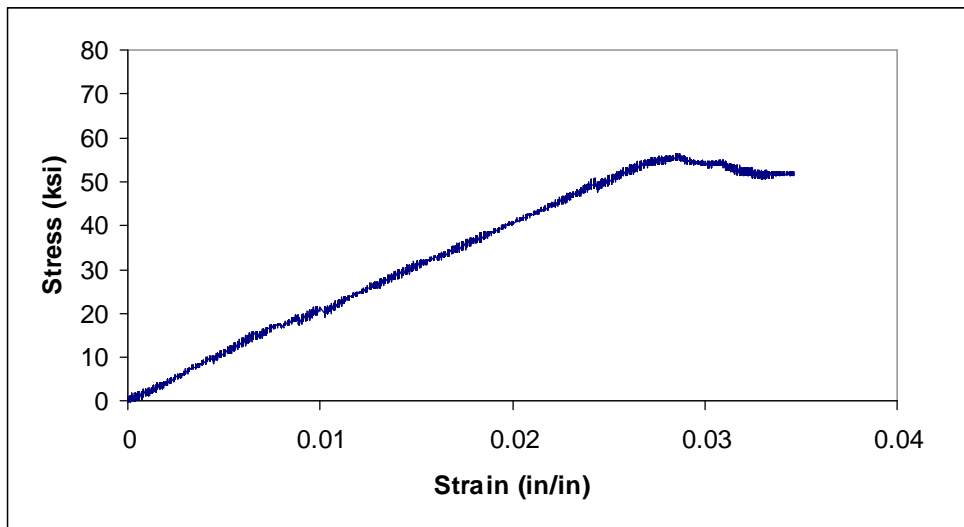


Figure J.4. Filling four point bending specimen 4.

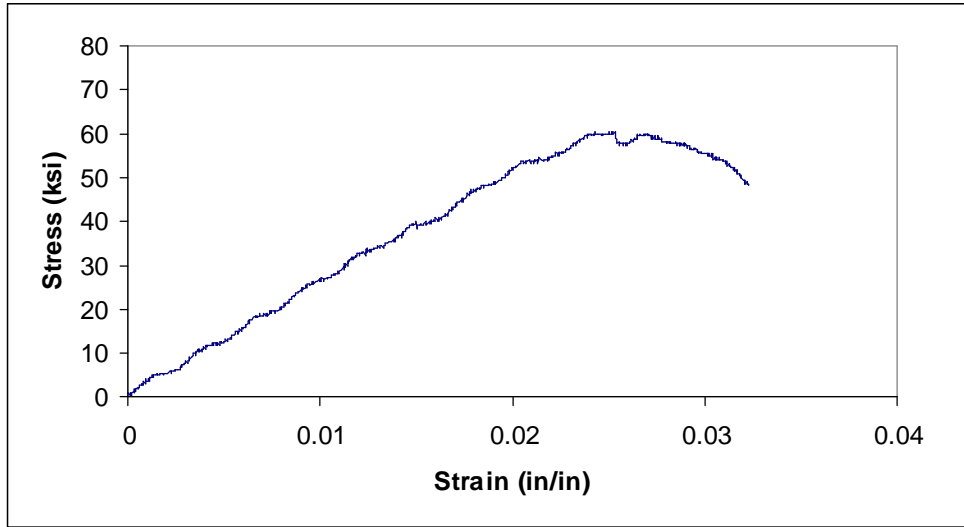


Figure J.5. Filling four point bending specimen 5.

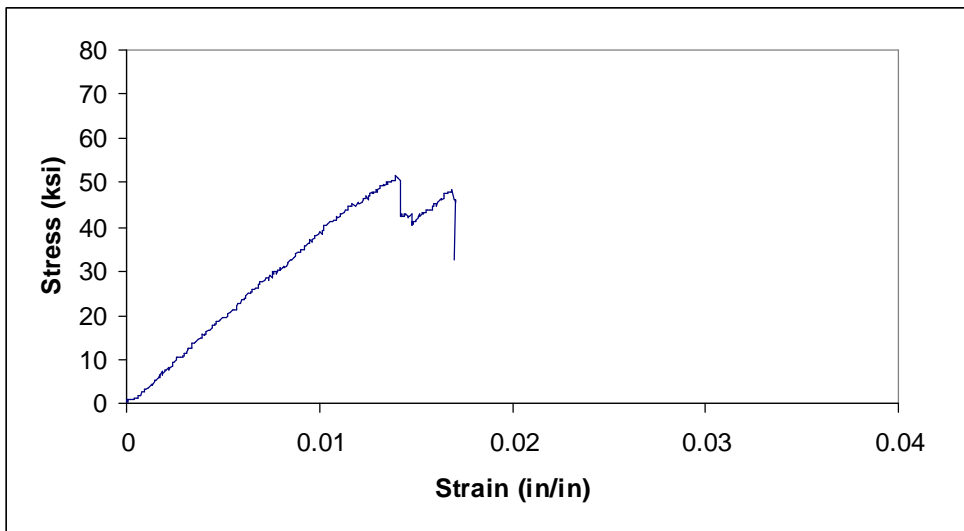


Figure J.6. Filling four point bending specimen 6.

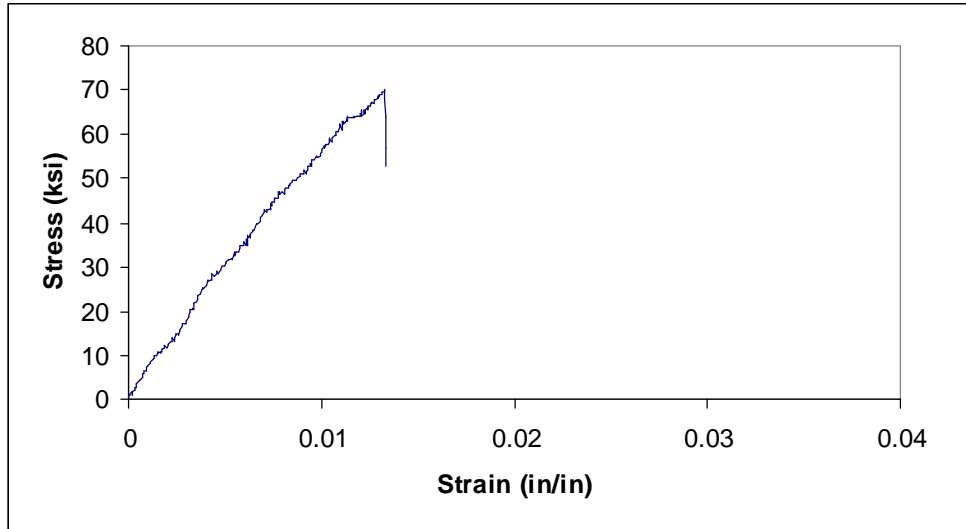


Figure J.7. Filling four point bending specimen 7.

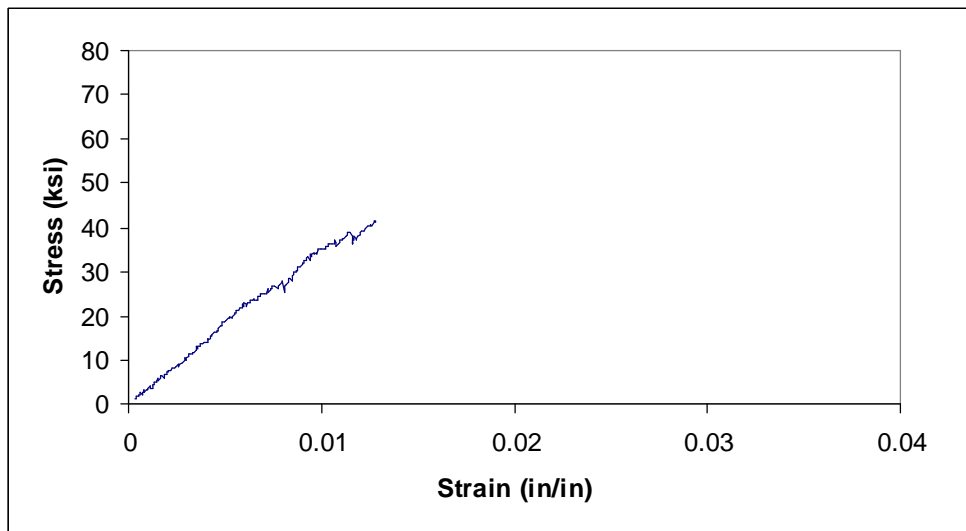


Figure J.8. Filling four point bending specimen 8.

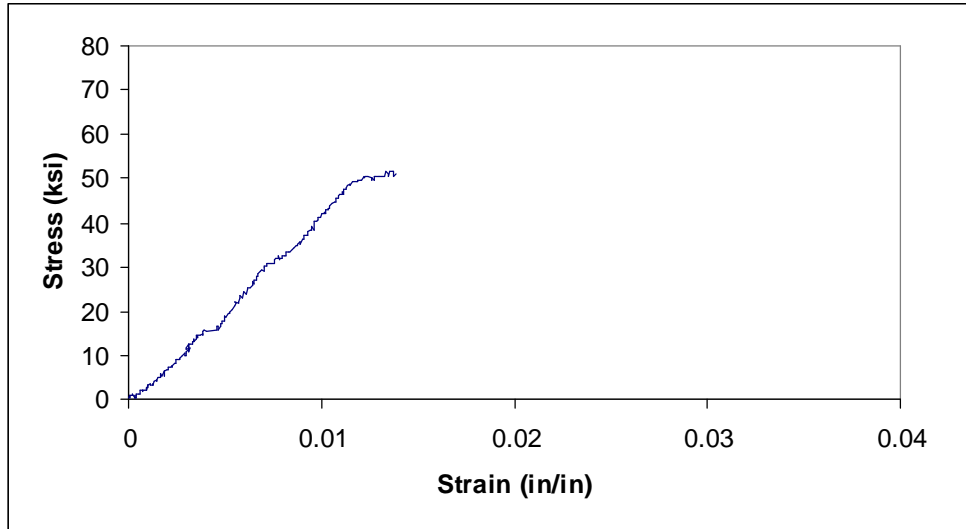


Figure J.9. Filling four point bending specimen 9.

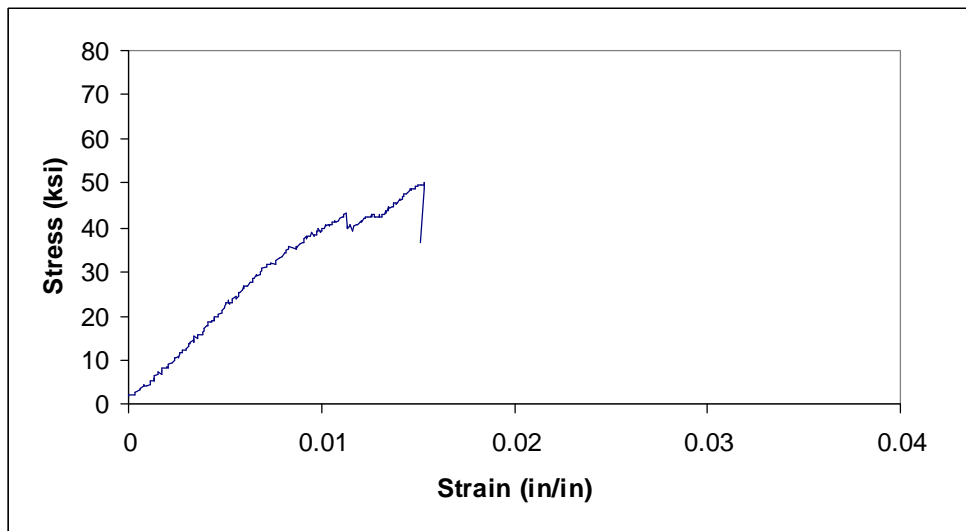


Figure J.10. Filling four point bending specimen 10.

Appendix K. Shear Connector Study

Table K.1. Vertical flange shear connector failure progression.

ID	Description of Progressive Failure
V1	<p>1st time loaded: reached capacity of 25 kip load cell concrete exhibited small shear cracks</p> <p>2nd time loaded: steel plate attached to GFRP surface debonded at 12 kips due to damage to bond and inadequate roughness Bottom plate was removed and surface of plate and specimen were roughened before reattaching the plate</p> <p>3rd time loaded: concrete shear cracks propagated at 25 kip load middle shear connector exhibited failure of all z-yarns GFRP skin delaminated from 96 oz/yd² fabric at top shear connector complete delamination of concrete topping</p>
V2	<p>Epoxy bond failure occurred above top shear connector Concrete shear cracks between top and middle shear connector and above middle shear connector Specimen reaches peak load Bottom steel plate debonds from FRP surface</p>
V3	<p>Concrete shear cracks visible at peak load Topping above top shear connector delaminates from GFRP topping, also delaminating the shear connector fabric from the 96 oz/yd² fabric Failure of middle shear connector z-yarns after large deflection Failure of bottom shear connector filling yarns</p>

Table K.2. Rectangular core shear connector failure progression.

ID	Description of Progressive Failure
R1	<p>Small shear cracks occur at peak load Uniform delamination of concrete topping, force is transferred to shear connectors causing partial failure of filling yarns in middle and bottom shear connector Shear connectors rotate due to large deflections under a low, constant load</p>
R2	<p>Shear crack occurs above top shear connector at peak load Concrete topping delaminates from shear connector fabric soon after with no other significant cracking of concrete Shear connectors rotate due to excessive deflections, failing filling yarns of all three shear connectors</p>
R3	<p>Concrete topping delaminates from shear connector fabric soon after with no other significant cracking of concrete Shear crack occurs above top shear connector at peak load Shear connectors rotate due to excessive deflections, failing filling yarns of all three shear connectors</p>

Table K.3. Tapered core shear connector failure progression.

ID	Description of Progressive Failure
T1	Concrete begins to debond from shear connector fabric above top skin Shear cracks noticeable in concrete below each shear connector Shear crack above upper shear connector propagates to top steel plate Failure of shear connectors results in delamination of overlapped fabric on middle shear connector, other shear connectors remain intact
T2	Concrete shear cracks occur at peak load above top shear connector and in-between all shear connectors Concrete topping begins to delaminate above top shear connector Load begins to drop Shear connector fabric completely delaminates from 96 oz/yd ² fabric, ending test
T3	Concrete shear crack occurs above top shear connector at peak load Concrete topping begins to delaminate Shear connector fabric delaminates from 96 oz/yd ² fabric at middle shear connector, allowing excessive rotation of middle shear connector and delamination of overlapped skins Bottom shear connector fails on upper side due excessive deflection

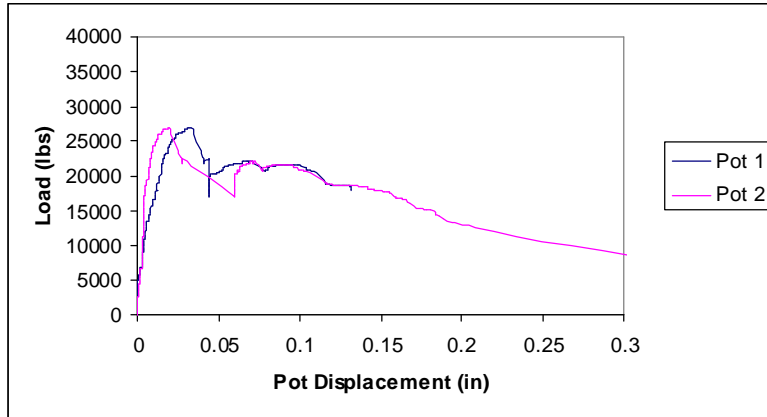


Figure K.1. Vertical flange specimen 1 (V1) load vs. pot displacement.

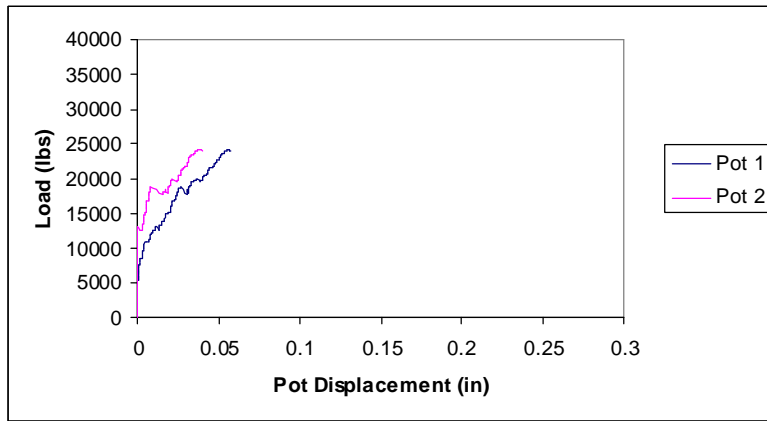


Figure K.2. Vertical flange specimen 2 (V2) load vs. pot displacement.

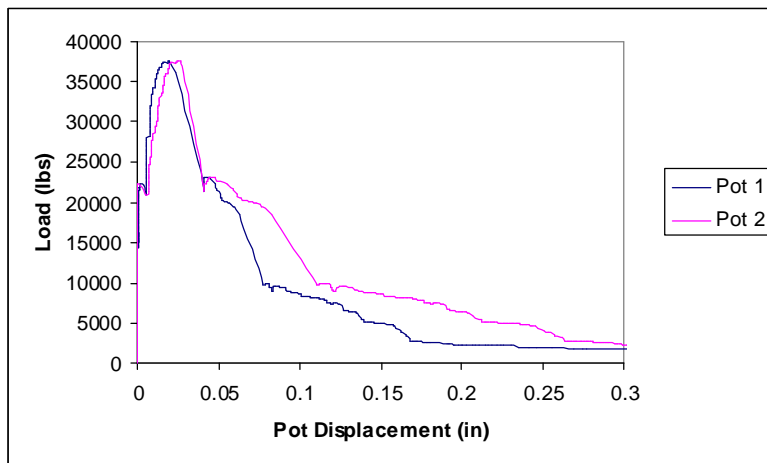


Figure K.3. Vertical flange specimen 3 (V3) load vs. pot displacement.

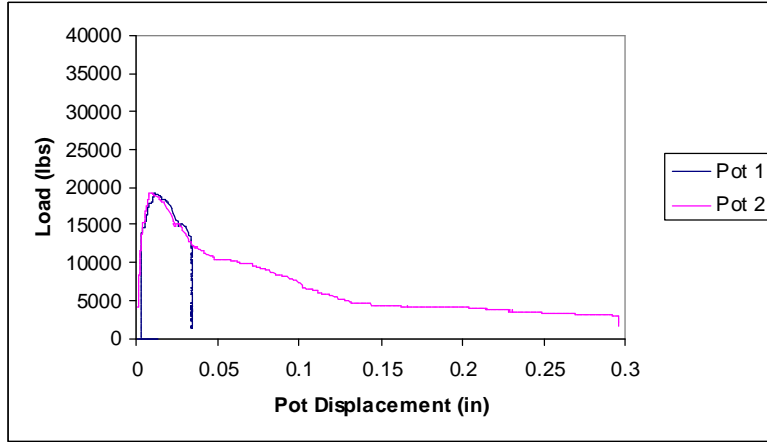


Figure K.4. Rectangular specimen 1 (R1) load vs. pot displacement curve.

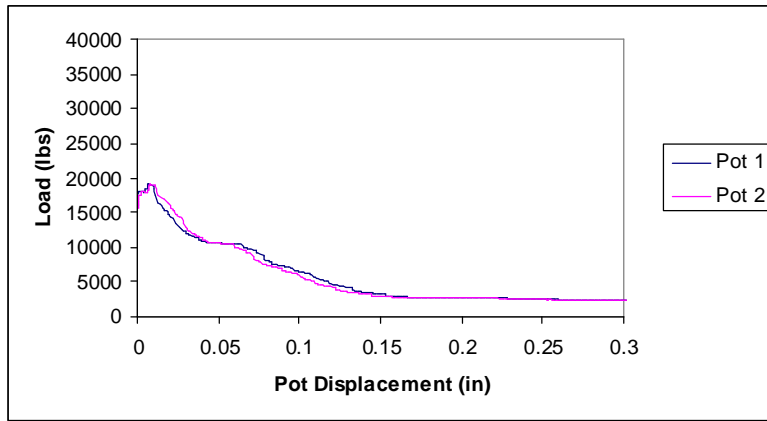


Figure K.5. Rectangular specimen 2 (R2) load vs. pot displacement curve.

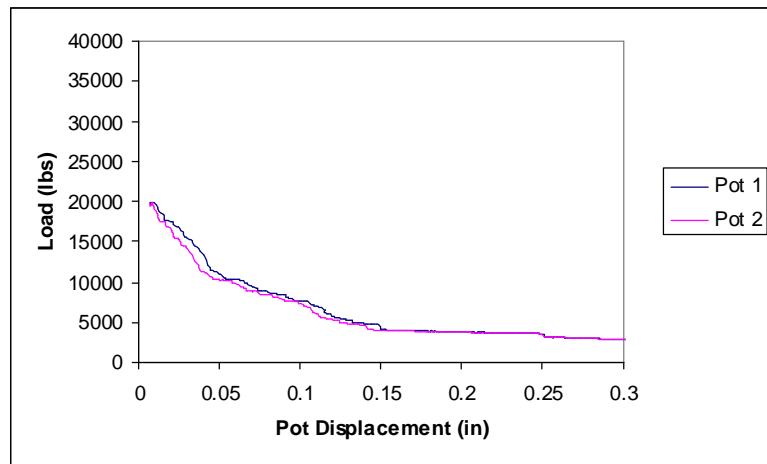


Figure K.6. Rectangular specimen 3 (R3) load vs. pot displacement curve.

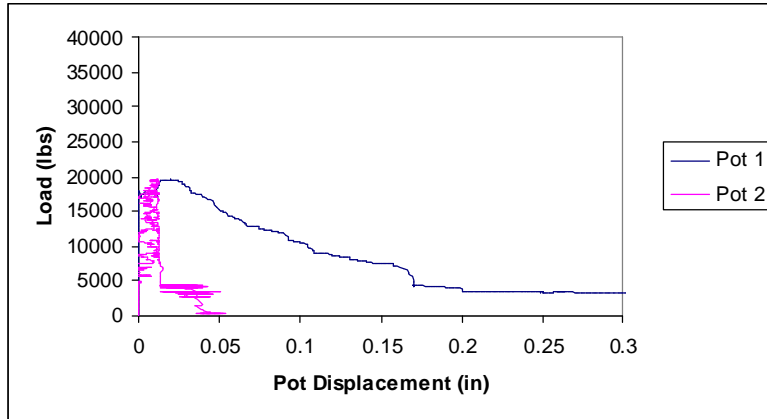


Figure K.7. Tapered specimen 1 (T1) load vs. pot displacement curve.

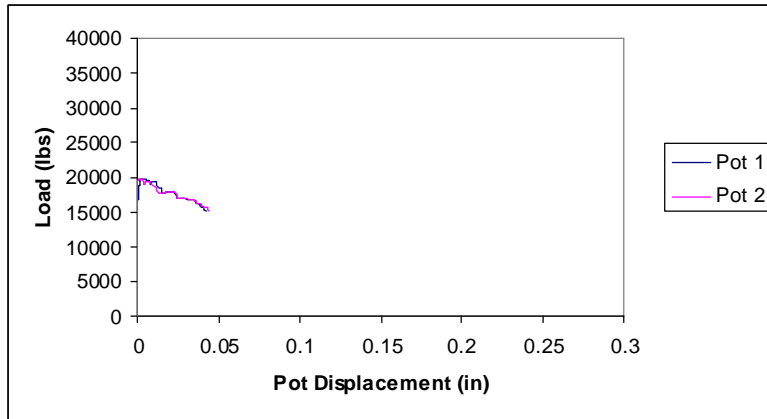


Figure K.8. Tapered specimen 2 (T2) load vs. pot displacement curve.

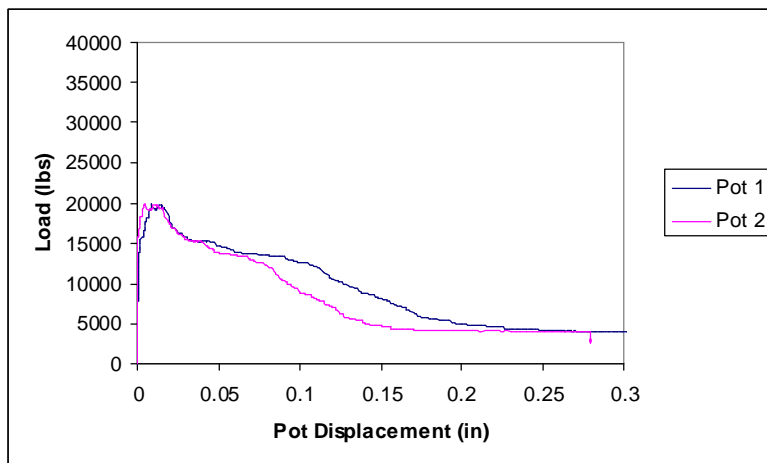


Figure K.9. Tapered specimen 3 (T3) load vs. pot displacement curve.

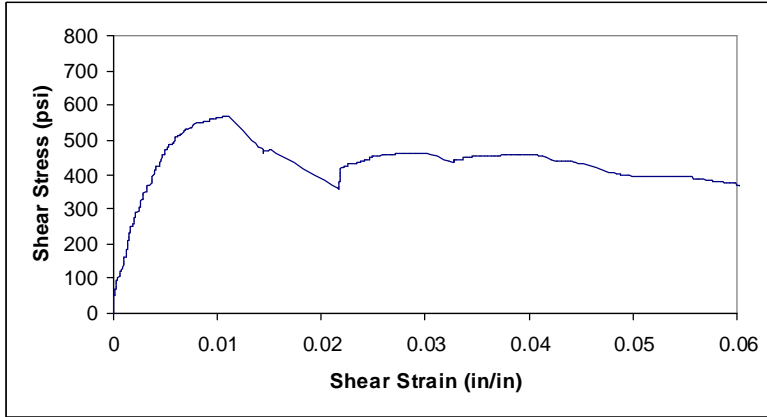


Figure K.10. Vertical flange specimen 1 (V1) stress vs. strain curve.

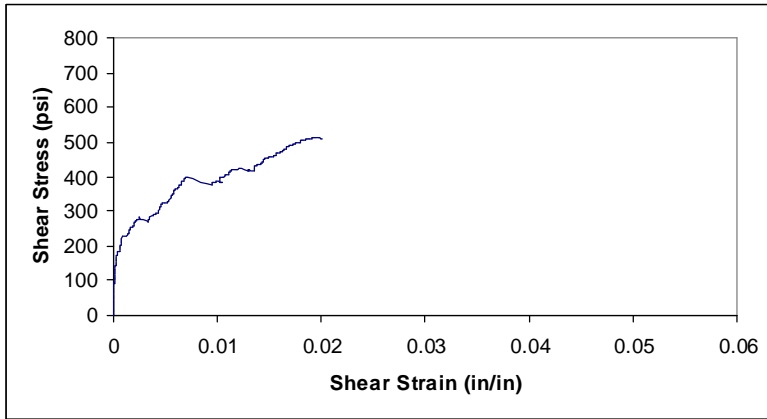


Figure K.11. Vertical flange specimen 2 (V2) stress vs. strain curve.

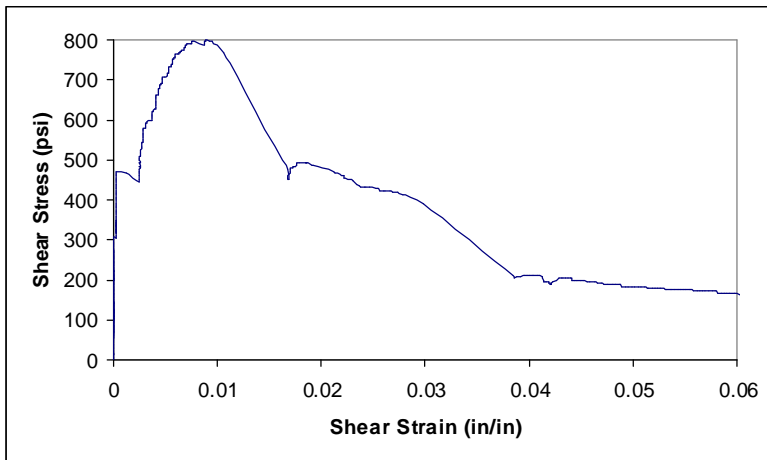


Figure K.12. Vertical flange specimen 3 (V3) stress vs. strain curve.

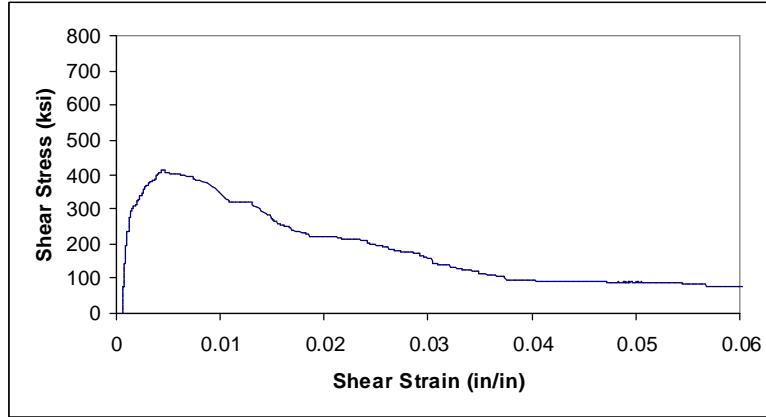


Figure K.13. Rectangular specimen 1 (R1) stress vs. strain curve.

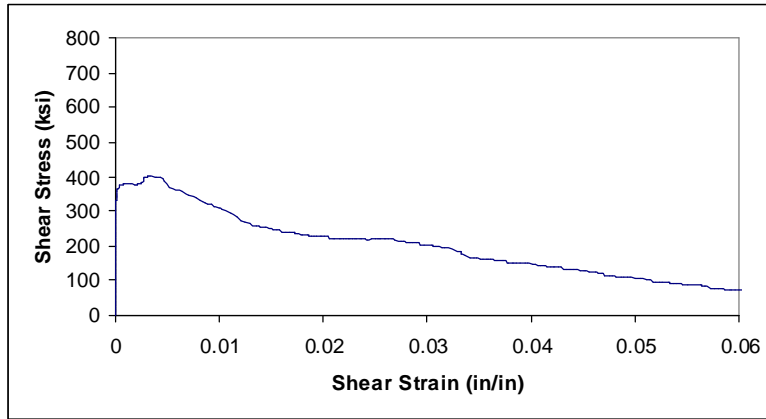


Figure K.14. Rectangular specimen 2 (R2) stress vs. strain curve.

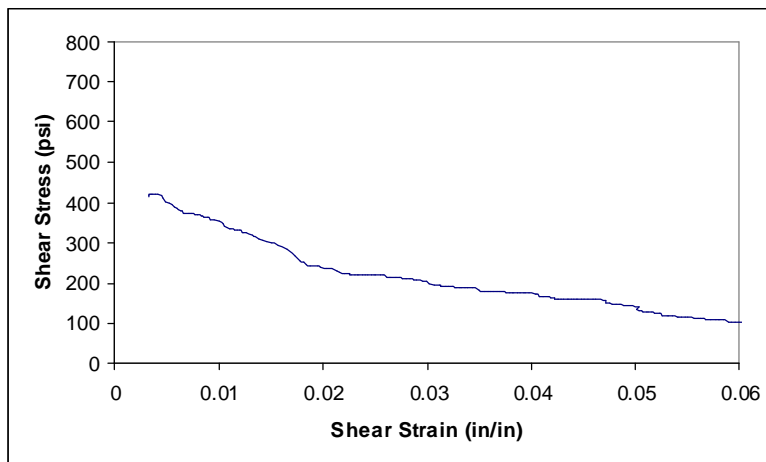


Figure K.15. Rectangular specimen 3 (R3) stress vs. strain curve.

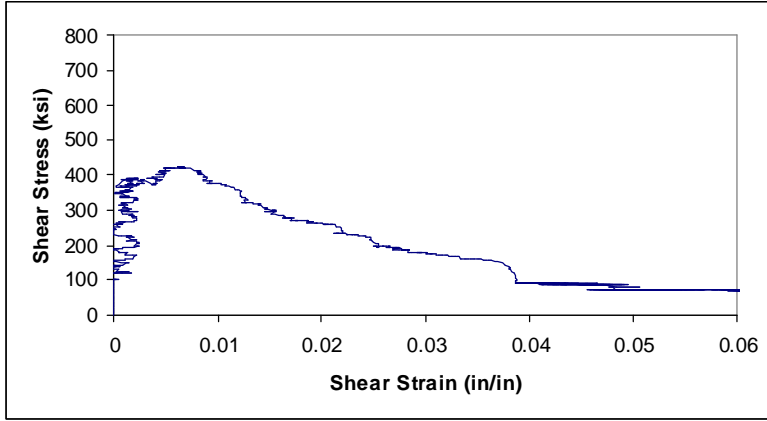


Figure K.16. Tapered specimen 1 (T1) stress vs. strain curve.

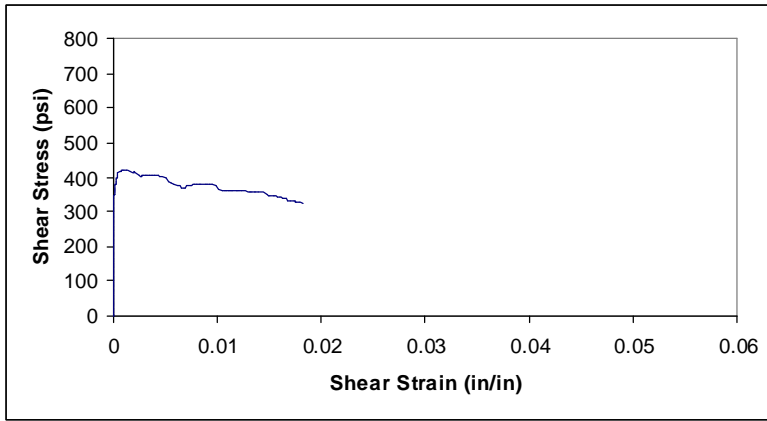


Figure K.17. Tapered specimen 2 (T2) stress vs. strain curve.

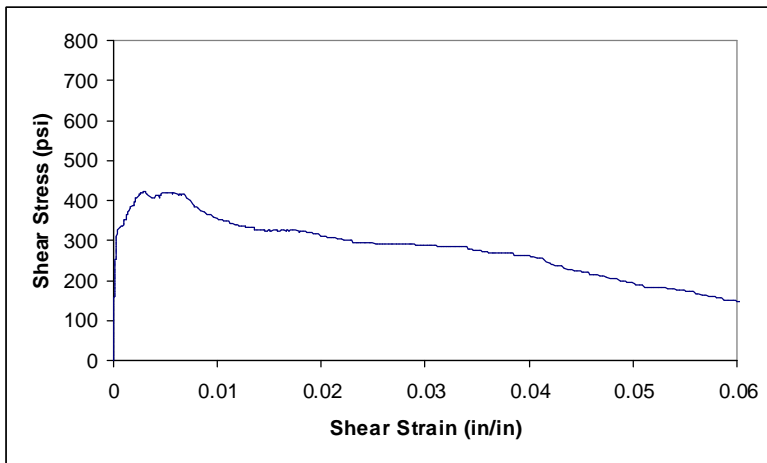


Figure K.18. Tapered specimen 3 (T3) stress vs. strain curve.

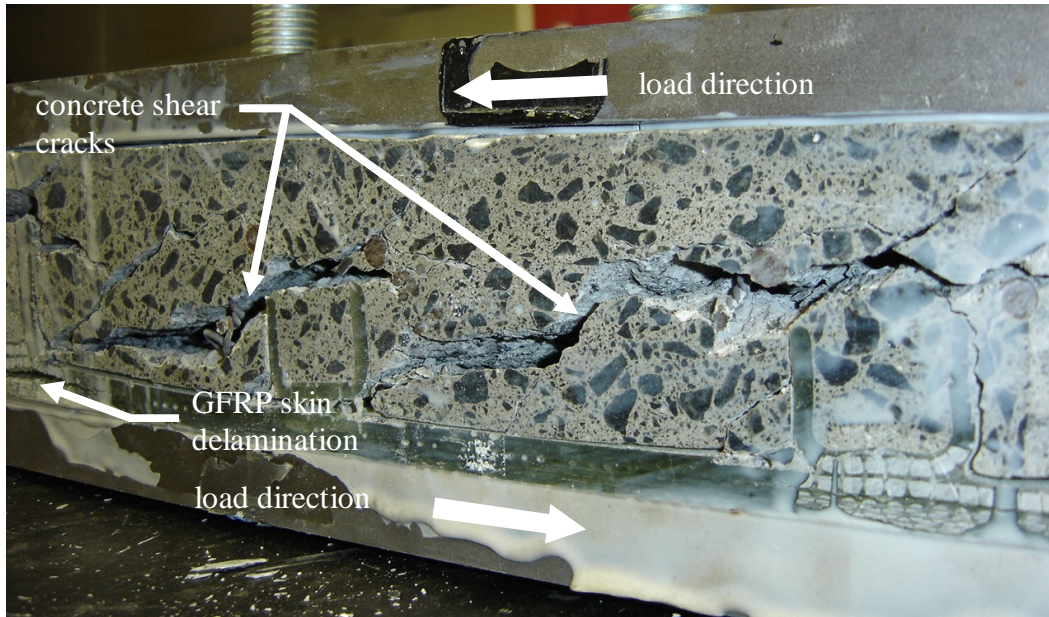


Figure K.19. Vertical flange specimen 1 (V1) failure mode.

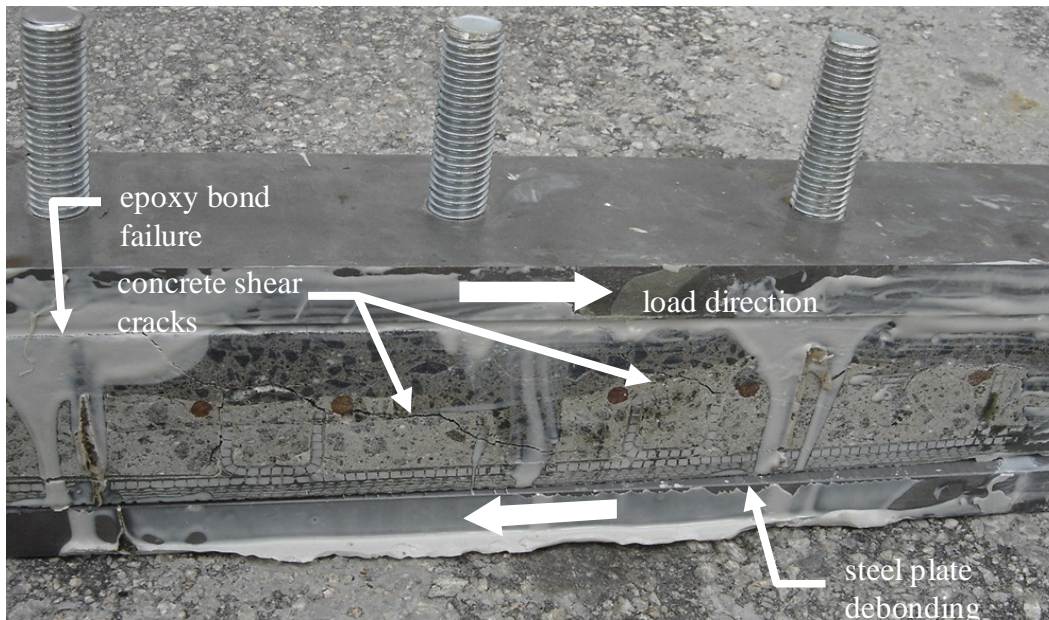


Figure K.20. Vertical flange specimen 2 (V2) failure mode.

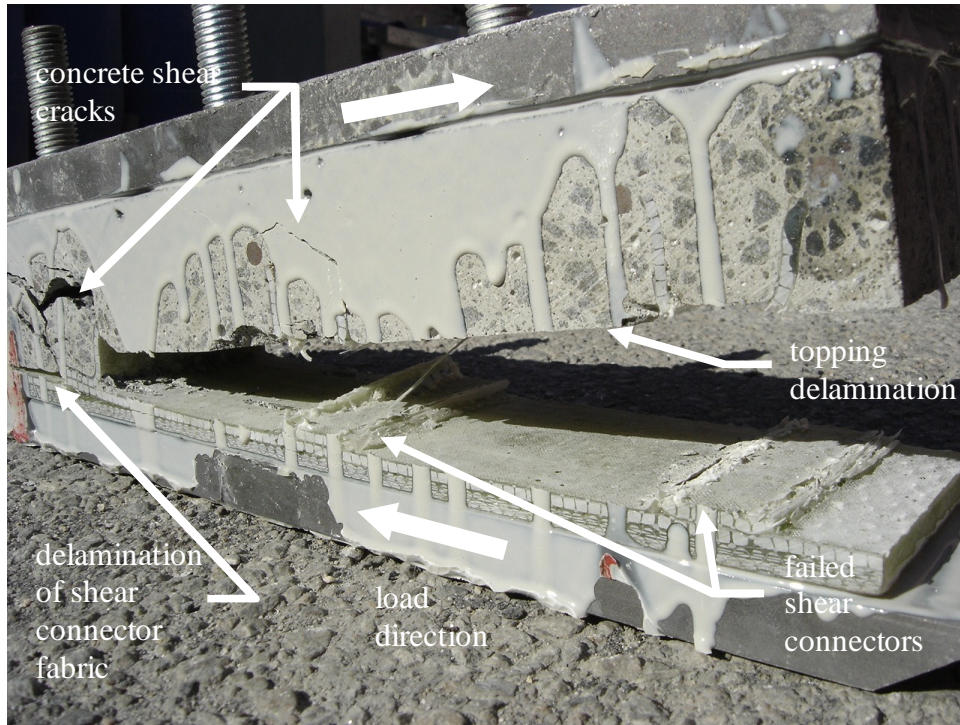


Figure K.21. Vertical flange specimen 3 (V3) failure mode.

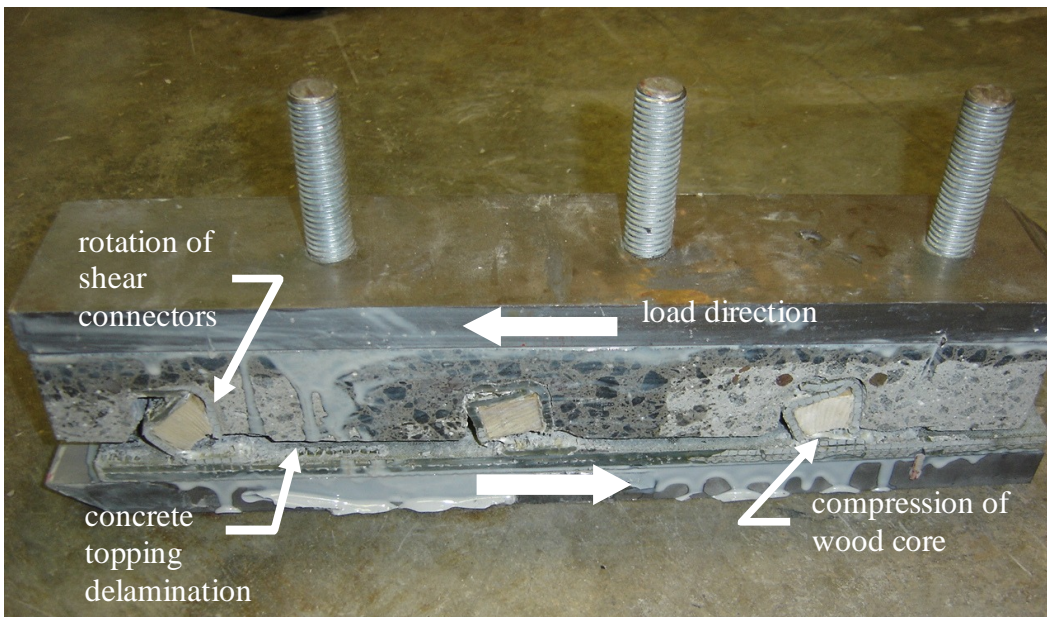


Figure K.22. Rectangular specimen 1 (R1) failure mode.

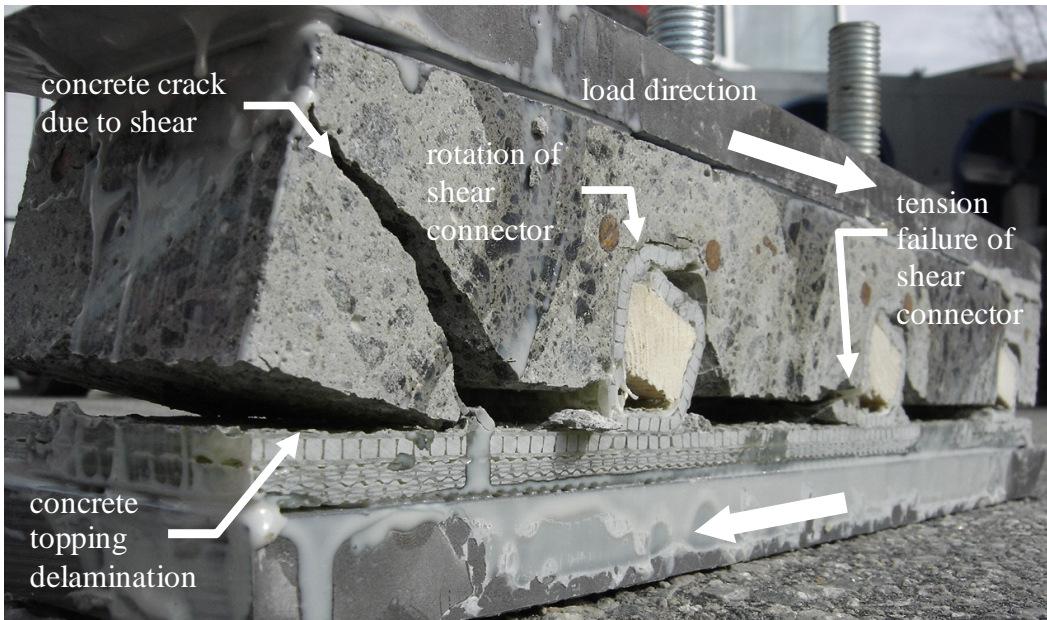


Figure K.23. Rectangular specimen 2 (R2) failure mode.

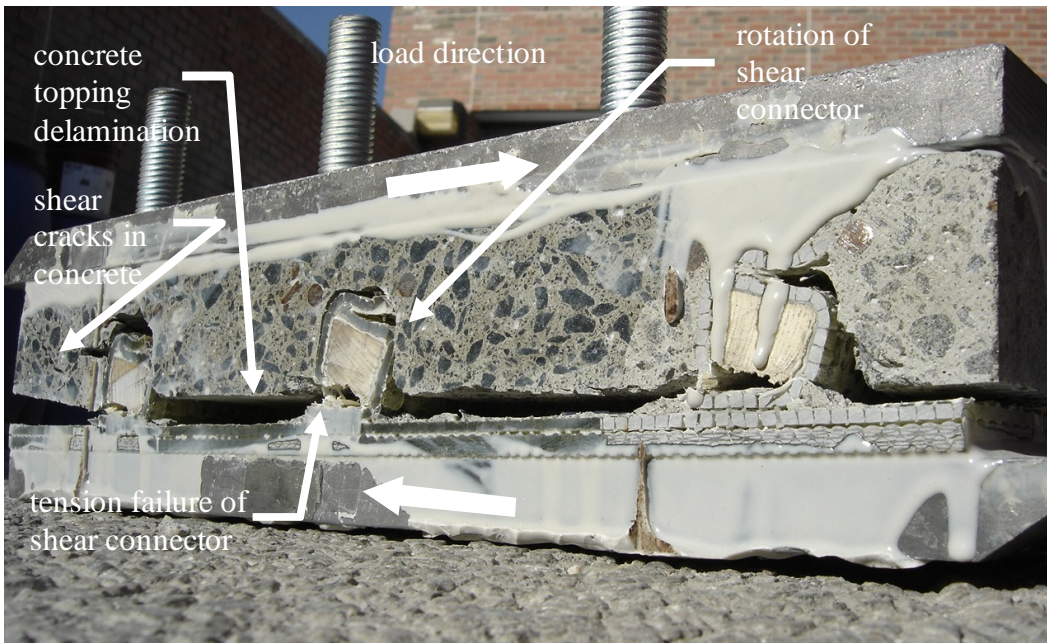


Figure K.24. Rectangular specimen 3 (R3) failure mode.

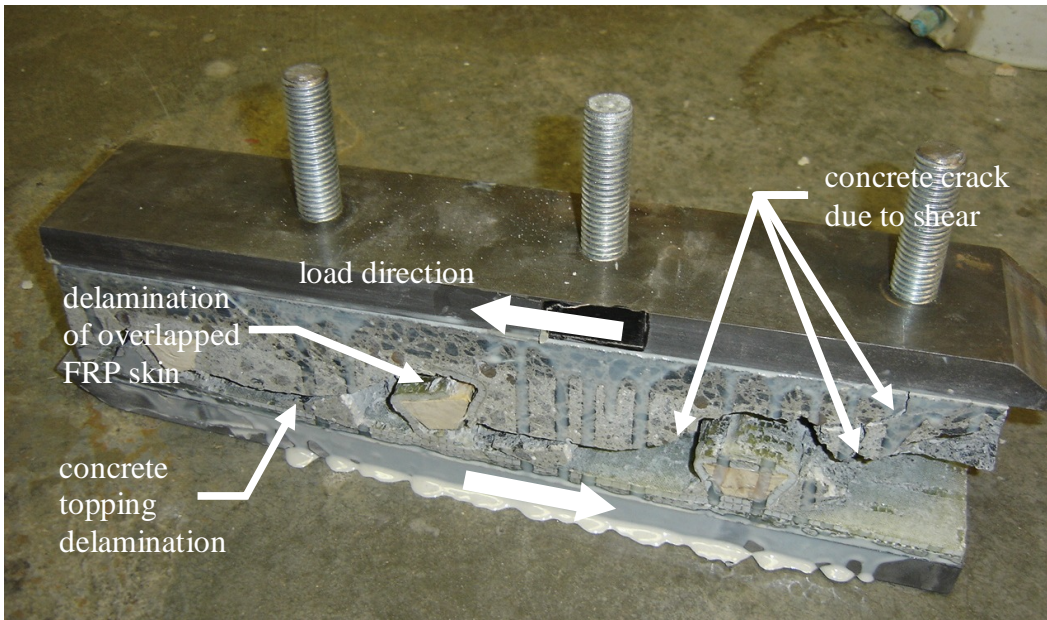


Figure K.25. Tapered specimen 1 (T1) failure mode.

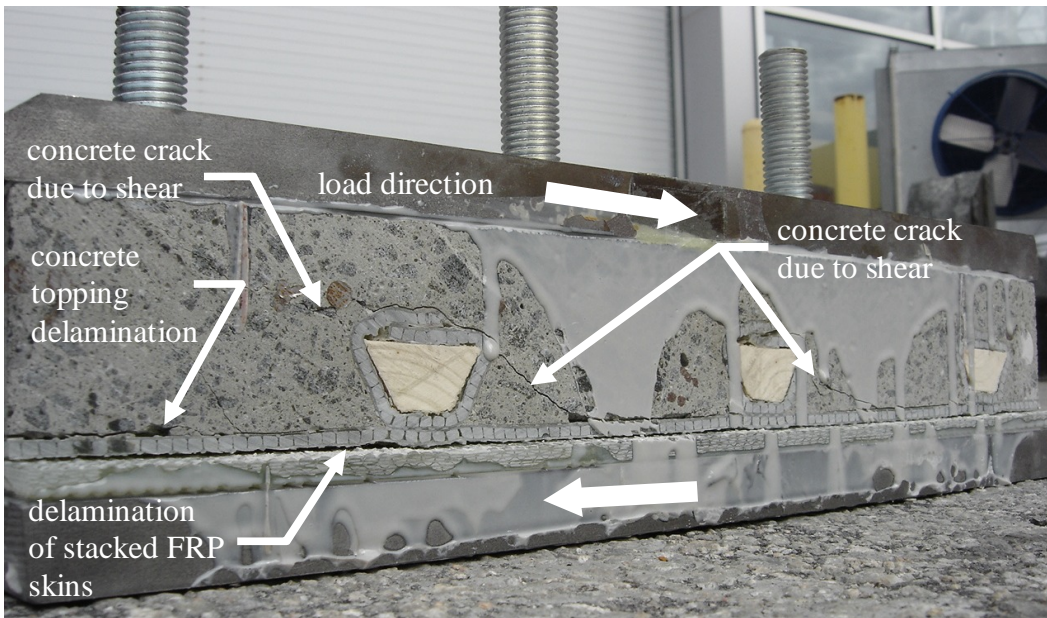


Figure K.26. Tapered specimen 2 (T2) failure mode.

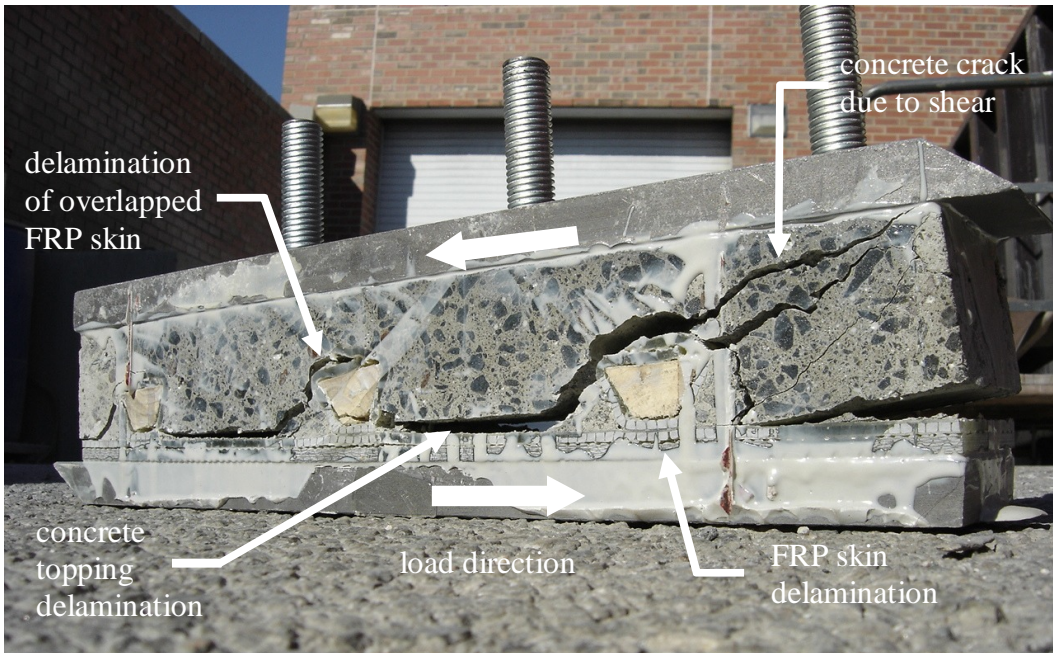


Figure K.27. Tapered specimen 3 (T3) failure mode.

Cited References

- 3TEX. (2004) “96 oz 3Weave™ E-Glass 2022 Silane Sized Product Data Sheet.”
<http://www.3tex.com/uploadedfiles/P3W-GE044.pdf>.
- AAA. (2006) “North Carolina’s Top 20 Substandard Bridges.”
<http://www.aaacarolinas.com/Newsroom/Pressrelease/downloads/021406NCTop20chart.htm>.
- AASHTO. (2004) AASHTO LRFD Bridge Design Specifications. 3rd ed. American Association of State Highway and Transportation Officials.
- ACI. (2002) ACI 318-02 Building Code and Commentary.
- AISC. (2001) Manual of Steel Construction, Load and Resistance Factor Design, 3rd ed. American Institute of Steel Construction.
- Alampalli, Sreenivas and Kunin, Jonathan. (2003) “Load testing of an FRP bridge deck on a truss bridge.” *Applied Composite Materials* Vol 10, pp 85-102.
- Aref, Amjad, Alampalli, Sreenivas, and He, Yihong. (2004) “Performance of a fiber reinforced polymer web core skew bridge superstructure. Part I: field testing and finite element simulations.” *Composite Structures* Vol 69, Issue 4, August, pp 491-499.
- Allen, Howard G. (1969) Analysis and Design of Sandwich Panels. Oxford: Pergamon Press.
- ASCE. (2005) “Report Card for America’s Infrastructure.” www.asce.org/reportcard.
- ASTM A 370-05 (2005). “Standard Test Methods and Definitions for Mechanical Testing of Steel Products.” ASTM International.

APPENDICES

- ASTM C 39/C 39M. (2005) “Standard Test Method for Compressive Strength of Cylindrical Concrete Specimens.” ASTM International.
- ASTM C 143/C 143M Rev A. (2005) “Standard Test Method for Slump of Hydraulic-Cement Concrete.” ASTM International.
- ASTM C 273. (2000) “Standard Test Method for Shear Properties of Sandwich Core Materials.” ASTM International.
- ASTM C 469-02. (2002) “Standard Test Method for Static Modulus of Elasticity and Poisson’s Ratio of Concrete in Compression.” ASTM International.
- ASTM D 3039/D 3039M-00. (2006) “Standard Test Method for Tensile Properties of Polymer Matrix Composite Materials.” ASTM International.
- ASTM D 3171-99. (2004) “Standard Test Methods for Constituent Content of Composite Materials.” ASTM International.
- ASTM D 6272-02. (2002) “Standard Test Method for Flexural Properties of Unreinforced and Reinforced Plastics and Electrical Insulating Materials by Four-Point Bending.” ASTM International.
- Bakis, C.E., Bank, L.C., Brown, V.L., Cosenza, E., Davalos, J.F., Lesko, J.J., Machida, A., Rizkalla, S.H., Triantafillou, T.C. (2002) “Fiber-Reinforced Polymer Composites for Construction—State-of-the-Art Review.” *Journal of Composites for Construction*, May.
- Carlson, Cheryl. (1995) “The influence of matrix modification on the properties of 3-D woven composites.” *Ph.D. Dissertation*. North Carolina State University.
- Chou, T.W. and Ko, F.K., eds. (1989) Textile Structural Composites, Composite Material Series Volume 3. New York: Elsevier Science Publishers B.V.

CRC Press. (2006) http://en.wikipedia.org/wiki/Filament_winding.

Davey, Scott, Gerard M. Van Erp, and Roy Marsh. (2001) “Fibre composite bridge decks—an alternative approach.” *Composites Part A: Applied Science and Manufacturing*, Vol 32, Issue 9, September, pp. 1339-1343.

Fiber-Tech. (2006) <http://www.fibertecheng.com/vartm.htm>.

Gu, Pu. (1994) “Analysis of 3-D woven performs and their composite properties.” *Ph.D. Dissertation*. North Carolina State University.

He, Yihong, and Aref, Amjad J. (2003) “An optimization design procedure for fiber reinforced polymer web-core sandwich bridge deck systems.” *Composite Structures* Vol 60, Issue 2, May, pp. 183-195.

Henderson, Mark P. (2006) “Design of FRP Structural Components.” Presentation to the 2006 Transportation Research Board. January 22, 2006.

Hull, D. and Clyne, T.W. (1996) An Introduction to Composite Materials, 2nd Ed. Cambridge.

“Hydeck - A Durable and Efficient Hybrid Bridge Deck System.” (2005) Nova Award Nomination 22. <http://www.cif.org/nom2005/nom-2005-22.pdf>.

Jeong, Sang-Mo, Kim, Sang-Jin, Kim, Young-Bum, Kim, Hyeong-Yeol, and Park, Ki-Tae. (2005) “Reliability analysis on flexural behavior of FRP bridge decks.” *2003 ECI Conference on Advanced Materials for Construction of Bridges, Buildings, and Other Structures III*, p. 8.

Karbhari, Vistasp. (2004) “E-glass/vinylester composites in aqueous environments: effects on short-beam shear strength.” *Journal of Composites for Construction* March/April, pp. 148-149.

- Karbhari, Vistasp, Wang, Dongqing, and Gao, Yanqiang. (2001) “Processing and performance of bridge deck subcomponents using two schemes of resin infusion.” *Composite Structures* Vol 51, Issue 3 March, pp. 257-271.
- Keller, T. (2003) “Use of fiber reinforced polymers in bridge construction.” *Structural Engineering Documents No. 7, International Association for Bridge and Structural Engineering IABSE*, ISBN 3-85748-108-0, 131 pages.
- Keller, Thomas and Gurtler, Herbert. (2005) “Composite action and adhesive bond between fiber-reinforced polymer bridge decks and main girders.” *Journal of Composites for Construction*, July/August, pp. 360-368.
- Kosmatka, S., Kerkhoff, B., and Panarese, W. (2002) Design and Control of Concrete Mixtures, 14th ed. Portland Cement Association.
- Kumar, Prakash, Chandrashekhara, K., and Nanni, Antonio. (2003) “Testing and evaluation of components for a composite bridge deck.” *Journal of Reinforced Plastics and Composites* Vol 22, No. 5, pp. 441-461.
- Lee, Chang Sung, Chung, Soon Wan, Shin, Heon, and Kim, Seung Jo. (2004) “Virtual material characterization of 3-D orthogonal woven composite materials by large-scale computing.” *Journal of Composite Materials* Vol 39, No. 10, pp. 851-863.
- Lew, H.S. and Reichard, T.W. (1978) “Prediction of Strength of Concrete from Maturity.” *ACI SP-56: Accelerated Strength Testing*. pp. 229-248.
- Loos, Alfred C. (2001) “Low-cost fabrication of advanced polymeric composites by resin infusion processes.” *Advanced Composite Materials* Vol 10, No. 2,3, pp. 99-106.

- Mohamed, M.H., Zhang, Z. and Dickinson, L. (1988) "Manufacture of multi-layer woven preforms." *ASME, Advanced Composites and Processing Technology*. MD-Vol. 5, Book No. 00484, pp. 81-89.
- Mohamed, Tarek. (2006) "Fabrication and behavior of three-dimensionally woven glass fiber reinforced polymeric bridge deck." Masters Thesis, North Carolina State University.
- Moses, Jonathan. (2005) "Evaluation of Effective Width and Distribution Factors for GFRP Bridge Decks Supported on Steel Girders." Masters Thesis, University of Pittsburgh.
- Nelson, James. (2005) "Behavior of GFRP Bridge Decks for Highway Bridges." Masters Thesis, North Carolina State University.
- Norton, Taylor. (2004) "3-D orthogonal woven glass fiber reinforced polymeric bridge deck: fabrication and experimental investigation." Masters Thesis, North Carolina State University.
- Nystrom, et al. (2003) "Financial Viability of Fiber-Reinforced Polymer Bridges." *Journal of Management in Engineering*. January.
- Park, Ki-Tae, Kim, Sang-Hyo, Lee, Young-Ho, and Hwang, Yoon-Koog. (2005) "Pilot Test on a developed GFRP bridge deck." *Composite Structures*. Vol 70, Issue 1. August, pp. 48-59.
- Reising, RMW, Shahrooz, BM, Hunt, VJ, Neumann, AR, Helmicki, AJ, and M Hastak. (2004) "Close look at construction issues and performance of four Fiber-Reinforced Polymer composite bridge decks." *Journal of Composites for Construction*. ASCE, January/February. pp. 33-42.

Shehata, Emile and Mufti, Aftab. (2005) “The ‘Manitoba’ GFRP Bridge Deck System.”

International Institute for FRP in Construction. Volume 2, Issue 1. February 2005, pp. 2-3.

Takatoya, Takeshi, and Susuki, Ippei. (2004) “In-plane and out-of-plane characteristics of three-dimensional textile composites.” *Journal of Composite Materials* Vol 39, No. 6, pp. 543-556.

Transonite®. (2006) Martin Marietta Composites.

<http://www.martinmarietta.com/Products/transonite.asp>.

Turner, Michael, Harries, Kent, Petrou, Michael, and Rizos, Dimitris, Rizos. (2004) “In situ structural evaluation of a GFRP bridge deck system.” *Composites Structures* Vol 65, Issue 2, August, pp. 157-165.

Williams, Brea, Shehata, Emile, and Rizkalla, Sami. (2003) “Filament-Wound Glass Fiber Reinforced Polymer Bridge Deck Modules.” *Journal of Composites for Construction*. ASCE, August.

Zetterberg, Tobias, Astrom, B, Backlund, Jan, and Burman, Magnus. (2001) “On design of joints between composite profiles for bridge deck applications.” *Composite Structures*, Vol 51, Issue 1, January, pp. 83-91.

Zhou, Aixi, and Keller, Thomas. (2005) “Joining techniques for fiber reinforced polymer composite bridge deck systems.” *Composite Structures* Vol 69, Issue 3, July, pp. 336-345.